Bubble growth and resorption in magma: insights from dissolved water distributions in volcanic glass

MCINTOSH, IONA,MARGARET

Bubble growth and resorption in magma: insights from dissolved water distributions in volcanic glass

Iona Margaret McIntosh

A thesis submitted in partial fulfilment of the requirements for the degree of Doctor of Philosophy at Durham University

Department of Earth Sciences, Durham University

2013

"Double, double, toil and trouble;

Fire burn, and cauldron bubble."

Shakespeare's Macbeth, Act IV Scene 1

Acknowledgements

This project was funded by the National Environment Research Council (NERC Doctoral Studentship NE/H524606/1). Additional funding was provided by the Japanese Society for the Promotion of Science Summer Program (2012), which enabled me to undertake FTIR analyses at the Japan Agency for Marine-Earth Science and Technology (JAMSTEC).

Four long years have gone into the making, if not the actual writing, of this thesis, and there are many people whose help and support I would like to acknowledge.

First and foremost I'd like to thank my primary supervisors, Ed Llewellin and Madeleine Humphreys. I have learned so much from you, both about science and how to be a scientist, and I am lucky to have had your support and guidance along the way.

Ed, you have been a fantastic supervisor. You always made time to talk, whether about science or logistics, and those signed blank requisition forms came in handy too. You could always be relied upon when I had a problem and have always provided excellent advice. More importantly, your approach to science has inspired me and will continue to influence me long after the PhD is finished. It has been a genuine pleasure discussing science and taking the piss in equal measure. Thank you.

Madeleine, thank you for sharing your BSEM and SIMS expertise and geochemistry knowledge in general, without which Ed and I would probably still be at the 'Let's zap it with… something…' stage. Ever since the 'Um, what the…?' moment during the original SIMS analysis in Edinburgh, I could rely on you to ask the important questions, and to help me find the answers.

I would also like to thank my second supervisor at Durham, Claire Horwell, whose support and input have been of great benefit to this work.

Next I'd like to thank the people who so generously provided the samples that made this project possible – Alain Burgisser, Ian Schipper, and Jessica Larsen. Your patience with my many questions about sample conditions and experimental procedures is greatly appreciated, and our discussions enabled me to arrive at my eventual conclusions.

At every stage of sample analysis I have been the grateful beneficiary of technical expertise and support. I would like to thank the sample technicians at Durham, David Sayles and Ian Chaplin, for their help with sample preparation, and David Wertheim at Kingston University for facilitating the confocal microscopy analysis.

I have necessarily spent many long hours on the SEM during this project, and I would like to thank Leon Bowen and Budhika Mendis of the GJ Russell Microscopy Facility at Durham for their technical expertise and their willingness to help, often out-of-hours, when sample coaters break or mystery alarms start to sound. Leon, I promise I'll make you that poster before I go.

Similarly, I have undertaken a couple of stints of intensive SIMS time at the Edinburgh Ion Microprobe Facility and I would like to thank Richard Hinton and John Craven for both their technical expertise and scientific discussion. In particular I'd like to thank Richard for his cheerful morning set up and running of standards while I enjoyed yet another B&B fried breakfast, and John for the frequent cups of tea that provided both caffeine and the ability to digest the aforementioned breakfasts.

Finally, I'd like to thank Alex Nichols for being my host researcher during my time at JAMSTEC, with all the paperwork that entails, and for providing an excellent intensive crash course in FTIR sample preparation, analysis and interpretation, as well as being an excellent tour guide and aficionado of local restaurants (and karaoke bars). I'm looking forward to the next two years. I'd also like to give a special shout out to Felix von Aulock – without your paintbrush tip, my samples would probably still be languishing in the bottom of a dish of acetone!

I'd also like to acknowledge the support of the members of the Durham Volcanology Group. I have learned so much at our DVG meetings (including some science!) and your collective input, varying from incredibly useful to totally mad, was always greatly appreciated. I would like to thank everyone for putting up with 4 years of bubble chat, including those honorary members of DVG who were only in it for the laughs and the 'fieldtrips' to chocolate factories.

In addition to the science, it's the friendships that really make the PhD experience, and I would like to thank the following people for all the fun we've had together in Durham: Amy, Ben, BJ, Claire Mc, Claire N, Dave A, Dave D, Dean, Fran, Harriet, Ian, Izzy, Jen, Kathy, Kay, Kirstie, Maddy, Pete, Sabina, Sam, Sarah H (née C), Sarah P, Simon, Suzie, Valentina, Vali, Viv, Wanda. Particular thanks go to my housemates over the years – Izzy, Suzie and Valentina. It has been a pleasure sharing your sofas. I reserve my biggest thanks for the two people that provided so much support during my write up. Izzy, your delight at my torment never failed to make me laugh (where would I be without your regularly emailed deadline countdowns?!), and you provided wisdom, distraction and humour when I needed it most. And Valentina, your unfailingly sunny disposition and boundless optimism ('See? You are doing that!') actually convinced me that the impossible could in fact be possible. Thank you for the garden and the conservatory, the guanciale and the cheese.

A huge thank you goes to all my 'non-Durham' friends: Becca, Lydia, Sophie, Chloe, Rachel, Becky, Liz. You have always been there for me when I have needed to escape the PhD life, and I am incredibly lucky to have you as my friends.

And last but not least, my biggest thanks go to my family: Mum, Dad, Alastair, Andrew, Eliza. You have been an incredible source of support throughout, and I love you all very much.

Abstract

Volcanic eruptions are driven by the growth of gas bubbles in magma, which grow and shrink as volatile species exsolve from and dissolve back into the melt in response to changes in the local environment, particularly in pressure and temperature. This movement of volatiles, particularly water, is recorded in the glass around vesicles and recent studies have used this record to interpret natural samples. This thesis investigates the processes that control bubble growth and resorption in magma, by measuring the distribution of dissolved H_2O in experimentally-vesiculated volcanic glasses. H_2O concentration profiles obtained using SIMS-calibrated BSEM imaging and H_2O speciation data obtained using FTIR spectroscopy, are interpreted in the context of the known pressure and temperature history of the samples.

Samples are found to have undergone partial bubble resorption during the quench to glass at the end of experiments, as a result of increasing H_2O solubility with decreasing temperature. Analysis of the lengthscale and timing of the resulting H_2O concentration profiles demonstrates that the majority of resorption occurs above the glass transition. This quench resorption is associated with a reduction in bubble volumes which creates characteristic textures, such as buckled melt films between adjacent vesicles and reoriented cracks around resorption halos. Highly disequilibrium H_2O speciation ratios within resorption halos are found to be diagnostic of quench resorption and can preserve evidence of pre-quench bubble growth

Quench resorption can increase sample H_2O concentrations and H_2O_m:OH ratios and reduce bubble volumes and sample porosities. Studies based on these parameters must therefore consider the potential impact of quench resorption, which is expected to be greatest for samples with high H_2O concentrations, slow quench and low initial sample porosities. H_2O speciation data offer a way to investigate these impacts in unconstrained natural samples and could provide a tool for forensic interrogation of their eruptive history.

Declaration

I declare that this thesis, which I submit for the degree of Doctor of Philosophy at Durham University, is my own work and not substantially the same as any which has previously been submitted at this or any other university.

Iona M. McIntosh
Durham University
September 2013

Table of Contents

List of Figures

Chapter 4: H_2O concentration profiles around vesicles

Chapter 5: Quench resorption textures

Chapter 6: Insights from H_2O speciation

List of Tables

Details of Personal Communications (*pers. comm.*):

Dr Alain Burgisser – Provided the ABG series of samples

ISTerre

Université de Savoie – CNRS

73376 LE BOURGET DU LAC – CEDEX

France

Dr C. Ian Schipper – Provided sample IS14

School of Geography, Environment and Earth Sciences

Victoria University of Wellington

PO Box 600

Wellington 6140,

New Zealand

Dr Jessica Larsen – Provided the MCN series of samples

Geophysical Institute

Department of Geology and Geophysics

Alaska Volcano Observatory

University of Alaska Fairbanks

Fairbanks, AK 99775

Chapter 1: Introduction

1.1 Thesis Rationale

This thesis investigates the processes that control the growth and resorption of gas bubbles in magma. The evolution of the gas phase of a magma is a key control on magma properties, including its vesicularity, buoyancy, rheology and permeability. When magmatic gas exsolves from silicate melt, the increase in the buoyancy of the magma created by the presence of a bubble population drives the magma body upwards through the crust until its ultimate eruption at the surface. Understanding and quantifying bubble growth is therefore one of the most fundamental challenges in physical volcanology.

Since the first major study of Sparks (1978), considerable effort has gone into determining the processes that control the dynamics of bubble growth and how these may influence the style of volcanic eruptions and the nature of the hazard that results. These studies have encompassed three main approaches: theoretical and numerical modelling of bubble growth; experimental studies of bubble growth under controlled conditions; and investigation of natural samples from eruptions of varying style. Together these studies have advanced understanding of bubble growth to the point where physical models of bubble growth can be incorporated into numerical models of volcanic eruptions.

Recently, attention has turned from bubble growth to processes of bubble resorption. The dominant physical control on bubbles in magma is the decompression experienced during magmatic ascent, which will tend to result in growth. Bubble resorption therefore points to additional controls that modify bubble growth history. Understanding the dynamics of bubble resorption can therefore inform our understanding of other processes occurring within volcanic systems. Recent studies have used observations of bubble resorption in natural samples to make

inferences about volcanic processes such as the rate of convection within volcanic conduits (Carey et al. 2013) and the occurrence of pressure cycling at conduit margins (Watkins et al. 2012), while experimental studies have investigated the impact of vapour fluxing on degassing processes (Yoshimura & Nakamura 2010).

The study of Watkins et al. (2012) is particularly pertinent in the context of this thesis, since it concerns bubble resorption in natural samples with similar composition (rhyolite) and H_2O contents as the experimental samples presented here. Watkins et al. analysed the distribution of H_2O around vesicles in obsidian pyroclasts from the 1340 AD eruption of Mono Craters, California, USA. They found that H_2O concentration in the glass increases towards the vesicle walls, which indicates that the bubbles were resorbing at the time that the concentration profiles were formed. The authors interpret this bubble resorption as evidence of pressure cycling at the conduit margins prior to eruption, and calculate that pressure increases of ~10 MPa would cause the observed resorption profiles. This model of bubble resorption is then used to calculate timescales of bubble resorption and placed in the context of pressure cycling at conduit margins that has been linked to annealing of fractures in pyroclastic obsidian (Cabrera et al. 2011) and the timing of hybrid earthquakes at silicic volcanoes (Tuffen et al. 2003).

As this thesis will demonstrate, however, both pressure and temperature conditions can control bubble resorption. The possible impacts of both pressure and temperature must therefore be considered when interpreting bubble resorption in natural samples, since the implications for volcanic systems of the observed resorption will be very different depending on whether resorption is determined to be caused by pressure or temperature. Similarly, the potential impact of bubble resorption on observed vesicles must be considered even in studies that are not designed to investigate bubble resorption. This is particularly important in experimental studies, where pressure and temperature are controlled in order to investigate the impact of different parameters on degassing processes. Experimental samples are quenched to glass at the end of

the experiment, and their vesicle characteristics (including size, shape and overall sample porosity) can be investigated in the context of the chosen experimental run conditions.

For example, Castro et al. (2012) investigated vesicle textures in experimentally decompressed rhyolite samples, including a sample (ABG1) analysed in this thesis. They observed that neighbouring vesicles in these samples are often separated by a sinuous melt film, and that the direction of melt film curvature is not related to the relative size of the vesicles. This is in contrast to the expectation that the melt film between two adjacent bubbles of equal size will be planar, or, for bubbles of different size, will curve towards the larger bubble as a result of higher internal gas pressure in the small bubble. Castro et al. interpreted these observations as evidence of unusual bubble coalescence mechanisms that occur at high pressures. This interpretation was made in the context of the pressure and temperature conditions of the experimental runs. However, although experimental samples are typically quenched isobarically, they necessarily experience a decrease in temperature from the experimental conditions, which could cause bubble resorption. This bubble resorption may then in turn affect the observed sample characteristics that are used to investigate degassing processes such as bubble coalescence. Understanding the causes of bubble resorption is therefore important not only for interpreting natural samples where resorption is observed, but also for considering the situations, in both natural and experimental studies, where observed bubble populations may have been modified by bubble resorption.

In this thesis, the growth and resorption of bubbles in magma is investigated through the analysis of dissolved H_2O distributions in vesicular volcanic glasses. The focus of this study is on H_2O because it is typically the most abundant magmatic gas, and also exerts a key control on important melt properties such as viscosity. This study utilises experimentally-vesiculated samples created under known conditions in order to relate observations to known environmental history. During bubble growth and resorption, H_2O concentrations in the melt are altered as H_2O either

diffuses into or out of the bubbles. When samples are quenched to glass, H_2O concentration profiles are preserved and can be related to the experimental conditions in order to constrain the processes controlling bubble growth and resorption.

1.2 Thesis Structure

This thesis is structured around three main results chapters that present the key observations and implications of different, but interrelated, aspects of the experimental samples. Chapter 2 provides a detailed background on the aspects of H_2O in silicate melts that are required to interpret the results, including H_2O solubility and diffusivity and the transition between silicate melt and glass. Chapter 3 presents the details of sample production, preparation and analytical methodologies, including discussion of errors and limitations. Chapter 4 presents H_2O concentration profiles around vesicles in glasses and determines their cause. Chapter 5 examines textural evidence in these samples that constrains the implications of the observed H_2O concentration profiles for sample characteristics. Chapter 6 then investigates the distribution of H_2O species around vesicles in order to further constrain the mechanisms that create the observed H_2O concentration profiles. Finally, Chapter 7 summarises the observations and interpretations of Chapters 4, 5 and 6 and discusses their implications for our understanding of bubble growth and resorption, and includes a proposed methodological framework for future investigations, before concluding with a summary of the findings of this thesis.

Chapter 2: H_2O and silicate melts

2.1 Introduction

Silicate melts contain dissolved volatile species that are weakly soluble in the melt, and exsolve to form bubbles. H_2O is the most important of these volatiles since it is typically the most abundant and exerts a strong control on melt properties, such as viscosity, that control magma degassing and eruption dynamics. This chapter presents an overview of the structure and composition of silicate melts and the factors affecting their viscosity and liquid-glass transition, the mechanisms and controls of H_2O solubility and diffusion in the melt, and finally how these factors interact during bubble growth and resorption.

2.2 Silicate melt

2.2.1 Melt composition and structure

Silicate melts consist primarily of silicon, oxygen, aluminium, alkalis (such as sodium, potassium, and calcium), magnesium, titanium and iron. The basic unit is a silicon atom in tetrahedral co-ordination with four oxygen atoms (e.g. Fig. 2.1). On their own, these silicate tetrahedra are charged anions, SiO_4^{4-}, and so they are usually found in conjunction with other silicate tetrahedra or charge balancing cations. A pure silicate liquid consisting only of Si and O would form an array of silicate tetrahedra linked together at all corners by strong Si-O covalent bonding (Bottinga & Weill 1972) (Fig. 2.1). In magmas this network is altered by the presence of other elements, which may be network formers, or network modifiers. Network formers are those elements which can substitute for Si in tetrahedral sites without affecting the melt structure, and include Ti^{4+}, Al^{3+} and Fe^{3+}. Owing to their lower charge, Al and Fe can only act as network formers in the presence of other cations which maintain charge balance (e.g. Bottinga & Weill 1972). If the supply of charge-balancing cations is exhausted, Al and Fe will instead act as network modifiers. Other network

modifiers include alkali and alkali earth metal cations such as Na^+, K^+, Mg^{2+} and Ca^{2+}, which bind with O and are together known as metal oxides (MO). These cations are network modifiers because they break the continuous Si-O-Si linkage by replacing some strong Si-O bonds with weaker M-O bonds, while simultaneously weakening adjacent Si-O bonds because the cations polarise the shared O (Bottinga & Weill 1972).

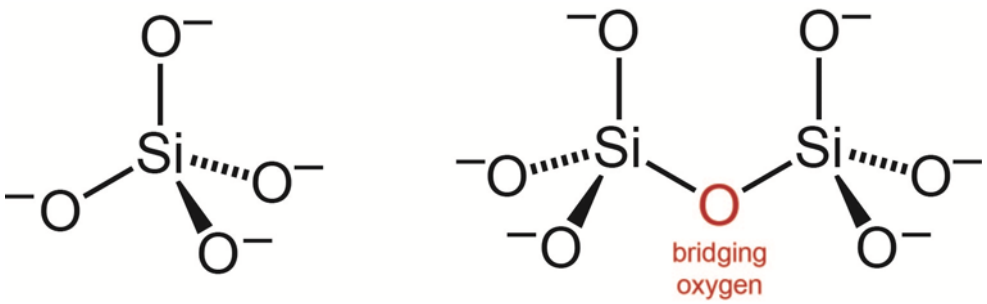

Fig 2.1 The basic silicate structure

Left: The basic unit of silicate structures is a silicate tetrahedron consisting of a silicon (Si) atom co-ordinated by four oxygen (O) atoms. Right: Silicate tetrahedra join together via bridging oxygens (red). Melts become depolymerised when network modifiers, such as H_2O, react with bridging oxygens and break the linking Si-O bonds.

2.2.2 Melt classification

In a silicate melt composed entirely of network formers in tetrahedral sites the melt structure would be fully polymerised. The addition of network modifiers breaks up this network of tetrahedra and so the silicate structure becomes increasingly depolymerised. The degree of polymerisation of a silicate melt has a strong control on melt viscosity. Silicate melts are classified according to their composition, which is typically characterised by the proportions of SiO_2 and alkalis (Na and K). These properties are represented by a Total Alkali Silica (TAS) plot (Fig 2.2). In general, melt polymerisation increases with increasing SiO_2 content and decreases with increasing alkali content.

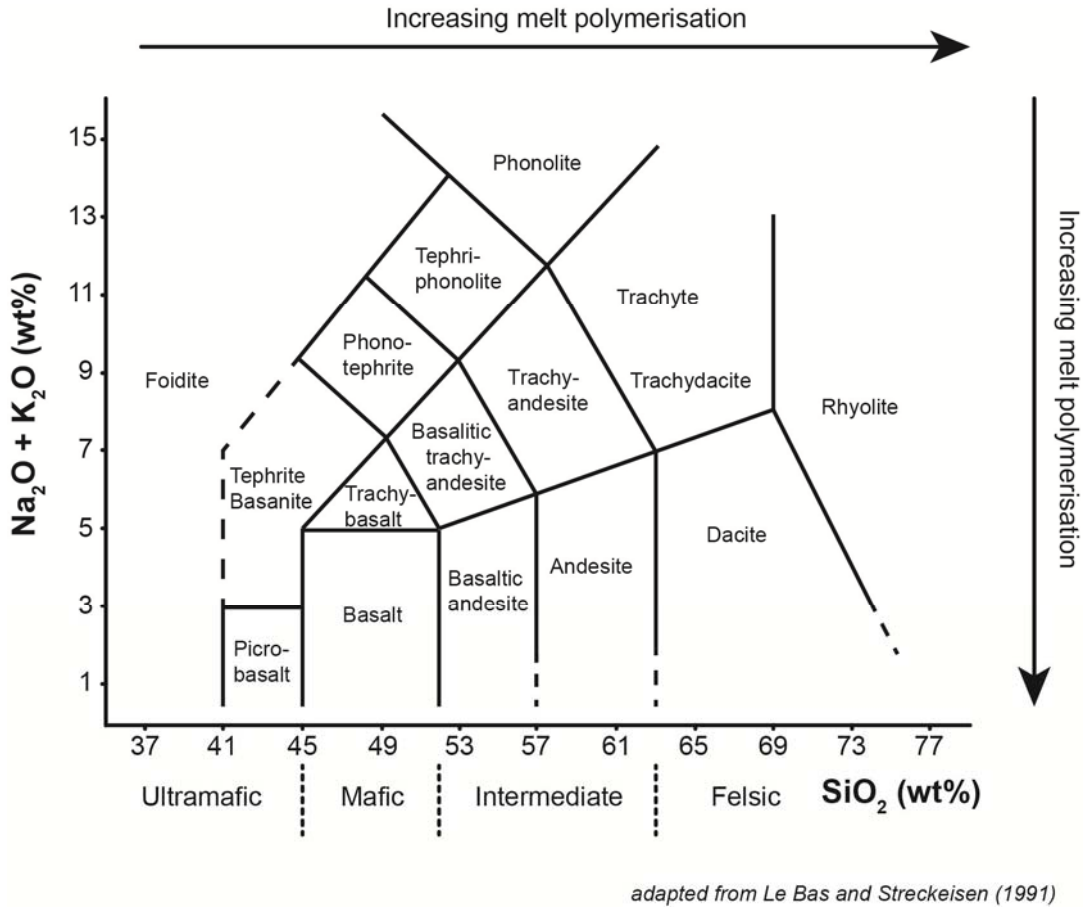

Fig 2.2 Total Alkali Silica (TAS) plot

Anhydrous silicate melt compositions are classified according to their SiO_2, Na_2O and K_2O contents. The degree of melt polymerisation (and associated melt properties such as viscosity) tends to increase with increasing SiO_2 and decreasing alkali content. Figure modified from Le Bas & Streckeisen (1991).

2.2.3 Volatile content

The TAS classification system outlined above is based on the anhydrous melt composition. Naturally occurring silicate melts will also contain a variety of dissolved volatiles, species which are weakly soluble in the melt. The most common magmatic volatiles are H_2O and CO_2 but also include S, Cl, and F-bearing species, among others. H_2O dissolved in a melt is present as two distinct species: molecular H_2O (H_2O_m) and hydroxyl groups (OH) (see Section 2.5 for full discussion of H_2O speciation). H_2O_m is neutral and so does not affect the melt structure whereas OH groups are anions (OH^-) and act as network modifiers by disrupting Si-O bonds, although the

exact nature of the changes to the melt structure caused by OH groups remains debated (see Section 2.3.2). CO_2 also dissolves in silicate melts as two distinct species, molecular CO_2 and carbonate groups (CO_3^{2-}). Like H_2O_m, CO_{2m} is neutral and does not affect melt structure, but CO_3^{2-} reacts with network modifying cations (rather than network formers) and so is not associated with further depolymerisation of the melt (e.g. Lowenstern 2001). Of the other volatiles, F (F^-) and to some extent Cl (Cl^-) are most likely to act as network modifiers and if present in sufficient quantities may cause significant depolymerisation of the melt (e.g. Giordano et al. 2004). However, the much greater abundance of H_2O makes H_2O the most significant modifier of the silicate structure in most melts.

2.3 Melt viscosity

2.3.1 Effect of temperature

Viscosity is a measure of a melt's resistance to flow. The strongest control on melt viscosity is temperature, with melt viscosity decreasing with increasing temperature. Early models assumed that the variation of melt viscosity with temperature follows an Arrhenian relationship, i.e. that viscosity varies linearly with reciprocal absolute temperature (1/T) (e.g. Bottinga & Weill 1972; Shaw 1972). This assumption is approximately true for viscosity over a limited temperature range, but more recent experimental studies, conducted over an extended temperature range, demonstrated that melt viscosity in fact displays non-Arrhenian behaviour, i.e. viscosity varies non-linearly with 1/T (e.g. Hess & Dingwell 1996) (Fig 2.3). All melt compositions exhibit decreasing viscosity with increasing temperature, but the exact nature of this temperature-dependence varies with the anhydrous composition and volatile content of the melt (e.g. Fig 2.4).

2.3.2 Effect of H_2O on melt viscosity

Dissolved OH groups act as network modifiers that reduce melt polymerisation, and so melt viscosity decreases with increasing H_2O concentration (Fig 2.3, Fig 2.4). Hess & Dingwell (1996)

demonstrated that the viscosity of rhyolite melts varies by more than seven orders of magnitude for H_2O concentrations of 0.01 to 8 wt% (Fig. 2.3). This decrease in viscosity with increasing H_2O is most significant for the addition of the first 1 wt% of H_2O, becoming smaller (though still significant) for every additional wt%. The temperature dependence of melt viscosity is also affected by H_2O concentration, with viscosity being most sensitive to H_2O at lower temperatures (Hess & Dingwell 1996); Fig. 2.3, 2.4).

Some aspects of the H_2O-dependence of melt viscosity are not yet fully understood. H_2O speciation varies with H_2O concentration, with OH favoured at low H_2O concentration (see Section 2.5.2.1). The observation that the greatest viscosity decrease occurs with the addition of the first 1 wt% H_2O is thus consistent with depolymerisation of the melt structure by OH groups. However, melt viscosity continues to decrease with additional H_2O even though, beyond a certain H_2O concentration (which varies with bulk composition) the concentration of OH groups remains fairly constant. Continued addition of H_2O simply increases the concentration of H_2O_m, which is not thought to affect the melt structure. Similarly, the proportions of OH and H_2O_m at a given H_2O concentration are temperature dependent. At high temperature, more H_2O will be present as OH and at low temperature more H_2O will be present as H_2O_m, yet the effect of H_2O concentration on melt viscosity is smallest at high temperature and greatest at low temperature. While it is clear that H_2O has a significant effect on melt viscosity, and this effect can be successfully modelled, the exact mechanism of H_2O dissolution and structural modification remains unclear and is likely to consist of several different mechanisms rather than just depolymerisation by OH groups (Whittington et al. 2001).

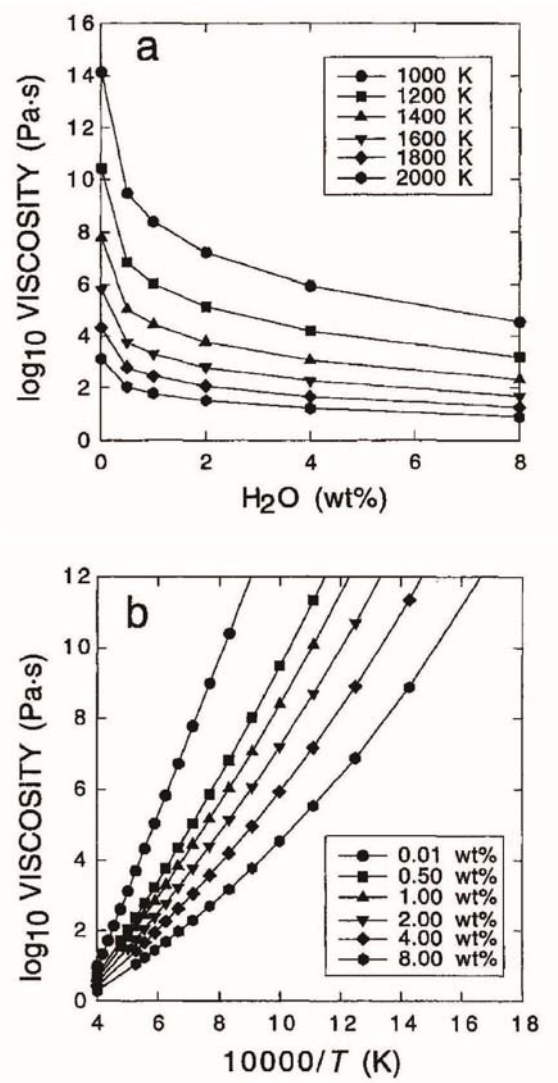

Fig. 2.3 Variation of calcalkaline rhyolite viscosity with temperature and H_2O concentration

a Isothermal variation of viscosity with H_2O concentration. **b** Variation of viscosity with temperature at constant H_2O concentration. Melt viscosity displays non-Arrhenian temperature dependence. The biggest change in viscosity occurs with the addition of the first wt% of H_2O, with the H_2O-dependence of melt viscosity being greatest at lower temperatures. Taken from Hess & Dingwell (1996).

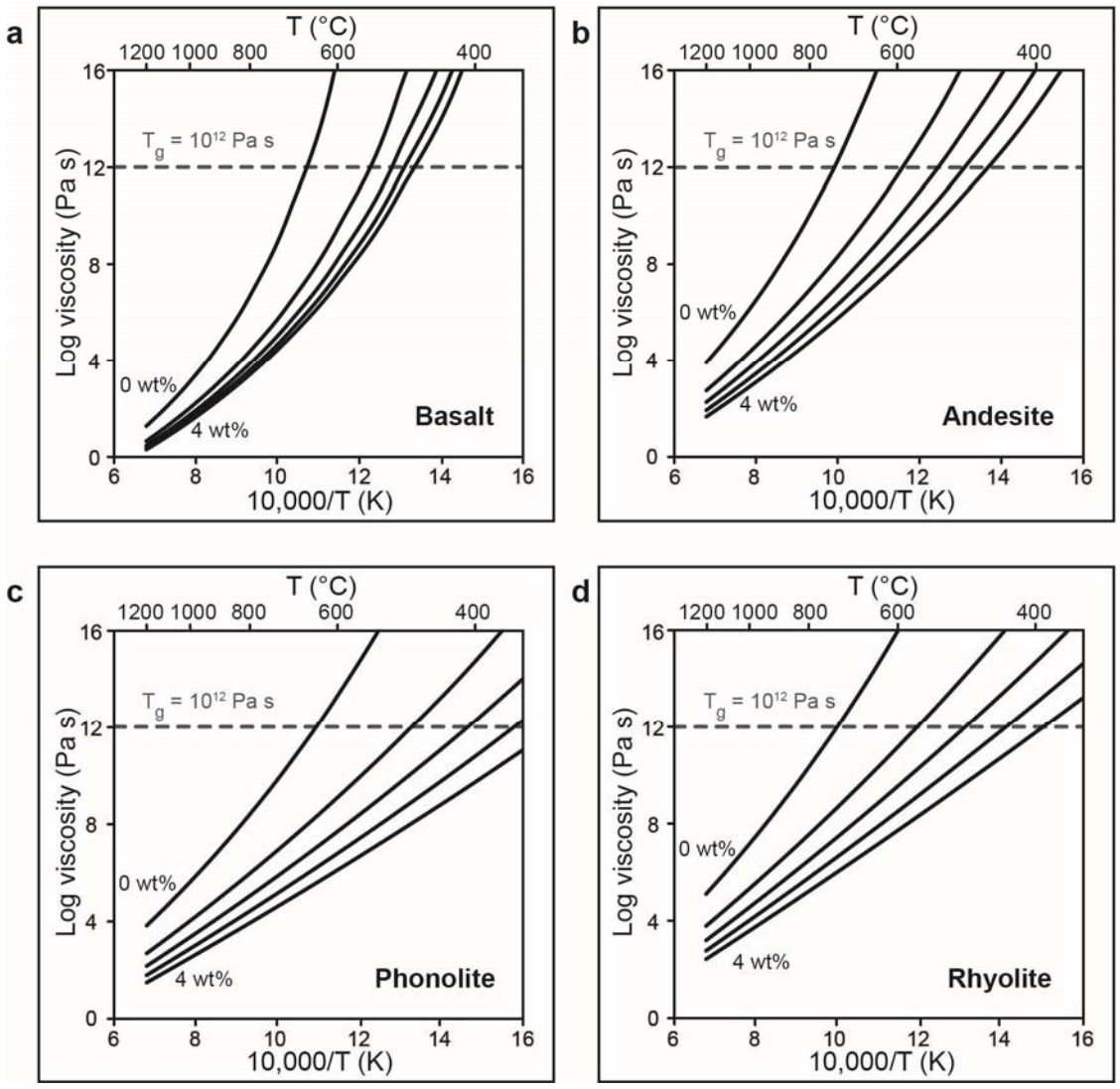

Fig. 2.4 Melt viscosity variation with melt composition, H_2O concentration and temperature

Melt viscosity as a function of H_2O concentration and temperature for **a** basalt **b** andesite **c** phonolite and **d** rhyolite. All melts exhibit increasing viscosity with decreasing temperature but the exact variation varies according to anhydrous composition and volatile content. Lines shown represent melts with 0, 1, 2, 3, and 4 wt% H_2O respectively. Where dashed line intersects viscosity curves indicates the glass transition temperature (T_g) for that composition and H_2O content, where T_g is defined as the temperature where melt viscosity equals 10^{12} Pa s. Viscosity computed from Giordano et al. (2008). Compositions used: Basalt 46.12 wt% SiO_2 (Okumura & Nakashima 2000); Andesite 62.37 wt% SiO_2 (Whittington et al. 2001); Phonolite 58.82 wt% SiO_2 (Whittington et al. 2001); Rhyolite 73.37 wt% SiO_2 (Di Muro et al. 2006).

Both the magnitude of its effect on melt viscosity and its high abundance in magma make H_2O the most significant volatile in determining melt viscosity. CO_2 is often the second most abundant magmatic volatile but because its dissolution does not affect the fundamental silicate melt structure (see Section 2.2.1) it consequently does not affect melt viscosity. Of the remaining volatiles, most are present in natural melts at very low concentrations and do not significantly affect melt viscosity. One exception is F, which in certain melts may be sufficiently abundant that its effect on melt viscosity becomes significant (Giordano et al. 2004).

2.3.3 Viscosity models

Melt viscosity is thus controlled by temperature, anhydrous composition, and the amount and type of volatiles dissolved in the melt. Sufficient experimental data have now been collected to enable robust modelling of the variation in melt viscosity with these parameters. Such models are crucial to the understanding and investigation of a range of volcanological phenomena. When considering the viscosity of a specific melt it is preferable to choose a model that is based on data from similar compositions, or from a similar range in temperature and volatile content. In other cases however it is useful to consider viscosity models devised for a broad range of compositions and conditions, of which the most recent are those of Hui & Zhang (2007) and Giordano et al. (2008). The model of Hui and Zhang is derived from data spanning 0.1 to 10^{15} Pa s, 573 – 1978 K (300 – 1705 °C), and 0 – 5 wt% H_2O (up to 12.3 wt% for rhyolites); the model of Giordano et al. (2008) spans $10^{0.1}$ to $10^{13.4}$ Pa s, 245-1580 °C and 0 - 8 wt% H_2O, and also accounts for 0 - 4 wt% F.

2.4 The glass transition

2.4.1 Cause of the glass transition

When silicate melt cools, it may form a rock consisting entirely of silicate minerals crystallised from the melt, or it may retain its amorphous state and become a glass. For the purposes of the following discussion, the term ‘melt’ is used for all non-crystalline silicate structures derived from

melting regardless of their physical state, i.e. whether they show liquid-like or glassy behaviour (Dingwell 2006). A silicate liquid possesses Newtonian viscosity (i.e. the strain rate of a liquid is proportional to the applied stress) and has no shear strength (i.e. deformation occurs as soon as a stress is applied), whereas a silicate glass exhibits a solid-like response to stress (i.e. the applied stress is accommodated elastically without deformation) (Dingwell 2006).

The transition between liquid-like and glass-like behaviour is known as the glass transition (Fig. 2.5). The transition from liquid to glass occurs when the liquid is unable to achieve an equilibrium response to an external perturbation (Dingwell & Webb 1989). In volcanic contexts this is most likely to result from cooling, or from deformation during flow. The ability of the melt to maintain an equilibrium state is controlled by the structural relaxation timescale of the melt, which is in turn controlled by the rate of self-diffusion of Si and O atoms in the liquid matrix (Dingwell 2006). The self-diffusion of Si and O atoms involves breaking strong Si-O bonds and is therefore the origin of the slowest (i.e. structural) relaxation of the melt (Dingwell & Webb 1989). If the timescale of perturbation (e.g. deformation rate) is more rapid than this structural relaxation timescale, the silicate structure is unable to deform rapidly enough to maintain an equilibrium liquid state and the melt begins to act like a solid i.e. becomes a glass.

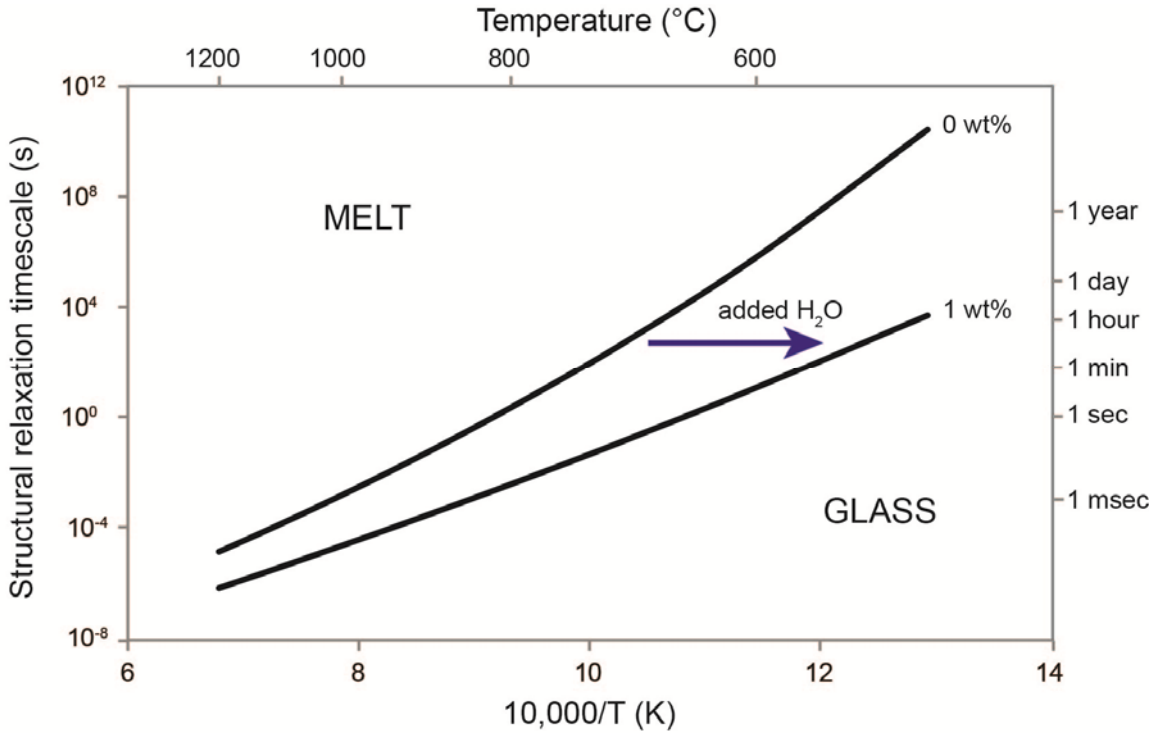

Fig. 2.5 Location of the glass transition in rhyolite melt

The glass transition (black lines) between liquid-like and glass-like behaviour varies in temperature-time space. The transition from melt to glass occurs when the timescale of perturbation is shorter than the structural relaxation timescale of the melt, which is related to melt viscosity. Accordingly, the glass transition occurs at high temperatures when perturbation timescales are short and at low temperatures when perturbation timescales are long. Since melt viscosity (hence structural relaxation timescale) is strongly influenced by the H_2O content of the melt, for the same timescale of perturbation the temperature of the glass transition will be lower for hydrous melt than anhydrous melt. The figure shows the impact on the glass transition temperature of adding 1 wt% H_2O to anhydrous rhyolite melt. Figure created using the viscosity model of Giordano et al. (2008) and rhyolite composition used in Fig. 2.4.

The structural relaxation timescale of a melt is given by the Maxwell relationship i.e. the ratio of shear viscosity to shear modulus:

$$\tau_s = \frac{\eta_s}{G^\infty} \qquad \text{Equation 2.1}$$

where τ_s is the structural relaxation timescale, η_s is the shear viscosity and G^∞ is the shear modulus. Since G^∞ can be considered to be constant (~10^{10} Pa; Dingwell & Webb 1989) regardless of melt temperature, composition or volatile content, this relationship demonstrates that the structural relaxation timescale is related to the melt viscosity. Consequently, the structural relaxation timescale of a melt varies with the same parameters (temperature, anhydrous composition, volatile content) that control melt viscosity.

The self-diffusion rate of Si and O, and thus the structural relaxation of the melt, is a strong function of temperature, becoming increasingly slow with decreasing temperature. For a given perturbation timescale a liquid will become a glass at one temperature but remain a liquid at a higher temperature. The glass transition is therefore best characterised as a curve in temperature-time space (Dingwell 2006) (Fig. 2.5). This curve separates the two states of silicate melts: the liquid field where the melt behaves like a liquid (characterised by long timescales of perturbation relative to the structural relaxation timescale), and the glass field where the melt behaves like a solid (characterised by short timescales of perturbation relative to the timescale of structural relaxation) (Dingwell & Webb 1989). This curve can therefore be crossed either by increasing or decreasing the perturbation rate, or by increasing or decreasing the temperature. The glass transition can be crossed in multiple directions, and multiple times (Dingwell 2006).

2.4.2 Temperature of the glass transition

The transition from liquid to glass, and vice versa, can therefore occur over a range of temperatures, depending on perturbation rate. However in the literature the glass transition is commonly characterised by a single temperature, T_g, the temperature of the glass transition. This

is because the laboratory methodologies used to determine the temperature of the glass transition use measurements made over the timescales of several seconds to several minutes, meaning that the time available for structural relaxation is essentially constant (Dingwell & Webb 1989). The single temperature, T_g, determined by such experiments can therefore be used to investigate how the temperature of the glass transition varies with changing conditions.

The exact definition of T_g differs slightly depending on which methodology is used to determine it. In the geosciences, the two most commonly used techniques are dilatometry and calorimetry. In dilatometry studies T_g is defined as the temperature at which the melt has a viscosity of 10^{12} Pa s. In calorimetry studies the exact location of T_g is slightly more complex. In the calorimetric method, a glass sample is repeatedly heated and cooled across the glass transition at different heating/cooling rates, in order to measure the variation in the specific heat capacity (c_p) of the glass with temperature. At the transition from glass to liquid there is a rapid increase in c_p (Fig. 2.6). The glass transition is defined as the temperature interval between which c_p deviates from the glassy state, as fitted by a Maier-Kelley equation, and the temperature at which c_p achieves a constant value (Giordano et al. 2005). From this, two distinct definitions of T_g can be obtained. The first is T_g peak, which is the temperature at which c_p reaches its highest value. The second is T_g onset, which is the temperature at which the extrapolations of the gradual c_p increase in the glassy state and the sudden increase in c_p during the glass transition interval intersect. As its name suggests, T_g onset marks the onset of the glass-liquid transition and so has more physical meaning; however the advantage of T_g peak is that it does not require extrapolation and so is subject to less uncertainty (Giordano et al. 2005).

The repeated cycles of heating and cooling rates used in calorimetry have shown that the value of T_g is influenced by the heating/cooling rate. Slower cooling creates a longer effective structural relaxation timescale which, for a given perturbation timescale, is exceeded at a lower temperature (and thus higher viscosity) than for faster cooling. T_g therefore decreases with

decreasing cooling rate. In order to compare T_g values from viscometry and calorimetry studies, T_g is usually quoted for a cooling rate of 10 K/min since this corresponds to a viscosity of ~10^{12} Pa s at T_g (Giordano et al. 2005; Dingwell & Webb 1989).

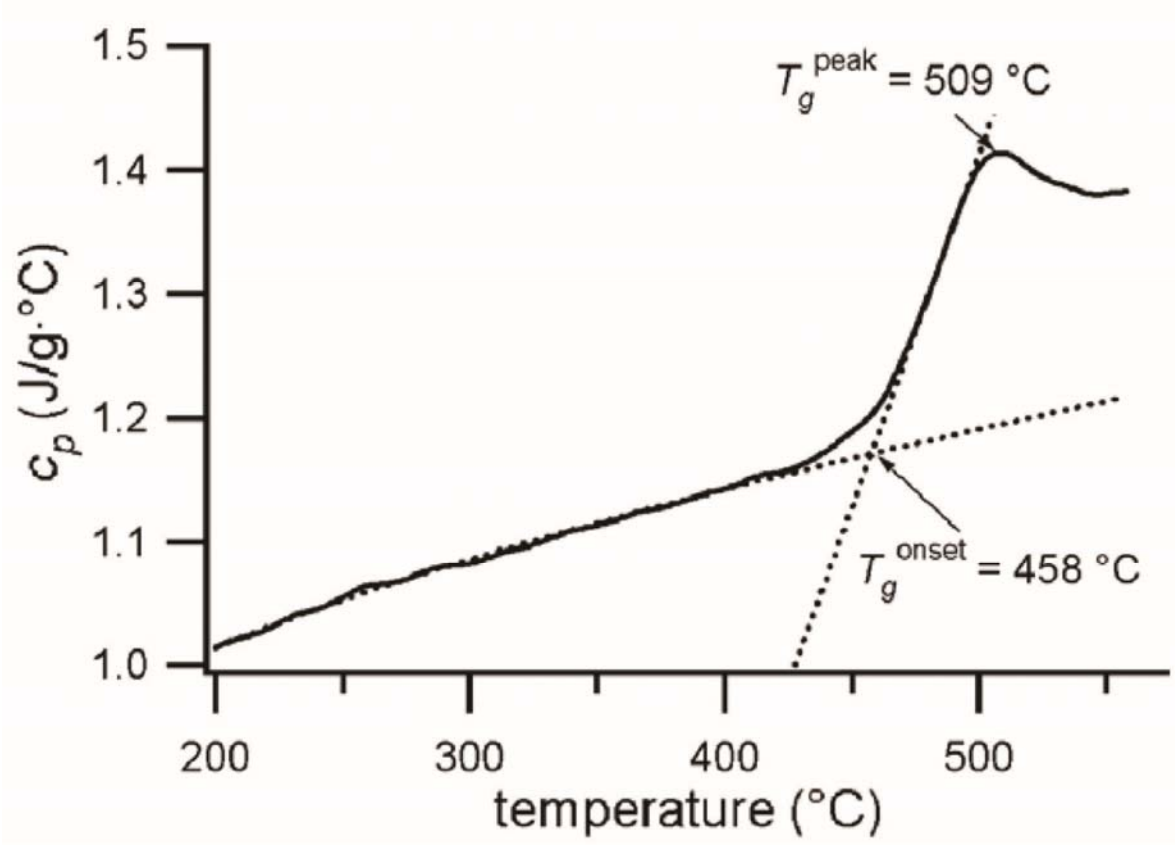

Fig. 2.6 Example determination of T_g using calorimetry

Graph shows the variation in specific heat capacity (c_p) with temperature across the glass transition for a hydrous phonolite sample, for cooling and heating rates of 10 K/min (Giordano et al. 2005). The glass transition interval is defined as the temperature interval between the temperature at which the c_p curve deviates from the glassy state and the temperature at which c_p reaches a constant value at temperatures above the c_p peak. From this calorimetry data two definitions of the glass transition temperature are derived: T_g peak is the temperature of the maximum c_p peak in the glass transition interval; T_g onset is the temperature where the extrapolations of the fit of the glassy state and the sudden increase in c_p intersect.

2.4.3 Controls on T_g

As demonstrated by calorimetry measurements, T_g is affected by quench rate, being higher for fast quench and lower for slow quench. In addition to this, T_g varies with the same factors that affect viscosity (anhydrous melt composition and volatile content) since these alter the structural relaxation timescale of the melt. Fig. 2.4 shows how T_g (as represented by the 10^{12} Pa s isokom) varies with H_2O concentration for different melt compositions. The T_g of rhyolite decreases from 727 °C to 560 °C with the addition of the first 1 wt% H_2O. The T_g of rhyolite and basalt with 1 wt% H_2O are very similar, highlighting that the effect of H_2O on T_g is greater for rhyolite melts than basalt melts.

2.5 H_2O speciation

H_2O is present in silicate melts as two species, molecular H_2O (H_2O_m) and dissociated hydroxyl groups (OH). The behaviour of these two species is fundamental to understanding H_2O solubility and diffusion, and provides insights into processes such as cooling histories and temperature of the glass transition, T_g.

2.5.1 Local environment of H_2O

Early studies of H_2O in silicate melts assumed that all H_2O in the melt is fully dissociated to OH groups, so that no H_2O_m is present (e.g. Burnham 1975; Burnham 1979; Burnham 1981). This view was widely held until the development of spectroscopy and its application to volcanic glasses in the 1980s and beyond demonstrated that molecular H_2O (H_2O_m) is also present in silicate melts in addition to OH (e.g. Stolper 1982; Silver & Stolper 1985; Silver et al. 1990; Dixon et al. 1995). The 'total water' (H_2O_t) content of a silicate melt is thus the sum of the OH and H_2O_m components. H_2O dissolves in the melt according to the vapour-melt equilibrium reaction:

$$H_2O_{(vapour)} \rightleftharpoons H_2O_{m\,(melt)} \qquad \text{Equation 2.2}$$

The interconversion reaction then acts to maintain equilibrium proportions of the species:

$$H_2O_{m\,(melt)} + O^{o}_{(melt)} \rightleftharpoons 2OH^{1-}_{(melt)},$$ Equation 2.3

In which H_2O_m reacts with bridging oxygens (O^o) to form OH groups that are bound to the silicate network (i.e. that act as network modifiers) (Stolper 1982).

2.5.2 Equilibrium speciation

The species interconversion reaction (Eq. 2.3) is a reversible reaction. The equilibrium position of the reaction is represented by the equilibrium constant *K*, which represents what proportions of the two species are expected to be present for a range of given conditions. This equilibrium constant can be defined in terms of the activity of the components, which can be approximated by their mole fractions, according to:

$$K = \frac{[OH]^2_e}{[H_2O_m]_e\,[O]_e}$$ Equation 2.4

where square brackets represent mean activities approximated by mole fractions, and the subscript 'e' refers to a stable or metastable equilibrium (e.g. Zhang & Ni 2010). The value of *K* determines the relative proportions of H_2O_m and OH in a melt for a given H_2O_t content when the system is in equilibrium, with higher values of *K* indicating higher proportions of OH. This 'equilibrium speciation' varies as *K* varies with pressure, temperature and melt composition (e.g. Stolper 1982; Stolper 1989; Silver et al. 1990; Hui et al. 2008).

2.5.2.1 Controls on the equilibrium constant, *K*

The strongest control on *K* and thus the equilibrium speciation, for any composition, is temperature. *K* varies with temperature (T) according to the relationship:

$$\ln K = A + \frac{B}{T}$$ Equation 2.5

where A and B are constants related to the standard state entropy and enthalpy of Eq. 2.3 (e.g. Zhang & Ni 2010). The increase in *K* with increasing temperature reflects that Eq. 2.3 is an endothermic process in the rightwards direction, i.e. the formation of OH groups requires heat

input to break bonds. For a constant pressure and H_2O_t content the temperature dependence of *K* varies with composition, with rhyolite exhibiting a sharper decrease in *K* with temperature than dacite and andesite melts (Zhang & Ni 2010). Accordingly, the constants A and B in Eq. 2.5 vary with composition.

Investigations of the variation of *K* with temperature are hampered by the quench effect (see Section 2.5.3.1), which limits the temperatures that can be investigated by quenching glasses from high temperature melts for analysis at room temperature. In situ measurements made at high temperature are difficult because melt density and molar absorptivity coefficients vary with temperature, although new constraints have made in situ studies feasible. The *K* relationship of Zhang et al. (1997) is commonly used in diffusion studies to obtain DH_2O_m from DH_2O_t for rhyolite compositions. This relationship is calibrated for temperatures of 400 – 600 °C and assumes that *K* is independent of H_2O_t for concentrations ≤2.4 wt% and therefore should not be extrapolated beyond these conditions. A more recent investigation by Nowak & Behrens (2001) for *K* in haplogranite is calibrated for 500 – 800 °C, 100 – 300 MPa, and 1.27 – 5.15 wt% H_2O_t. A comparison of these two models is shown in Fig. 2.7. Both studies assume that *K* depends only on temperature, and extrapolation beyond their calibration datasets is expected to produce large errors (Zhang et al. 1997; Nowak & Behrens 2001). Fig. 2.8 shows the variation in speciation (using *K* from Nowak & Behrens, 2001) expected for 600 and 800 °C. At 600 °C *K* is lower and so H_2O_m becomes the dominant species at lower H_2O_t concentrations.

K is also expected to be dependent on melt composition (e.g. Silver et al. 1990), but this dependence is not well characterised. Data for some compositions (e.g. basalt, trachyte) are entirely lacking, while for others (e.g. phonolite) they are limited. Studies of more silicic melts show that *K* increases slightly from rhyolite to dacite to andesite melts (e.g. Zhang & Ni 2010), although the variation is less than for temperature.

The effect of pressure on *K* has also been investigated (Hui et al. 2008). The pressure dependence of *K* is complicated and it may increase or decrease with increasing pressure. However the effect is negligible for pressures <1 GPa and so the pressure effect can be considered negligible for studies of crustal processes.

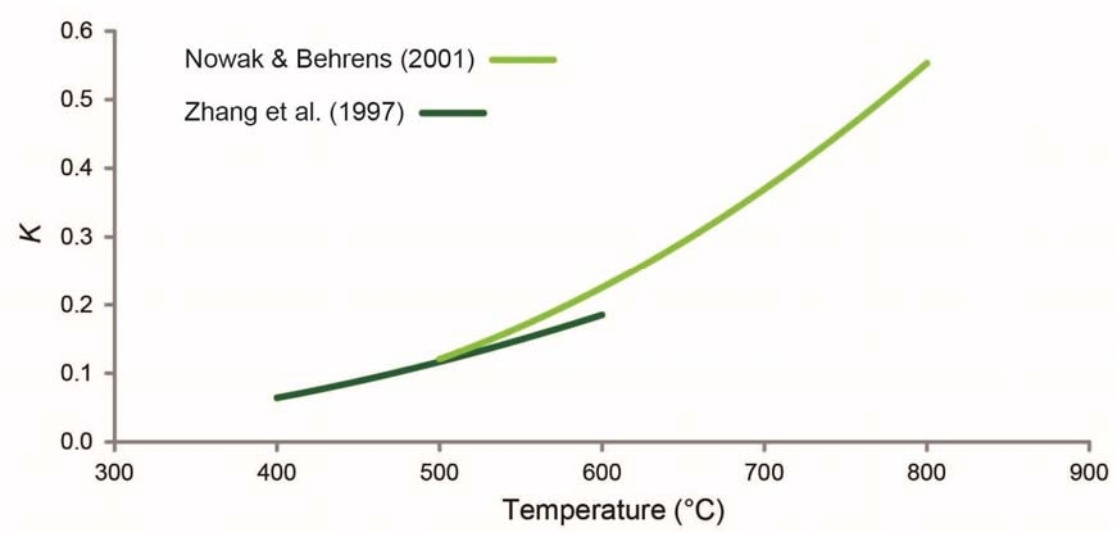

Fig. 2.7 Temperature-dependence of equilibrium H_2O speciation constant *K*

Comparison of the variation of *K* with temperature for rhyolite melts, according to Zhang et al. (1997) and Nowak & Behrens (2001). Both models assume that *K* depends only on temperature. Extrapolation of the relationships beyond the temperature limits shown is expected to result in large errors.

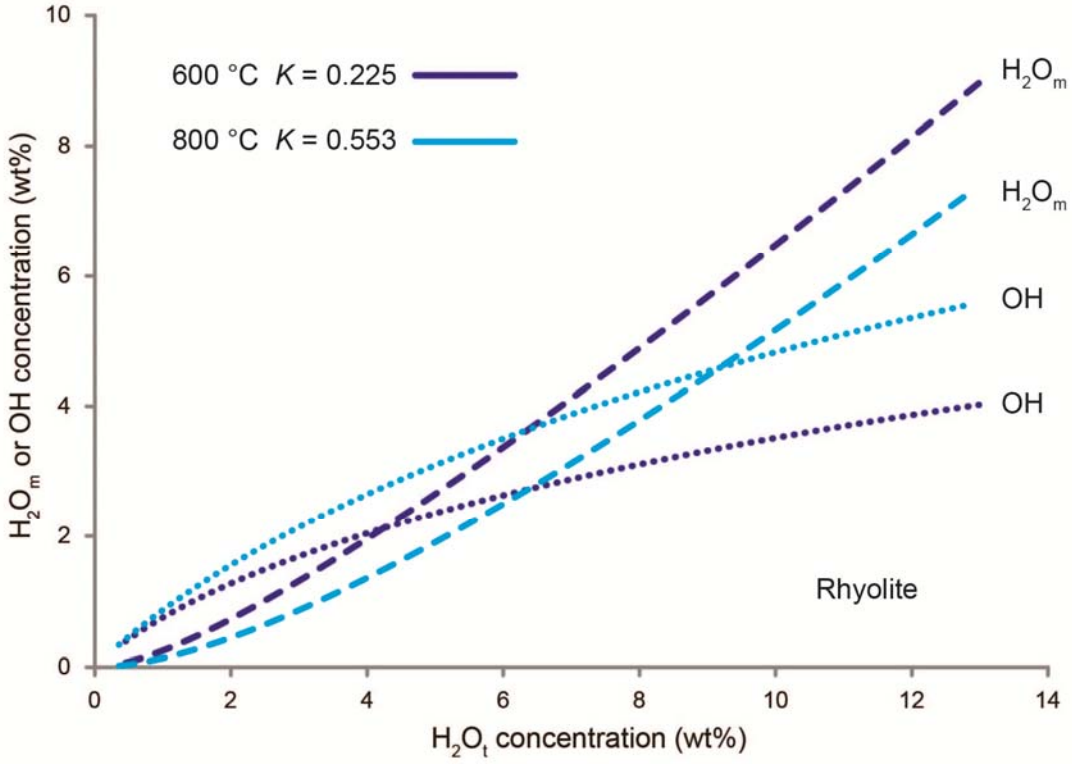

Fig. 2.8 Variation in equilibrium speciation with temperature and H_2O_t concentration

The ratio of H_2O_m:OH increases with increasing H_2O_t concentration. The equilibrium speciation constant *K* decreases with decreasing temperature and so the H_2O_m:OH ratio at a given H_2O_t concentration is higher for melts at lower temperature and vice versa. *K* taken from Nowak & Behrens (2001).

Some early studies suggested that *K* also varies as a function of H_2O_t concentration (e.g. Stolper 1982), with *K* decreasing with increasing H_2O_t concentration. This variation has not been highlighted in more recent studies and may therefore have been an artefact of analysing samples of different compositions, or which may have been affected by the quench effect (see Section 2.5.3.1). As a result a variation of the equilibrium constant *K* with H_2O_t is unconfirmed, but 'speciation' will vary with H_2O_t since, for a given temperature and melt composition, the H_2O_m:OH ratio increases with increasing H_2O_t (Fig. 2.8).

2.5.3 Reaction rate

The reaction rate of Eq. 2.3 determines the timescale necessary for the system to return to equilibrium speciation after a perturbation. This reaction rate is affected by temperature and H_2O_t content, being fastest for high temperatures and high H_2O_t contents. At magmatic temperatures (>800°C), the reaction rate is sufficiently fast that equilibrium is attained within miliseconds (Zhang et al. 1995). However the rate decreases drastically with decreasing temperature, taking minutes to hours at ~600°C and days at ~400°C (Stolper 1989; Zhang et al. 1991; Zhang et al. 1995).

2.5.3.1 Origin of the 'quench effect'

The temperature-dependence of the interconversion reaction rate leads to a phenomenon known as the 'quench effect' (Fig. 2.9). This refers to how faithfully (or otherwise) speciation related to experimental (or magmatic) conditions is preserved when the melt is quenched to glass. Early experimental studies of melts at high temperature (e.g. Stolper 1989; Silver et al. 1990) are now known to have been affected by this quench effect, wherein the rapidity of the interconversion reaction during the initial stages of quench can keep pace with cooling and maintain equilibrium speciation until the reaction slows at lower temperatures. This results in a final H_2O speciation that reflects equilibrium with a cooler intermediate temperature rather than the original

experimental temperature. Therefore instead of the equilibrium constant *K*, speciation data affected by the quench effect can be described by the apparent equilibrium constant, *Q*:

$$Q = \frac{[\mathrm{OH}]^2}{[\mathrm{H_2O_m}][\mathrm{O}]} \qquad \text{Equation 2.6}$$

This expression is identical to that of *K* (Eq. 2.4), except that *K* is only appropriate when the system is in equilibrium (e.g. Zhang & Ni 2010). For a sample affected by the quench effect, the measured speciation will have an apparent equilibrium constant *Q* that is lower than the true equilibrium constant, *K*, of the original hotter temperature. Thus samples affected by the quench effect have higher H_2O_m:OH ratios than occur at the higher temperature. The magnitude of the difference between *K* and *Q* is determined by the quench rate, with bigger differences caused by slower quench (Fig. 2.9).

When investigating the equilibrium speciation for different conditions it is therefore important to use experimental temperatures and quench rates that will not be unduly affected by the quench effect, while ensuring that the temperature is sufficiently high to ensure that equilibrium speciation is attained within the duration of the experiment. These conditions will vary according to the H_2O_t content of the sample, since these parameters affect the reaction rate of Eq. 2.3, but in general rapidly quenched experiments conducted at intermediate temperatures (~380 – 620 °C) will maintain their original speciation (Zhang & Ni 2010).

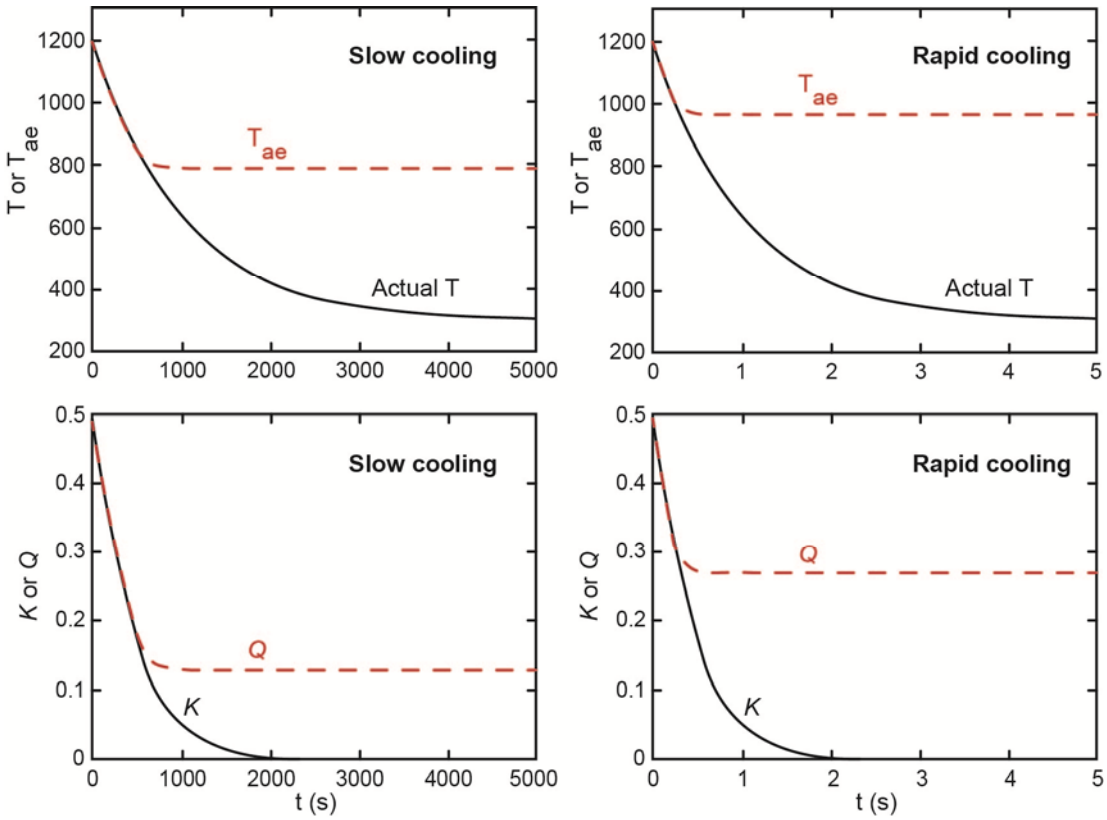

Fig. 2.9 Variation in *Q* and T_{ae} with quench rate

Schematic figure showing how the apparent equilibrium constant, *Q*, and temperature of apparent equilibrium (T_{ae}) vary with quench rate. Deviations from the true equilibrium constant, *K*, and temperature, T, corresponding to the conditions prior to quench, are greatest for slow quench and smallest for rapid quench. Adapted from Zhang & Ni (2010).

2.5.3.2 Temperature of apparent equilibrium, T_{ae}

Although it complicates studies of equilibrium speciation, the quench effect phenomenon can be used to obtain further information about samples. Like *K*, the apparent equilibrium constant *Q* can be related to temperature:

$$\ln Q = \mathrm{A} + \frac{\mathrm{B}}{\mathrm{T_{ae}}} \qquad \text{Equation 2.7}$$

where T_{ae} is the temperature of apparent equilibrium, i.e. the temperature that would correspond to the measured species concentrations if they were equilibrium concentrations. This relationship

forms the basis of geospeedometry studies that use T_{ae} to determine how rapidly a sample was quenched (Fig. 2.9).

The point at which the interconversion reaction stops (at least for the timescale of observation) has been linked to the transition of the melt from liquid to glass. The temperature T_{ae} is therefore the same as the temperature of the glass transition, T_g, as defined by viscosity (see Section 2.4.2 above) (e.g. Dingwell & Webb 1990; Zhang et al. 1997; Zhang & Xu 2007). As with T_g, T_{ae} varies with quench rate (being higher for faster quench) and H_2O_t concentration (being lower for higher H_2O_t concentration). For an unknown sample, determining T_{ae} can reveal both the glass transition temperature and the cooling rate at the time of the glass transition. The variation in T_{ae} with cooling rate is now known for cooling rates of 10^{-6} K/s to 100 K/s (Zhang et al. 1997; Zhang et al. 2000; Zhang & Xu 2007), and has been applied as a geospeedometer to determine cooling rates of naturally erupted samples from pyroclastic flows and Plinian fall deposits (e.g. Zhang et al. 2000; Xu & Zhang 2002; Wallace et al. 2003).

2.6 H_2O solubility

2.6.1 Theory of H_2O solubility

Solubility is the concentration of a substance that can be dissolved in a solvent at equilibrium. In the case of magma the solvent is the silicate melt and the solute is the volatile species of interest, in this case H_2O. If the silicate melt is saturated with respect to the volatile then two phases, melt and fluid, exist in equilibrium. Although at low pressures the volatile phase may be present as a gas the term fluid is usually used, since for many temperature and pressure conditions relevant to volcanic systems the volatile species will be above their critical point, i.e. the point above which separate liquid and gas phases cannot be distinguished (Baker & Alletti 2012). For example, the critical point of pure H_2O is ~374°C and ~22 MPa (Pitzer & Sterner 1994). Above these pressure and temperature conditions water exists as a supercritical fluid; below it exists as a gas or liquid.

There are many gases whose solubilities follow Henry's Law, which states that the solubility of a gas in a solvent at fixed temperature is proportional to the partial pressure of the gas:

$$C = k\, P_{gas} \qquad \text{Equation 2.8}$$

where C is solubility (or concentration) in the solvent, P_{gas} is the partial pressure of the gas, and k is Henry's Law constant, which depends on the gas, the solvent and the temperature. Henry's Law only applies in situations where only one gas species is present, and the solubility of H_2O is therefore complicated by the speciation of H_2O. From the equation of vapour-melt equilibrium (Eq. 2.2), it can be seen that the solubility of H_2O_m is proportional to the partial pressure of the H_2O vapour. The solubility of OH, however, is proportional to the square root of H_2O_m concentration (as seen in Eq. 2.4) and therefore OH solubility is proportional to the square root of the partial pressure of H_2O vapour (Zhang et al. 2007). The solubility of H_2O_t is therefore given by:

$$[\mathrm{H_2O_t}] = k_1 \sqrt{P_{H_2O}} + k_2\, P_{H_2O} \qquad \text{Equation 2.9}$$

where the first term on the right hand side results from OH groups and the second term results from H_2O_m (Zhang et al. 2007).

For a given temperature, at low pressures H_2O_t concentration is low and OH will be the dominant species as determined by the equilibrium speciation. As pressure increases, H_2O_t concentration also increases and the H_2O_t-dependence of the equilibrium speciation reaction will result in increasing proportions of H_2O_m. As H_2O_m becomes the more dominant species, H_2O_t solubility will begin to increase more rapidly than if it continued to follow a square root dependence on pressure (Zhang et al. 2007).

2.6.2 H_2O solubility in silicate melts

Measured H_2O concentrations in naturally occurring silicate melts vary from the order of thousands of parts-per-million (ppm) in ocean-floor basalts to many wt% in some granitic melts (Baker & Alletti 2012). In order to understand the cause of these variations, the effect of pressure,

temperature and melt composition on H_2O solubility have been widely investigated. The earliest geologically relevant studies were conducted by Goranson in the 1930s, who investigated H_2O solubility in relatively simple albitic melts (e.g. Goranson 1931; Goranson 1938). These studies showed that silicate melts could contain abundant dissolved H_2O, from 4 wt% in shallow crust to as much as 15 wt% in the deep crust and upper mantle (Baker & Alletti 2012). While pressure was found to be the greatest control on H_2O solubility, with solubility increasing with increasing pressure (see Section 2.6.1), these studies demonstrated that H_2O solubility is also temperature dependent and that this temperature dependency is retrograde (i.e. solubility increases with decreasing temperature) at low pressures but prograde at higher pressures.

More recent studies of rhyolitic melts have confirmed that H_2O solubility increases with increasing pressure and that the temperature-dependence of H_2O solubility switches from retrograde to prograde at pressures greater than 500 MPa (e.g. Yamashita 1999; Tamic et al. 2001; Liu et al. 2005). H_2O solubility remains best constrained for rhyolitic and granitic melts. Studies of intermediate compositions including andesites (e.g. Moore et al. 1998; Botcharnikov et al. 2006), trachytes (e.g. Moore et al. 1998; Di Matteo et al. 2004) and phonolites (e.g. Carroll & Blank 1997; Iacono Marziano et al. 2007; Schmidt & Behrens 2008) confirm that these melts follow the same trends in H_2O solubility with pressure and temperature as for silicic melts and also show that, for a given pressure, H_2O solubility increases with increasing alkali content. Although mafic melts have historically been more difficult to study owing to their tendency to crystallise during quench, H_2O solubility has now been characterised for both basalts and alkali basalts and exhibit similar behaviour (e.g. Dixon et al. 1995; Moore et al. 1998; Lesne et al. 2011) although there are indications that temperature dependence does not become prograde at higher pressures as with more silicic melts (e.g. Papale et al. 2006).

In naturally occurring magmas, the silicate melt is unlikely to be in equilibrium with a fluid consisting of a single volatile species. Other volatiles that may be present in significant quantities

include CO_2 (which may in some cases be more abundant than H_2O), F, Cl, S-bearing species (e.g. H_2S, SO_2) and noble gases. According to thermodynamic principles the presence of additional volatile species would lower the solubility of H_2O compared to a melt that is in equilibrium with a pure H_2O fluid (e.g. Baker & Alletti 2012). Experimental studies have shown that H_2O solubility can be assumed to be independent of CO_2 concentration, for pressures below 400 MPa (Blank et al. 1993), although addition of CO_2 gas may lower the concentration of H_2O in a melt by diluting the H_2O vapour phase (e.g. Lowenstern 2001). Several studies have investigated how H_2O solubility changes when a mixed fluid is present, from H_2O-CO_2 in rhyolites (e.g. Tamic et al. 2001) to H_2O-CO_2-S-Cl in basalts (e.g. Witham et al. 2012). As with pure H_2O fluids, these mixed fluid studies have shown that solubility is predominantly controlled by pressure, with weaker control of temperature and melt composition.

2.6.3 H_2O solubility in rhyolitic melts

H_2O solubility in rhyolites is well constrained for a wide range of pressures and for intermediate to high temperatures. Several empirical studies of specific melt compositions exist (e.g. Zhang 1999; Tamic et al. 2001; Liu et al. 2005) and work well for the investigated range of pressure and temperature conditions, but are not recommended for extrapolation beyond these limits. The empirical model of Moore et al. (1998) calculates H_2O solubility as a function of the anhydrous melt composition and can be applied to rhyolitic melts for pressures up to 300 MPa and temperatures of 700 °C – 1200 °C, but cannot be extrapolated beyond these parameters.

Solubility models based on thermodynamic principles allow greater interpolation and extrapolation beyond calibration datasets, and several have been proposed for rhyolitic melts. The early models of Wasserburg (1957), Shaw (1964) and Burnham (1975) were used extensively until their assumption of total dissociation of H_2O to OH groups was shown to be incorrect by the speciation work of Stolper and co-workers in the 1980s, which created the foundation for the solubility models commonly in use today. Newman & Lowenstern (2002) created the VolatileCalc

H_2O-CO_2 solubility model for rhyolitic and basaltic melts, while Papale et al. (2006) model H_2O-CO_2 solubility for a range of compositions including intermediate melts as well. For silicic and intermediate compositions these models are capable of replicating experimental data to within 0.5 wt% (Baker & Alletti 2012).

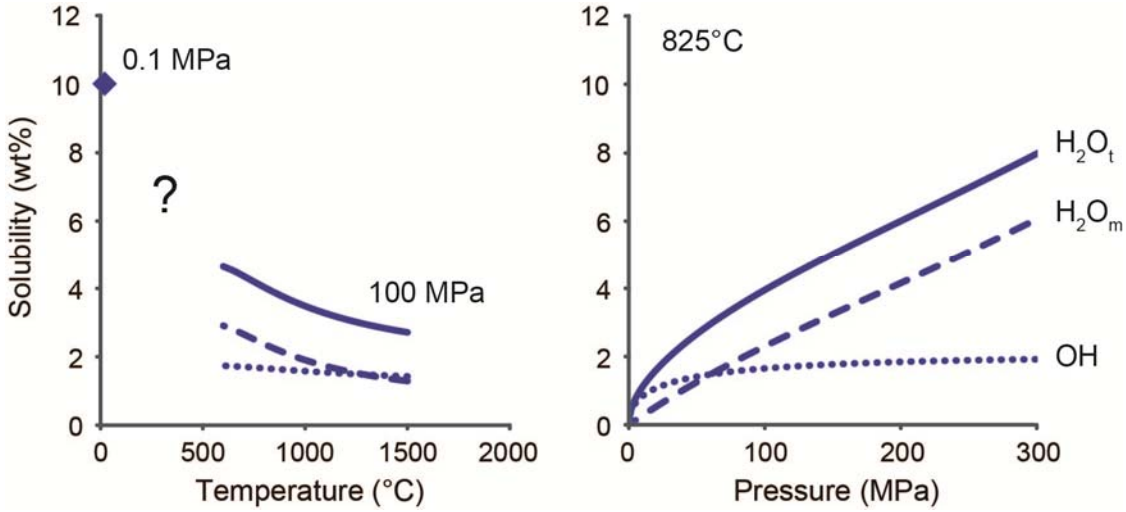

Fig. 2.10 H_2O solubility in rhyolite as a function of temperature and pressure

H_2O solubility increases with decreasing temperature and increasing pressure. A data gap exists for low to intermediate temperatures, with the only constraint for ambient conditions coming from measurement of hydrated obsidian artefacts (Anovitz et al. 1999). Data, including speciation, for high temperatures and pressure calculated using the VolatileCalc solubility model (Newman & Lowenstern 2002).

It is therefore now possible to model H_2O solubility, including mixed H_2O-CO_2 fluids, in a wide range of melt compositions and pressure and temperature conditions. For rhyolitic melts the VolatileCalc model is valid for ≤11 wt% H_2Ot and 10,000 ppm CO_2, pressures ≤ 500 MPa and temperatures of 600 – 1500 °C. The model of Papale et al. (2006) is valid up to pressures of a few GPa, and temperatures of 800 – 2000 °C. Below 500 MPa, these models are interchangeable (Baker & Alletti 2012) and so this discussion will focus on the VolatileCalc model since it covers a larger portion of the temperature range that is relevant to the following work. Accordingly, Fig. 2.10 shows the variation with pressure and temperature of H_2O solubility in rhyolitic melt for a

pure H_2O fluid. While variation with pressure is well constrained, the variation in solubility below near-magmatic temperatures is almost entirely unconstrained. The only data available for H_2O solubility in rhyolite below 600 °C come from studies of hydrated obsidians at ambient pressure and temperature, which may have H_2O concentrations of up to 10 wt% (Anovitz et al. 1999) (Fig. 2.10). This data gap between ambient and magmatic temperatures represents a significant challenge to interpretations of observed H_2O concentrations in rhyolitic melts and glasses, as will be discussed in subsequent chapters.

2.7 H_2O diffusion

2.7.1 Diffusion theory

Diffusion occurs as a result of thermally activated random motion of particles (atoms, ions or molecules) that leads to a net flux of particles when the concentration of a component is not uniform (Zhang 2010). This net flux is described by Fick's first law, which relates net flux to the concentration gradient:

$$\boldsymbol{J} = -D\,\frac{\partial C}{\partial x} \qquad \text{Equation 2.10}$$

Where $\boldsymbol{J}$ is the diffusive mass flux (a vector), D is the diffusion coefficient (i.e. diffusivity) in units of length^2/time (typically m^2/s), C is concentration in units of mass per unit volume, $\frac{\partial C}{\partial x}$ is the concentration gradient (a vector), and the negative sign indicates that flux moves from high to low concentration. Large concentration gradients are therefore associated with large diffusive fluxes.

The relationship between concentration, space and time, which is necessary to understand how a concentration profile will evolve over time, is given by Fick's second law for diffusion in one dimension:

$$\frac{\partial C}{\partial t} = \frac{\partial}{\partial x}\left(D\,\frac{\partial C}{\partial x}\right)$$ Equation 2.11

For the case of 1-D diffusion in a semi-infinite homogeneous medium, where *D* is constant and the initial and new concentrations are held constant, the distance *L* at which the concentration is halfway between the maximum and minimum values at a given time *t* is given by (Crank 1975; Zhang 2010):

$$L = 0.9539\sqrt{Dt} \approx \sqrt{Dt}$$ Equation 2.12

This 'rule of thumb' is commonly used in the geosciences for calculating diffusion distances, and is also termed the 'hall-fall distance' (e.g. Anovitz et al. 1999) or 'half-peak distance' (e.g. Gardner et al. 2012) (Fig. 2.11).

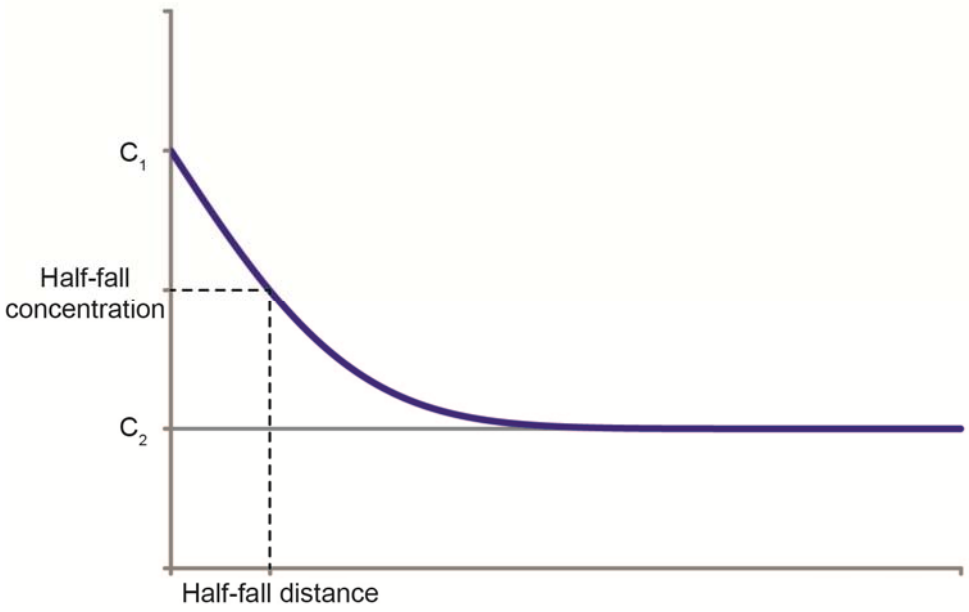

Fig. 2.11 Calculation of half-fall distance

The half-fall distance is the distance at which the concentration is the average of the maximum (here, C_1) and minimum (C_2) concentrations of the profile. This calculation assumes 1-D diffusion in a semi-infinite medium, where diffusivity is independent of concentration and C_1 and C_2 are held constant.

H_2O diffusion is a form of multispecies diffusion, since H_2O is present as both H_2O_m and OH and the proportions of these vary according to the equilibrium interconversion reaction (Eq. 2.3). To avoid having to include the interconversion reaction in the treatment of H_2O diffusion, Fick's second law can be modified to give the diffusion of H_2O_t as the sum of the diffusion of each species (Zhang 2010):

$$\frac{\partial C_{H_2O_t}}{\partial t} = \frac{\partial}{\partial x}\left(D_{H_2O_m}\frac{\partial C_{H_2O_m}}{\partial x}\right) + \frac{1}{2}\frac{\partial}{\partial x}\left(D_{OH}\frac{\partial C_{OH}}{\partial x}\right) \qquad \text{Equation 2.13}$$

Here concentrations are in mol/m^3 so the factor ½ is introduced to account for the 2 mol of OH that are produced by the interconversion reaction for every 1 mol of H_2O_m (Eq. 2.3).

This equation however still assumes that diffusivity, *D*, is independent of H_2O concentration. In reality, however, decades of experimental work on H_2O diffusion in silicate melts have shown that this assumption is incorrect. Modelling H_2O diffusion therefore requires numerical modelling approaches, with empirical relationships for *D* as a function of H_2O_t concentration.

2.7.2 Diffusion of H_2O

The first study of H_2O diffusion in geologically-relevant silicate melt was undertaken by Shaw (1974), who investigated the mass gain of melt during hydration and concluded that H_2O_t diffusivity (DH_2O_t) was strongly dependent on H_2O_t concentration. The development of the ion microprobe led to investigations of H_2O_t concentration profiles created during diffusion experiments (e.g. Delaney & Karsten 1981; Karsten et al. 1982), which were subsequently superseded with the application of Fourier Transform Infra-Red (FTIR) spectroscopy to measure the concentration profiles of the H_2O_m and OH species themselves. This was first undertaken by Zhang et al. (1991) who measured H_2O_m and OH concentration profiles in experimentally dehydrated obsidians. They demonstrated that OH diffusivity (DOH) is much slower than H_2O_m diffusivity (DH_2O_m), to the point that H_2O_m can be considered to be the only diffusing species. OH

concentration profiles are therefore formed indirectly by diffusion of H_2O_m and subsequent readjustment to equilibrium speciation via the interconversion reaction (Eq. 2.3). This difference in diffusivity results from the fact that H_2O_m is a small, neutral molecule that can more easily diffuse through a melt than OH groups that are bonded to cations and require strong bonds to be broken in order to diffuse (Zhang et al. 1991).

Subsequent studies have confirmed that H_2O_m is the diffusing species, and gone on to investigate H_2O diffusion as functions of temperature, pressure, H_2O_t content, and silicate melt composition. At low H_2O_t concentrations (i.e. ≤ 2 wt%) DH_2O_m is roughly independent of H_2O_t content and DH_2O_t is proportional to H_2O_t concentration (e.g. Zhang et al. 1991). Subsequent studies of melts with higher H_2O_t contents demonstrated that for H_2O_t concentrations greater than 3 wt%, DH_2O_t increases exponentially with H_2O_t concentration, implying that DH_2O_m is dependent on H_2O_t for > 3 wt% H_2O_t. This exponential increase is consistent with the diffusivity behaviour of other neutral molecules such as Ar (Behrens & Zhang 2001). The variation of DH_2O_t with H_2O_t concentration therefore follows the variation of DH_2O_m with H_2O_t concentration, but will always be lower than DH_2O_m for a given set of pressure, temperature and H_2O_t conditions.

As with diffusivity coefficients of other components, DH_2O_t and DH_2O_m are strongly dependent on temperature and follow an Arrhenian relationship, increasing exponentially with increasing temperature (e.g. Zhang 2010). Additionally, the temperature dependence of DH_2O_m on H_2O_t becomes stronger at lower temperatures, which is consistent with the stronger dependence of melt viscosity on H_2O_t concentration at lower temperatures (e.g. Zhang et al. 2003; Zhang & Ni 2010). The effect of pressure is more complex, and DH_2O_t and DH_2O_m may either increase or decrease with increasing pressure (Zhang & Ni 2010). For small pressure intervals however, the effect is generally sufficiently small to be considered negligible (e.g. Ni & Zhang 2008).

2.7.2.1 H_2O diffusion in rhyolite

H_2O diffusion has now been widely studied in many different silicate melt compositions, including basalt (e.g. Zhang & Stolper 1991; Okumura & Nakashima 2006), andesite (e.g. Okumura & Nakashima 2006; Ni et al. 2013), phonolite and trachyte (Fanara et al. 2013), dacite (e.g. Behrens et al. 2004; Ni et al. 2009) and rhyolite (e.g. Zhang et al. 1991; Nowak & Behrens 1997; Zhang & Behrens 2000; Ni & Zhang 2008), for a range of temperature, pressure and H_2O_t concentrations. Of the melt compositions investigated rhyolite is the best constrained, with the study of Ni & Zhang (2008) combining all available data in the literature to give a relationship for DH_2O_t and DH_2O_m for conditions of 676 – 1900 K (403 – 1627 °C), 0 – 1.9 GPa and 0 – 8 wt% H_2O_t. Using this relationship, the variation in DH_2O_t and DH_2O_m for a hydrous rhyolite with temperature, pressure and H_2O_t concentration conditions relevant to subsequent chapters are given in Fig. 2.12. From this it can be seen that the effect of pressure on diffusivity is negligible for crustal pressures (<300 MPa) while the effect of temperature causes diffusivity to vary over 4 orders of magnitude between 403 – 1627 °C (Fig. 2.12).

Below 400 °C however, there are little to no data on DH_2O_t and DH_2O_m. What data there are come from archaeological studies of obsidian hydration, which aim to date ancient artefacts or reconstruct paleoclimate on the basis of the concentration profiles formed by surface hydration of obsidian (e.g. Friedman & Long 2013; Anovitz et al. 1999; Riciputi et al. 2002; Anovitz et al. 2004; Anovitz et al. 2006). Anovitz et al. (2006) conducted hydration experiments for obsidian at atmospheric pressure over a temperature range of 30 – 150 °C, reporting data as the half-fall distance (Eq. 2.12) vs time. Diffusivity would be expected to vary throughout the duration of the experiments as the H_2O concentration gradient varies with time, but by assuming a constant diffusivity the half-fall distance equation can be used to obtain DH_2O_t values that are characteristic of the hydration process at low temperatures (Fig. 2.12).

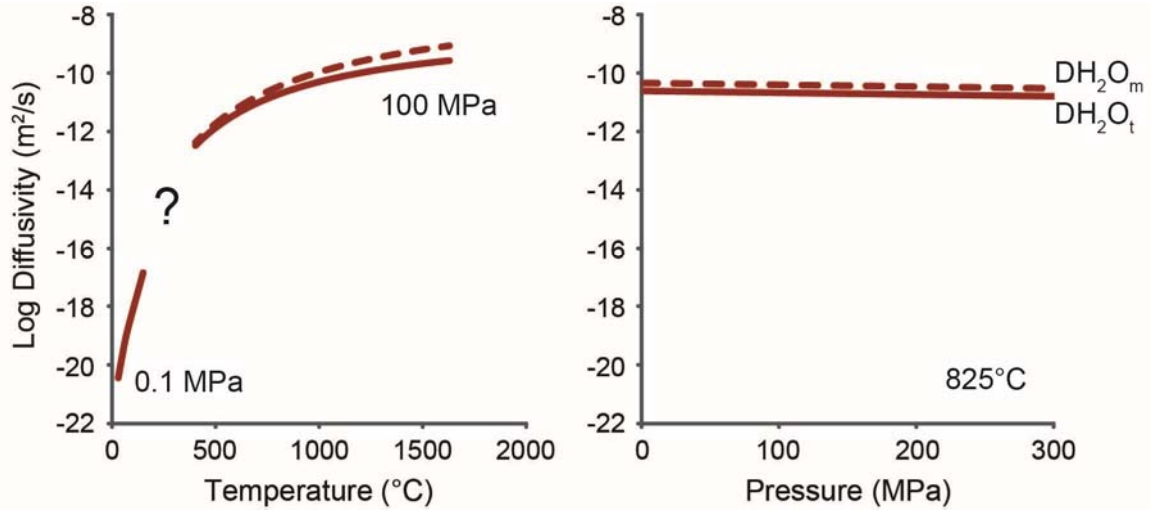

Fig. 2.12 H_2O diffusivity in rhyolite

The variation in H_2O_t diffusivity (DH_2O_t, solid line) and H_2O_m diffusivity (DH_2O_m, dashed line) with temperature and pressure. DH_2O_m is always larger than DH_2O_t. Diffusivity decreases by orders of magnitude between 0 and 1600 °C, while the effect of pressure is negligible for the pressure range 0 – 300 MPa. A data gap exists for low and intermediate temperatures. High temperature and pressure data computed assuming 4 wt% H_2O_t concentration from Ni & Zhang (2008). Low temperature data from (Anovitz et al. 2006).

2.7.2.2 Effect of disequilibrium speciation conditions

A major reason for the limited dataset below 400 °C is the length of time necessary to undertake diffusion experiments at these temperatures. Diffusion studies that utilise Eq. 2.13 require the H_2O species to be in equilibrium in order to avoid including terms related to the kinetics of the interconversion reaction (Eq. 2.3). The rate of this reaction is strongly temperature dependent however, and by 400 °C it may take days to achieve equilibrium speciation (see Section 2.5.3). Below this temperature the reaction rate will continue to decrease and increasingly long timescales will be required to achieve equilibrium speciation.

The effect of disequilibrium speciation conditions on H_2O diffusion have been reported in some experimental studies at intermediate temperatures (Zhang et al. 1991; Jambon et al. 1992). In these studies, it was observed that DH_2O_t is lower than expected for dehydration experiments (where H_2O diffuses out of the sample) and higher than expected for hydration experiments

(where H_2O diffuses into the sample). For these experiments, Zhang et al. (1991) found that along the H_2O diffusion profile, H_2O_m concentration is lower than its expected equilibrium concentration in dehydration experiments and higher than expected in hydration experiments. Since H_2O_m is the diffusing species, during dehydration H_2O_m is lost from a site (while during hydration H_2O_m is added to a site), and conversion of OH to H_2O_m (or H_2O_m to OH during hydration) is necessary to achieve equilibrium H_2O_m concentration. The authors therefore concluded that the interconversion reaction rate was too slow to achieve this equilibrium speciation, and H_2O_m concentration therefore remains lower than expected in dehydration profiles and higher than expected in hydration profiles, corresponding to lower DH_2O_t and higher DH_2O_t respectively. During hydration of obsidian at ambient temperature the interconversion reaction rate is expected to be much slower than during these reported examples. Low temperature hydration is therefore expected to occur under conditions of disequilibrium speciation, resulting in higher DH_2O_t than would be expected for equilibrium speciation conditions. This has been suggested to be the cause of the poor fit between DH_2O_t values derived from low and high temperature datasets (Zhang & Ni 2010) and emphasises the current lack of understanding of H_2O diffusion and speciation at low and intermediate temperatures.

2.8 Bubbles in magma

2.8.1 Bubble formation

Bubbles form when volatiles (of which H_2O is the most volumetrically abundant) dissolved in a melt become supersaturated and exsolve to form a gas phase. Supersaturation may occur either when a change in pressure and/or temperature conditions cause the equilibrium solubility value to fall below the concentration of H_2O dissolved in the melt, or if addition of H_2O to the melt increases the dissolved H_2O concentration above the equilibrium H_2O solubility of the system. In volcanic contexts, bubbles typically form as magma ascends through the crust. The accompanying

decrease in the overburden pressure reduces the confining pressure of the system and thus the magma can hold less dissolved H_2O (e.g. Fig. 2.10). However bubble formation may also occur, for example, when growth of anhydrous crystal phases increase the concentration of H_2O dissolved in the remaining melt above the equilibrium solubility value.

When a critical supersaturation is reached in the melt, bubbles will nucleate. Supersaturation is defined as the pressure difference between the pressure at which the melt becomes supersaturated and the pressure at which bubbles nucleate. The degree of supersaturation required for nucleation varies according to whether nucleation is homogeneous or heterogeneous. Homegeneous nucleation takes place in pure melt systems where there are no nucleation sites, such as crystals, to help overcome the surface tension barrier to nucleation while heterogeneous nucleation occurs in the presence of such nucleation sites. Homogeneous nucleation may therefore require supersaturation pressures of up to 200 MPa (e.g. Mourtada-Bonnefoi & Laporte 2004), whereas heterogeneous nucleation may occur at supersaturation pressures of only 5 MPa (e.g. Gardner et al. 1999). In practice, the presence of magmatic crystal phases make homogeneous nucleation unlikely in natural systems, and even in experimental investigations of pure melts bubbles are likely to nucleate heterogeneously on the sides of the capsules (e.g. Iacono Marziano et al. 2007).

2.8.2 Bubble growth

When a bubble is nucleated, the H_2O concentration at the bubble wall is the equilibrium H_2O solubility value for the current local pressure and temperature conditions. Away from the bubble wall the supersaturated melt contains more H_2O that the new equilibrium solubility value, and so H_2O will diffuse down a concentration gradient towards the bubble wall and into the bubble. Bubble growth therefore occurs through diffusive mass transfer, with additional growth through simple decompressive expansion in cases where the magma is being decompressed (Sparks 1978). When a bubble is in equilibrium with the melt (i.e. neither growing nor shrinking), H_2O

concentration in the surrounding melt is uniform with distance from the bubble wall (Fig. 2.13 a), while if a bubble is growing, H_2O concentration decreases towards the bubble wall (Fig. 2.13 b).

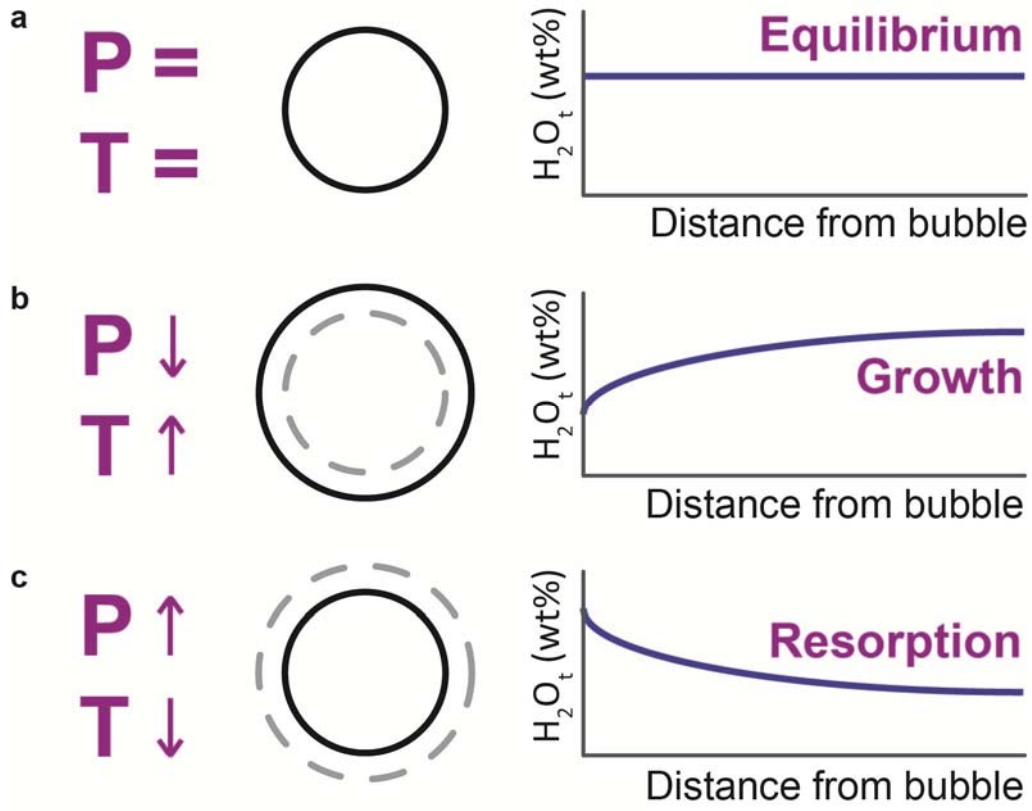

Fig. 2.13 Linking concentration profiles with bubble growth and resorption

Schematic figure linking the pressure (P) and temperature (T) conditions, state of bubble growth, and associated concentration profiles in the melt. H_2O concentration at the bubble wall is always the equilibrium H_2O concentration for the P,T conditions. **a** Where P,T are constant, the bubble neither grows nor shrinks and the profile of H_2O concentration in the melt is uniform with distance from the bubble wall. **b** With decreasing P and/or increasing T, H_2O solubility decreases and the bubble grows as H_2O diffuses down a concentration gradient into the bubble. **c** With increasing pressure and/or decreasing temperature, H_2O solubility increases and the bubble shrinks as H_2O diffuses from the bubble back into the melt.

Bubble growth models use the variation over time of this concentration gradient in the melt to model the H_2O flux into the bubble and its subsequent expansion. Initially bubble growth models considered the case of a single bubble growing in an infinite melt (e.g. Sparks 1978). In practice however bubble growth will be affected by the growth of neighbouring bubbles, which compete for volatiles and will begin to impinge on one another as they expand. Subsequent bubble growth models therefore introduced growth in a finite melt shell (Fig. 2.14). Here a bubble is considered to grow inside a spherical shell of melt, surrounded in a close packing arrangement by other bubbles growing in identical shells of melt (Prousevitch et al. 1993). Bubble growth is modelled by calculating how the concentration gradient between the bubble wall and the edge of the melt shell varies over time (Fig. 2.14). Successive generations of bubble growth models have included the effects of advective flux of melt as the bubble boundary moves (Proussevitch et al. 1993), decompression (e.g. Lensky et al. 2004), and the coupling of H_2O concentration, melt viscosity and H_2O diffusivity (e.g. Blower et al. 2001; Lensky et al. 2001).

One of the main findings from bubble growth models are the conditions under which bubble growth can keep pace with changing conditions. For example, at slow decompression rates the excess H_2O in the supersaturated far field may diffuse into the bubble sufficiently rapidly that the concentration gradient is approximately flat. In such cases the bubble size will be in equilibrium with the pressure and temperature conditions of the system, and the melt experiences 'equilibrium degassing'. Conversely, if the equilibrium solubility value decreases rapidly (for example as a result of rapid decompression) the rate at which H_2O can diffuse from the supersaturated melt may be too slow to maintain uniform concentration in the melt, and the melt would experience 'disequilibrium degassing' where the melt retains a degree of supersaturation. This effect is also investigated in experimental studies of bubble growth, which use the measured bubble sizes and porosities of experimentally vesiculated samples to examine the degree of disequilibrium degassing associated with different pressure and temperature conditions (e.g. Burgisser & Gardner 2005). This meaning of disequilibrium degassing is distinct from

'nonequilibrium' degassing which is sometimes applied where two volatiles (typically H_2O and CO_2) are degassing but diffuse at different rates, resulting in disequilibrium proportions of the two volatile components (e.g. Gonnermann & Manga 2005).

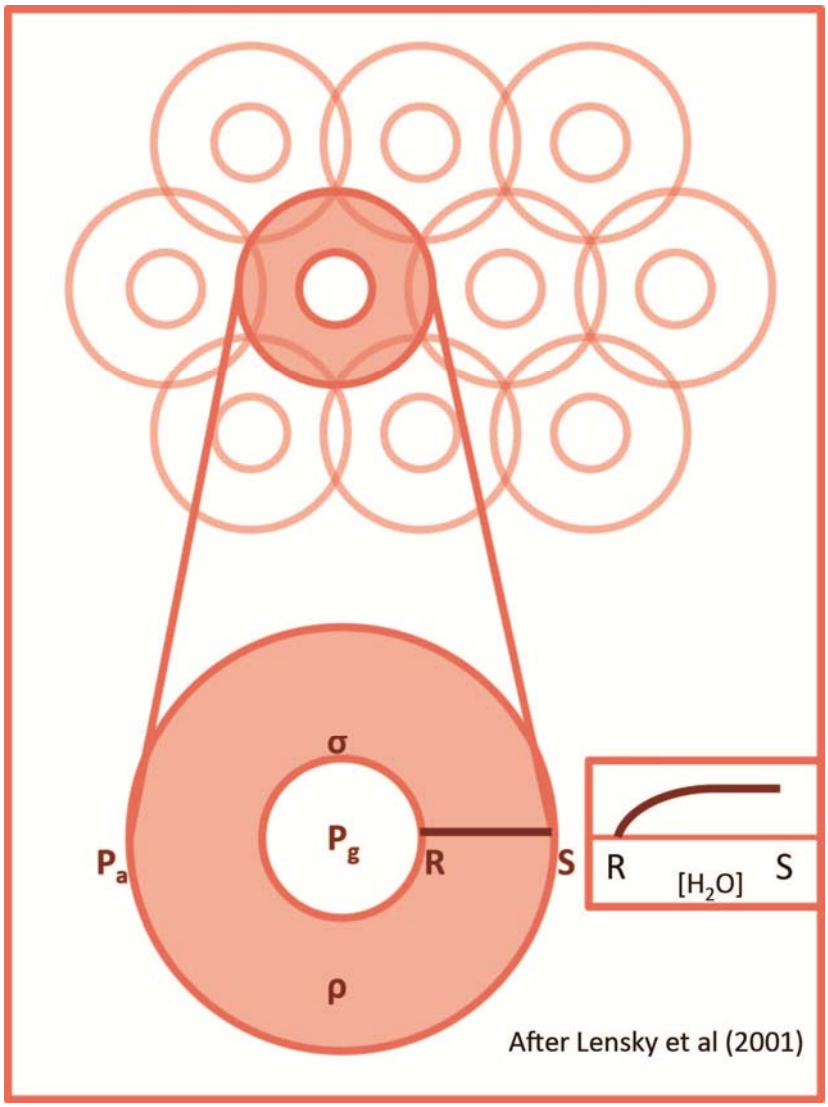

Fig. 2.14 Outline of a bubble growth model

Bubble growth models typically consider a bubble growing in a shell of melt of finite volume (e.g. Lensky et al. 2001). Terms include the internal gas pressure, ambient pressure, melt density and surface tension. Bubble growth is modelled by calculating how H_2O concentration varies along a profile from R, the bubble wall, to S, the boundary of the melt shell, as a function of time. H_2O concentration, H_2O diffusivity and melt viscosity are strongly coupled and interact to control bubble growth.

2.8.3 Bubble resorption

During bubble resorption, a decrease in the equilibrium H_2O solubility causes the H_2O concentration at the bubble wall to increase above the concentration of H_2O dissolved in the melt, and so H_2O diffuses from the bubble down a concentration gradient back into the melt (Fig. 2.13 c). This transfer of mass back into the melt will cause the bubble to shrink, or resorb.

Few studies have investigated bubble resorption in magmatic contexts. Yoshimura & Nakamura (2008) showed that bubble resorption could occur in an open degassing scenario by holding vesicular melt in apparatus that maintains a pressure difference between the melt and the outside. H_2O vapour is capable of escaping the higher pressure sample chamber, and so H_2O was lost by diffusion from sample margins resulting in the resorption of bubbles along the margins. Yoshimura & Nakamura (2010) extended this study to a mixed H_2O-CO_2 system. A H_2O-rich melt containing bubbles of H_2O was surrounded by a pure CO_2 fluid, and bubbles were seen to shrink initially as fast-diffusing H_2O moved from the melt into the surrounding fluid and H_2O moved from the bubbles into the melt to maintain an equilibrium H_2O concentration in the melt. Conversely, CO_2 moved from the fluid into the melt and ultimately into the bubbles, but the slower timescale of CO_2 diffusion caused temporary bubble resorption.

Two recent studies have reported observations of bubble resorption in natural samples, and have attributed the cause of resorption to an increase in pressure. Watkins et al. (2012) measured H_2O concentration profiles around vesicles in obsidian pyroclasts from Mono Craters, California, which revealed that the bubbles were resorbing prior to the glass transition. The authors interpreted these as evidence of cycles of pressure increase in the conduit prior to eruption.

The second study, by Carey et al. (2013), found indirect evidence of bubble resorption in basaltic clasts from an eruption of the Halema'uma'u lava lake, Kīlauea, Hawai'i. Although H_2O concentrations in the samples were too low to analyse, bubble resorption was inferred from a vesicle population where large vesicles were surrounded by a halo of smaller vesicles. These were

inferred to represent bubbles which had begun to resorb as they sank during conduit convection, which caused an increase in pressure and thus in the equilibrium H_2O solubility. Upon pressure decrease, either as a result of further convection or eruption, the H_2O-rich melt surrounding the partially resorbed bubble became supersaturated and nucleated a secondary bubble population. These observations were used to estimate the rate of convection within the conduit.

Chapter 3: Sample Production and Analytical Methods

3.1 Introduction

This chapter provides an overview of the samples analysed in this study – their provenance, composition, and production conditions – and the methodologies used to produce the analyses in Chapters 4-6.

3.2 Sample production

All samples presented in this thesis are vesicular volcanic glasses obtained from pre-existing experimental suites. The samples were manufactured under controlled pressure and temperature conditions (Table 3.1) and were designed to produce bubble populations that were either in equilibrium with the melt (solubility experiments) or in a state of growth (decompression experiments) at the point of quench. Details of each sample suite are given below.

Sample		T_{exp} (°C)	P_{syn} (MPa)	P_i (MPa)	Duration P_i (hr)	P_f (MPa)	dP/dt (MPa/s)
Rhyolite *Quench: 3-10 s*	ABG1	825	150	100	0.17	100	N/A
	ABG2	825	150	100	0.17	60	0.1
	ABG6	825	150	100	0.17	80	0.1
	ABG14	825	150	100	0.25	80	0.5
	ABG15	825	150	100	0.25	60	0.5
Phonolite *Quench: 3-10 s*	IS14	1050	200	200	>3	100	0.024
Rhyolite *Quench: 30-60 s*	MCN13	825	80	80	72	80	N/A
	MCN14	850	80	80	72	80	N/A
	MCN28	825	100	100	73	100	N/A
Rhyolite *Quench: 3-10 s*	MCN15	825	80	80	72	56	4
	MCN33	840	120	120	72	85	0.6

Table 3.1: Experimental conditions of sample production

Experiments were undertaken isothermally at experimental temperature (T_{exp}). Pressure of sample synthesis (P_{syn}), initial pressure (P_i) and final pressure (P_f) conditions are given. *dP/dt* refers to decompression between P_i and P_f.

Oxide composition	ABG series[1]	IS14[2]	MCN series[3]
SiO_2	75.64	57.15	76.32
TiO_2	0.08	0.30	0.21
Al_2O_3	12.38	21.34	13.02
FeO*	0.94	2.70	1.03
MnO	0.07	0.14	*ND*
MgO	0.03	0.39	0.04
CaO	0.54	3.26	0.53
Na_2O	4.17	5.16	3.93
K_2O	4.72	9.46	4.73
P_2O_5	0.01	0.09	*ND*
Total	98.58	99.99	99.81

ND – not determined.

Table 3.2: Sample composition

Sample compositions as determined by electron microprobe analyses by [1]Mangan & Sisson 2000 (as used by Burgisser & Gardner 2005, [2]Iacono Marziano et al. (2007) and [3]J. Larsen (*pers. comm.*).

3.2.1 ABG series

The ABG samples were provided by Alain Burgisser. They are part of an experimental suite previously published in Burgisser & Gardner (2005), a study that was designed to investigate the influence of decompression conditions on magma degassing processes. The samples were made using rhyolite glass from Panum Crater Dome in California, USA (composition given in Table 3.2). This glass was held at 150 MPa (pressure of synthesis, P_{syn}) and 825 °C (experimental temperature, T_{exp}) with excess H_2O to create a starting melt that was H_2O-saturated and fully equilibrated. Samples were then instantaneously decompressed to 100 MPa to nucleate bubbles. Samples were held at this pressure (initial pressure, P_i) for 10 – 15 minutes to ensure the bubble population had reached equilibrium with the surrounding melt. One sample (ABG1) was then quenched without subsequent decompression and is therefore expected to have had an equilibrium bubble population prior to quench. The other ABG samples were decompressed at different rates and to different final pressures (P_f) before being quenched, and are therefore expected to have had bubble populations that were growing prior to quench. Fig. 3.1 shows a schematic diagram of how pressure varied throughout the experiment for ABG1 (Fig. 3.1 a) and ABG2 (Fig. 3.1 b). All experiments were conducted isothermally at T_{exp} until quench.

The ABG samples were created using an externally heated pressure vessel fitted with a water-cooled rapid quench attachment (Jacobs & Kerrick 1980). Temperature was not measured during the quench process so the quench rate is not directly known but can be calculated using the model of Xu & Zhang (2002) (see Chapter 5 Section 5.4.1.1). A small, transient pressure fluctuation is observed at the beginning of quench (Alain Burgisser, *pers. comm.*). This fluctuation comprises a pressure increase of < 10 MPa and lasts for < 1 s, and occurs as the pressure medium re-equilibrates as the sample capsules drop into the quench attachment (e.g. Holloway et al. 1992). Quench is otherwise isobaric at the final pressure.

The samples contain ~0.1 vol% of crystals that are Fe-Ti oxide rods of ~10 μm length (Burgisser & Gardner, 2005). Bubbles are often attached to these crystals and so bubble nucleation is expected to have occurred heterogeneously (Burgisser & Gardner, 2005). Sample porosities and mean bubble diameters measured by Burgisser & Gardner (2005) are given in Table 3.3.

Sample	Porosity (vol %)	Mean bubble diameter (μm)
ABG1	5.6 (0.2)	35 (7)
ABG2	21.8 (0.8)	60 (11)
ABG6	13.3 (1.1)	60 (14)
ABG14	6.7 (0.2)	38 (6)
ABG15	19.1 (1.3)	63 (9)

Table 3.3: Porosities and mean bubble diameter of ABG samples
Porosities and mean bubble diameter as reported by Burgisser & Gardner (2005). Errors given as ± 1 standard deviation.

Using empirically-derived H_2O solubility data for a melt with the same composition (Mangan & Sisson 2000), Burgisser & Gardner (2005) calculated expected sample porosity as a function of final pressure (P_f), assuming that all excess H_2O in the melt exsolved to form a bubble population that was in equilibrium with the melt. The effect of decompression rate on magma degassing was then investigated by comparing observed and expected sample porosities. Where observed sample porosities were lower than expected, samples were concluded to have experienced disequilibrium degassing (see Chapter 2 Section 2.8.2). The authors used these data to define three distinct bubble growth regimes. An equilibrium bubble growth regime occurs for decompression rates < 0.1 MPa/s, while a slow bubble growth rate regime was defined for decompression rates > 0.2 MPa/s where disequilibrium degassing creates lower than expected sample porosities. A further fast bubble growth rate regime was defined for final pressures < 60 MPa where sample porosities begin to approach expected equilibrium values once more. The experimental data were then used to fit a model of magma ascent in a conduit in order to investigate the impact of disequilibrium degassing on conduit flow dynamics.

The ABG sample chips had previously been mounted on glass slides using epoxy resin. Samples that are mounted using epoxy are unsuitable for FTIR analysis since epoxy interferes with the absorption peaks used to determine H_2O concentration (see Section 3.3.2). The ABG samples were therefore only analysed using SIMS-calibrated BSEM imaging (see Section 3.3.1; Chapter 4 and Chapter 5).

3.2.2 IS14

Sample IS14 was provided by C. Ian Schipper. IS14 was created using a K-phonolite glass from the 'white pumice' of the AD 79 eruption of Mt Vesuvius. This starting glass was also used by Iacono Marziano et al. (2007) in their experimental study of decompression-induced degassing and so compositional information is taken from their study (Table 3.2). IS14 was part of an unpublished study that replicates the pressure and temperature conditions investigated by Iacono Marziano et al. (2007). The glass was held at 200 MPa (P_{syn}) and 1050 °C (T_{exp}) for > 3 hours with excess H_2O in order to create a homogeneous water-saturated melt. Decompression began from P_{syn} (i.e. there was no separate nucleation step as for the ABG samples, thus $P_{syn} = P_i$) and the sample was quenched immediately upon reaching the final pressure. A schematic of the pressure variation during the experiment is shown in Fig. 3.1 c.

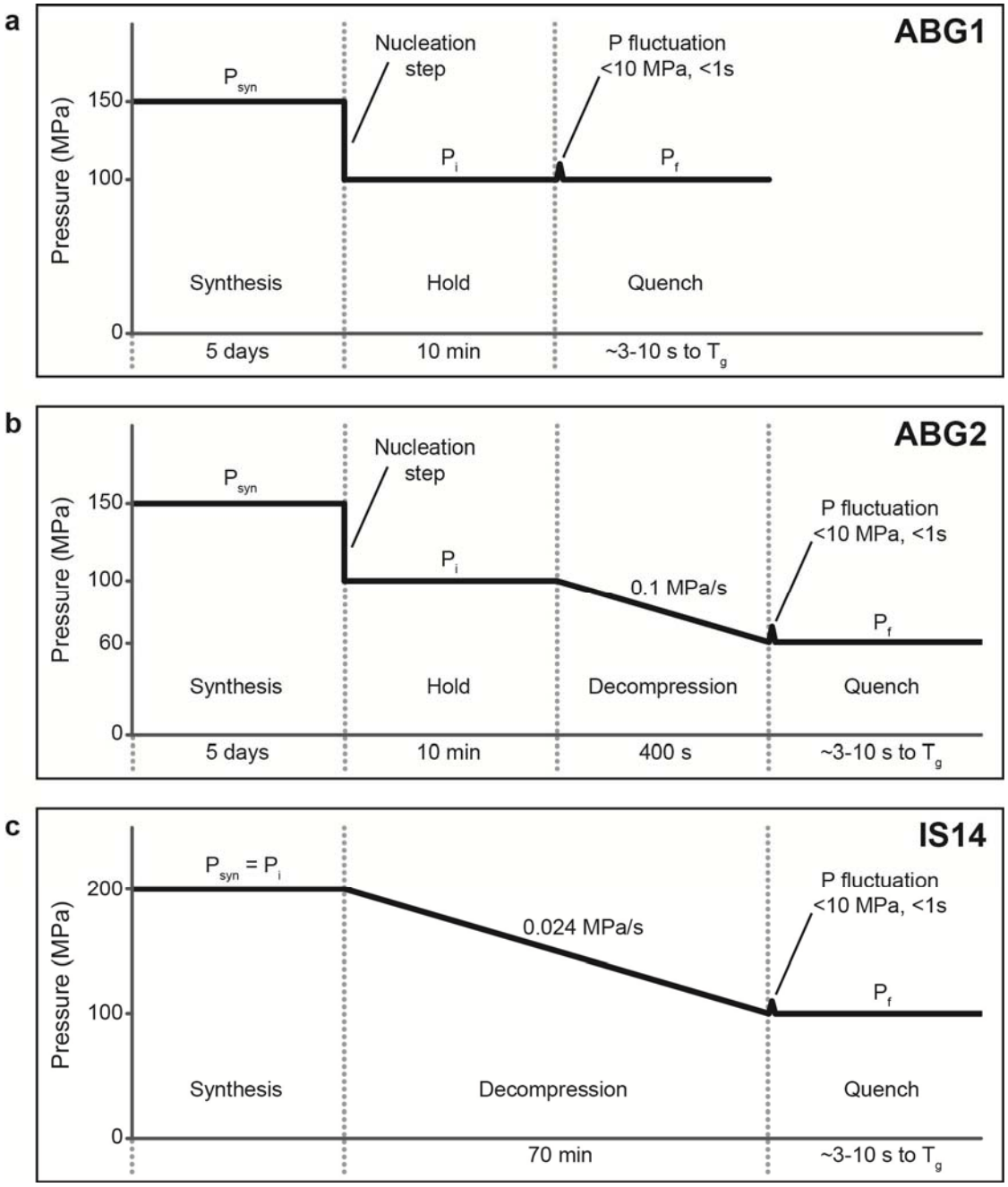

Fig. 3.1 Pressure-time histories of ABG and IS14 samples

Schematic diagrams of how pressure varies during experimental runs, showing pressure of synthesis (P_{syn}), initial pressure (P_i) and final pressure (P_f). All ABG samples undergo initial pressure drop to nucleate bubbles and are then held (ABG1, 2, and 6 for 10 minutes, ABG14 and 15 for 15 minutes) prior to decompression and isobaric quench. **a, b** ABG1 (equilibrium bubble population expected) and ABG2 (bubble growth expected) shown as examples. **c** IS14 has no intermediate nucleation step, thus $P_{syn} = P_i$. All samples experience a small (<10 MPa), brief (<1 s) pressure fluctuation at the beginning of quench as the pressure medium re-equilibrates following sample drop into the quench attachment.

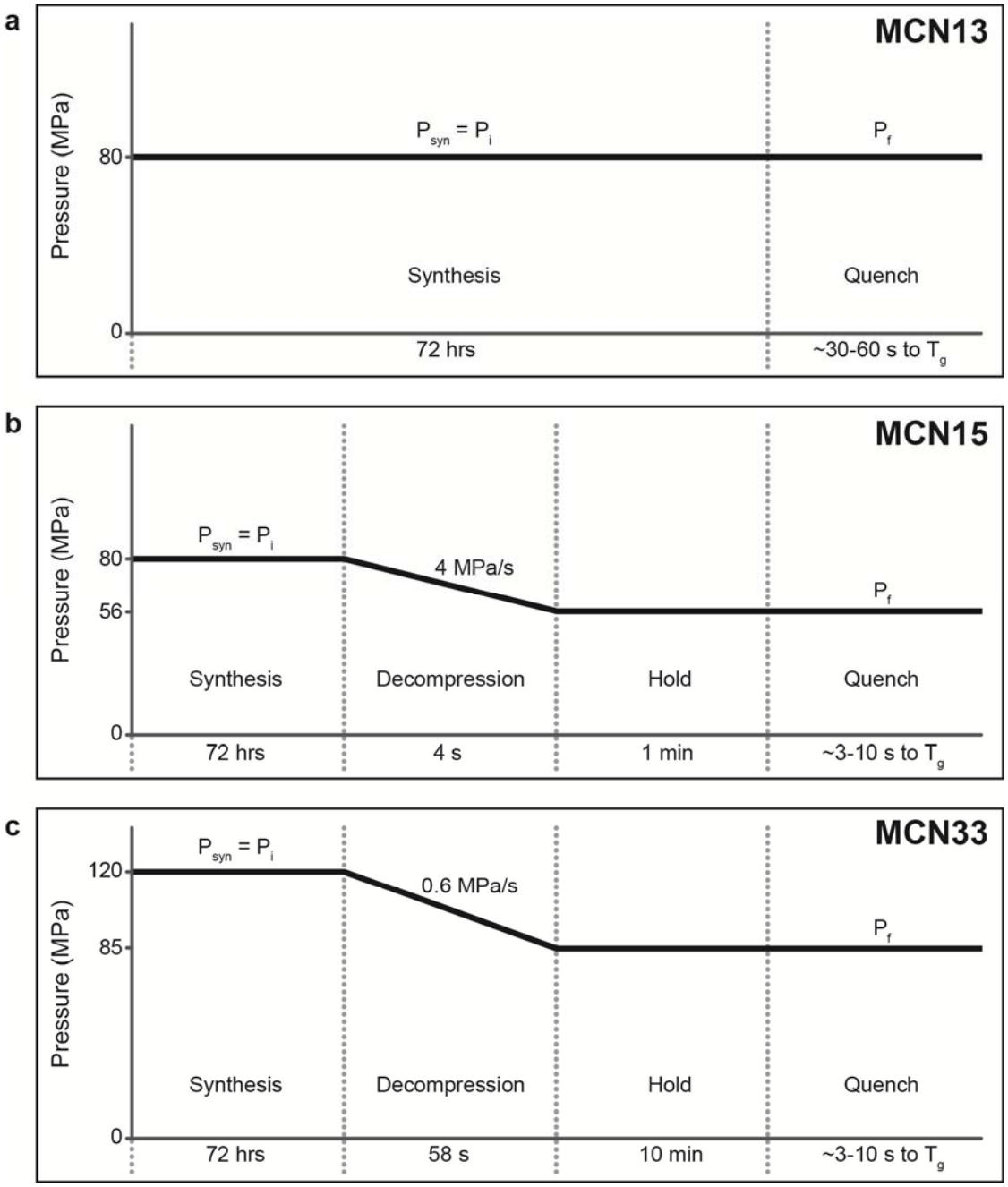

Fig. 3.2 Pressure-times histories of MCN samples

Schematic diagrams of how pressure varies during experimental runs, showing pressure of synthesis (P_{syn}), initial pressure (P_i) and final pressure (P_f). MCN13 is typical of the MCN solubility samples, with $P_{syn} = P_i = P_f$ (**a**). **b**, **c** show the decompression experiments MCN15 and MCN33, respectively, which underwent decompression and were then held at P_f prior to quench. MCN33 was decompressed more slowly and held at P_f for longer than MCN15.

IS14 was created in an internally heated pressure vessel, following the experimental procedure of Di Carlo et al. (2006). Quench was conducted using an Ar-cooled rapid quench attachment. Temperature was not measured during quench, but is estimated to decrease at ~ 100 °C/s (Di Carlo et al., 2006). As with the ABG samples, a brief pressure fluctuation of < 10 MPa lasting < 1 s was observed as the sample capsule moved into the cold quench vessel and the pressure medium equilibrated between the hot and cold parts of the vessel (Holloway et al, 1992; Di Carlo et al., 2006).

The study of Iacono Marziano et al. (2007) investigated the effect of decompression rate on bubble nucleation and magma degassing. All samples experienced heterogeneous nucleation of bubbles at the capsule-melt interface, with samples decompressed rapidly (1.7 and 4.8 MPa/s) experiencing additional homogenous nucleation in the melt when a critical supersaturation is reached. For the sample conditions replicated by IS14 (decompressed at 0.024 MPa/s), bubble nucleation occurred heterogeneously and bubble growth occurred under disequilibrium degassing conditions. The authors compared their experimental data with observations of the natural pumice textures and concluded that the AD 79 Vesuvius plinian event was likely to have involved both heterogenous and homogenous bubble nucleation, with homogenous nucleation probably occurring at a depth of ~3 km as a result of rapid ascent and decompression of the magma.

3.2.3 MCN series

The MCN samples were provided by Jessica Larsen. They were made using rhyolite glass from Mono Craters (composition given in Table 3.2). The MCN samples comprise two types: the first are solubility experiments designed to constrain melt H_2O_t contents at a given pressure and temperature condition. These samples are therefore expected to have had bubble populations in equilibrium with the melt prior to quench. The second type are decompression experiments which were designed to investigate bubble growth.

The MCN samples had not previously been mounted in epoxy and were therefore suitable for FTIR analysis (Chapter 6). One sample, MCN13, was also analysed using SIMS-calibrated BSEM imaging (Chapter 4).

3.2.3.1 Solubility samples

The solubility samples were created by holding the sample with excess H_2O at high pressure and temperature for 3 days and then quenching. These experiments were therefore both isothermal and isobaric (i.e. $P_{syn} = P_i = P_f$) throughout (Fig. 3.2 a). These samples have not previously been published but were produced following the procedure of Larsen (2008). The samples were created using Waspaloy hydrothermal cold seal pressure vessels placed in a furnace. Quench was achieved by removing the pressure vessels from the furnace and cooling initially with compressed air until the vessels stopped glowing, and then placing them in a water bucket to reach ambient temperature. Cooling rate was not measured but is estimated at ~30-60 s to the glass transition (J. Larsen, *pers. comm.*; see Chapter 6 Section 6.4.2.2).

3.2.3.2 Decompression experiments

Samples MCN15 and MCN33 are decompression experiments. These were synthesised at high pressure (P_{syn}) and temperature (T_{exp}) before decompression to the final pressure P_f (i.e. $P_{syn} = P_i$). Upon reaching P_f they were held for some time prior to decompression. MCN15 was decompressed at a faster rate and held for a shorter time than MCN33 (Fig. 3.2 b, c). Neither sample has previously been published but both were created according to the procedure of Larsen et al. (2004). Samples were created in rapid quench cold seal pressure vessels and quenched by pulling the sample capsules against the water-cooled seal. They are therefore expected to have similar quench rates to the ABG samples.

3.3 H_2O measurement

H_2O concentration in the sample glasses was analysed using backscatter Scanning Electron Microscope (BSEM) images, Secondary Ion Mass Spectrometry (SIMS) and Fourier Transform Infra Red (FTIR) spectroscopy. These analytical techniques offer high spatial resolution coupled with small uncertainties. These features are necessary in order to extract concentration profiles along radial distances of the order of tens to hundreds of microns (representing the typical bubble-bubble separation of these samples) where the greatest variation is expected to be contained within a small portion close to the vesicle wall. SIMS results in concentrations of total H_2O (H_2O_t), while FTIR is used to extract water speciation data that can be used to investigate the conditions under which the observed H_2O_t concentration profiles form.

3.3.1 SIMS-calibrated BSEM images

3.3.1.1 Principle

The method of obtaining H_2O_t data from SIMS-calibrated BSEM images was pioneered by Humphreys et al. (2008), who measured H_2O concentration profiles along tube shaped melt inclusions (i.e. melt inclusions that have not been completely sealed off from the surrounding silicate melt) in plagioclase crystals from the May 18th 1980 eruption of Mt St Helens, USA. Degassing during magma ascent caused the H_2O content of the melt surrounding the crystals to decrease and consequently H_2O began to diffuse outwards from the high H_2O content pre-eruptive melt within the crystal along the connecting melt channel. Upon eruption the melt quenched to glass and the resulting concentration profiles were preserved.

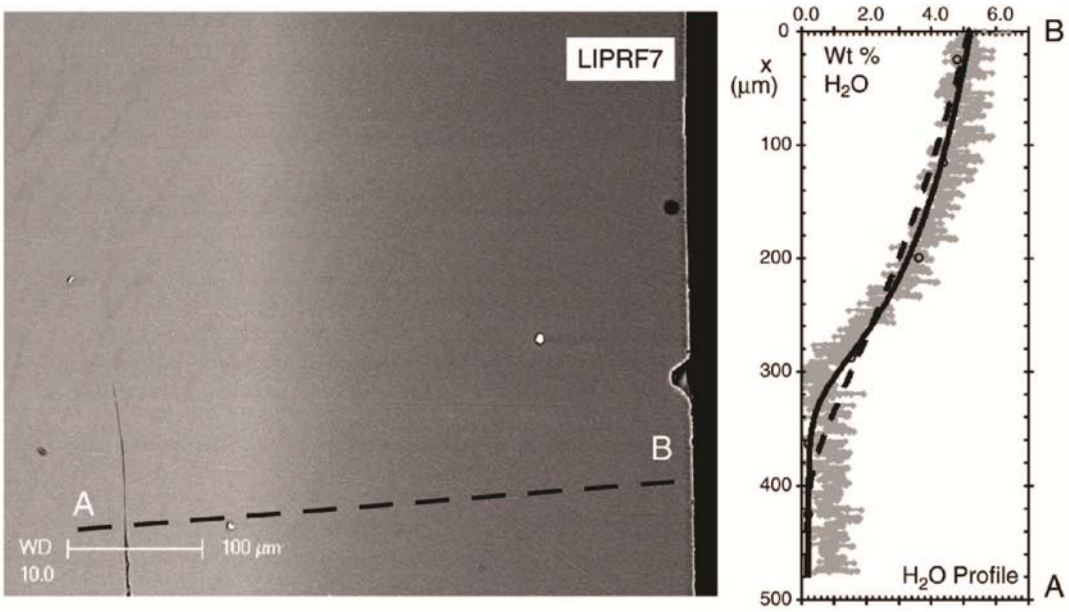

Fig. 3.3 H_2O concentration variation in BSEM images

Humphreys et al. (2008) demonstrated that greyscale variation in BSEM images can be used to extract H_2O concentration profiles. Moving from A to B along the transect shown, glass appears increasingly dark in BSEM image, corresponding to increasing H_2O concentration. Small grey triangles represent H_2O data from calibrated greyscale values, while black solid and dashed lines are curves from diffusion modelling. Taken from Fig. 6 in Humphreys et al. (2008).

Humphreys et al. (2008) demonstrated that greyscale variations in backscatter SEM (BSEM) images of volcanic glass are related to the H_2O content of the glass, with H_2O-rich glass appearing darker than H_2O-poor glass (Fig. 3.3). In a SEM, high energy electrons interact with the atoms in the sample surface. In backscatter mode, only those electrons which are 'back-scattered' from the sample surface via elastic scattering in the sample atoms are detected. Atoms with higher atomic number (*Z*) have a larger atomic radius than atoms with lower *Z*, and are therefore more likely to encounter, and cause elastic scattering of, incident electrons. Areas of a sample where the composition has a high mean *Z* will therefore backscatter more electrons to the detector and appear brighter in BSEM images than areas of comparatively low mean *Z*, which will backscatter fewer electrons and appear darker in BSEM images (Newbury 1975).

For given beam settings, an incident electron beam interacts with a similar volume of atoms (i.e. the interaction volume) regardless of whether the sample is H_2O-rich or H_2O-poor. For example, using the empirical relationships of Potts (1987), p 336-7 the approximate depth and width of the interaction volume for a 15 keV electron beam are 2.41 μm and 1.81 μm for anhydrous rhyolite, and 2.48 μm and 1.91 μm for rhyolite with 4 wt% H_2O. H_2O consists of two light elements, H (Z = 1) and O (Z = 8). The silicate framework consists primarily of O but also includes heavier elements such as Si (Z = 14) and Al (Z = 13). Addition of H_2O to the anhydrous silicate network depolymerises the network by breaking Si-O bonds (see Chapter 2 Section 2.2) so that for the same structural unit of the silicate framework, an anhydrous melt will have a higher mean Z than a hydrous melt containing additional H (and O) atoms. This effect is reflected in the decrease of glass density with increasing H_2O concentration (e.g. Ochs III. & Lange 1997). Within the same interaction volume the mean Z of H_2O-rich glass is lower than that of H_2O-poor glass, and H_2O-rich glass accordingly appears darker than H_2O-poor glass in BSEM images.

If glass composition is homogeneous except for H_2O concentration, BSEM images can therefore be used to show qualitative variations in glass H_2O concentration. Owing to the magnification potential of the SEM, this can be done with extremely high spatial resolution. The ultimate unit of resolution is the size of a pixel in the BSEM image, which can easily be <<1 μm. The greyscale values of pixels are directly correlated with the H_2O content of the imaged glass and so qualitative H_2O profiles can be extracted by measuring how greyscale varies along a transect. BSEM images alone however cannot give quantitative information about H_2O concentrations.

To obtain quantitative H_2O_t data from BSEM images it is necessary to calibrate them using a quantitative analytical technique, such as SIMS. In SIMS analyses, a beam of charged ions (e.g. O^-) is directed onto the sample surface. These ions collide with atoms in the sample surface and ionise them by knocking out electrons. These 'secondary ions' then enter a mass spectrometer which identifies the type and quantity of elements present in the sample. The output from SIMS is

'counts per second' (cps). Elements present in high concentrations in the sample have high cps compared with elements present in lower concentrations (Fig. 3.4 a). The cps output is converted into quantitative compositional data by calibration using known standards. For the analysis of H_2O in silicate glass, the standards are silicate glasses with similar anhydrous composition to the samples to be analysed and with a range of independently measured H_2O concentrations. Analysis under the same beam settings reveals what cps value is expected for H for different H_2O contents. The ratio of $^{1}H^{+}/^{28}Si^{+}$ cps is used in order to account for matrix effects, following Blundy & Cashman (2005). These values are then used to create a working curve (e.g. Fig. 3.4 b) whereby the $^{1}H^{+}/^{28}Si^{+}$ cps of an analysed sample of unknown H_2O content can be used to determine its H_2O concentration in wt% (Fig. 3.4 c). SIMS spot analyses typically have spatial resolution of ~10 x 10 µm, and analyse (destructively) the top ~3 µm of the sample surface (although this analysis pit increases in depth with increasing analysis time). Analytical errors are typically 10% relative.

The spot size of SIMS is too large to give sufficient spatial resolution to analyse concentration profiles in the necessary detail. However by using SIMS spot analyses of H_2O concentrations to calibrate the greyscale values in BSEM images Humphreys et al. (2008) demonstrated that the SIMS-calibrated BSEM method can be used to extract quantitative H_2O_t data at sufficiently high spatial resolution (Fig. 3.3).

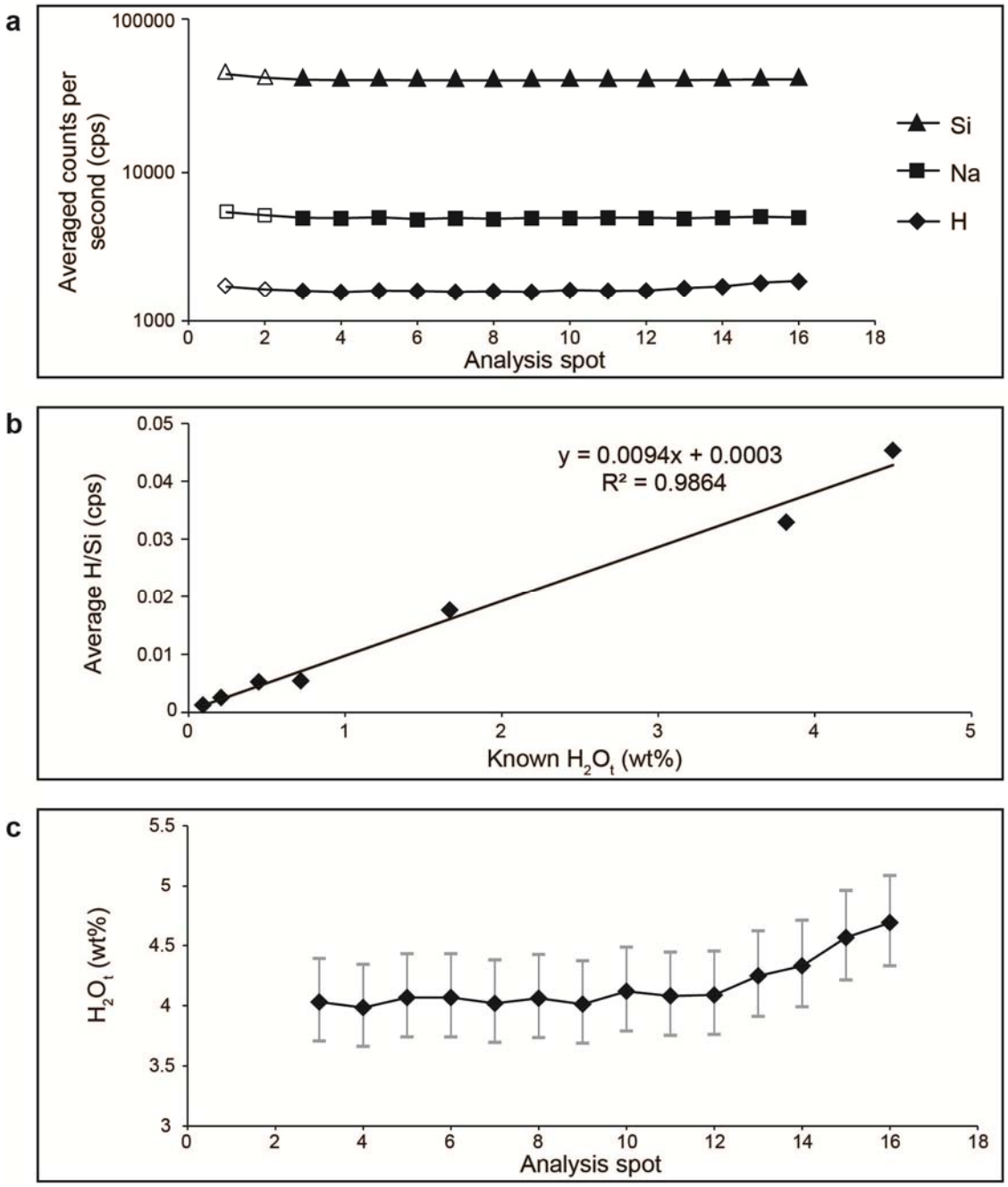

Fig. 3.4 SIMS analysis of H_2O concentration

a Secondary ions created during SIMS analysis are analysed by a mass spectrometer and ouput as the averaged counts per second (cps) of each element of interest. **b** By analysing glass standards of known H_2O concentration, a working curve of H/Si cps and H_2O concentration is created. **c** Application of this calibration to H/Si cps of an unknown sample provides quantitative H_2O concentration, with errors typically 10% relative. The first two spots of each SIMS profile are anomalous as the beam burns through the sample coat and therefore excluded (**a**, **c**). H_2O concentration profile in **c** corresponds to cps data shown in **a**.

3.3.1.2 Sample preparation

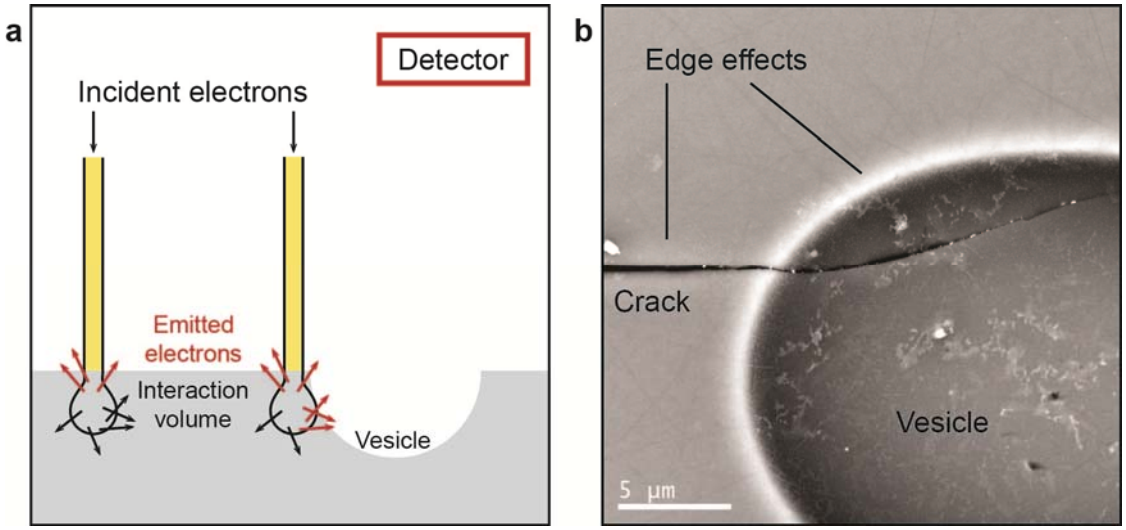

Fig. 3.5 Edge effects in BSEM

a When an incident electron beam interacts with the sample surface, some electrons escape the sample surface (red arrows) while others are lost within the sample (black arrows). If the beam approaches a change in topography, such as a cavity related to an unfilled vesicle, electrons that would otherwise have been lost within the sample can now escape the sample surface and are detected, resulting in a brighter signal. **b** This signal is seen as an anomalously bright edge along cracks and vesicle walls (particularly unfilled vesicles) in BSEM images.

Samples were prepared at Durham University by sample technician David Sayles. Vesicular glass samples were embedded in epoxy resin and ground down to expose a flat glass surface with exposed vesicles, which constitute cavities in an otherwise planar surface. For both BSEM imaging and SIMS analysis it is necessary to prepare the sample such that there is a continuous flat surface, in order to reduce topographic 'edge effects' (Newbury 1975). Topographic edge effects can occur in two ways and are of particular importance in BSEM imaging. Firstly, because the incident electron beam and detector are situated at an angle to the sample surface, if there is any variation in surface height across the sample surface it will affect the probability of backscattered electrons reaching the detector leading to an effect analogous to shadow in a photographic image. Secondly, as the incident beam approaches an edge (such as an unfilled vesicle) electrons that would otherwise have been lost within the sample are able to escape the sample through the

exposed edge and thus to reach the detector (Fig. 3.5 a). In BSEM imaging these edge effects are seen as an anomalously bright signal at the edge (e.g. Fig. 3.5 b). In order to reduce these edge effects the samples were covered in a second layer of epoxy and subsequently ground down to the original surface such that the glass was once more exposed but the vesicles remained resin-filled. Edge effects still occur as the beam approaches a change in medium (i.e. from glass to epoxy) but they are significantly reduced. Final polishing was conducted using 1 μm diamond paste in order to ensure a high-quality, scratch-free surface for imaging.

Once prepared, example samples were examined using confocal microscopy at Kingston University to check that this preparation results in a uniform, flat surface (Fig. 3.6). The surfaces of infilled vesicles were found to be within 1 μm of the surrounding glass surface and there was no visible gap between the glass and resin at vesicle edges that might occur if the resin shrank during curing. The sample surface as a whole was found to be flat with no evidence of 'shouldering' or sloping down towards vesicle walls. After several successive rounds of polishing by hand to remove carbon and gold coats necessary for BSEM and SIMS analyses, some samples exhibited evidence of sloping towards vesicle edges. Such vesicles were avoided during analyses so that topographic effects could not affect extracted greyscale values.

The epoxy resin used was Specifix-20. This was chosen from the list of resins recommended by the Edinburgh Ion Microprobe Facility for preparing sample mounts owing to its balance of relative hardness and low exothermic heat output during setting. Throughout the sample preparation process heating was minimised to avoid any alteration of H_2O distribution. Sample mounts were therefore left to cure at room temperature in the vacuum oven rather than heated as is standard.

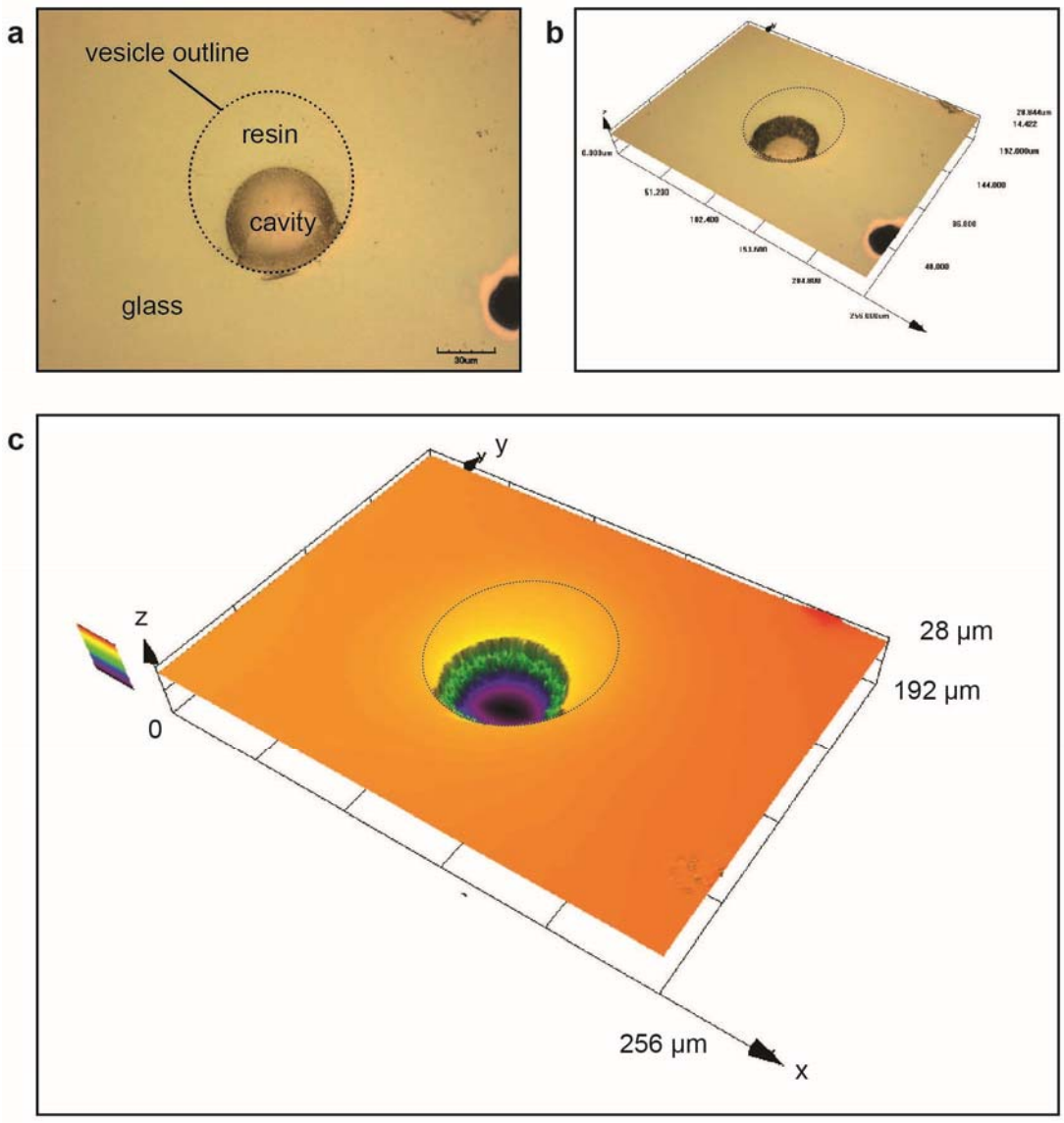

Fig. 3.6 Confocal microscopy analysis of sample surface

A partially infilled vesicle in a sample was analysed by confocal microscopy to check sample preparation, and is shown in reflected light (**a**, plan view; **b**, 3D view) and coloured according to surface height (**c**). The join between the glass and resin is smooth with less than 1 micron variation in surface height, with no gradient in the slope of the glass approaching the vesicle. This is in contrast to unfilled vesicles where cavities may be tens of microns deep, as in the unfilled portion of the vesicle shown.

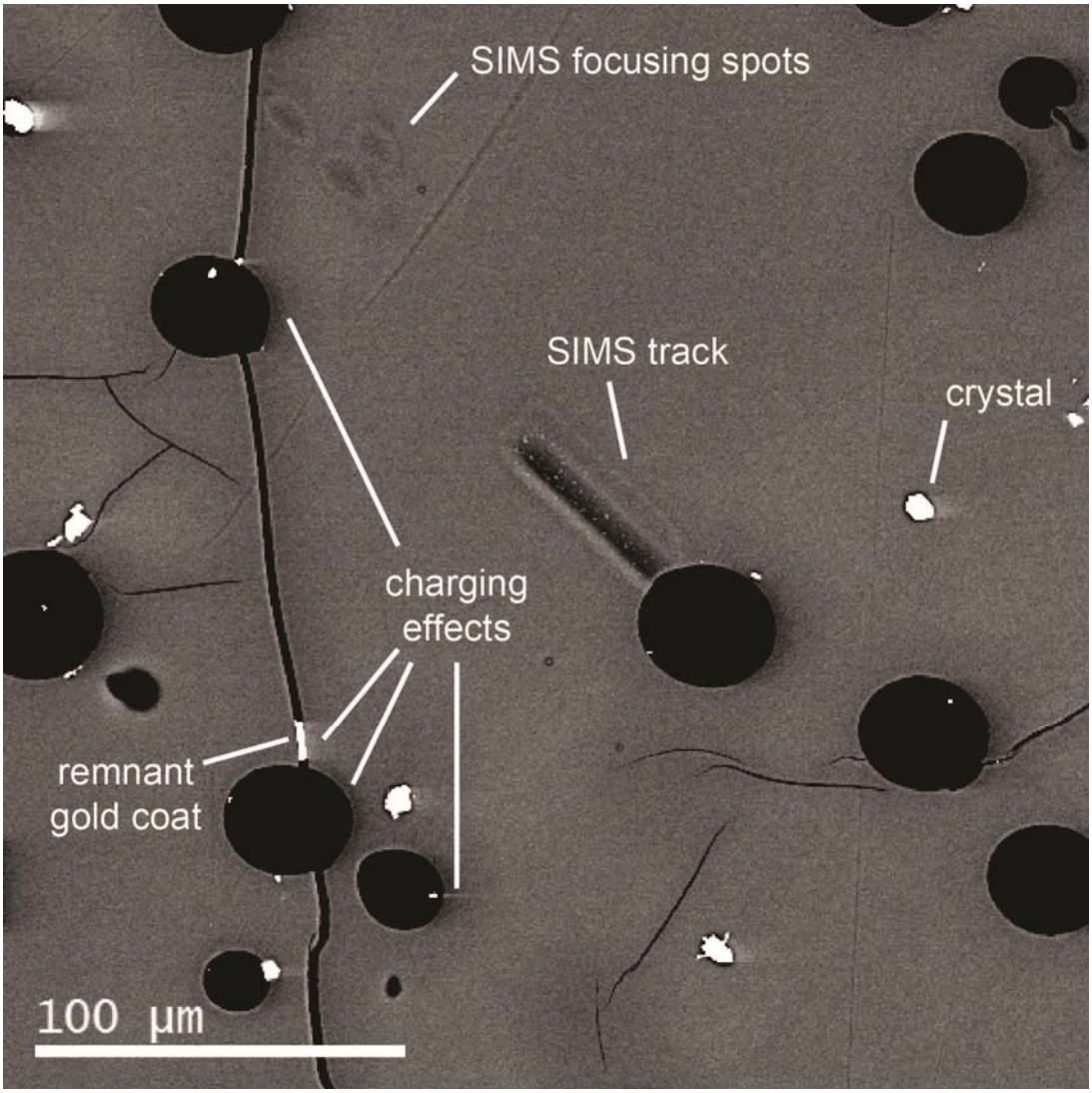

Fig. 3.7 Factors affecting quality of BSEM images

Greyscale variations in BSEM images of these samples may be affected by several factors. In addition to narrow, bright edge effects (<2 µm), charging effects may create 'streaks' of high or low greyscale values alongside areas of high mean *Z* (e.g. remnant gold polish, crystals) and low mean *Z* (e.g. cracks, vesicles). These effects are distinguished from topographic effects because they appear in the same direction (e.g E-W on right hand side of objects in image shown) even when the sample is rotated. If information is required from an area affected by charging effects it can be obtained by rotating the sample or the direction of beam raster. Topographic effects will always be associated with the same area regardless of sample orientation to beam raster and are avoided during analysis. SIMS analyses are destructive and leave pits and troughs in the sample surface that are seen as greyscale variations if not removed by polishing. Image shown is of sample ABG14.

3.3.1.3 BSEM imaging

BSEM images were acquired by IMM at the GJ Russell Microscopy Facility at Durham University with a Hitachi SU-70 Analytical High Resolution SEM with attached Gatan Mono CL and associated DigitalMicrograph software. Images were taken using a 15 keV electron beam in backscatter mode with a working distance of 15 mm. Samples were coated with carbon (30 nm thickness) to avoid charge build up. Infilling of vesicles with resin confined edge effects to thin (<2 μm) bright white rims at vesicle boundaries. In some images taken after SIMS analyses, residual gold coat remains in cracks and vesicle interiors and appears bright white in BSEM owing to the high atomic number of gold (Z = 79) (e.g. Fig. 3.7).

3.3.1.4 Major element composition

The major element composition of the glass was analysed using Energy Dispersive X-ray spectroscopy (EDS). Analyses were performed by IMM at the GJ Russell Microscopy Facility at Durham University using the Oxford Instruments EDX system and interpreted using Oxford Instruments INCA software. Radial profiles from vesicle walls were analysed with a 2 μm step size in order to check for systematic variation in major element composition with distance from vesicle walls. No variation in major element composition was observed (Fig. 3.8). This step was required to demonstrate the major element concentrations are spatially uniform, since it is assumed that all greyscale variations result from changes in H_2O concentration alone.

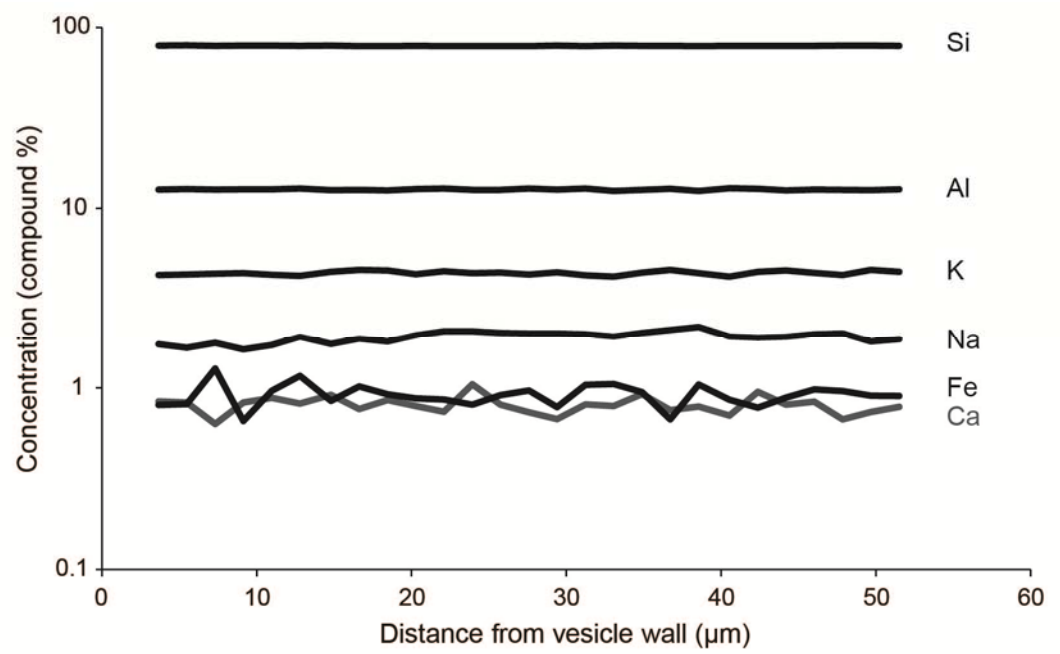

Fig. 3.8 Major element composition of glass

Major element composition of glass was analysed using EDS. Ca is coloured grey to distinguish from Fe. Profile shown is from sample ABG1 (which has a H_2O_t concentration half-fall distance of 12 µm) and is typical of other samples. No significant variation in major element composition is observed with distance from vesicle wall.

3.3.1.5 SIMS analyses

SIMS analyses were conducted at the Edinburgh Ion Microprobe Facility with a CAMECA ims-4f ion microprobe. Samples were gold coated (200 nm thickness) to prevent charge build up. Prior to analysis, samples were held under vacuum to allow the epoxy resin to outgas. Subsequently a good vacuum was achieved in the sample (analytical) chamber which results in a low background relative to sample H_2O contents. A 10.7 keV, 6 nA, O^- primary beam was accelerated onto the sample with a net impact energy of 15 keV. Positive secondary ions were accelerated to 4.25 keV and collected sequentially on the electron multiplier detector, using a 75 eV offset with a 40 eV energy window. The high H_2O contents of the samples enabled the use of the smallest field aperture to ensure all collected ions originated from the centre of the sputter crater. The analysed spot size was therefore ~5 x 5 µm, a particularly good spatial resolution for SIMS analyses. $^{1}H^{+}$, $^{23}Na^{+}$ and $^{28}Si^{+}$ were analysed in radial profiles towards vesicles. The use of step

scan mode with close step spacing removed the need for pre-analysis raster cleaning of the sample surface, since the beam began to burn through the gold coat of the adjacent step. 3 cycles of element measurements were made at each spot.

H_2O_t concentration was calculated from a working curve of $^{1}H^{+}/^{28}Si^{+}$ which was calibrated twice daily using well constrained standards of varying SiO_2 and H_2O content (Table 3.4). Matrix effects related to the bulk glass composition, whereby H and Si ion yields decrease with increasing H_2O_t concentration, have been observed in rhyolite glasses for H_2O_t contents > 1.5 wt% (Hauri et al. 2002). In such cases a polynomial fit is usually a better fit for the working curve than a linear regression trend. Applying a polynomial fit to the working curve created no appreciable improvement in the fit as described by the R^2 value, and so a linear regression trend was applied (Fig. 3.4 b). Analytical errors, based on the scatter of standards around the calibration line, are ±10% relative.

Standard	H_2O_t (wt%)	SiO_2 (wt%)
Lipari	0.72	74.03
KRA	0.45	72.17
Run 84	3.82	58.12
Run 101	1.67	57.56
Run 100	0.21	59.22
Run 121	4.5	67.38
H2VF	0.094	58.35

Table 3.4: Hydrous glass standards used in SIMS analysis
Standards varied from andesite to rhyolite in composition, and contained up to 4.5 wt% H_2O. Used courtesy of Madeleine Humphreys.

Profiles were run in scan mode with a 5 µm step size, with each analysed spot approximately 5 x 5 µm and <3 µm deep. On homogeneous glass, e.g. the glass standards, the first one or two spots in each profile analysed would deviate slightly from subsequent spot analyses. This deviation is likely due to the initial burning through of the gold coat, whereas subsequent analyses are made once a part of the sample surface has been exposed and the local charge environment modified

accordingly. The first two spots in each radial transect were discarded as a precaution, and transects for vesicular samples were begun in the far field rather than at the vesicle wall where the most important concentration variations were anticipated to be located (Fig. 3.4 a).

3.3.1.6 SIMS-BSEM calibration and data processing

After SIMS analysis, BSEM images were made of the area surrounding the SIMS track. Greyscale values were extracted using Gatan Digital Micrograph software along a 5 µm-wide profile taken either immediately adjacent to the visible SIMS track, or in the same location as the SIMS track after the damaged surface had been removed. Extracted greyscale profiles therefore do not correspond to the exact glass analysed by SIMS, but are close enough that good correlations with H_2O (typically $R^2 > 0.90$) are obtained. It was generally preferred to take adjacent profiles, which will be nearly radially symmetric, than profiles in the same orientation but below the plane of SIMS analysis. The shape of the observed concentration profile will vary depending on where the vesicle is cross-sectioned relative to its equator, and the removal of ~5 µm of surface material could affect the profiles, and thus image calibration, of vesicles with small radii.

The mean greyscale value of 5 µm segments of the greyscale profile were plotted against the corresponding SIMS spot analyses (Fig. 3.9 b). Errors on these values are caused by errors on SIMS H_2O analyses (y axis, ~±10% relative) and errors on the average greyscale value of the profile segment resulting from noise in the BSEM image (x axis, 1 standard deviation from the mean). A linear regression fit was applied and the resulting calibration equation used to extract quantitative data in the same image (Fig. 3.9 c). Each new image, even if it encompasses the same SIMS track, requires a separate calibration to account for the possible effect of changes in magnification or raster settings on greyscale values. 'Edge effects' at vesicle walls are narrow and anomalously bright and thus easily removed from extracted profiles. As a result, presented profiles begin a few micrometres from the vesicle wall. Images were enhanced using the same Gatan Digital Micrograph software to make greyscale variations more apparent to the human eye

by varying brightness, contrast and gamma settings; these settings do not alter the raw greyscale values used for calibration and data extraction.

For each sample, multiple radial profiles were extracted around multiple vesicles (e.g. Fig. 3.9 d). Once all extracted greyscale data were converted to H_2O data using the relevant image calibration equation, these were compiled to create a composite dataset of H_2O as a function of distance from vesicle wall for the sample. Mean H_2O value was calculated for 2 μm segments; these mean values form the H_2O profile for each sample. Errors shown are twice the standard error of the mean. Averaging all extracted profiles for bubbles in one sample thus accounts for the variation resulting from vesicles that are sectioned at different distances from their equator (which affects the profile gradient, with steepest profiles for those sectioned directly at the equator), and for variation in H_2O_t resulting from the use of multiple SIMS tracks (which affects the position on the y axis but not the gradient of the profile).

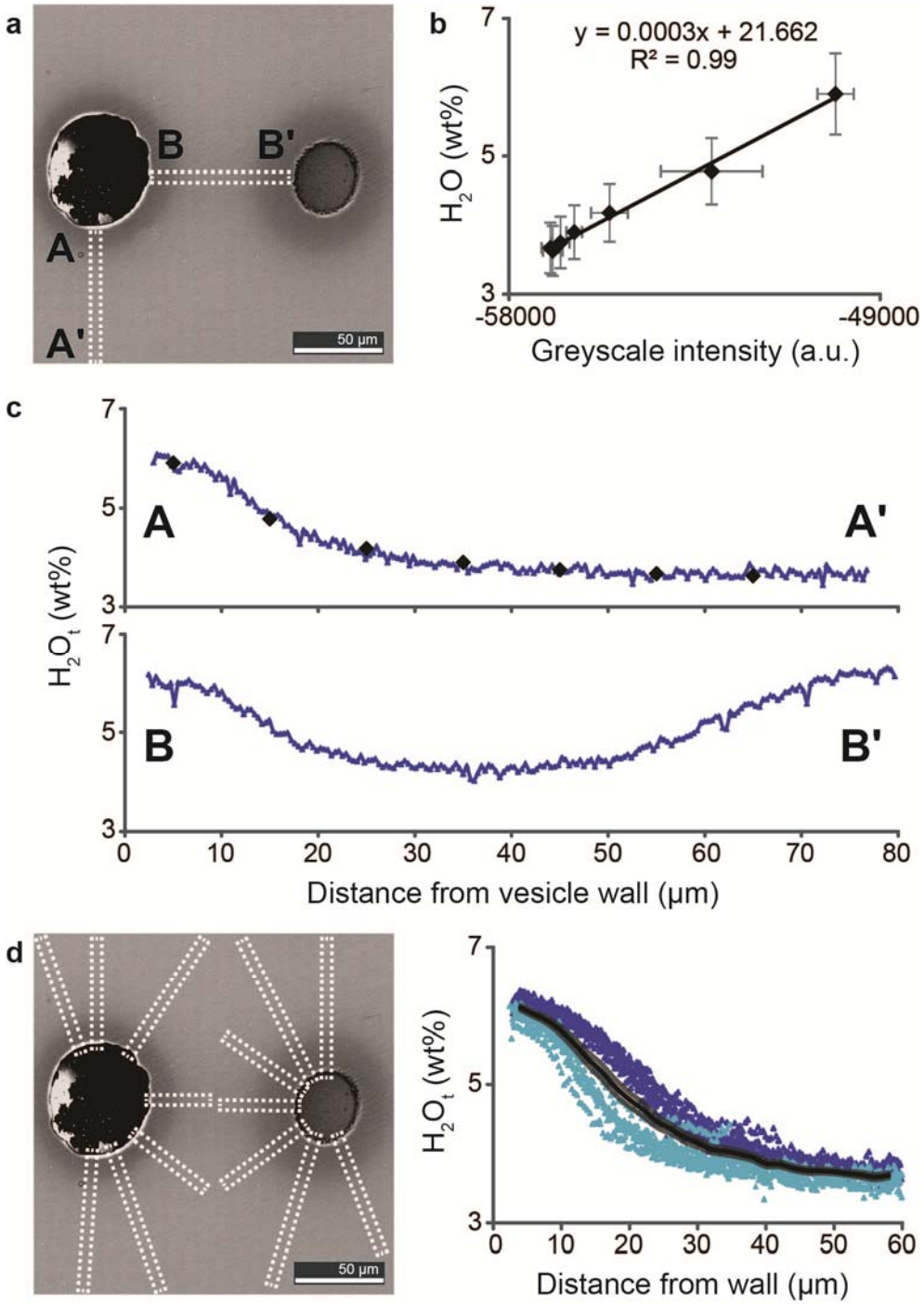

Fig. 3.9 Measuring H_2O concentration profiles using SIMS-calibrated BSEM imaging

a BSEM image of vesicles in phonolite glass showing dark water-rich halos. Note thin bright white edge effect at vesicle walls. **b** Calibration of SIMS H_2O_t data from profile A-A' with corresponding BSEM greyscale intensity values. **c** Profile A-A' shows H_2O_t measured by SIMS (black diamonds) and high spatial resolution H_2O_t concentrations extracted from calibration of greyscale values (blue triangles). Profile B-B' shows H_2O_t data extracted from greyscale values using the calibration equation derived from A-A'. **d** Several (>3) radial profiles taken around each vesicle, for multiple

vesicles (>12) in each sample. All extracted H_2O_t data for the sample are plotted against distance from vesicle wall and mean H_2O_t is calculated in 2 µm windows (solid black line). Upper and lower bounds are twice the standard error of the mean (semi-transparent solid lines). Left vesicle (light blue triangles) is sectioned closer to its equator so data follow a steeper curve than right vesicle (dark blue triangles). By averaging all data this sectioning variation is also averaged.

3.3.1.7 Sectioning effects

Bubble growth and resorption concentration profiles are radial from the bubble wall. If a vesicle is sectioned directly at its equator then the measured concentration profile is the same as the radial profile. However if a vesicle is sectioned at some other 'latitude' from the equator, the shape of the measured concentration profile will be determined not by the distance from the observed bubble wall as observed in a 2D image, but by the distance from the bubble wall along a radial profile. Here the influence of this sectioning effect on observed concentration profiles is assessed for different latitudes of sectioning (see Appendix A1 for full derivation).

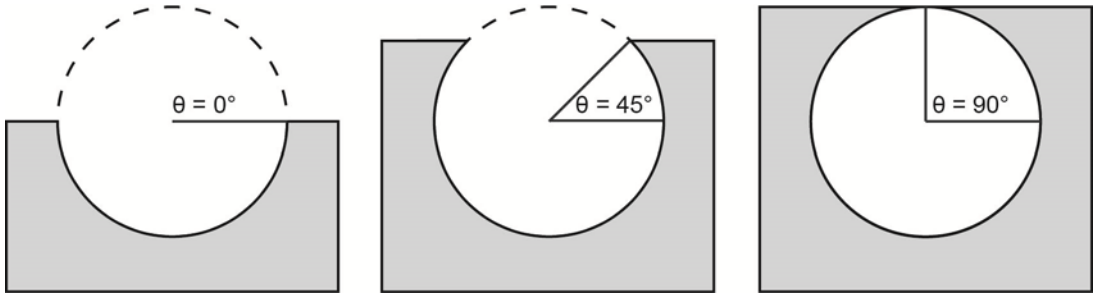

Fig. 3.10 Latitude of sectioning

The angle at which the vesicle is sectioned affects the observed H_2O concentration profile. The latitude of sectioning is given by the angle θ, where θ = 0° is a section taken at the vesicle equator, and θ = 90° is an enclosed vesicle.

The latitude of the observed plane with reference is described by the angle θ (Fig. 3.10). Fig. 3.11 shows profiles calculated for different angles of θ for vesicles with radii of 10 and 100 µm. The shape of the profile is always steepest for vesicles sectioned at their equator (θ = 0°), and

becomes increasingly S-shaped with increasing latitude. At the extreme of θ = 90°, the profile runs across the top of the vesicle and is initially convex before becoming concave with distance from the vesicle wall.

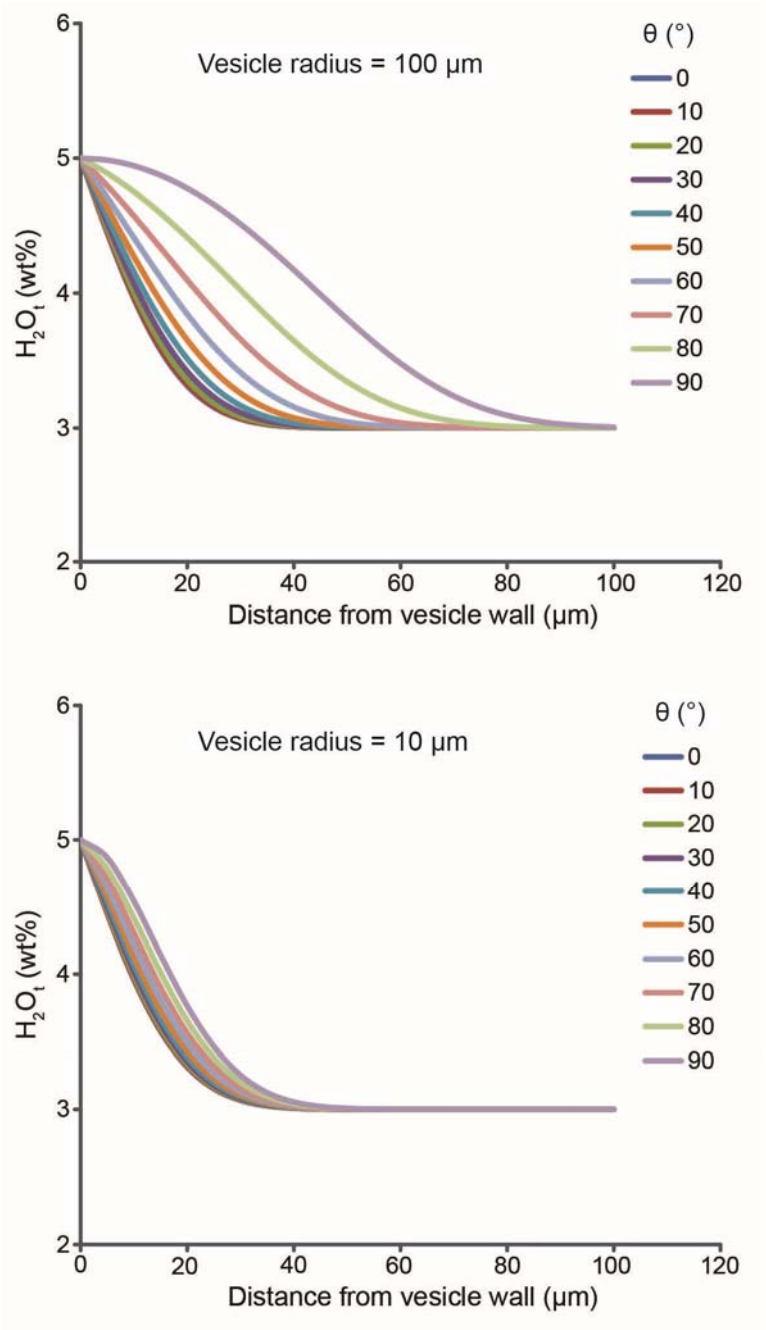

Fig. 3.11 Influence of sectioning effect on observed H_2O concentration profile

Graphs show how a measured H_2O concentration profile will vary according to the angle at which the vesicle is sectioned. θ = 0° is a profile measured at the equator, and will always be steeper than profiles from other latitudes. The observed difference in measured profiles is controlled by the size of the vesicle, being greater for larger vesicles and vice versa.

The use of H_2O concentration profiles from multiple vesicles sectioned at different latitudes to form an average H_2O concentration profile for each sample introduces error into the shape of the concentration profile. For this reason, variables such as H_2O half-fall distances should be calculated from individual vesicles rather than the average sample profile (e.g. Chapter 4 Section 4.4.3.3). However the difference in measured profiles is minor for vesicles sectioned within 30° of the equator, and becomes smaller for smaller vesicles (Fig. 3.11). The H_2O concentrations measured at the vesicle wall and in the far field will be the same regardless of the latitude of sectioning.

3.3.1.8 Use of multiple SIMS tracks

The impact of using multiple SIMS tracks for extracting H_2O data from multiple vesicles in the same sample is illustrated in Fig.s 3.12 and 3.13. Fig. 3.12 shows two different BSEM images of sample IS14, which cover the same vesicle. Each image contains a different SIMS track and so the H_2O_t concentration profile for the vesicle in question is calculated using two different greyscale calibrations (Fig. 3.13). Error on the SIMS calibration of BSEM greyscale values, which results from the error on SIMS measurements (± 10% relative) and the averaging of greyscale values adjacent to the SIMS track, result in different H_2O_t concentration profiles for the same vesicle being derived from the two different images (Fig. 3.13). This error does not affect the lengthscale of the extracted profiles (i.e. the half-fall distances are the same), but leads to different H_2O_t values at the vesicle wall and in the far field (Fig. 3.13 a). The extracted H_2O datasets from the two images are therefore combined and a mean concentration profile calculated (Fig. 3.13 b). In order to account for this error on observed H_2O_t concentrations, all extracted H_2O data from all vesicles in all images of a sample are combined and a mean H_2O_t concentration profile for the sample is calculated. This profile provides the values of H_2O_t at the vesicle wall and in the far field that are used to compare samples. The half-fall distance for each sample, however, is calculated using the vesicle with the steepest H_2O_t concentration profile, in order to limit the error introduced by sectioning effects (see Section 3.3.1.7; Chapter 4 Section 4.4.3.3).

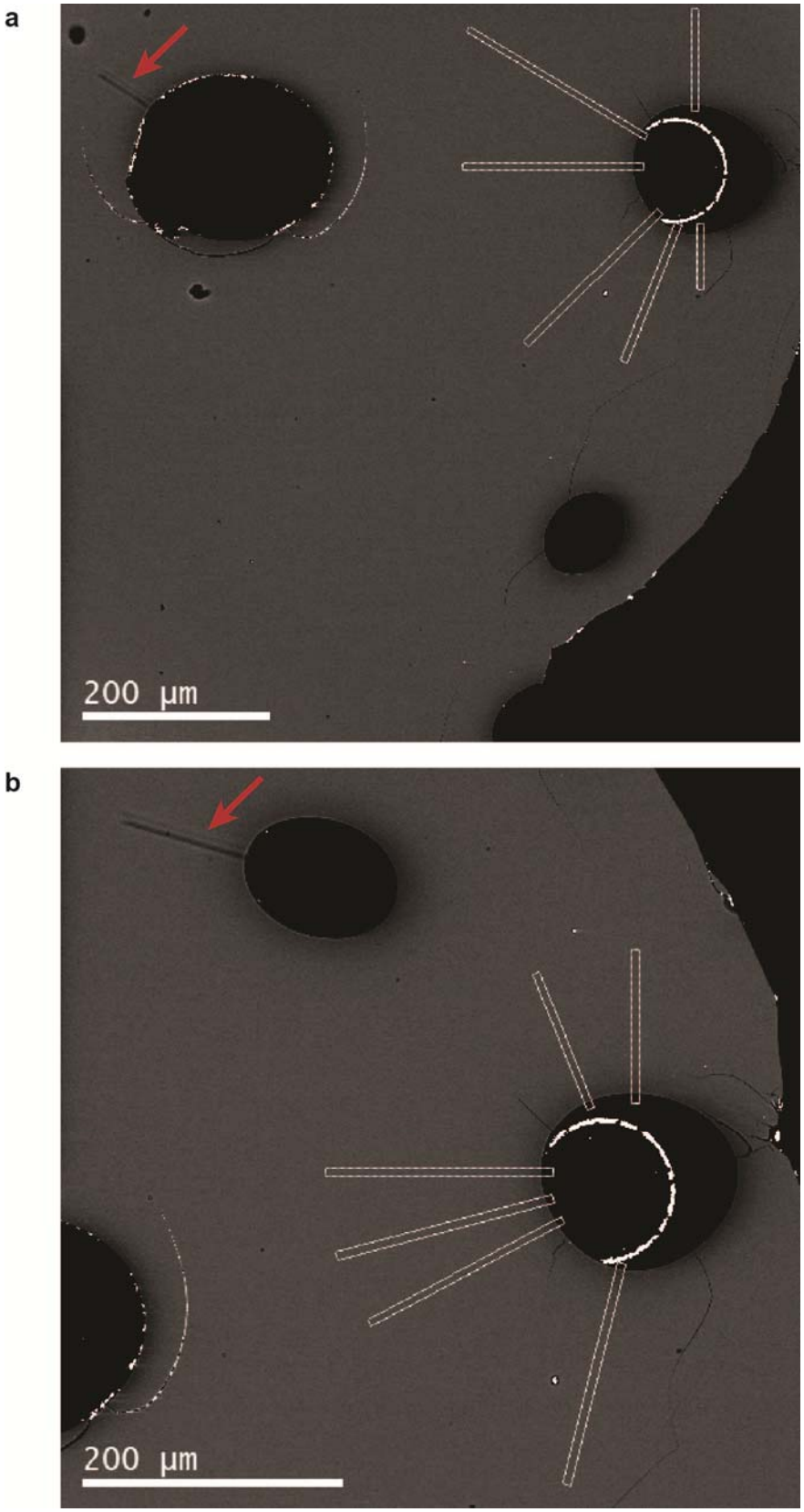

Fig. 3.12 H_2O concentration profile extraction from images with different SIMS tracks

Extracted profiles (white) around the same vesicle in sample IS14, seen in two different BSEM images containing different SIMS tracks (indicated by red arrows).

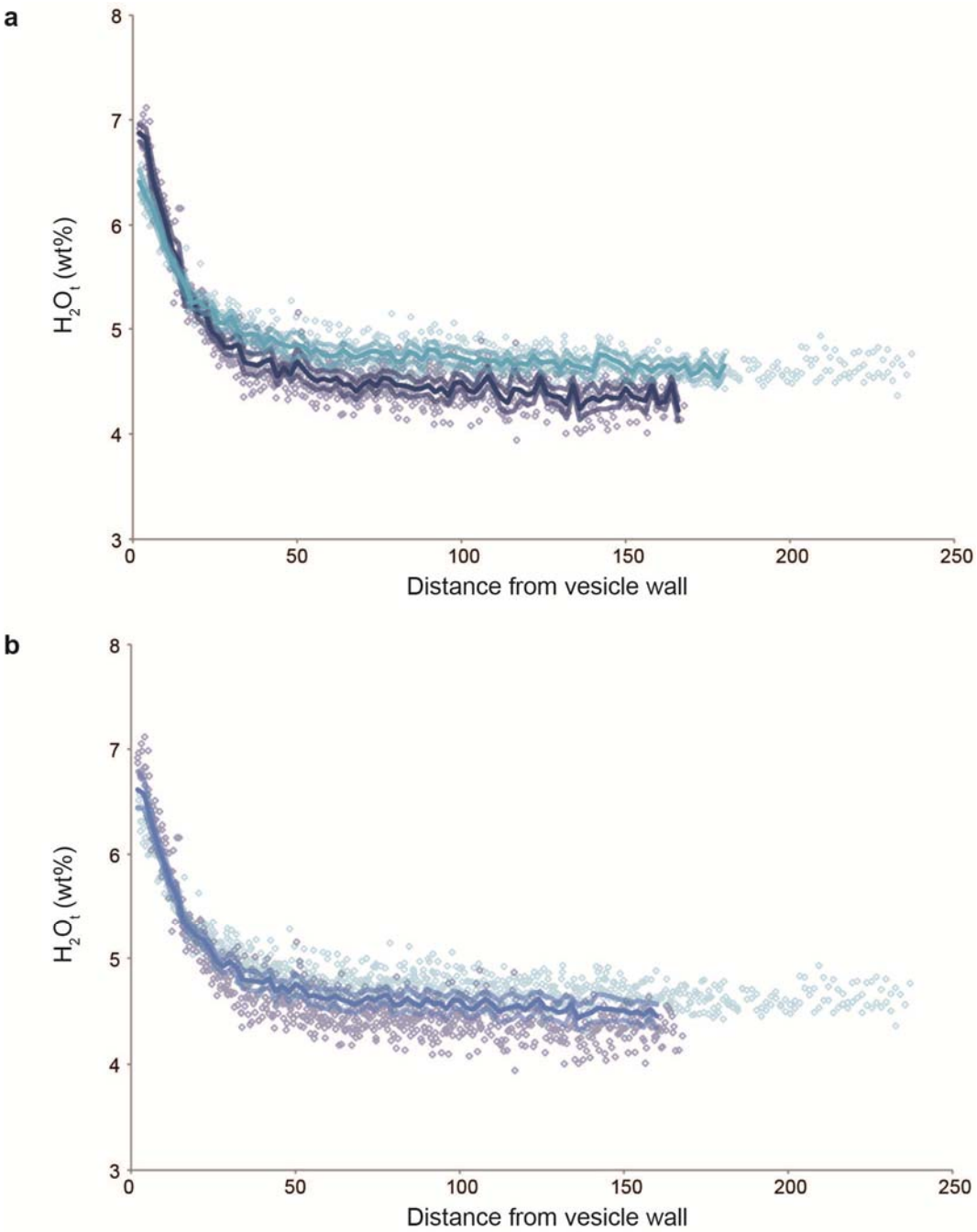

Fig. 3.13 Comparison of extracted H_2O_t profiles using different SIMS calibrations

a Extracted H_2O_t data (diamonds) and mean H_2O_t concentration profiles (solid line) for the same vesicle using different SIMS calibrations. Pale blue data correspond to image Fig. 3.12 a, dark blue data correspond to image Fig. 3.12 b. The use of different SIMS calibrations produces different concentration profiles for the same vesicle. **b** The mean calculated H_2O_t concentration profile for the same vesicle is calculated using the combined dataset. Transparent lines represent twice the standard error of the mean.

3.3.2 FTIR

3.3.2.1 Principle

Fourier Transform Infra Red spectroscopy (FTIR) can be used to obtain H_2O_t, H_2O_m and OH concentrations (see Chapter 2 Section 2.5). FTIR is a non-destructive analytical technique and can resolve a wide range of concentrations, from ppm to several wt% (Newman et al. 1986). In FTIR studies using single point analysis, spot sizes range from 30 – 100 µm for conventional IR sources down to 3 – 5 µm for synchrotron sources. In FTIR imaging studies, which use multichannel detection, 2D areas of a few square millimetres can be analysed in a single data collection, with individual spot sizes of ~2.5 - 5 µm (Della Ventura et al. 2010).

In the FTIR technique, infra red (IR) radiation is passed through a glass sample of known thickness. As the radiation passes through the sample it interacts with the molecules present in the glass, triggering transitions in molecular vibrations of covalent bonds. The wavelength of IR radiation that corresponds to the frequency of the molecular vibration is absorbed by these transitions. Different bonds have different frequencies of molecular vibration and accordingly absorb different wavelengths of IR radiation, allowing identification of the molecular species present. These absorptions can be converted into quantitative concentrations using the Beer-Lambert law, which states that the intensity of the absorption is proportional to the number of absorbers per unit area in the light path (e.g. Stolper 1982, Newman et al. 1986)

FTIR is particularly useful for identifying H-O groups because these bonds tend to be highly polarised and are therefore particularly efficient absorbers of IR radiation (Della Ventura et al. 2010). Several different absorption bands exist for H_2O groups, being associated with different 'modes' of bond transitions (Fig. 3.14). In the near infra red (NIR) region (i.e. wavenumbers >4000 cm^{-1}), absorption bands occur at ~7100, ~5200, ~4500 and ~4000 cm^{-1}. Of these the strongest absorptions occur for the ~5200 cm^{-1} band, which is attributed to the combination stretching and bending mode of H_2O_m (Scholze 1960; Bartholomew et al. 1980), and the ~4500 cm^{-1} band, which

is attributed to the combination modes of Si-OH and Al-OH groups (Stolper 1982). The weaker absorption band at ~7100 cm^{-1} is an overtone of the OH stretching mode (Bartholomew et al. 1980), while the origin of the band at ~4000 cm^{-1} is uncertain but thought to be the result of both H_2O_m and OH groups (Newman et al. 1986). In the IR region (i.e. wavenumbers <4000 cm^{-1}) the bands related to H_2O bonds are the ~3500 and ~1630 cm^{-1} bands. The ~3500 cm^{-1} band is broad and asymmetric (Fig. 3.14) and is attributed to the fundamental OH stretching vibration (Nakamoto 1978), which is present in both H_2O_m and OH groups. The breadth and asymmetry of the peak reflects the distribution of H-bond strengths within the glass (Newman et al. 1986). The ~1630 cm^{-1} band is approximately symmetrical and is attributed to the fundamental bending mode of H_2O_m (Nakamoto 1978).

The absorption bands in the IR region have much greater intensities than those in the NIR region (note the different absorption scales in Fig. 3.14) because the molar absorptivity coefficients of IR bands are significantly higher than those of the NIR bands (Stolper 1982). In addition to the absorption bands associated with H_2O, Fig. 3.14 shows several other features typical of an FTIR spectrum of volcanic glass. The noise seen at ~2350 cm^{-1} corresponds to molecular CO_2 (Newman et al. 1986). Provided that the FTIR analysis is conducted in a fully purged N_2 atmosphere, so that atmospheric CO_2 is not present, absorption in this band highlights the presence of molecular CO_2 within the glass. Small absorbance bands at ~2000 and ~1800 cm^{-1} (discernible in Fig. 3.14) and also at ~1600 cm^{-1} (not discernible) are attributed to the vibration of aluminosilicate portions of the silicate framework that are not H-bearing (Newman et al. 1986). The tendency for a rising background to higher wavenumbers in the NIR region is thought to be caused by both the high energy tail of the fundamental OH band at ~3500 cm^{-1} and by absorptions by dissolved iron (Stolper 1982).

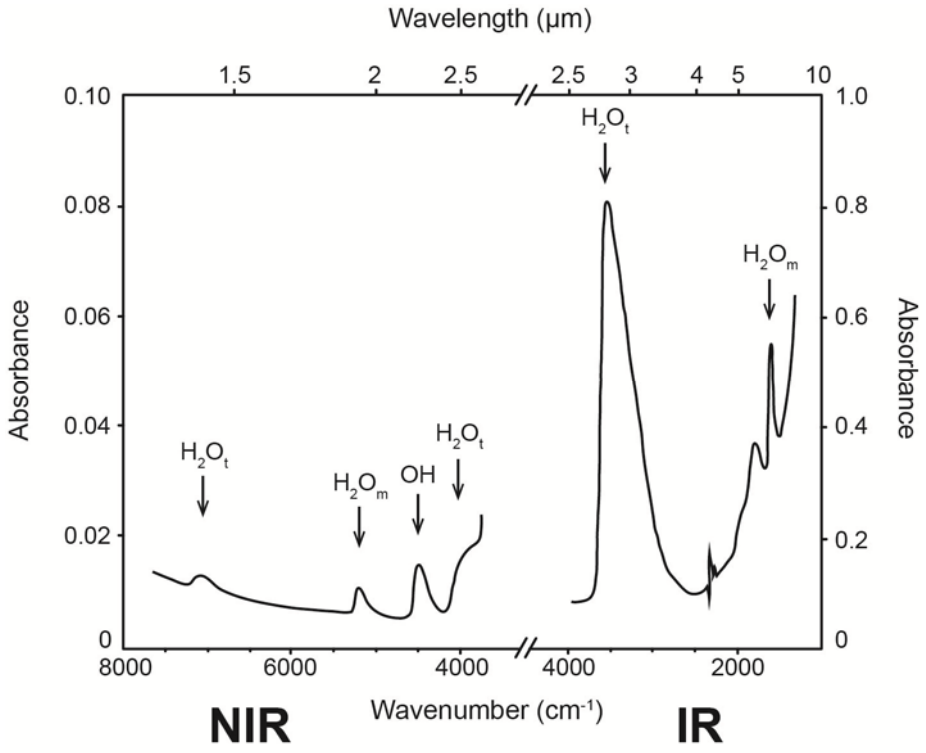

Fig. 3.14 H-O absorptions in FTIR spectra

Schematic figure showing the positions of the major H-O absorption bands in near infra red (NIR, higher wavenumbers) and infra red (IR, lower wavenumbers) light. NIR bands are weaker absorbers (refer to lefthand absorbance scale) and require thicker samples for analysis than IR bands (righthand absorbance scale). The noise seen at ~2350 cm^{-1} is caused by molecular CO_2 which may be present either in the glass or atmospheric background (if analysis is not conducted under fully purged conditions). Figure modified from Fig. 6 of Newman et al. (1986).

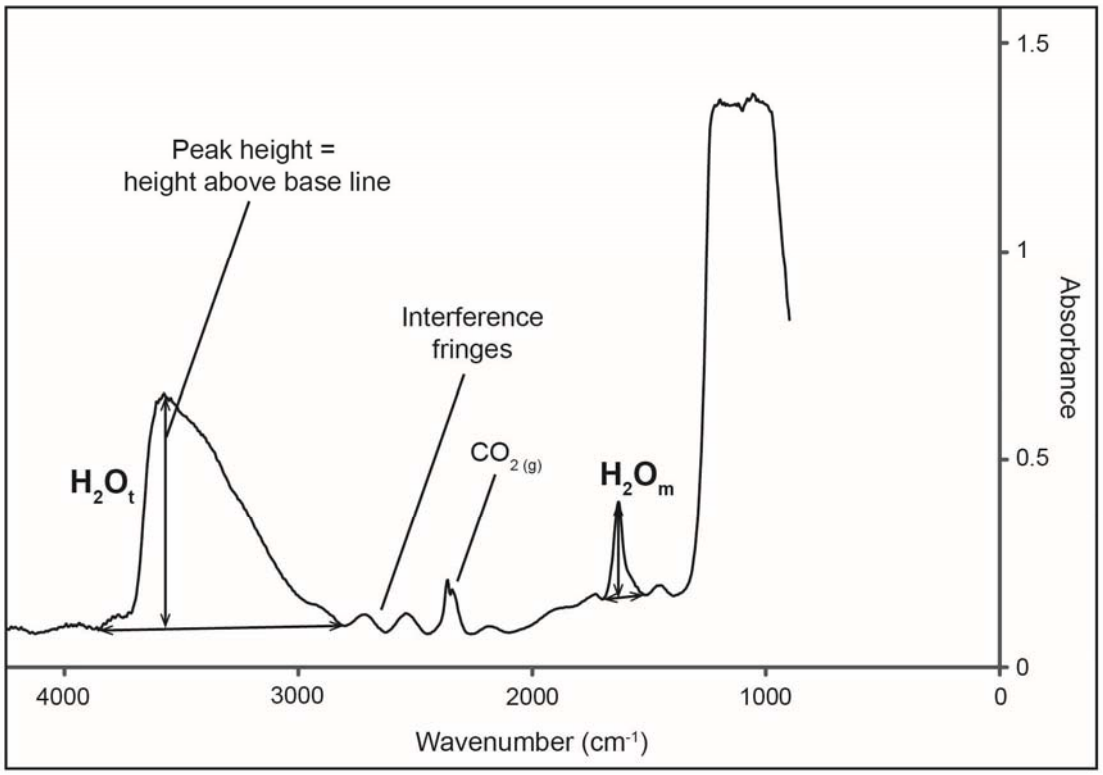

Fig. 3.15 Peak height fitting of absorbance bands

FTIR spectrum of a hydrous rhyolite. Peak heights (absorbance) of each band are obtained by subtracting the background, as fit by a linear baseline drawn between two points tangential to the peak. This process can be complicated by the presence of interference fringes in the background (see Section 3.3.2.5). Molecular CO_2 is present as a result of incomplete N_2 purge during sample analysis.

In order to extract quantitative concentration data from FTIR spectra it is necessary to calculate the absorbance of each particular band by conducting a background subtraction. The most common method is to measure the peak height above the background (Fig. 3.15) but it is also possible to use the area under the peak (the integrated absorbance). This latter method is generally considered less reliable because it is more affected by uncertainties in the background subtraction (Newman et al. 1986). For the ~3500 cm^{-1} band the background is essentially flat and a linear background tangent to either side of the absorbance peak can be used (Newman et al. 1986). For other peaks located on a sloping background or close to other absorbance bands, e.g. the ~1630 cm^{-1} peak, the method of background subtraction is more problematic. In some cases it

is possible to analyse a dehydrated sample of the same composition and to subtract this anhydrous spectrum from the spectrum of interest. This method still has uncertainties associated with it since it is particularly sensitive to glass composition (Newman et al. 1986) and in any case is not always possible given available samples. Instead the background is fit using either a linear background or a French curve, or flexible ruler. For modern FTIR analyses where software is used for data processing (as opposed to analysing printouts by hand) the use of a linear background is common (e.g. Fig. 3.15).

Having obtained the band absorbances, quantitative concentrations can be obtained through the use of the Beer-Lambert law (e.g. Stolper 1982; Newman et al. 1986):

$$\text{Concentration} = \frac{(18.02)(\text{Absorbance})}{\rho d \varepsilon} \times 100 \qquad \text{Equation 3.1}$$

Where concentration is in wt%, 18.02 is the molecular weight of H_2O, Absorbance is the height of the absorption peak above the background, ρ is density of sample in gl^{-1}, d is sample thickness in cm, and ε is the molar absorptivity in l mol^{-1} cm^{-1}.

Molar absorptivities are defined in terms of the amount of H_2O that would be released from the sample if all the H contributing to a given band were converted to molecular H_2O (Bartholomew et al. 1980, Stolper 1982, Newman et al. 1986). Thus H_2O_m and OH concentrations in wt% as determined by FTIR together give the concentration in H_2O_t. Molar absorptivity coefficients must be determined using an independent method of determining H_2O content of the sample, e.g. manometry. Molar absorptivity coefficients vary with anhydrous glass composition but the variation is sufficiently small that coefficients can be applied to all glasses that fall within the same TAS classification i.e. the same coefficient can generally be applied to all rhyolites but a different coefficient applies to basalts.

3.3.2.2 Sample preparation

Before beginning sample preparation it is necessary to estimate the expected H_2O_t content of the glass so that a target sample thickness can be selected that will not result in absorbances that saturate the detector or that are below the detection limits. This was done by calculating the expected equilibrium solubility of the sample from the melt composition and the final pressure and temperature conditions of the experiment prior to quench. From this the best choice of thickness and absorbance bands could be derived.

It was first attempted to get speciation data directly from the ~5200 and ~4500 cm^{-1} bands (Fig. 3.14) and samples were accordingly prepared to appropriate thicknesses of ~300 µm. Increasing noise in the signal for higher wavenumbers made peak height picking difficult for these bands, while the large sample thickness relative to vesicle diameters (with sample thickness typically an order of magnitude greater than vesicle diameter) resulted in unacceptable levels of error from volumetric averaging (Fig. 3.16). In order to minimise this error it was decided to use the ~3500 and ~1630 cm^{-1} bands in the IR region. The high H_2O_t contents of the samples combined with the high absorptivity coefficients of these bands required thin (~20 µm) samples which are difficult to prepare but which significantly reduce the error from volumetric averaging over the path length.

Samples were prepared as free standing wafers polished on both sides. Parallel polished surfaces are necessary to prevent scattering of the IR beam as it passes through the sample (Della Venture et al. 2010). Samples were mounted on a glass slide with Crystalbond 509 and ground with silica carbide grit before polishing with 3 µm and 1 µm diamond paste to produce a flat, polished surface. Samples were then flipped and remounted polished side down and ground and polished from the other side. Thickness was monitored during polishing using a digital micrometer on the glass surface. As target thickness was approached, micrometer measurements were conducted on the adjacent crystalbond to avoid damaging the delicate sample. Final thickness was determined using interference fringes on reflectance FTIR spectra. Samples were finally removed from the

slide by dissolving the crystalbond with acetone and a paintbrush (rather than tweezers) was used to remove the fragile wafers from the acetone bath.

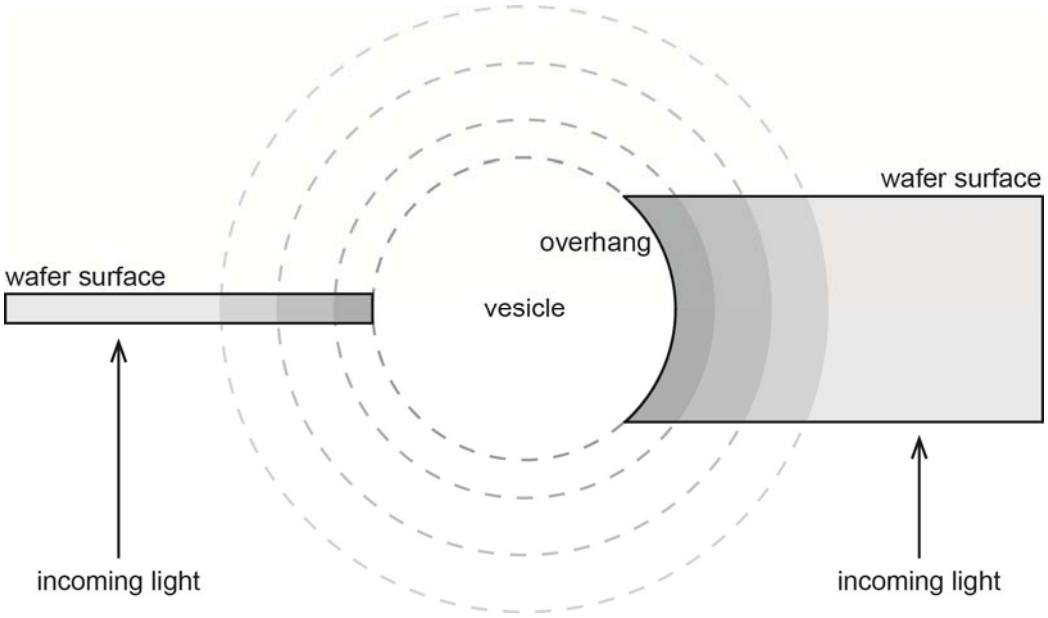

Fig. 3.16 Sample thickness and volumetric averaging

Schematic showing sample wafers of different thicknesses either side of a vesicle surrounded by concentric variations of H_2O (represented by different shades of grey). The thicker sample is affected by volumetric averaging of glass with different H_2O concentrations and may also be affected by the overhang created by the curved vesicle wall.

3.3.2.3 FTIR data acquisition

FTIR images were acquired by IMM at the Institute for Research on Earth Evolution (IFREE), Japan Agency for Marine-Earth Science and Technology (JAMSTEC), using the Varian FTS Stingray 7000 Micro Imager Analyzer spectrometer with an attached UMA 600 microscope. Mid-IR (6000 – 700 cm^{-1}) transmittance spectroscopic images were collected over 512 scans at a resolution of 8 cm^{-1} using a heated ceramic (globar) infra-red source, a Ge-coated KBr beamsplitter, and the Varian Inc. Lancer Focal Plane Array (FPA) camera housed in the microscope, which consists of a liquid-nitrogen cooled infrared photovoltaic $HgCdTe_2$ (MCT) array detector. The array detector is comprised of 4096 channels (arranged 64 x 64) across a 350 x 350 µm area giving a channel, or

spectral, resolution of 5.5 x 5.5 µm. The FPA camera was calibrated regularly. Samples were placed on a KBr window under N_2 purge and areas were selected for analysis using the microscope. The image was always focussed on the sample surface in order to avoid optical sectioning effects resulting from varying depths of focus (e.g. Della Ventura et al. 2010). Initially a background image of the KBr window was collected, which was subtracted from the sample image. New background images were taken approximately every 300 minutes. In addition to the transmittance images, reflectance images were also taken at the same locations in order to extract thickness measurements from interference fringes (see Section 3.3.2.4).

3.3.2.4 FTIR data processing

Images were processed using Varian Win-IR Pro software (v3.3.1.014). Individual spectra for use in transects were extracted from the images and H_2O concentrations were calculated by entering the height (absorbance) of the relevant peak above a linear background into the Beer–Lambert law (Stolper 1982b; Eq. 3.1). H_2O_t was calculated from the peak at ~3500 cm^{-1} and H_2O_m from the peak at ~1630 cm^{-1}, using respective molar absorptivity coefficients of 90 ± 4 l mol^{-1} cm^{-1} (Hauri et al. 2002) and 55 ± 2 l mol^{-1} cm^{-1} (Newman et al. 1986). OH values were calculated by subtracting calculated H_2O_m from H_2O_t. Sample density was calculated iteratively from major element compositions (R.A. Lange & Carmichael 1987) and H_2O_t content (Ochs III. & Rebecca A. Lange 1997). Sample thicknesses for spectra along the transects were determined using the frequency of interference fringes on reflectance spectra (e.g. Nichols & Wysoczanski 2007). Images were collected in reflected light of exactly the same area that had been analysed in transmitted light, and spectra at the same coordinates were extracted and processed. A refractive index of 1.5 (Long & Friedman 1968) was used for rhyolite. Errors on sample thickness determinations are ±3 µm (Nichols & Wysoczanski 2007). Since thickness measurements for transect spectra all fall within 3 µm of each other with no systematic variation along transect, the average sample thickness along the transect was used when processing each spectrum. FTIR

images are output in terms of absorbance. They were converted to concentration by applying the Beer-Lambert law, as above, using the mean sample thickness.

3.3.2.5 Errors on FTIR data

There are several sources of potential error for FTIR data. For calculations of concentration using the Beer-Lambert law (Eq. 3.1), the greatest analytical error comes from the error on thickness. Thickness measurements from reflectance spectra are estimated to have an error of ±3 µm, corresponding to an error of 15% for a sample with a thickness of 20 µm. This in turn corresponds to an error of ±13% on calculated H_2O_t concentration for a 20 µm thick sample with 4 wt% H_2O_t (i.e. 4 ±0.52 wt% H_2O_t). This error increases with decreasing sample thickness and decreases with increasing sample thickness, and so analytical errors on FTIR concentrations are given as ±15% relative. Importantly, however, changes in sample thickness (hence absolute species concentration) will not alter the ratio of H_2O_m:OH.

With regards to obtaining representative concentration profiles around vesicles, additional sources of error also need to be considered. Whereas SIMS and BSEM give concentrations for the exposed glass surface, FTIR concentrations are derived from volumetric averaging of concentration variations throughout the thickness of the sample wafer. If the sample wafer is thin relative to the diameter of the vesicle, then there is little variation in concentrations within the analysed volume (Fig. 3.16). If the sample wafer is thick relative to the vesicle, the concentric nature of H_2O variations around a sphere results in greater variation in H_2O content within the analysed volume of glass (Fig. 3.16). For the same vesicle, the concentrations measured at the vesicle wall will therefore be lower for a thick wafer relative to a thin wafer. Thin samples, such as those used in this study, are therefore less affected by volumetric averaging, but are more affected by errors in thickness measurement. Profiles derived from thin wafers will therefore have greater analytical uncertainty but will be more representative of the true shape and H_2O_m:OH ratio of the radial concentration profile.

The effect of volumetric averaging is also an important consideration in selecting spectra for processing when taking radial profiles from vesicle walls. There is no systematic change in thickness along transects, and all observed variations fall within the measurement error of ±3 µm. However if the analysed volume has some overlap with the vesicle (i.e. a void) then the amount of glass in the beampath will be less and H_2O_t and H_2O_m concentrations will appear to decrease at the vesicle wall.

In addition to this, there are likely to be issues of refraction and dispersion as the beam interacts with the vesicle boundary (Fig. 3.17). Where the beampath encounters the sample surface at 90° it passes through without a change in orientation. This is the basis for preparing samples with parallel polished surfaces. Where the beampath encounters a vesicle wall at a different angle it is refracted. Passing from a dense medium (glass) into a less dense medium (trapped vapour, or background atmosphere) causes the incident light to move away from the normal, and vice versa.

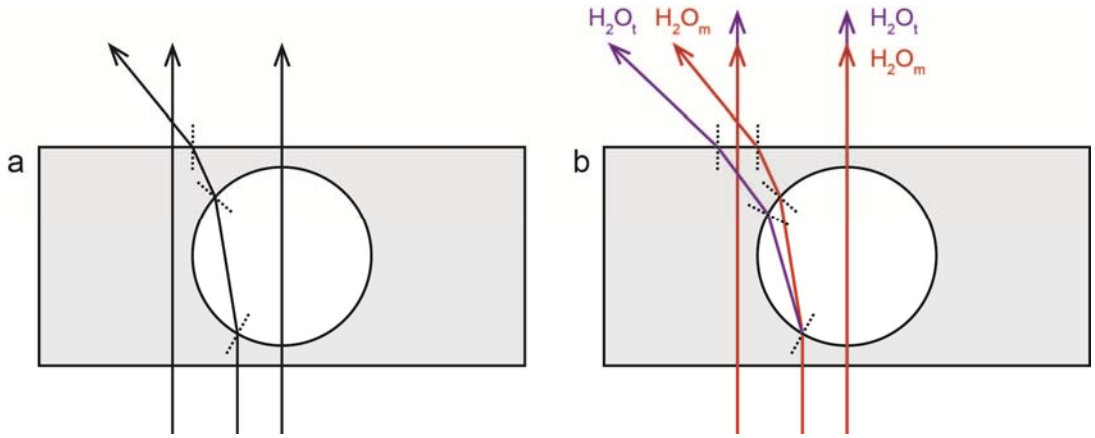

Fig. 3.17 Effects of refraction and dispersion at vesicle boundaries

a Incoming light that encounters changes in medium density can pass through the sample without deviation. Where the vesicle wall boundary is not parallel to the wafer surface the incident light is refracted away from the normal (dashed lines) when passing from glass to vapour and vice versa. Light encountering a vesicle at an angle will therefore always be refracted away from the vesicle and may contribute to spectra taken at other locations. **b** The magnitude of refraction varies with the wavelength of the incident light. Light wavelengths associated with absorption by H_2O_t (purple) may therefore be refracted to a greater extent than wavelengths associated with absorption by H_2O_m (red). Angles of refraction shown are for illustrative purposes only.

Light that encounters a vesicle will therefore always be refracted away from the vesicle wall, towards the rest of the sample wafer. Spectra collected at vesicle margins may therefore be affected by light that has passed through less glass and therefore has less absorption in its H-O bands. This would result in artificially low H_2O_t and H_2O_m concentrations. The effect of light dispersion may also cause this phenomenon to affect H_2O_t values to a greater degree than H_2O_m, since the apparent refractive index of a material varies with wavelength. The H_2O_t band of interest has a higher wavenumber, hence lower wavelength, and therefore experiences more refraction than the H_2O_m band. H_2O_t concentrations would therefore be expected to be affected by a greater amount than H_2O_m concentrations. It is noted that spectra that were discarded for overlapping with the vesicle tended to show a greater relative decrease in H_2O_t than H_2O_m, which is consistent with this error from refraction.

The proximity of each selected spectrum along a transect was checked both by visual inspection of where the spectrum location corresponds to on a transmitted light image of the sample, and by inspection of the shape of the spectrum itself. FTIR spectra collected too close to vesicle walls were characterised by a 'trough' in the baseline at low wavenumbers, just to the right of the H_2O_m peak (Fig. 3.18). This trough is found in spectra taken at or near a sample edge, and so is a feature of edges in general, rather than a feature related to vesicles or their associated H_2O concentration varaitions. Although the exact cause of this feature is not known it is a reliable indicator of when a vesicle wall has been reached, as verified by visual inspection of spectra locations. In addition, in spectra where a significant trough is present, the H_2O_m peak fitting can be affected by the rapid decrease in the baseline and result in artificially high H_2O_m concentrations. Spectra where this trough is present are therefore removed from the transect. As a result, concentration variations cannot be measured as close to the vesicle wall as in the SIMS-calibrated BSEM method.

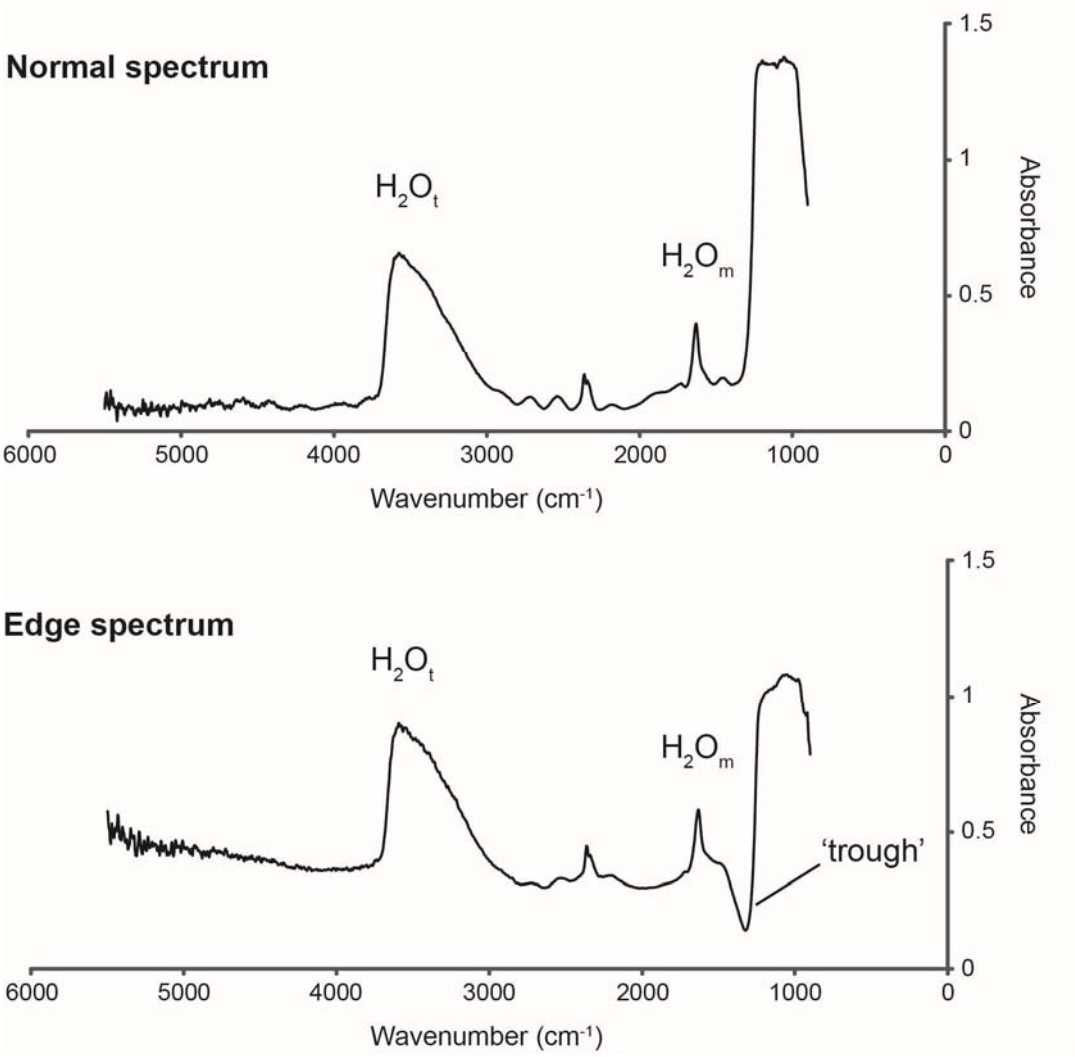

Fig. 3.18 Variations in FTIR spectra at vesicle walls

Comparison of spectra from a hydrous rhyolite. The top spectrum was taken in the far field and shows no decrease in the baseline to the right of the H_2O_m peak, whereas a spectrum from the vesicle boundary displays a deep trough. Such spectra were discarded from analysed profiles.

The final consideration in interpreting the FTIR data is the effect of interference fringes (e.g. Fig. 3.15, Fig. 3.19). These fringes are seen as a regularly undulating background in FTIR spectra and increase in amplitude and wavelength as sample thickness decreases. For thin samples they can therefore affect measured absorbances. If the spacing of the interference fringes varies from spectrum to spectrum, the superposition of the interference fringe and the absorption band of interest can artificially increase or decrease the measured absorbance (e.g. Fig. 3.19 c, d). The

effect is greatest for the H_2O_m band because this has a smaller absorbance than the H_2O_t band. The effect of these interference fringes is seen in H_2O_m images of samples (Fig. 3.19 a, b). In such images, concentration variations caused by other factors (e.g. variations around vesicles) can still be seen, superimposed against a rhythmically varying background, but cannot be processed quantitatively.

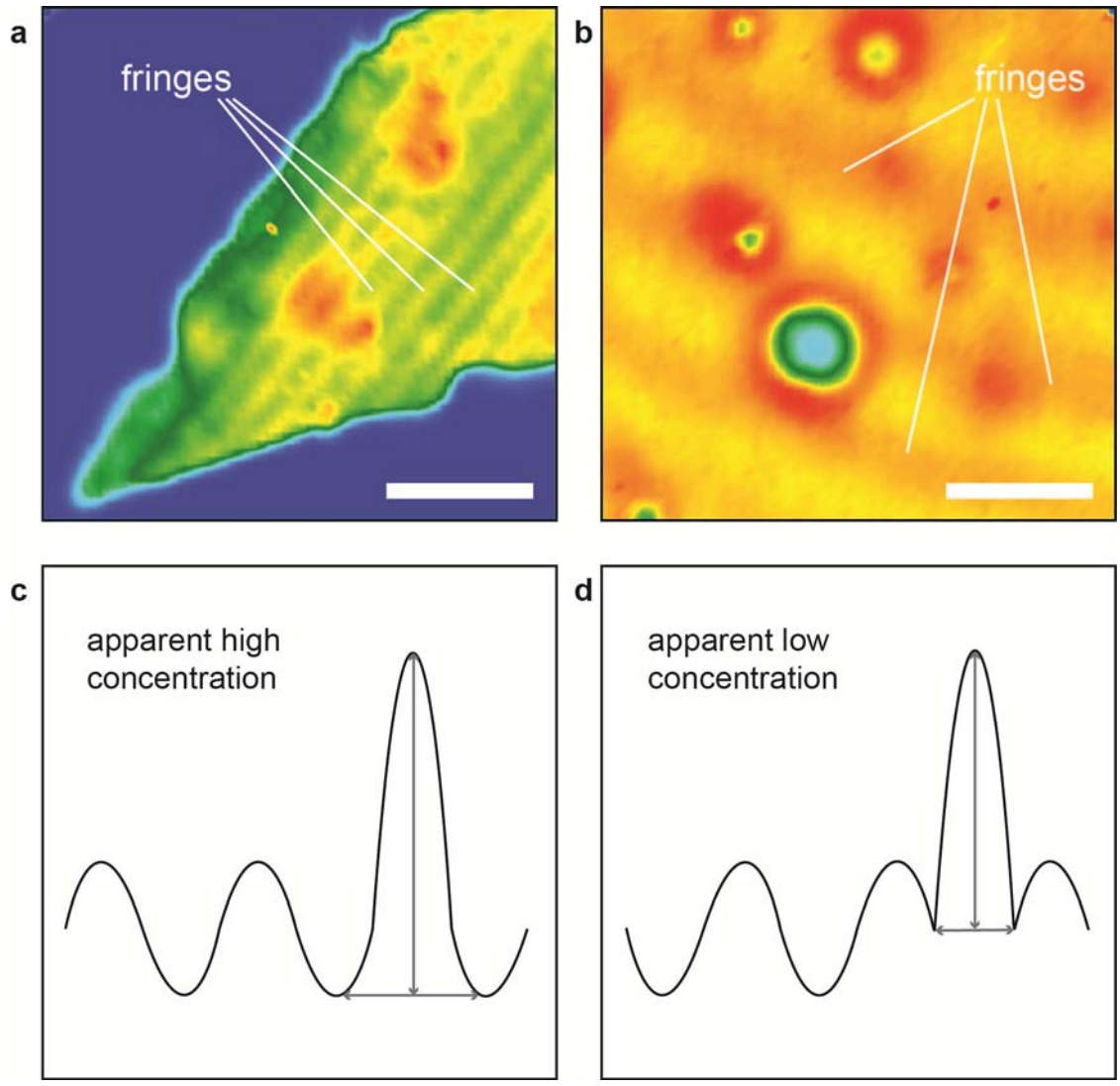

Fig. 3.19 Interference fringes in FTIR images

a, **b** Interference fringes (stripes) seen in H_2O_m images of thin samples. Colour indicates concentration - blue low concentration, red high concentration. White scalebar in each image represents 100 µm. **c**, **d** Interference fringes in images are caused when the superposition of the absorbance peak and interference fringes in spectra baseline varies systematically across the sample.

Chapter 4: H_2O concentration profiles around vesicles

4.1 Introduction

This chapter presents data from H_2O_t analyses of vesicular volcanic glasses, created under known pressure and temperature conditions. Radial H_2O_t concentration profiles around vesicles are compared with the concentration profiles that would be expected for the production conditions in order to investigate the processes that control magma degassing and the preservation of bubble populations when melt is quenched to glass.

4.2 Samples and Methods

The samples analysed in this chapter are experimentally vesiculated volcanic glasses (Table 4.1, see Chapter 3 Section 3.2 for full details of sample composition and production). In summary, these samples comprise five experimentally vesiculated rhyolites created under a range of decompression conditions (ABG series), one decompression experiment of phonolite composition (IS14) and one solubility experiment of rhyolite composition (MCN13). Bubble populations were expected to be either in equilibrium with the melt or in a state of growth prior to quench.

Sample		T_{exp} (°C)	P_{syn} (MPa)	P_i (MPa)	Duration P_i (hr)	P_f (MPa)	dP/dt (MPa/s)
Rhyolite *Quench: 3-10 s*	ABG1	825	150	100	0.17	100	N/A
	ABG2	825	150	100	0.17	60	0.1
	ABG6	825	150	100	0.17	80	0.1
	ABG14	825	150	100	0.25	80	0.5
	ABG15	825	150	100	0.25	60	0.5
Phonolite *Quench: 3-10 s*	IS14	1050	200	200	N/A	100	0.024
Rhyolite *Quench: 30-60 s*	MCN13	825	80	80	72	80	N/A

Table 4.1: Summary of experimental conditions. For further details, see Chapter 3 Section 3.2.

Radial H_2O_t concentration profiles around vesicles in these samples were analysed using the SIMS-calibrated BSEM imaging methodology of Humphreys et al. (2008). This method is used to obtain quantitative H_2O_t concentration data with high spatial resolution. For full details of analytical methodology, see Chapter 3 Section 3.3.1.

Using this methodology, radial profiles of glass H_2O_t concentration were analysed around vesicles. Several profiles were measured for each analysed vesicle, and multiple vesicles were analysed for each sample. The data were then compiled to create an average H_2O_t concentration profile for each sample. Table 4.2 shows the total number of calibrated BSEM images, vesicles and individual profiles analysed for each sample. Each sample uses calibrations from two or more different SIMS tracks for calibration of BSEM images.

Sample	Number of BSEM images	Number of vesicles	Number of profiles
ABG1	5	15	64
ABG2	4	20	83
ABG6	3	13	59
ABG14	3	12	48
ABG15	3	14	58
IS14	7	8	68
MCN13	3	15	66

Table 4.2: Summary of analysed data

Number of BSEM images, vesicles and individual profiles analysed using SIMS-calibrated BSEM and used to produce the average H_2O_t concentration profile for each sample.

4.3 Results

4.3.1 BSEM imaging

In BSEM images, variations in greyscale intensity correspond to variations in H_2O_t concentrations in the glass, with H_2O_t-rich glass appearing dark and H_2O_t-poor glass appearing light. H_2O_t distributions can therefore be examined qualitatively in BSEM images (see Fig. 4.1, 4.2). In all samples, all vesicles are surrounded by halos of dark, H_2O_t-rich glass. The width of these H_2O_t-rich halos varies for different vesicles within the same sample. Glass in the far-field (i.e. at a distance from vesicle walls) appears lighter and thus is relatively H_2O_t-poor. In some areas of the far field dark circles of H_2O_t-rich glass can be seen, although no vesicle is visible (e.g. Fig. 4.1 a, c; 4.2 b). In such cases optical microscopy can often discern the presence of a vesicle just below the exposed glass surface. Where no vesicle can be seen below the surface of an H_2O_t-rich circle of glass, it is assumed that this is an H_2O_t-rich imprint of a vesicle which was previously above the observed surface that has now been removed during sample preparation. These observations confirm the existence of an H_2O_t-rich shell surrounding each vesicle in three dimensions. When vesicles are exposed, this shell appears as an H_2O_t-rich halo around the sectioned vesicle.

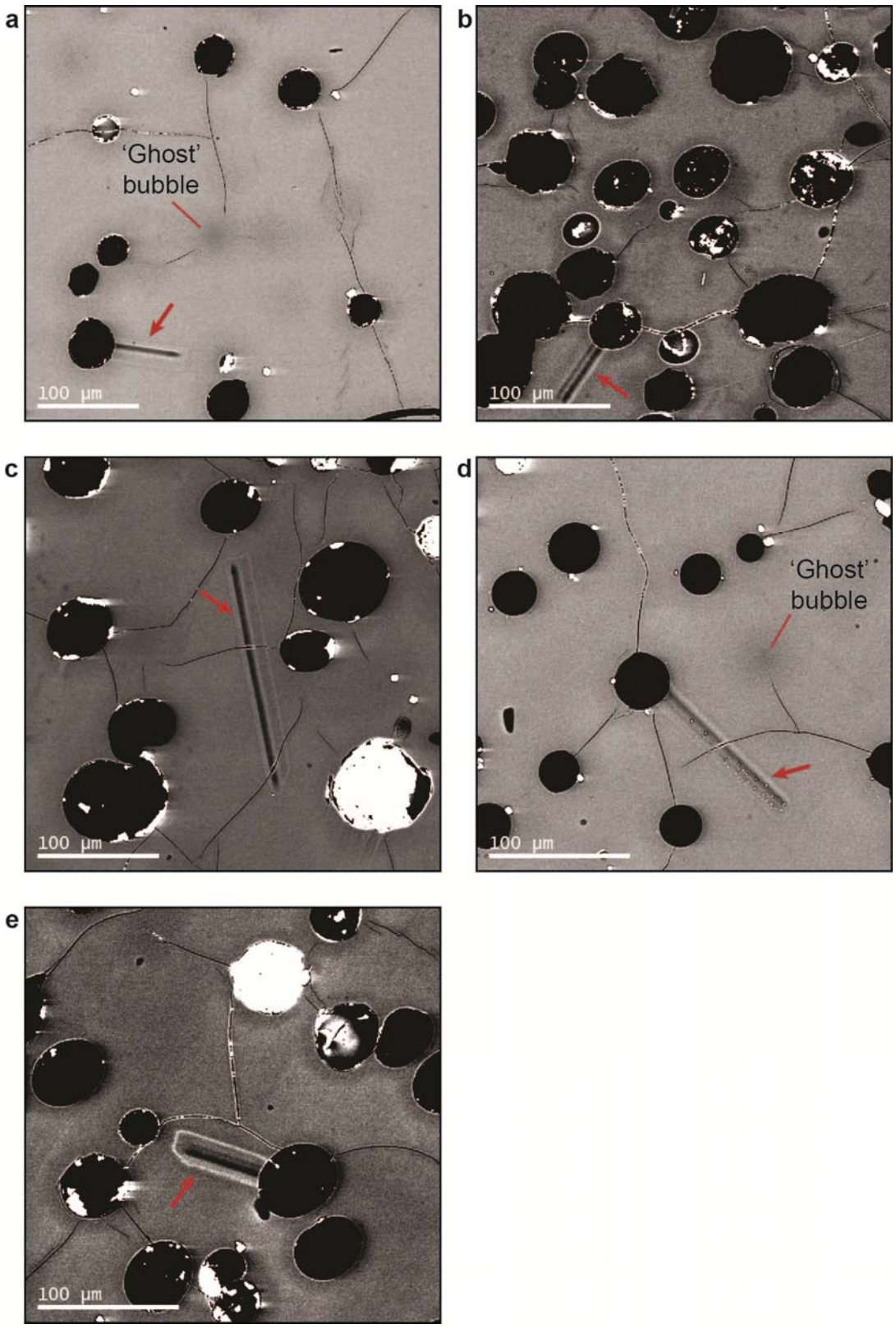

Fig. 4.1 BSEM imaging of ABG samples

BSEM images show typical distribution of H_2O_t-rich (dark) and H_2O_t-poor (light) glass, in **a** ABG1, **b** ABG2, **c** ABG6, **d** ABG14 and **e** ABG15. H_2O_t-rich halos are seen around vesicles. H_2O_t-rich imprints of 'ghost bubbles' corresponding to bubbles above or below sample surface are highlighted (**a**, **d**). Red arrows indicate SIMS tracks.

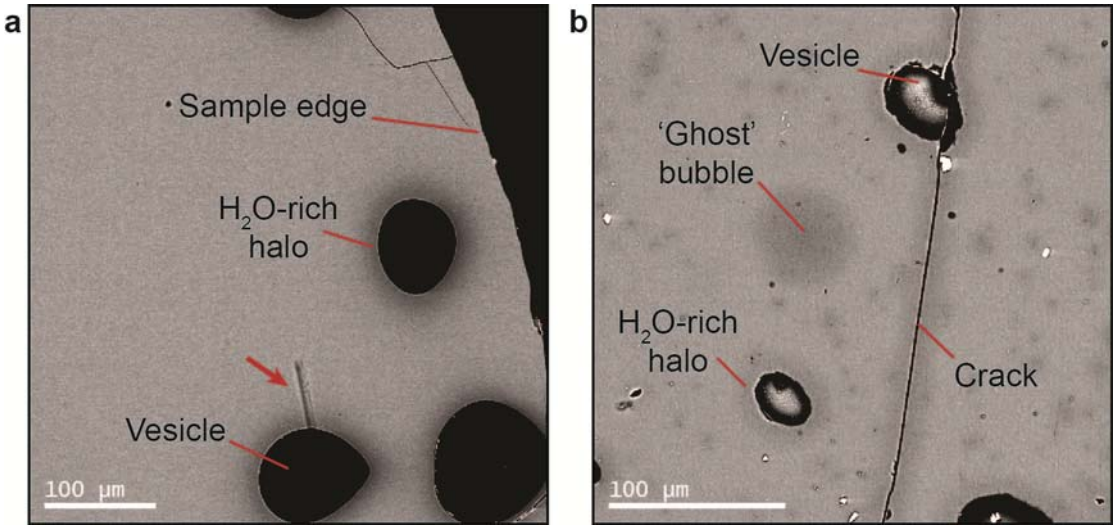

Fig. 4.2 BSEM imaging of IS14 and MCN13

BSEM images show typical distribution of H_2O_t-rich (dark) and H_2O_t-poor (light) glass, in **a** IS14 and **b** MCN13. H_2O_t-rich halos are seen around vesicles. H_2O_t-rich imprint of 'ghost bubble' and hydration along crack margins shown in **b**. Red arrow indicates SIMS track.

4.3.2 H_2O_t concentration profiles

Fig. 4.3 shows the average H_2O_t concentration profiles from all analysed vesicles within each sample. Figures showing the full H_2O_t dataset from which these concentration profiles are derived are shown in Appendix A2. The use of a mean H_2O_t concentration profile for each sample accounts for the effect of different SIMS calibrations on extracted H_2O_t concentrations (see Chapter 3 Section 3.3.1.8) and enables values at the vesicle wall and in the far field to be compared between samples. In the following discussion of these concentration profiles, 'at the vesicle wall' refers to the left hand end of the H_2O_t concentration profile. This represents the closest measured H_2O_t concentration to the vesicle wall. It should be noted that the H_2O_t concentration directly at the vesicle wall could not be measured due to analytical limitations such as 'edge effects' (see Chapter 3 Section 3.3.1.6); hence the concentration profiles typically begin at ~2µm from the vesicle wall. The term 'far field' is used to describe the right hand side of the concentration profile, which is at the greatest distance from the vesicle wall. It is emphasised however that these concentration profiles are the average of concentration profiles recorded around several

different vesicles. Thus for any given vesicle in the sample the concentration profiles of neighbouring vesicles may interfere at a shorter (or, indeed, greater) distance from the vesicle wall than the distance shown in the presented average concentration profile for each sample.

Each profile has highest H_2O_t concentration at the vesicle wall, with H_2O_t concentration decreasing with increasing distance from the vesicle wall. In some cases (ABG2, ABG15), H_2O_t concentration increases slightly once again in the far field. Near the vesicle wall, two distinct concentration profile shapes are observed. Some samples (e.g. IS14) have a steadily decreasing profile gradient with distance from the vesicle wall, i.e. their concentration profiles are steepest at the vesicle wall. Others (e.g. ABG2) have S-shaped profiles, with the profile gradient initially increasing with distance from the vesicle wall before once again decreasing with distance into the far field. This is interpreted to be an artefact caused by averaging concentration profiles from vesicles sectioned at different latitudes (Chapter 3 Section 3.3.1.7).

The H_2O_t concentration recorded at the vesicle wall varies among samples, from 3.82 wt% for ABG2 to 6.50 wt% for IS14, as does the H_2O_t concentration recorded in the far field, from 3.28 wt% for ABG2 to 4.92 wt% for ABG14 (Table 4.3). Similarly the total magnitude of H_2O_t decrease from the vesicle wall to the far field varies between samples, from 0.33 wt% for ABG15 to 2.03 wt% for IS14 (Table 4.3).

The half-fall distance, used to characterise the diffusion lengthscale of the observed concentration profiles (see Chapter 2 Section 2.7.1), is given for each sample in Table 4.3. This distance is calculated for the vesicle cross-sectioned closest to its equator, since this vesicle will have a concentration profile that is least affected by sectioning effects (see Chapter 3 Section 3.3.1.7, and this Chapter Section 4.4.3.3). The vesicle and corresponding H_2O_t concentration profile from which the half-fall distance is derived is shown for each sample in Fig.s 4.4 to 4.10.

Sample	$H_2O_{t,wall}$ (wt%)†	$H_2O_{t,far}$ (wt%)†	Half-fall distance (μm)†
ABG1	5.37 (0.097)	4.27 (0.056)	12 (9-13)
ABG2	3.82 (0.041)	3.28 (0.023)	7 (5-8)
ABG6	4.86 (0.031)	4.29 (0.040)	5 (5-7)
ABG14	5.46 (0.044)	4.92 (0.055)	4 (3-4)
ABG15	4.04 (0.037)	3.71 (0.031)	8 (7-9)
IS14	6.5 (0.079)	4.47 (0.047)	12 (11-13)
MCN13	4.64 (0.059)	3.47 (0.050)	10 (10-11)

Table 4.3: Observed H_2O_t concentrations and half-fall distance

Average sample H_2O_t concentrations measured at the vesicle wall ($H_2O_{t,wall}$) and in the far field ($H_2O_{t,far}$). The half-fall distance is the distance from the vesicle wall at which H_2O_t concentration falls to halfway between the maximum ($H_2O_{t,wall}$) and minimum ($H_2O_{t,far}$) values in the profile from the vesicle determined to be cross-sectioned closest to the equator. †Measurement errors given in brackets. SIMS-calibrated BSEM errors given as twice standard error of the mean sample profile, errors on half-fall distance represent range of values obtained when error in H_2O_t value (two times the standard error of the mean) is propagated.

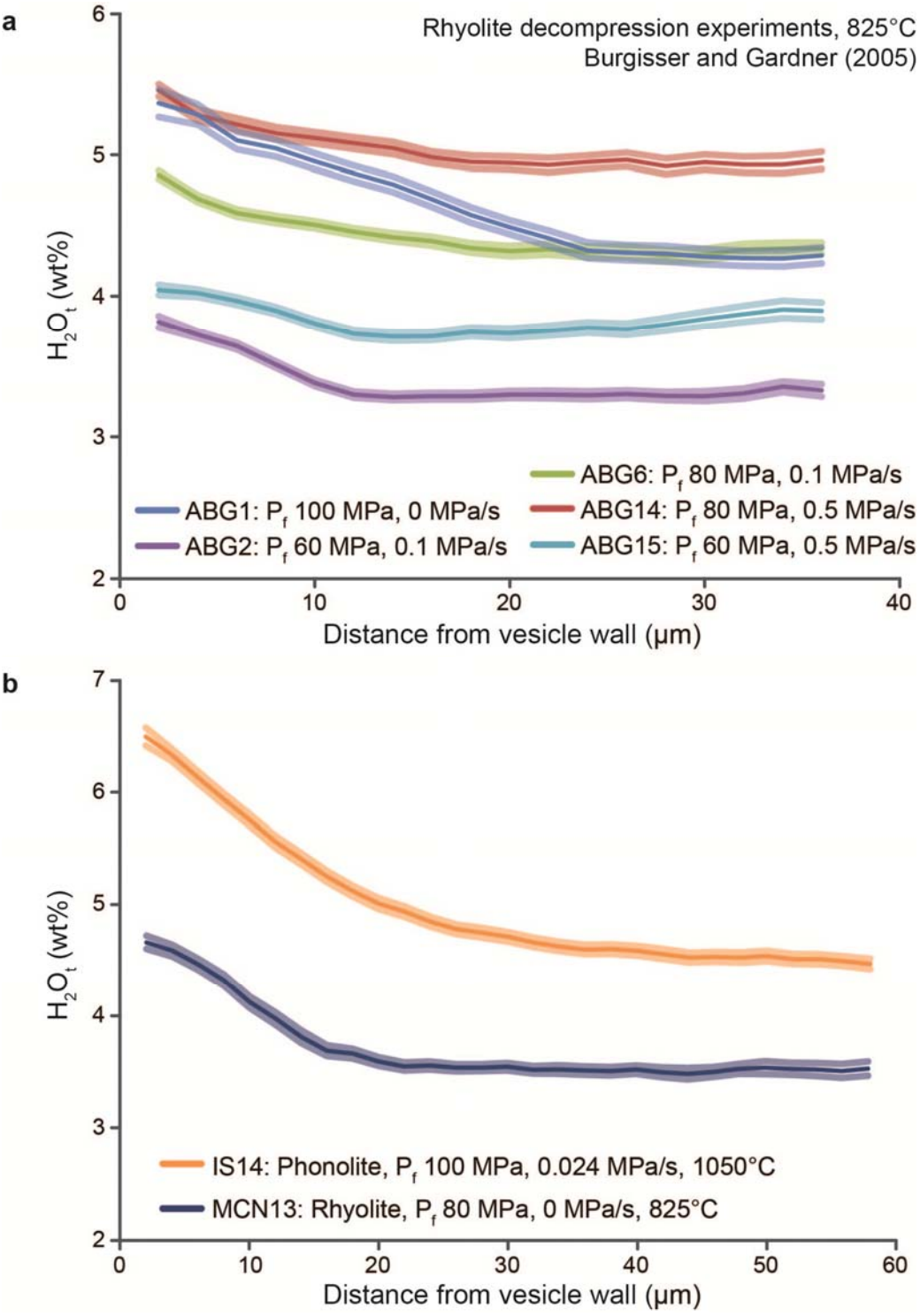

Fig. 4.3 Sample average H_2O_t concentration profiles

H_2O_t profiles extracted using SIMS-calibrated BSEM imaging, showing variation in H_2O_t concentration with distance from the vesicle wall. Each curve represents the average of all extracted concentration profiles for vesicles in that sample. **a** Rhyolite decompression experiments from the ABG series. **b** Phonolite decompression experiment (IS14) and rhyolite solubility experiment (MCN13). Semi-opaque boundaries indicate twice the standard error of the mean.

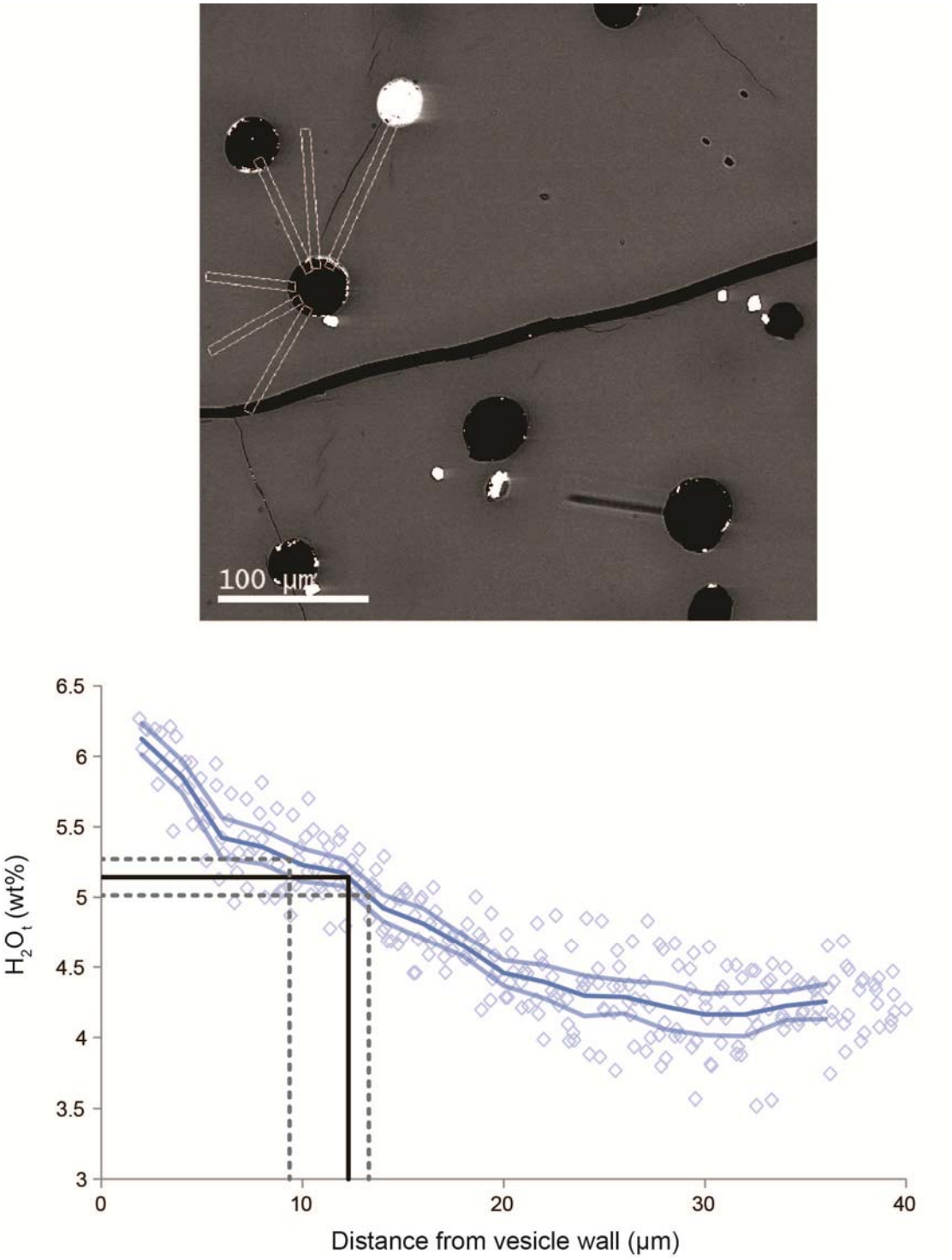

Fig. 4.4 Half-fall distance for sample ABG1

Top: BSEM image showing extracted greyscale profiles from vesicle with steepest H_2O concentration gradient in sample, used to calculate half-fall distance for sample. Bottom: Black lines correspond to half-fall H_2O_t concentration and half-fall distance, dashed grey lines show error resulting from applying twice the standard error of the mean to H_2O_t concentration values used in the half-fall H_2O_t concentration calculation.

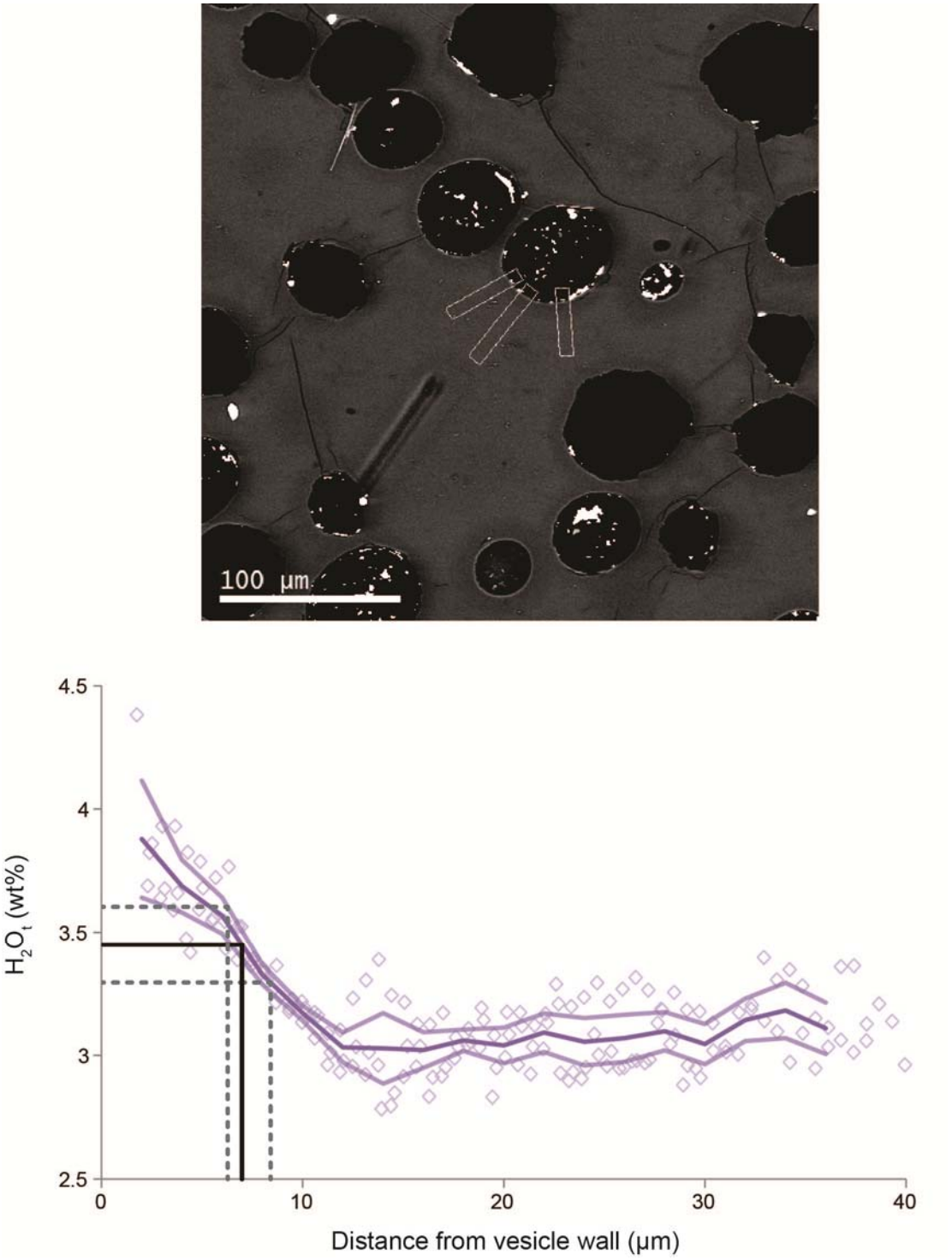

Fig. 4.5 Half-fall distance for sample ABG2

Top: BSEM image showing extracted greyscale profiles from vesicle with steepest H_2O concentration gradient in sample, used to calculate half-fall distance for sample. Bottom: Black lines correspond to half-fall H_2O_t concentration and half-fall distance, dashed grey lines show error resulting from applying twice the standard error of the mean to H_2O_t concentration values used in the half-fall H_2O_t concentration calculation.

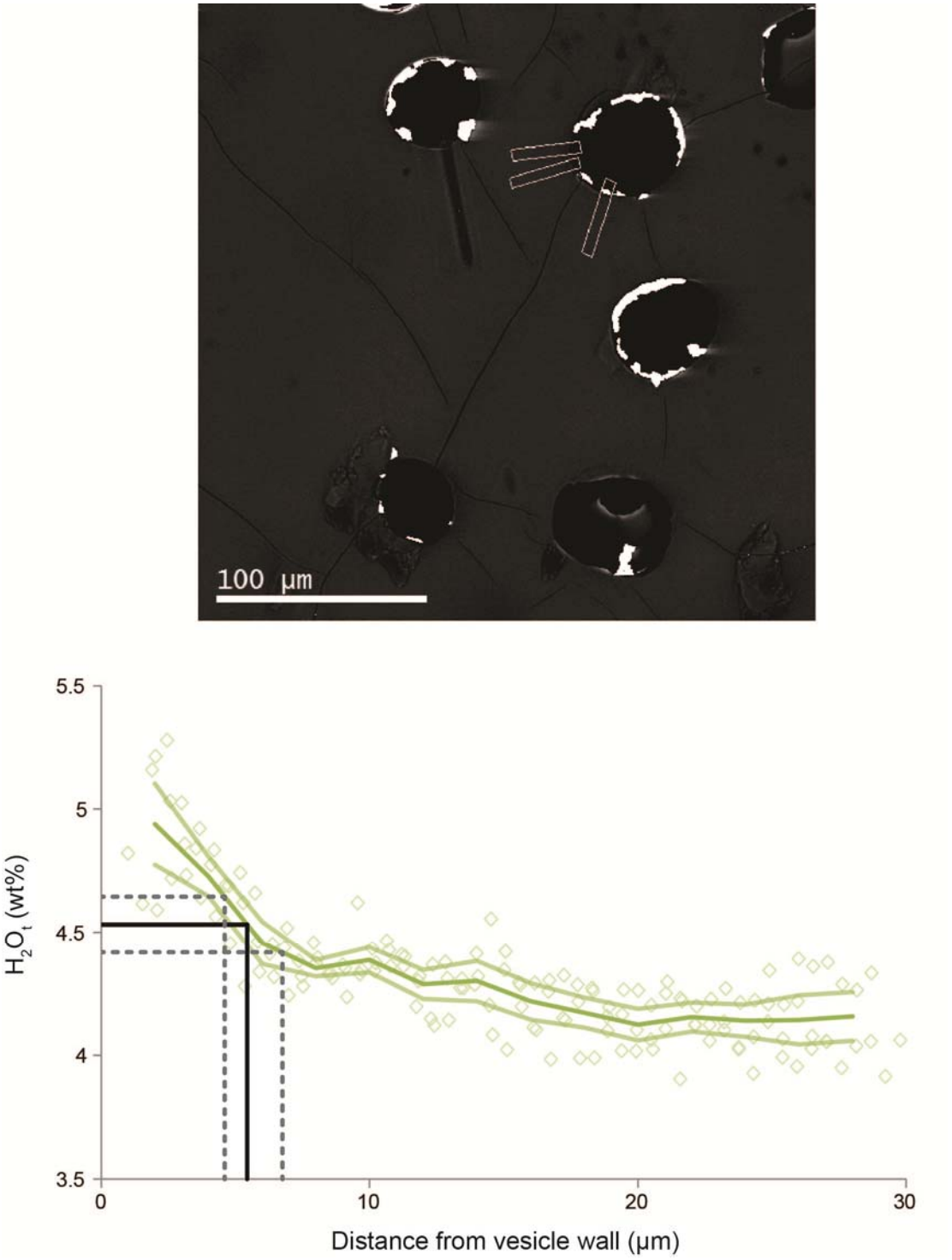

Fig. 4.6 Half-fall distance for sample ABG6

Top: BSEM image showing extracted greyscale profiles from vesicle with steepest H_2O concentration gradient in sample, used to calculate half-fall distance for sample. Bottom: Black lines correspond to half-fall H_2O_t concentration and half-fall distance, dashed grey lines show error resulting from applying twice the standard error of the mean to H_2O_t concentration values used in the half-fall H_2O_t concentration calculation.

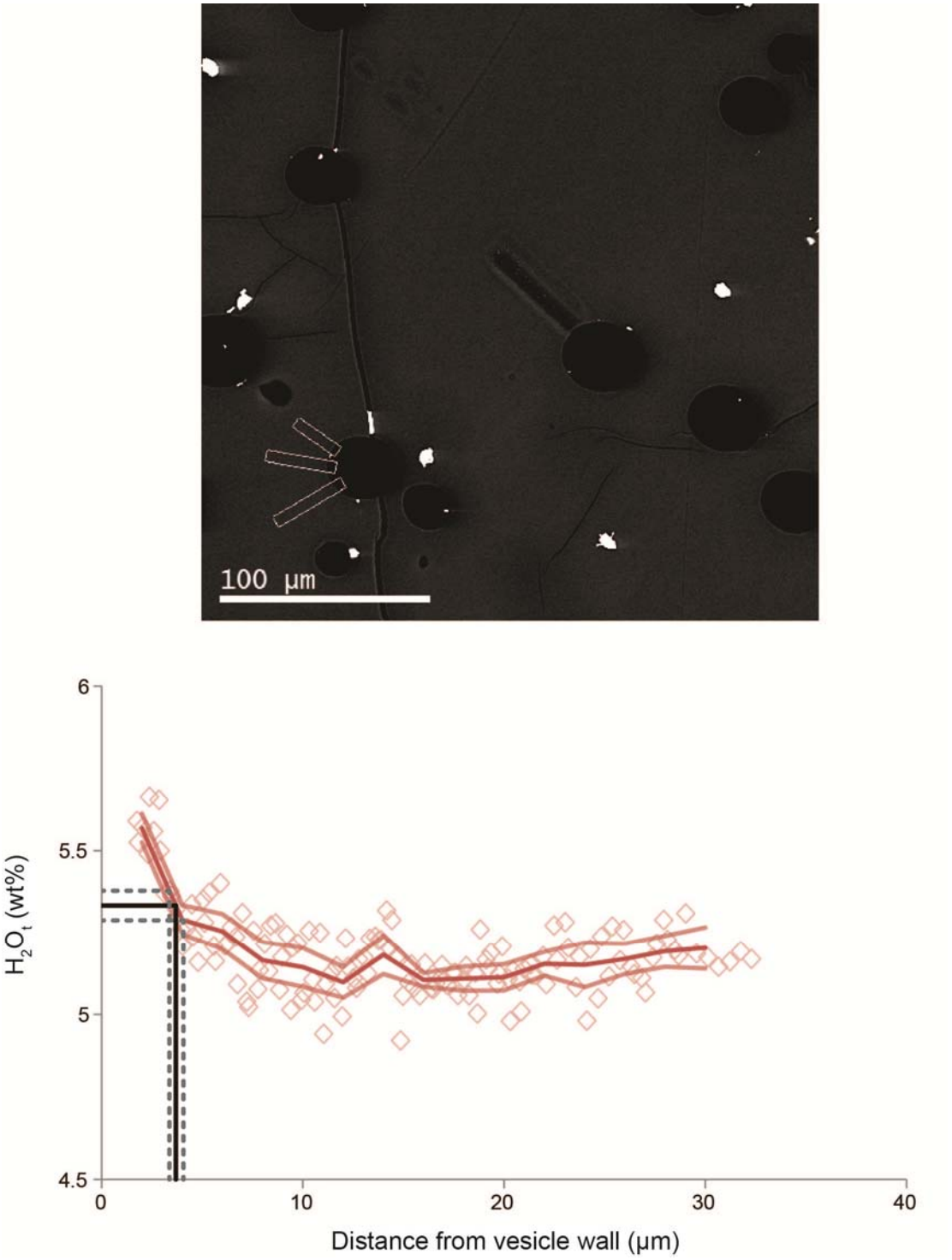

Fig. 4.7 Half-fall distance for sample ABG14

Top: BSEM image showing extracted greyscale profiles from vesicle with steepest H_2O concentration gradient in sample, used to calculate half-fall distance for sample. Bottom: Black lines correspond to half-fall H_2O_t concentration and half-fall distance, dashed grey lines show error resulting from applying twice the standard error of the mean to H_2O_t concentration values used in the half-fall H_2O_t concentration calculation.

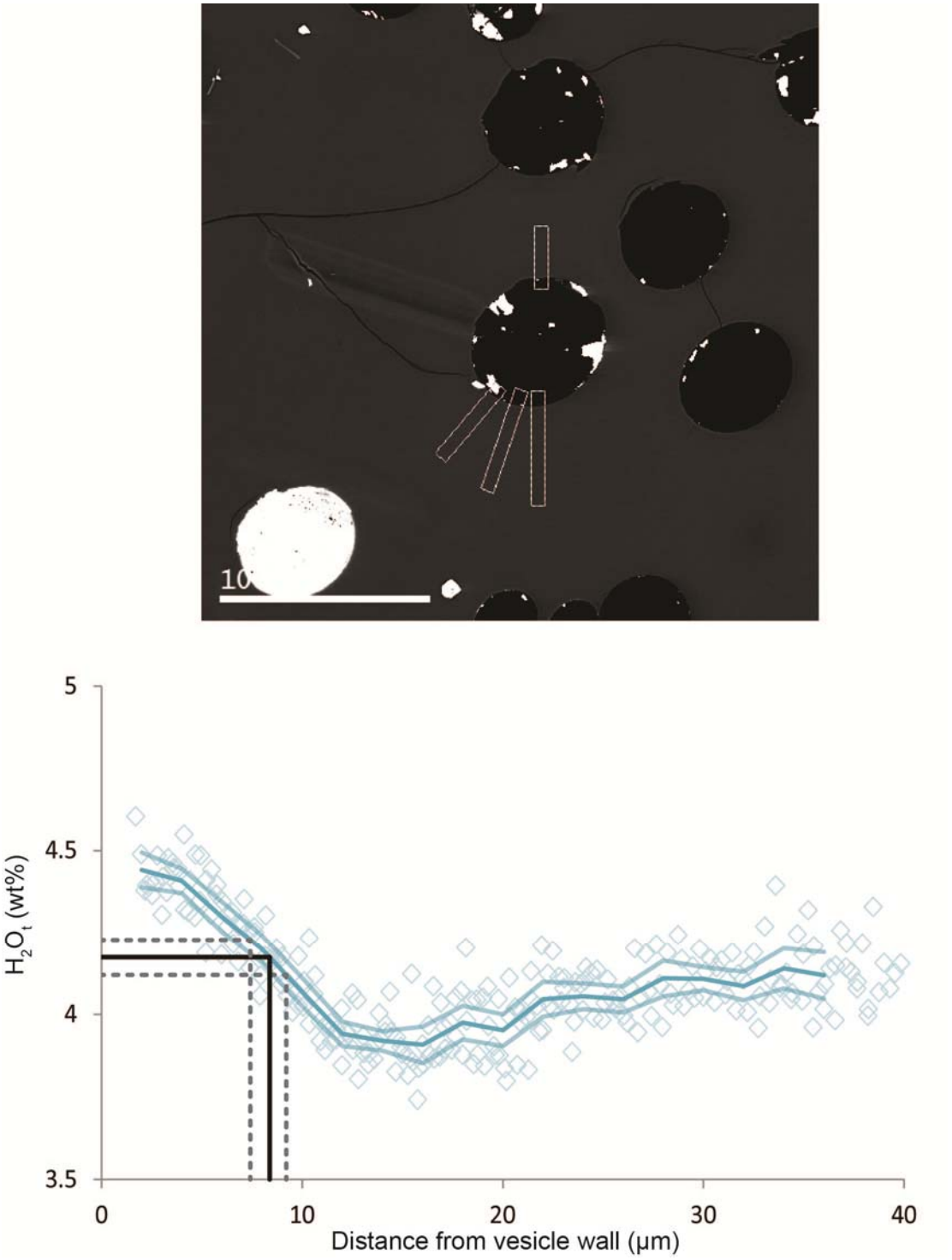

Fig. 4.8 Half-fall distance for sample ABG15

Top: BSEM image showing extracted greyscale profiles from vesicle with steepest H_2O concentration gradient in sample, used to calculate half-fall distance for sample. Bottom: Black lines correspond to half-fall H_2O_t concentration and half-fall distance, dashed grey lines show error resulting from applying twice the standard error of the mean to H_2O_t concentration values used in the half-fall H_2O_t concentration calculation.

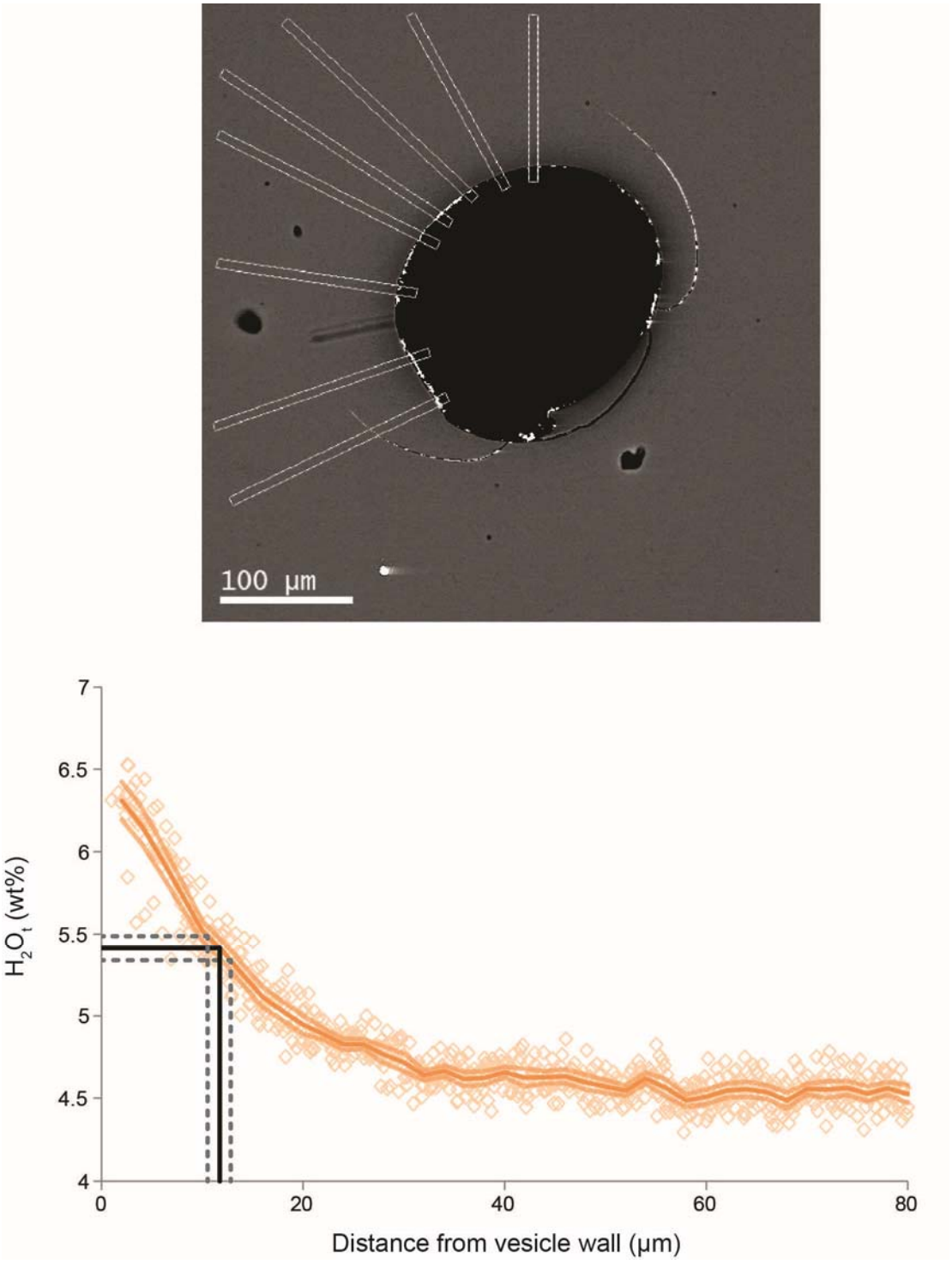

Fig. 4.9 Half-fall distance for sample IS14

Top: BSEM image showing extracted greyscale profiles from vesicle with steepest H_2O concentration gradient in sample, used to calculate half-fall distance for sample. Bottom: Black lines correspond to half-fall H_2O_t concentration and half-fall distance, dashed grey lines show error resulting from applying twice the standard error of the mean to H_2O_t concentration values used in the half-fall H_2O_t concentration calculation.

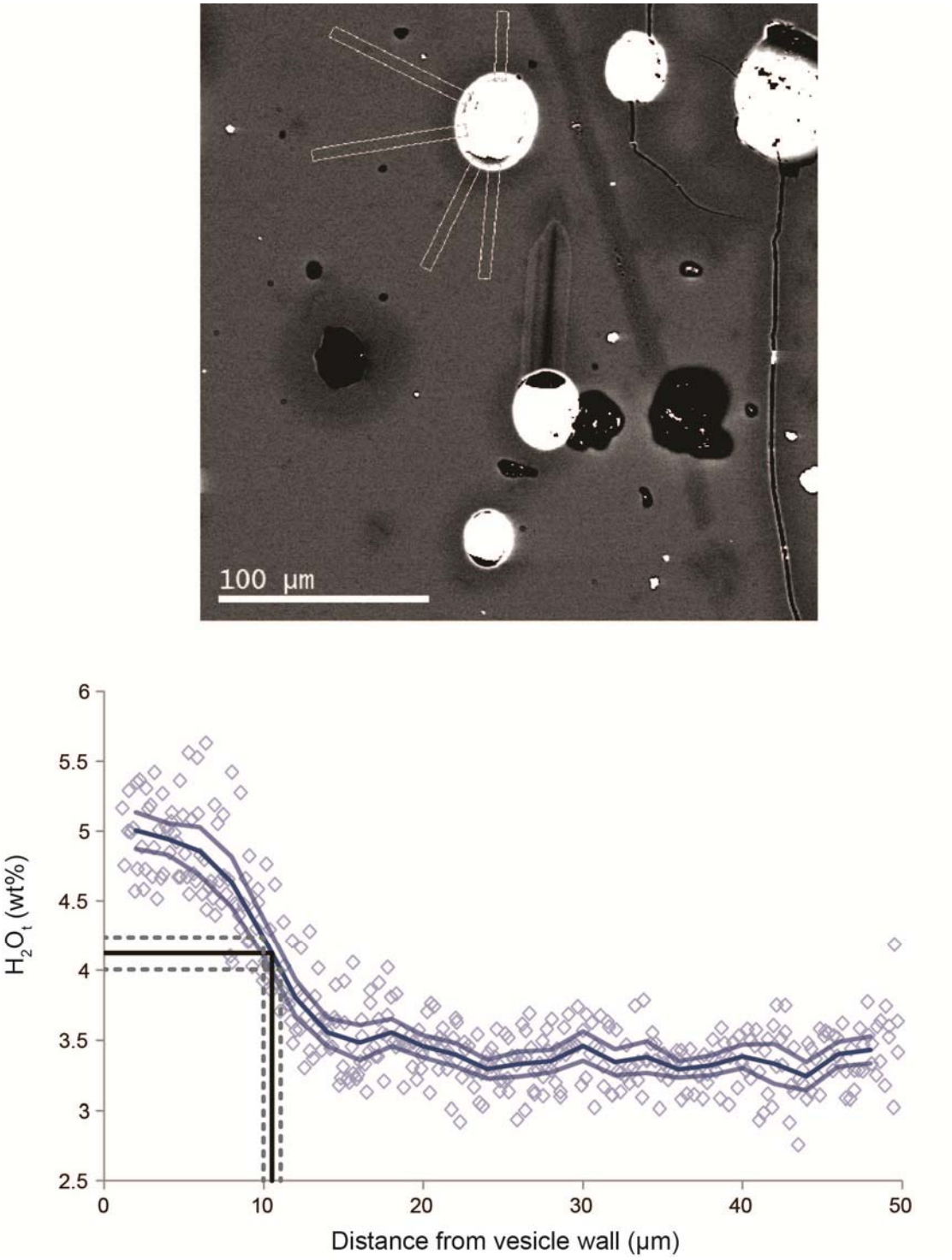

Fig. 4.10 Half-fall distance for sample MCN13

Top: BSEM image showing extracted greyscale profiles from vesicle with steepest H_2O concentration gradient in sample, used to calculate half-fall distance for sample. Bottom: Black lines correspond to half-fall H_2O_t concentration and half-fall distance, dashed grey lines show error resulting from applying twice the standard error of the mean to H_2O_t concentration values used in the half-fall H_2O_t concentration calculation.

4.4 Discussion

4.4.1 Shape of H_2O_t profiles

The shape of the H_2O_t concentration profile indicates the direction of H_2O diffusion, since H_2O diffuses down a concentration gradient. The observation that the H_2O_t concentration profiles all have H_2O_t concentrations that are highest at the vesicle wall and decrease with distance into the far field demonstrates that H_2O was diffusing from the bubble/vesicle out into the melt/glass (timing with respect to the glass transition will be discussed Section 4.4.3 and Chapter 5). These observations are markedly different from the H_2O_t concentration profiles that were expected given the experimental pressure and temperature conditions (Table 4.1). ABG1 and MCN13 were held at constant pressure and temperature and were therefore expected to have bubble populations that were in equilibrium with the melt, with flat profiles of uniform H_2O_t concentration with distance from the bubble wall (see Chapter 2, Fig. 2.13 a). The other samples experienced isothermal decompression and were expected to produce bubble populations in a state of growth (since H_2O solubility in the melt decreases with decreasing pressure), with H_2O_t concentration lower at the bubble wall than in the far field and H_2O thus diffusing from the far field towards and into the bubble (Chapter 2 Fig. 2.13 b).

The general shape of the observed concentration profiles is the same for all samples regardless of the experimental conditions (run temperature, run pressure, decompression conditions, etc.), the melt composition, and the experimental apparatus used in sample production. This suggests that the mechanism that causes the observed profiles is common to all the experimental samples.

4.4.2 Mechanism

In the case of a bubble of pure H_2O fluid co-existing with a silicate melt, the H_2O_t concentration at the bubble wall is always the equilibrium H_2O solubility in the melt for the given melt composition and pressure and temperature conditions (Chapter 2 Section 2.6.1). To create a concentration

profile like those observed, H_2O solubility in the melt must have increased so that the silicate melt became undersaturated with respect to H_2O. Melt at the bubble wall will always stay saturated with H_2O because of its proximity to the excess H_2O contained in the bubble. When H_2O solubility increases, melt at the bubble wall would therefore contain more H_2O than the undersaturated far field melt. In response to this concentration gradient H_2O diffuses from the area of high concentration (the bubble wall) into the area of low concentration (the far field melt). Given sufficient time this diffusion will ultimately result in a flat H_2O_t concentration profile at a concentration value either below the new equilibrium solubility value (and complete resorption of the bubble) or at the new equilibrium solubility value (and partial resorption of the bubble). The fact that the observed concentration profiles retain a gradient demonstrates that the resorption process is not complete.

Sample	H_2O_{eq} at T_{exp}, P_f (wt%)	$H_2O_{t,wall}$ (wt%)[†]	P_{nec} (MPa)	T_{nec} (°C)	H_2O_{eq} at 600°C, P_f (wt%)
ABG1	3.96; *3.44*	5.37 (0.097)	~170; ~*240*	<600	4.64
ABG2	2.95; *2.66*	3.82 (0.041)	~90; ~*120*	<600	3.71
ABG6	3.48; *3.08*	4.86 (0.031)	~140; ~*200*	<600	4.22
ABG14	3.48; *3.08*	5.46 (0.044)	~170; ~*250*	<600	4.22
ABG15	2.95; *2.66*	4.04 (0.037)	~100; ~*140*	<600	3.71
IS14	3.61	6.50 (0.079)	>250	<950	-
MCN13	3.48	4.64 (0.059)	~130	<600	4.22

Table 4.4 Comparison of expected and observed H_2O solubility

Comparison of observed H_2O_t concentration at the vesicle wall ($H_2O_{t,wall}$) with the equilibrium H_2O solubility value (H_2O_{eq}) expected for the final temperature (T_{exp}) and pressure (P_f) conditions of the experiments. P_{nec} is pressure necessary to explain observed $H_2O_{t,wall}$ at T_{exp}, T_{nec} is temperature necessary to explain observed $H_2O_{t,wall}$ at P_f. H_2O_{eq}, P_{nec} and T_{nec} are calculated using the VolatileCalc solubility model of Newman & Lowenstern (2002) for rhyolite composition (lower T limit of model: 600 °C), with the model used by Burgisser & Gardner (2005) also shown in italics, and using the experimental data of Iacono Marziano et al. (2007) (valid 30-250 MPa, 950 - 1050 °C) for the phonolite sample IS14. [†]Measurement errors given in brackets are twice standard error of the mean sample profile

The H_2O concentration at which the melt is saturated (i.e. H_2O solubility) varies with pressure, temperature, and melt composition (see Chapter 2 Section 2.6). Table 4.4 shows the expected equilibrium H_2O solubility (H_2O_{eq}) of each sample based on its final pressure (P_f) and temperature (T_{exp}) immediately prior to quench, alongside the average H_2O_t values recorded at the vesicle wall for each sample. For rhyolite samples H_2O_{eq} is calculated using the VolatileCalc solubility model of Newman & Lowenstern (2002) with the empirical relationship used by Burgisser & Gardner (2005) also shown for the ABG samples; for IS14 the solubility data of Iacono Marziano et al (2005) are used. Errors on solubility models are expected to be ~10% relative (e.g. Baker & Alletti, 2012).

For all samples the observed H_2O_t values at vesicle walls are significantly higher (considering errors from SIMS measurements and solubility models) than the expected H_2O_{eq} based on experimental conditions immediately prior to quench. The mechanism responsible for causing the observed concentration profiles therefore caused H_2O solubility to increase above that of the final experimental pressure and temperature conditions.

For pressures <500 MPa, H_2O solubility in rhyolite and phonolite melt compositions increases with increasing pressure and decreasing temperature (e.g. Yamashita 1999; Tamic et al. 2001; Liu et al. 2005; Iacono Marziano et al. 2007). Two possible mechanisms could therefore have caused the observed profiles – an increase in pressure, or a decrease in temperature (or a combination thereof). Since the samples were created under known pressure and temperature conditions, it is possible to examine these potential causes. Using the aforementioned models of H_2O solubility, the pressure necessary to cause the observed H_2O concentrations at the bubble wall (P_{nec}) are calculated (Table 4.4). Although the solubility relationship used by Burgisser & Gardner is included for completeness, the values from VolatileCalc are preferred since the Burgisser & Gardner relationship requires extrapolation for pressures greater than 200 MPa and the VolatileCalc model in any case produces more conservative values (Newman & Lowenstern 2002). For every sample, the pressure necessary to produce the observed solubility at the vesicle wall is higher than the

final experimental pressure (P_f) and in four cases exceeds even the highest pressure experienced by the sample, the pressure of synthesis (P_{syn}). The observed H_2O_t concentrations at vesicle walls in the rhyolite samples would require an increase of pressure of 30 to 90 MPa above P_f under isothermal conditions (Newman & Lowenstern 2002), while an increase of >50 MPa would be required for the phonolite sample IS14. Since pressure was strictly controlled during the experimental runs such pressure increases could not have occurred prior to quench.

Once the final experimental conditions are reached, the samples are quenched to glass. This quench process is described as isobaric, but in fact there is a small, transient pressure increase as the pressure medium re-equilibrates as the sample moves into the quench apparatus (e.g. Holloway et al. 1992; see Chapter 3 Section 3.2). In the ABG and IS14 experiments described here, this phenomenon was seen to cause a pressure fluctuation of less than 10 MPa that lasted for less than 1 second (A. Burgisser, *pers. comm.*). Comparison with the calculated values of P_{nec} demonstrate that this transient pressure increase is much too small to have caused the observed profiles while the rate of H_2O diffusion (e.g. DH_2O_t in rhyolite is ~ 2 x 10^{-11} m^2/s for 825 °C, 4 wt% H_2O_t; Ni & Zhang 2008) is too slow to create the observed profile lengthscales in the one second for which this pressure fluctuation occurs. Fig. 4.11 shows the expected H_2O_t profile for a pressure increase from 100 to 110 MPa, held for 1 second, in comparison with the observed H_2O_t for sample ABG1 (P_f = 100 MPa). Even in this 'worst case scenario' of a 10 MPa increase held for a full second, the maximum H_2O_t concentration that could be attributed to the transient pressure fluctuation is more than 1 wt% less than the observed H_2O_t value, while the expected lengthscale of hydration (as quantified by the half-fall distance, see Section 4.4.3.3) is only 4 µm in comparison to the 12 µm observed (Table 4.3). Since the samples were stored at ambient pressure after their production and never again subjected to high pressures, it is concluded that a pressure increase is not the cause of the observed bubble resorption.

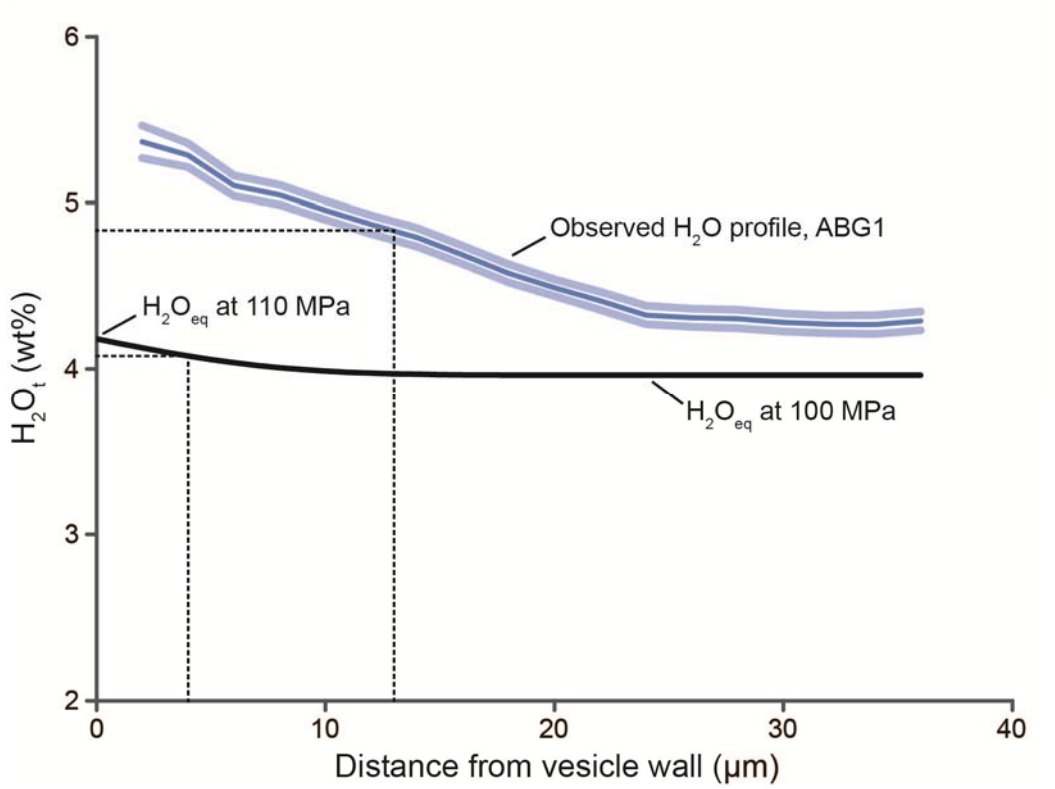

Fig. 4.11 Maximum influence of quench pressure fluctuation on H_2O concentration profile

Observed H_2O_t concentration profile from sample ABG1 (blue line, pale blue lines are twice the standard error in the mean) is compared with the H_2O_t concentration profile that could be caused by the transient pressure fluctuation during the quench process (black line). Dashed black lines show the half-fall concentration and half-fall distance for each profile. The profile for pressure fluctuation is calculated assuming 1-D Fickian diffusion for an increase in H_2O solubility from the equilibrium solubility value at 100 MPa (P_f for ABG1) to 110 MPa, for diffusion lasting 1 second. A pressure increase of 10 MPa for a full second is more than was observed, and so this profile represents the maximum H_2O diffusion that could be produced by the pressure fluctuation during quench. Both the vesicle wall H_2O_t concentration and half-fall distance are much smaller than for the observed ABG1 concentration profile.

The remaining mechanism for increasing H_2O solubility is a decrease in temperature. Current understanding of the temperature-dependence of H_2O solubility in silicate melts is outlined in Chapter 2 (Section 2.6). There are few data at ambient temperatures and there are no data at all for intermediate temperatures between 100 °C and magmatic temperatures. The VolatileCalc solubility model of Newman & Lowenstern (2002) is valid for rhyolite melt compositions down to

a temperature of 600 °C. Comparison of the observed H_2O_t concentrations at vesicle walls of the rhyolite samples with this model reveals that a solubility higher than that at 600 °C is required to explain them (Table 4.4, Fig. 4.12). Fig. 4.12 compares the observed vesicle wall H_2O_t concentrations with what is currently known about the variation in H_2O solubility with temperature. The temperature-dependence of H_2O solubility does not appear to follow a simple linear trend (Chapter 2 Fig. 2.10), and reliable interpolation between the ambient and > 600 °C datasets (which are derived for different pressures) is not possible. Fig. 4.12 suggests that the observed H_2O_t concentrations are more likely to correspond to temperatures of ~400 – 600 °C than to temperatures < 400 °C, but without a comprehensive H_2O solubility model this assessment remains qualitative. It is however possible to say that the observed vesicle wall H_2O_t concentrations can be explained by temperatures that are lower than the experimental temperature, but higher than ambient temperature.

All experiments were conducted isothermally at high temperature, with experimental temperatures in the range 825 – 1050 °C. The proposed temperature decrease could not have occurred during the experimental runs. However after the final experimental conditions were reached, all samples experienced a temperature decrease as they cooled to ambient temperature.

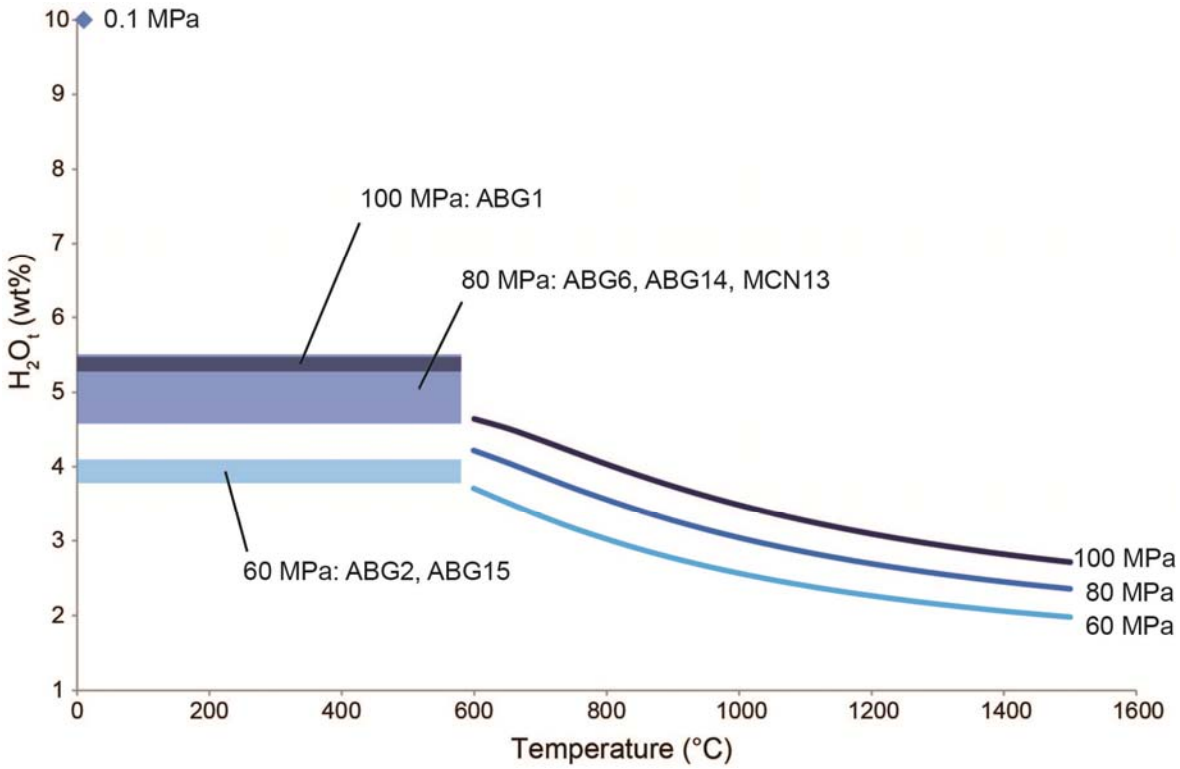

Fig. 4.12 Comparison of observed H_2O_t at vesicle walls and temperature-dependent H_2O solubility

The increase in H_2O solubility with decreasing temperature is shown for the experimental pressures investigated (blue lines), according to the VolatileCalc solubility model of Newman & Lowenstern (2002). The H_2O solubility data of Anovitz et al. (1999) for ambient temperature and pressure is also shown (blue diamond). The range in H_2O_t concentrations measured at vesicle walls is represented by boxes coloured according to experimental pressure, in order to assess the temperatures that are recorded by the analysed concentration profiles.

4.4.3 Timing of profile formation

4.4.3.1 Defining 'quench'

The process of cooling at the end of an experiment is generally referred to as 'quench', or 'the quench process.' More specifically, 'quench' is often used to describe the process of cooling the silicate melt until it reaches the glass transition, rather than cooling all the way to ambient temperature. The temperature of the glass transition, T_g, varies with melt composition, H_2O_t concentration and cooling rate, and therefore differs for each sample. For clarity, this discussion will use the terms 'quench process' to describe the general cooling process at the end of an experiment, 'quench to glass' to describe cooling to the temperature of the glass transition, and 'cooling to ambient temperature' to describe the full cooling cycle from experimental to ambient temperature.

4.4.3.2 Eliminating glass hydration at ambient conditions

H_2O solubility in silicate melts is known to increase with decreasing temperature, and continues to do so even in the solid (i.e. glass) state. It has been known for many years that naturally produced silicate glasses are undersaturated with respect to ambient temperature and pressure conditions and are affected by the hydration of glass surfaces. This process has been studied by archaeologists who have attempted to date obsidian artefacts by analysing H_2O_t gradients in surface layers and using diffusion modelling to date the time to form these hydration profiles (e.g. (Friedman & Long 1976; Lawrence M Anovitz et al. 1999; Riciputi et al. 2002; L M Anovitz et al. 2004). These studies have resulted in many of the data points that exist for H_2O solubility and diffusivity at low temperature in silicate glasses (see Chapter 2 Section 2.7.2.1). In volcanology this hydration process is termed 'secondary hydration' since the resulting H_2O_t concentration gradients are formed after eruption and emplacement by the diffusion of secondary (e.g. meteoric) H_2O rather than primary (i.e. magmatic) H_2O (e.g. Giachetti & Gonnermann 2013).

In the case of a vesicular glass at ambient temperature and pressure, H_2O trapped in vesicles will begin to diffuse back into the undersaturated glass. Such diffusion could potentially result in concentration profiles that resemble those observed here. A fine distinction can be made here regarding the relevant terminology – if hydration profiles are formed by diffusion of magmatic H_2O from a vesicle back into the glass this H_2O is technically still 'primary' and the term 'glass rehydration' is more appropriate than 'secondary hydration'. There are two lines of evidence however that suggest that neither glass rehydration nor secondary hydration at ambient temperature is the cause of the observed concentration profiles. The first is that the observed H_2O_t concentrations at vesicle walls are higher than expected equilibrium solubilities at 600°C, but lower than those (admittedly sparse) measurements of solubility at ambient temperature (Chapter 2 Fig. 2.10). The observed profiles are therefore consistent with being formed at temperatures below 600°C but greater than ambient temperature, which would imply that they were not formed by rehydration after production. It should be noted however that the observed H_2O_t concentrations 'at vesicle walls' are actually located 2 μm from the actual vesicle wall. Since the equilibrium solubility value occurs directly at the vesicle wall it is possible that if the profiles could be extended as far as the vesicle wall, at a sufficiently high spatial resolution, higher H_2O_t concentrations (corresponding to lower temperature conditions) would indeed be observed.

More pertinent is the rate at which H_2O diffuses in glass at ambient conditions. H_2O diffusivity in rhyolite glasses (obsidians) is now characterised for temperatures up to 150 °C (Anovitz et al. 2006). At 30 °C, DH_2O_t is ~10^{-21} m^2/s (Anovitz et al. 2006). At this temperature it would therefore take approximately 30 years for diffusion to create a H_2O_t hydration profile with a half-fall distance of 1 μm (see Chapter 2 Section 2.7.1, Eq. 2.12). The observed profiles are much broader than this (Table 4.3), yet the samples were produced <10 years ago. In the case of IS14 less than 6 months elapsed between sample production and analysis. It is therefore not possible that the observed profiles were created by glass rehydration at ambient conditions after sample production. Moreover, any modification of the profiles (since diffusion is still ongoing, albeit at a

very slow rate) in the time since sample production is limited to lengthscales that are smaller than the observation lengthscale (e.g. each averaged concentration profile for a given sample consists of data binned in 2 µm segments). It can therefore be concluded that the observed profiles were formed during the quench process that followed the experiment.

4.4.3.3 Evidence from characteristic diffusivity

The formation of the observed profiles is controlled by changes in H_2O solubility and diffusivity. These properties are functions of temperature, and temperature is itself a function of time as the sample cools during quench. Understanding the timescale over which the observed H_2O_t profile formed in the context of the timescale of temperature variation during the quench process is important for assessing the relative importance of H_2O diffusion back into the silicate structure above the glass transition (bubble resorption) and below the glass transition (glass rehydration).

The rapid decrease in H_2O diffusivity with decreasing temperature might suggest that the bulk of the profile lengthscale formed at high temperatures at the beginning of quench when H_2O diffusivity was high. However, the rate of cooling is expected to have been greatest in the initial stages of quench and to have continuously decreased as ambient temperature was approached. The samples may therefore have spent only a short time at temperatures where H_2O diffusivity was high but longer at intermediate temperatures where H_2O diffusivity was lower, yet still higher than at ambient temperature.

The temperature dependence of H_2O solubility and diffusivity is poorly constrained for ambient and intermediate temperatures, while the variation in temperature during the quench process was not directly measured and can only be estimated. Quantitative modelling of these processes is therefore not yet possible. Instead the relative importance of diffusion at high versus intermediate and low temperatures is assessed by using the concept of characteristic diffusivity (e.g. Riciputi et al. 2002; Anovitz et al. 2004).

A characteristic diffusivity DH_2O_{ch} for diffusion during the quench process can be derived from the lengthscale of the observed profile (L) and the timescale over which diffusion occurs (t), by rearranging:

$$L = \sqrt{DH_2O_{ch}\, t} \qquad \text{Equation 4.1}$$

This is a form of the 'half-fall distance' derived for 1-D Fickian diffusion (see Chapter 2 Section 2.7.1, Eq. 2.12). For the case of ideal Fickian diffusion at constant diffusivity D and with boundary conditions of constant H_2O concentration, $DH_2O_{ch} = D$ when L is the half-fall distance (i.e. the distance at which the concentration falls to midway between the maximum and minimum values along a profile) and t is the time since the onset of diffusion. In these samples, both diffusivity and solubility vary as a function of time as the sample cools, so DH_2O_{ch} represents a time-integrated 'average' diffusivity over the duration of resorption/hydration.

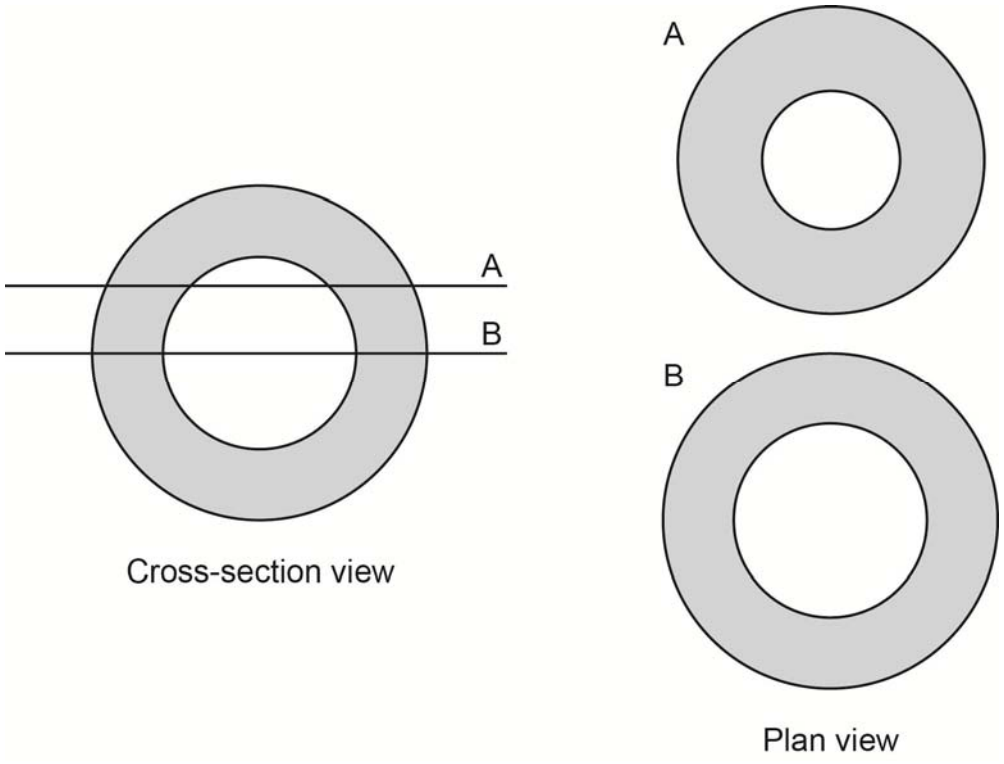

Fig. 4.13 Selection of vesicle for half-fall distance *L*

Figure shows a vesicle (white) in cross-section surrounded by a resorption halo (grey) of uniform width. Transects A and B represent sections through the vesicle at high latitude and at the equator, respectively. The corresponding observed vesicle diameter and resorption halo width are

shown in plan view. The section at the equator (B) provides the most accurate measure of resorption halo width, and is identified by having the higher ratio of bubble diameter to resorption halo width. Note that this method requires vesicles to be of a similar size.

To calculate DH_2O_{ch}, a representative half-fall distance *L* for the sample must be used. This is derived from the most representative single analysed vesicle rather than from the averaged H_2O_t concentration profile, since this profile is affected by the averaging of multiple vesicles sectioned at different latitudes (see Chapter 3 Section 3.3.1.7). The vesicle is chosen by selecting the vesicle with the greatest ratio of vesicle diameter to halo width (as measured by the half-fall distance of that vesicle's H_2O_t profile) (Fig. 4.13). This vesicle will be the vesicle that is sectioned closest to its equator and will therefore have the most representative H_2O_t concentration profile and half-fall distance. Although this method assumes that all vesicles in a sample are of a similar size, this assumption is justified by the fact that all vesicles selected in this manner are also judged visually to have the steepest concentration profile for vesicles in that sample. Half-fall distances for each sample are shown in Table 4.3.

In order to derive the quench timescale, *t*, the temperature decrease over time during quench must be modelled. This is done for the ABG samples using the model of Xu & Zhang (2002) for sample quench in a water medium (Fig. 4.14). This model assumes that the sample surface cools instantaneously upon immersion in the quench medium and that there is no heating or convection of the medium. Accordingly quench timescales derived from this modelled temperature-time history are likely to be an underestimate. From this, the timescale for diffusion during quench for the ABG samples is estimated to be between 3 and 10 seconds. 3 seconds is expected to be an underestimate of the true diffusion timescale, but is representative of previous assumptions of the time to the glass transition for these samples (Burgisser & Gardner 2005; Castro et al. 2012) (see Chapter 5 Section 5.4.1.1 for an updated T_g calculation for ABG1 that accounts for increasing H_2O_t content during cooling). Some diffusion may also occur below the

glass transition, however, and so an upper limit of 10 seconds is chosen, based on the time taken for the sample to cool to 300 °C. Although diffusivity data below 400 °C requires extrapolation of the Ni & Zhang diffusivity model beyond its temperature range, doing so suggests that diffusivity decreases another order of magnitude between 400 and 300 °C, requiring 10 seconds to form a 1 µm hydration lengthscale (Ni & Zhang 2008). Since the sample spends only ~1 second in the temperature range 310 – 290 °C, profiles are therefore not expected to be significantly modified below 300 °C.

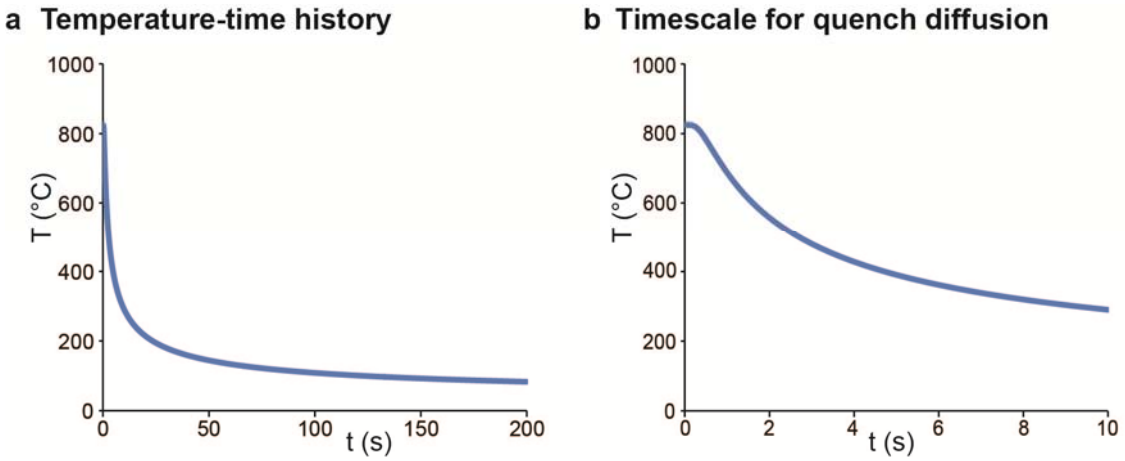

Fig. 4.14 Estimated temperature variation during quench

The cooling history during quench of the ABG samples as calculated using the model of Xu & Zhang (2002). **a** Temperature variation from the onset of quench to a time of 200s. Temperature initially decreases rapidly before slowing as ambient temperature is approached. **b** The temperature-time history for the first 10 seconds of the quench process, which is taken to be the maximum timescale for formation of the observed diffusion profiles. The temperature history is calculated for the centre of the sample so the slight inflection at the beginning of quench corresponds to the time taken for heat to diffuse to the edge of the capsule.

Sample ABG1 was expected to have an equilibrium (i.e. flat) H_2O_t profile prior to quench, and its observed half-fall distance should therefore not have been affected by any prior H_2O_t concentration gradient. Accordingly, using values of L = 12 µm and t = 3 and 10 , DH_2O_{ch} for ABG1 is calculated as ~6 x 10^{-11} m^2/s to ~8 x 10^{-12} m^2/s, for 3 to 10 seconds respectively. These values are high when compared to values of DH_2O_t of 2 x 10^{-11} m^2/s at T_{exp} (with 4 wt% H_2O_t) and 1 x 10^{-12}

m^2/s at 400 °C (with 5 wt% H_2O_t; computed from Ni & Zhang 2008). This indicates that the bulk of the observed H_2O_t concentration profiles must be formed at high temperature during the early part of the quench process. At these temperatures the silicate structure is still molten, therefore the term 'quench resorption' is used to describe the temperature-controlled formation of the observed H_2O_t concentration profiles. Further textural evidence associating the observed H_2O_t concentration profiles with bubble resorption is presented later in Chapter 5.

4.4.4 Controls on quench resorption

4.4.4.1 Effect of quench timescale and H_2O diffusivity

The lengthscale of the H_2O concentration profile formed during quench resorption will vary as a function of quench timescale and H_2O diffusivity. For the same change in concentration between the bubble wall and the far field melt, the concentration profile for a rapidly quenched sample would be expected to be shorter than the profile for a slowly quenched sample (Fig. 4.15). Meanwhile, for the same quench timescale, profiles will also vary according to the exact temperature-time history, with different profile lengthscales according to the amount of time spent at high versus low temperatures. Since DH_2O_t is temperature dependent, more time spent at high temperatures will result in a higher DH_2O_{ch} for the given timescale, and accordingly the concentration profile will be longer. This will also impact the amount of bubble resorption that occurs for a given profile lengthscale.

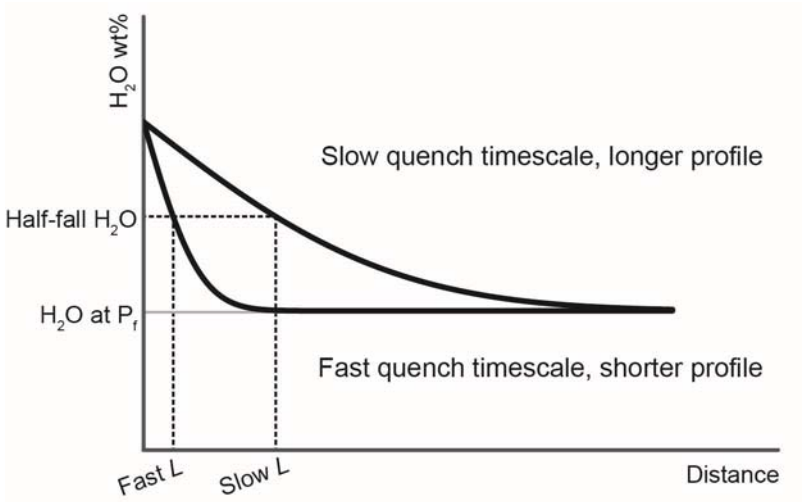

Fig. 4.15 Quench timescale control on quench resorption profile

Schematic figure showing the different H_2O_t concentration profiles (black lines) and half-fall distances (*L*, dashed lines) for identical samples quenched over different timescales. Slow quench timescales will result in longer half-fall distances than fast quench timescales.

In addition to temperature, DH_2O_t is also affected by H_2O_t concentration, pressure and melt composition, of which H_2O_t concentration is the most important parameter (see Chapter 2 Section 2.7.2). Therefore, for a given temperature-time history during quench, a melt with higher H_2O_t concentration will form a longer concentration profile (Fig. 4.16). H_2O_t concentration in the melt is a strong function of pressure, with higher H_2O_t concentration associated with higher pressures. Thus samples quenched at high pressure, where H_2O_t concentration and thus DH_2O_t are high, would be expected to form longer profile lengthscales than those quenched at lower pressure.

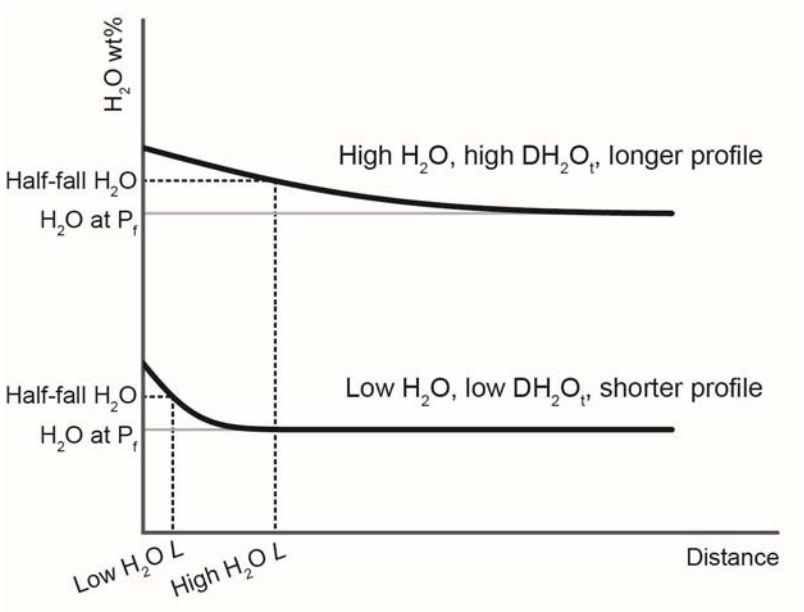

Fig. 4.16 H_2O_t concentration control on quench resorption profile

Schematic figure showing the different H_2O_t concentration profiles (black lines) and half-fall distances (*L*, dashed lines) for samples of different initial H_2O_t concentrations quenched over identical timescales. Samples with high initial H_2O_t concentrations will have faster DH_2O_t and will therefore have resorption profiles with longer half-fall distances than samples with lower initial H_2O_t concentrations.

In the context of these variables, the observed H_2O_t concentration profiles of samples ABG1 and MCN13 are compared. Both samples were expected to have bubble populations in equilibrium with the melt prior to quench, and so would initially have had flat H_2O_t concentration profiles. ABG1 was quenched faster than MCN13 (Table 4.1), and so might be expected to have a shorter profile than MCN13. However, ABG1 was held at a higher pressure and so had a higher initial H_2O_t concentration than MCN13 (Table 4.4). As a result of concentration dependent diffusivity ABG1 may therefore be expected to have a longer profile than MCN13. In fact, these two opposing influences counterbalance each other, and the half-fall distances of ABG1 and MCN13 lie within error of each other (Table 4.3). This finding is consistent with the model of quench resorption, and highlights the different factors that may interact during the quench process to determine the observed concentration profiles.

4.4.4.2 Effect of pre-quench H_2O concentration profile

Another factor that will affect the H_2O profile formed during quench is the shape of the H_2O profile prior to quench. Both ABG1 and MCN13 had uniform concentration profiles prior to quench. Samples which had growing bubble populations prior to quench would instead have had concentration profiles that were depleted at the bubble wall. This initial depletion will act to reduce the lengthscale of the resorption profile (Fig. 4.17). Until sufficient H_2O has diffused from the bubble back into the melt to fill in the concentration depletion, H_2O will still be diffusing from the far field in towards the bubble down the concentration gradient. Only when the initial concentration depletion has been removed can H_2O diffusion from the bubble contribute towards making the observed H_2O resorption profile, and thus the lengthscale will be shorter than for a sample where the initial concentration profile was uniform. Additionally, H_2O concentration-dependent diffusivity means that DH_2O_t will be lower in the depleted region and so the DH_2O_{ch} during quench will be lower, resulting in a shorter profile.

The ABG samples all experienced the same quench process, and so the control of the temperature-time history on the resorption profile is the same for each sample. ABG1 has a longer half-fall distance than the other ABG samples that were decompressed and therefore experienced bubble growth prior to quench. This is consistent with the physical model of the quench resorption process, where a sample with high, uniform H_2O_t concentration prior to quench has a longer half-fall distance than samples that had lower initial H_2O_t concentration contents and profiles that were depleted near bubble walls.

The effect of initial H_2O_t concentration and profile shape on the observed resorption profile might be expected to vary with decompression rate (Fig. 4.17). Undecompressed (equilibrium) samples would be expected to have the longest resorption profiles (Fig. 4.17 a). Samples that experienced rapid decompression would have only a narrow band of concentration depletion at the vesicle wall and high far-field H_2O_t concentrations as a result of disequilibrium degassing. The small

depletion and otherwise high H_2O_t concentration would therefore result in long resorption profiles (Fig. 4.17 b). Samples that underwent intermediate decompression rates would have broader concentration depletions and so would have shorter resorption profiles than more rapidly decompressed samples (Fig. 4.17 c). Conversely however, samples that experienced slow decompression would have initial H_2O_t profiles resulting from bubble growth that would be close to equilibrium degassing. In this case the concentration depletion would be so broad as to approximate a uniform profile, and so, depending on the H_2O_t concentration of the far field, slowly decompressed samples would also be expected to have longer resorption profiles than samples decompressed at an intermediate rate (Fig. 4.17 d).

The ABG samples were decompressed to different final pressures at different decompression rates, however (with the exception of the equilibrium sample ABG1) the resolution of the dataset is not sufficient to resolve any trends with these parameters. Half-fall distances are derived from H_2O_t concentration profiles that are composed of data averaged into 2 μm segments, and quoted errors include two times the standard error of the mean for the profile. Additionally, if the selected vesicles for half-fall distance are not all sectioned directly at the equator, the half-fall distances will not be comparing like with like. For the rapidly quenched ABG samples, with relatively short half-fall distances, these errors are therefore too large to distinguish changes in resorption lengthscale resulting from experimental conditions.

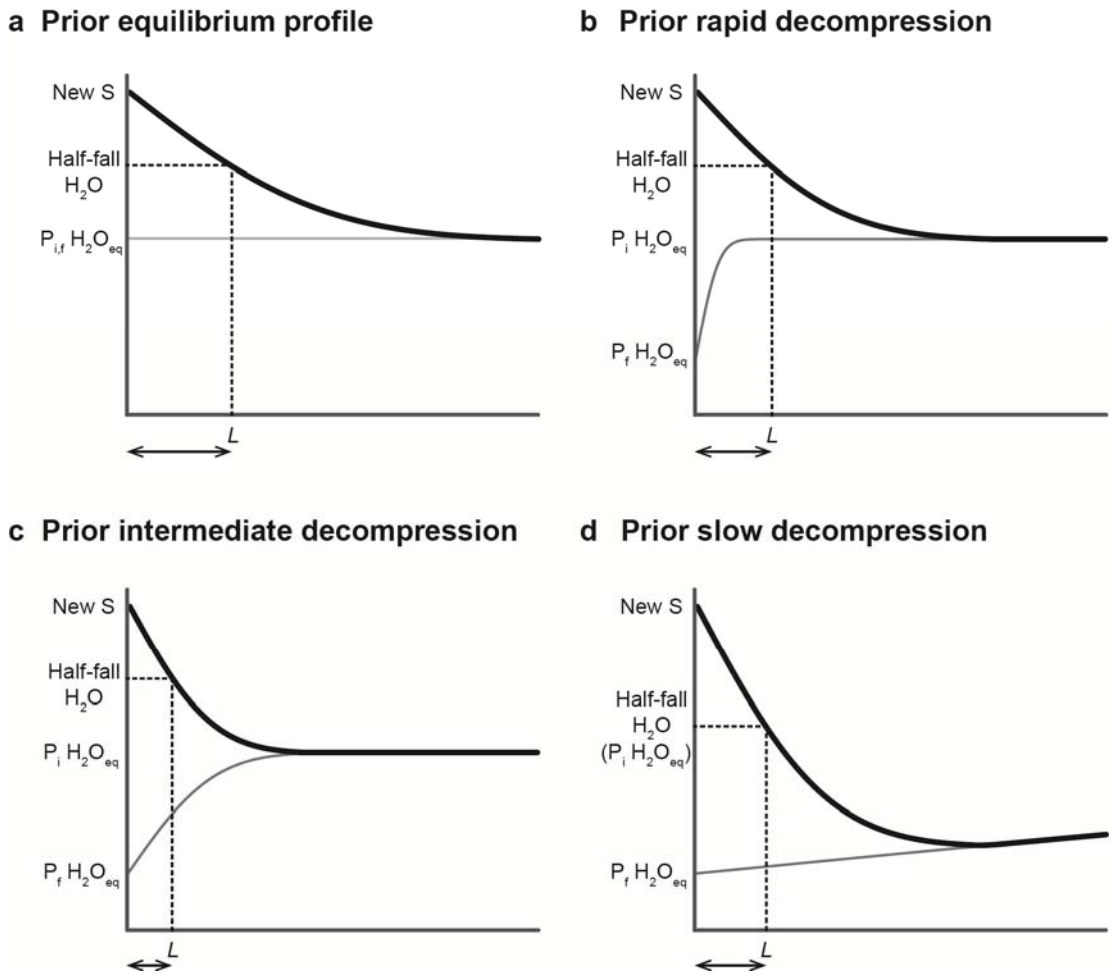

Fig. 4.17 Control of decompression rate and initial H_2O_t concentration profile on quench resorption

Schematic figure showing the different H_2O_t concentration profiles (black lines) and half-fall distances (*L*, dashed lines) for samples decompressed between the same initial (*Pi*) and final (P_f) pressure at different rates of decompression. **a** Equilibrium sample quenched at high pressure has high, uniform initial H_2O_t concentration profile and so has a large half-fall distance. **b** Rapid decompression to P_f leads to narrow H_2O_t depletion at vesicle wall and high far field concentration in pre-quench H_2O_t concentration profile; half-fall distance is therefore smaller than for **a** but still large. **c** Intermediate decompression rate creates wider depletion in initial H_2O_t concentration profile that must be filled in during quench resorption; half-fall distance is therefore shorter than **b**. **d** Slow decompression rate results in initial H_2O_t concentration profile that approximates uniform concentration profile. With no H_2O_t depletion to fill in, half-fall distance will vary as a function of the H_2O_t concentration and may be longer than for **c**.

4.4.5 Far field hydration versus disequilibrium degassing

Quench resorption alters the H_2O_t concentration profile resulting from syn-experimental bubble growth in the vicinity of the bubble wall, but at a certain distance from the bubble wall it is possible that the concentration profile remains unaltered during quench. If this is the case, then the far field portion of the profile can provide some insight into the degassing processes that took place prior to quench. For example, the Burgisser & Gardner (2005) study from which the ABG samples were sourced investigated the effect of decompression conditions on the degree of disequilibrium degassing (see Chapter 2 Section 2.8.2). If decompression rate exceeds the rate at which excess H_2O in the supersaturated far field can diffuse into the bubble, the far field profile will have higher H_2O_t concentrations than the equilibrium solubility value for the experimental conditions. In order to extract information from far field concentrations it is therefore necessary to distinguish between original concentration profiles and those that have been affected by hydration. This hydration may come from either the bubble under consideration, or from the resorption halos from neighbouring bubbles.

When extracting greyscale profiles from BSEM images, care was taken not to extend the profiles beyond the Voronoi distance which demarcates the region of influence of a particular bubble. As applied to a 2D section of the sample (the BSEM image), this method cannot however account for the distribution of vesicles in three dimensions and so, while obviously hydrated regions such as 'ghost bubbles' were avoided (e.g. Fig. 4.1, 4.2), it is possible that individual profiles extended into areas of glass that had been hydrated by neighbouring resorbing bubbles. When considering the profiles in Fig. 4.3 it is important to consider also the average bubble-bubble spacing of each sample, which determines the distance at which a profile is likely to be affected by a neighbouring bubble. This is known for the ABG series (see Chapter 5 Section 5.5.1) and is typically ~10 µm shorter than the presented profiles.

All ABG samples were held at 100 MPa prior to decompression and so the equilibrium H_2O solubility (H_2O_{eq}) value at 100 MPa (3.96 wt%; Newman & Lowenstern 2002) represents the maximum H_2O_t value in the far field that could be explained without hydration during resorption. If far field H_2O_t concentrations are greater than 3.96 wt% they must result from hydration from resorbing bubbles, rather than preserved H_2O_t concentration profiles derived from syn-experimental degassing. All ABG profiles except one have far field H_2O_t concentrations that are within error of 3.96 wt%. The exception is ABG14, which has a far field concentration of 4.92 wt%. This discrepancy is too great to be caused by analytical error on the SIMS measurement or by errors in the solubility model and so the H_2O_t concentration profile for ABG14 has been affected by the interaction of concentration gradients surrounding neighbouring vesicles.

Where far field H_2O_t concentrations are equal to or lower than their initial H_2O_t concentrations it becomes more problematic to determine whether they have been affected by far field hydration. ABG6 was decompressed to 80 MPa but has far field H_2O_t concentrations within error of the initial H_2O content at 100 MPa. Since ABG6 was decompressed slowly (0.1 MPa/s) it would be unlikely to exhibit a strong disequilibrium degassing trend and so this sample profile is also likely to have been affected by far field hydration. ABG2 was decompressed to 60 MPa at 0.1 MPa/s and was expected to exhibit a near-equilibrium concentration profile. The observed far field concentrations are ~0.3 wt% higher than the expected H_2O_{eq} for P_f, and could be explained by analytical error, slight disequilibrium degassing or far field hydration. By contrast, ABG15 was also decompressed to 60 MPa but at the faster rate of 0.5 MPa/s. For this sample, far field concentrations are ~0.8 wt% higher than the expected H_2O_{eq} (Table 4.3, 4.4). Such far field concentrations could be explained by either hydration or disequilibrium degassing. Burgisser & Gardner (2005) concluded that the threshold for disequilibrium degassing in the ABG samples occurs at decompression rates greater than 0.15 MPa/s. Although these conclusions were based on porosity measurements, which have been shown to be likely to be affected by bubble resorption during quench, the decompression rate of 0.5 MPa/s is sufficiently rapid that

disequilibrium degassing may be expected. The observed profile, with its increasing concentration in the far field (Fig. 4.3), may therefore record disequilibrium degassing processes occurring prior to quench.

The phonolite sample IS14 has far field concentrations ~0.9 wt% higher than the expected H_2O_{eq} at P_f (Table 4.3, 4.4). IS14 was produced under conditions that reproduce those of the study by Iacono Marziano et al. (2007). In that study, sample B54 was produced under the same conditions and was found to have a gradient in H_2O_t from the non-vesicular sample interior towards the capsule walls where bubbles had nucleated, with the far field being oversaturated by 0.55 wt%. The authors concluded that the decompression rate was therefore sufficiently rapid to induce disequilibrium degassing, and it is likely therefore that the concentration profile of IS14 represents the same phenomenon.

The final sample, MCN13, was a solubility experiment and therefore expected to have a uniform concentration in the melt at the H_2O_{eq} value. While the profile has been overprinted at the vesicle wall by quench resorption, the far field concentrations are as expected for the experimental conditions. This suggests that the bubble-bubble spacing and resorption halo widths for this sample are such that far field concentrations are not overprinted by quench resorption.

4.5 Implications

The H_2O_t concentration profiles presented here reveal that quench resorption is capable of overprinting the concentration profiles created during bubble growth, even for rapid quench timescales of the order ~10 seconds. The evidence from calculated DH_2O_{ch} values suggests that the majority of the diffusion that forms the observed profiles takes place at temperatures above the glass transition, when the loss of H_2O from the bubble may be offset by a reduction in bubble volume. This aspect of quench resorption is explored in more detail in the next chapter.

The analyses in this chapter have shown that the lengthscale of the observed resorption profile is controlled by the temperature-time history of the quench process, H_2O concentration-dependent DH_2O_t, and the shape of the initial H_2O_t concentration profile that existed prior to quench. The concept of DH_2O_{ch} links these parameters and can be used to consider the situations in which quench resorption is likely to create resorption profiles with significant lengthscales (Fig. 4.18).

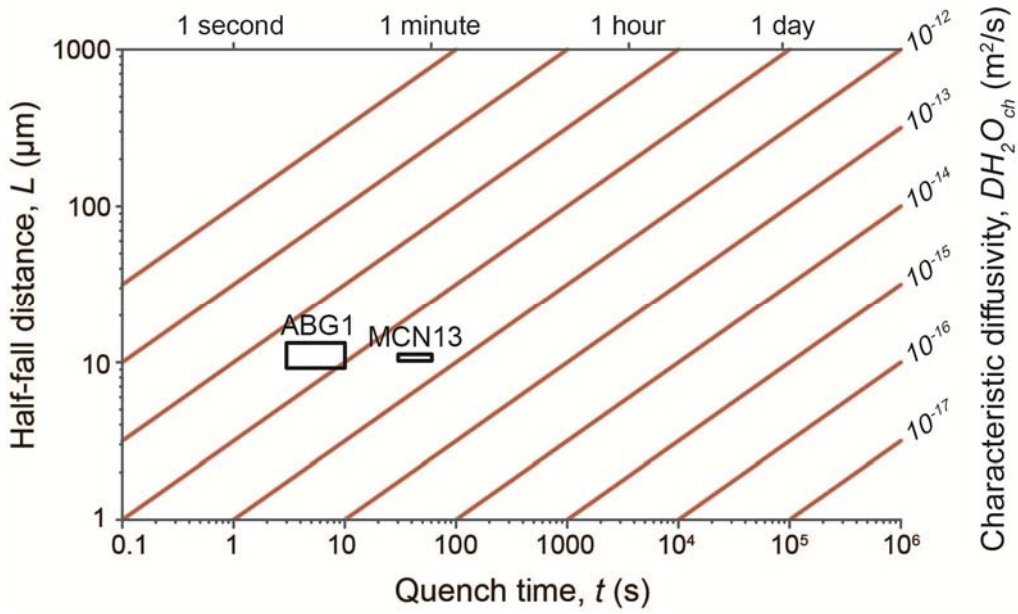

Fig. 4.18 Quench resorption and the relationship between *L*, DH_2O_{ch} and *t*

The half-fall distance, *L*, of quench resorption profiles is determined by the characteristic diffusivity DH_2O_{ch} and the quench timescale, *t*. The potential impact of quench resorption for different samples can therefore be estimated by considering the likely quench timescale and H_2O diffusivity for the sample conditions. Black boxes show the measured half-fall distances of ABG1 and MCN13 (including error on half-fall and quench timescale of 3 – 10s and 30 – 60 s respectively). The lower DH_2O_{ch} for MCN13 reflects its lower DH_2O_t (as a result of lower H_2O_t concentration), but it has the same half-fall distance as ABG1 as a result of its longer quench timescale.

4.5.1 Experimental samples

Experimental samples, such as the ones analysed in this study, are often used to investigate processes that occur in the volcanic system prior to eruption. They are therefore often conducted

at high pressures and temperatures. The pressure-dependence of H_2O solubility means that such samples will typically have high H_2O_t contents of a few wt%. The strong control of H_2O_t concentration on H_2O diffusivity means that these samples are susceptible to significant modification of H_2O_t profiles by resorption during quench, even for samples that are quenched rapidly on timescales of seconds.

Studies of experimental samples are grounded in the assumption that the observed products are the direct result of the chosen experimental conditions. The evidence presented here shows that samples can be modified as a result of the temperature decrease during quench, and suggests that interpretation of experimental samples must evaluate the possible impacts of quench resorption on investigated parameters. Vesicular samples are often used in solubility experiments, which measure H_2O concentrations in melts held at different experimental conditions in order to constrain how H_2O solubility varies as a function of pressure and temperature for different melt compositions. Although they do not require the presence of a bubble population, bubbles are often present (particularly if the sample is produced from a powdered starting material e.g. Gardner et al. 1999; Larsen et al. 2004) and are used as a sign that the sample was fully H_2O-saturated prior to quench. However if these bubbles begin to resorb during quench, the resulting resorption halos increase the H_2O content of the melt above that of the investigated experimental conditions. In the solubility sample MCN13 presented here the far field H_2O concentrations have not been overprinted by resorption, however the ABG samples show that such far field hydration can occur at similar conditions. If the average bubble-bubble spacing in the sample is small compared to the size of the resorption halos then the measured H_2O_t concentrations are likely to be affected. Studies of vesicular solubility samples therefore need to evaluate the possible impact of quench resorption on far field H_2O_t concentrations and wherever possible should utilise analytical methods with high spatial resolution that can analyse far field H_2O_t concentrations without overlapping with high-H_2O_t resorption halos.

4.5.2 Natural samples

The evidence that H_2O_t concentration profiles that are characteristic of bubble resorption can be caused by temperature decrease during quench has important implications for the interpretation of natural samples. Two recent studies (Watkins et al. 2012; Carey et al. 2013) have observed bubble resorption in natural pyroclasts either directly (Watkins et al.) or indirectly (Carey et al.) and concluded that resorption was caused by a pressure increase in the conduit prior to eruption. This chapter has shown that temperature decrease is also a viable mechanism for causing bubble resorption, and highlights the need to consider both mechanisms when interpreting unconstrained natural samples. All erupted samples will have experienced a temperature decrease during the quench to glass, and could therefore have been altered by quench resorption. A pressure increase mechanism for bubble resorption is expected to be less common, since erupting magma will experience decompression as it ascends through the crust. Bubble resorption caused by pressure increase would therefore be a sign of unusual eruptive conditions, such as pressure cycling at conduit margins (Watkins et al. 2012) or magma convection within a conduit (Carey et al 2013). In the dynamic context of volcanic eruptions it is likely that bubble concentration profiles are in fact affected by variations in both pressure and temperature, rather than one or the other. However, since temperature decrease is a universal process for erupted material, the contribution of quench resorption must be considered before observations of bubble resorption can be attributed to pressure increase.

The significance of quench resorption in natural samples is expected to vary widely, due to the large range in H_2O_t contents and quench timescales that can apply to volcanic eruptions. Half-fall distances will vary with H_2O_t content, and so samples that are erupted with low H_2O_t concentrations may be less affected by quench resorption than cases where H_2O_t contents are higher, e.g. in pyroclastic obsidians or samples erupted under the confining pressure of an ice body or water column. In cases where quench is very rapid (e.g. 'hyperquenched' samples that

have been observed in submarine settings (Helo et al. 2013)) little to no modification of bubble concentration profiles may occur. However, many naturally erupted samples undergo slower cooling than the experimental samples investigated here. For example, cooling rates as low as 0.003 K/min have been recorded in rheomorphic phonolite flows in Tenerife, Canary Islands (Gottsmann & Dingwell 2001). In situations with long quench timescales, even low H_2O_t concentrations could result in significant resorption profiles. In these scenarios, quench resorption may be an important control on melt viscosity and the temperature of the glass transition. The dependence of melt viscosity on H_2O_t concentration is greatest at low temperatures and low H_2O_t concentrations (e.g. Hess and Dingwell 1996; see Chapter 2 Section 2.3.2). The contribution of H_2O_t to the melt by quench resorption may therefore have important implications for processes such as obsidian and rheomorphic flows.

4.6 Conclusions

The analysis of H_2O_t concentrations in vesicular experimental samples has demonstrated that the increase in H_2O solubility during the quench process causes H_2O to diffuse from the bubble/vesicle back into the melt/glass. Consideration of the lengthscale and timing of this diffusion suggests that the majority of the diffusion profile is formed at temperatures above the glass transition, and so this process is referred to as quench resorption.

Quench resorption has implications for the interpretation of both experimental samples, where H_2O_t concentrations may be affected by elevated H_2O_t concentrations in the far field, and for natural samples, where both pressure- and temperature-controlled changes in H_2O solubility must be considered as potential causes of bubble resorption. The magnitude of quench resorption will vary with the temperature-time history of quench, the H_2O_t concentration of the sample and the initial shape of the concentration profile prior to quench. A qualitative, first order estimate of the amount of quench resorption can be obtained using BSEM images, where dark glass corresponds

to high H_2O_t concentrations and lighter glass to lower H_2O_t concentrations. For more quantitative assessments, SIMS-calibrated BSEM imaging has been shown to provide quantitative data at high spatial resolution.

The current lack of H_2O solubility and diffusivity data for low and intermediate temperatures is an impediment to accurate modelling of the quench resorption process. Future studies of these parameters and investigations of quench resorption under controlled conditions will enable better constraints of how bubble resorption profiles vary over the timescale of quench. This will enable better interpretation of observed bubble resorption profiles and the impact of melt rehydration, and may provide a framework for using bubble resorption as a geospeedometer for constraining magma cooling rates and glass transition temperatures.

Chapter 5: Quench resorption textures

5.1 Introduction

In the previous chapter it was demonstrated that the temperature dependence of H_2O solubility causes H_2O to diffuse from bubbles back into the melt during the quench to glass. Analysis of the resulting H_2O_t diffusion profiles suggests that the majority of this diffusion occurs at temperatures above the glass transition, when loss of H_2O vapour from bubbles may be accompanied by a reduction in bubble volumes. This chapter utilises resorption profiles and textural analysis to assess the magnitude of this quench resorption.

5.2 Samples and Methods

The samples discussed in this chapter are the ABG samples analysed previously in Chapter 4. They are experimentally-vesiculated rhyolites of which one (ABG1) was expected to have a bubble population in equilibrium with the melt prior to quench, and the others were expected to have bubble populations that were growing prior to quench. The ABG samples were quenched in a rapid quench attachment. No direct measurements of temperature were made during the cooling process (see Chapter 3 Section 3.2.2).

Sample textures were investigated using BSEM imaging (see Chapter 3 Section 3.3.1.3 for analytical details). Analysis with BSEM enables imaging of textures with the additional context of compositional information as revealed by greyscale variations, in this case related to spatial variations in the dissolved H_2O_t content of the glass.

5.3 Results

5.3.1 Bubble morphology

The majority of vesicles are seen to be round in cross section, although the effects of bubble crowding can begin to be seen in samples decompressed to lower final pressures. Where neighbouring bubbles impinge upon one another the film of melt between them typically has a sinuous, or buckled, shape (Fig. 5.1).

5.3.2 Cracks

Two main populations of cracks are seen in these samples (Fig. 5.2). The far field glass contains long curving cracks that extend between vesicles but which usually terminate short of the vesicle wall. This stopping distance often corresponds to the limit of the observed resorption halo. These cracks often show a change of direction as they approach the vesicle so that they finish parallel to the vesicle wall. Cracks may also change direction in the far field but these correspond to dark areas of glass associated with 'ghost bubbles' above or below the sample surface (Fig. 5.2 e), suggesting that changes in crack direction are linked to distance from vesicles. These far field cracks are typically smooth, but may show a more stepped morphology close to their termination.

The second set of cracks occur at the vesicle wall. These cracks are less common than the cracks in the far field and are only seen in some vesicles. Cracks extend radially from the vesicle wall out into the resorption halo, typically for lengths of <10 µm. Some then change direction and extend parallel to the vesicle wall (Fig. 5.2 d).

Most cracks in the far field have margins of H_2O_t-rich glass, seen in BSEM images as dark glass. These margins are of variable width, but are narrower than the H_2O_t-rich resorption halos seen around neighbouring vesicles. Calculated half-fall distances for hydrated cracks in ABG1 range from 1 to 3 µm (Fig. 5.3).

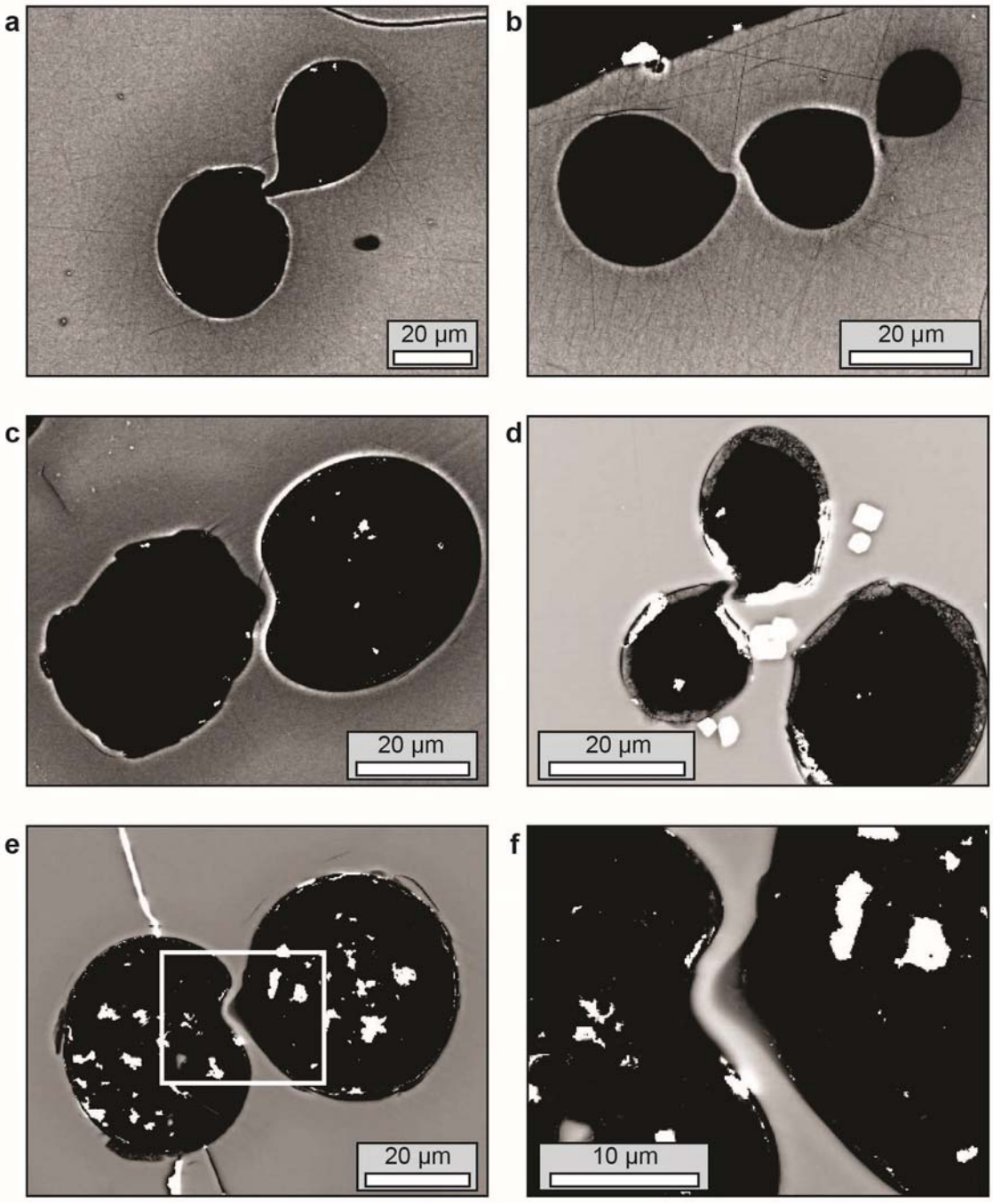

Fig. 5.1 Buckled melt films between adjacent vesicles

BSEM images of adjacent vesicles in ABG rhyolite samples. Melt films are sinuous rather than planar. Images **a** – **c** show H_2O_t-rich resorption halos surrounding vesicles (dark glass). Similar reosorption halos exists around the vesicles in **d** – **f** but brightness and contrast settings are optimized instead to show detail of the buckled films. The white area highlighted in **e** is shown in **f**, revealing some of the 3D morphology of the films. Bright white patches in glass correspond to Fe-Ti oxides; in cracks and vesicle interiors correspond to remnants of gold coat that was not removed by polishing. a, b, d show ABG1; c, e show ABG2. For further images see Appendix A4.

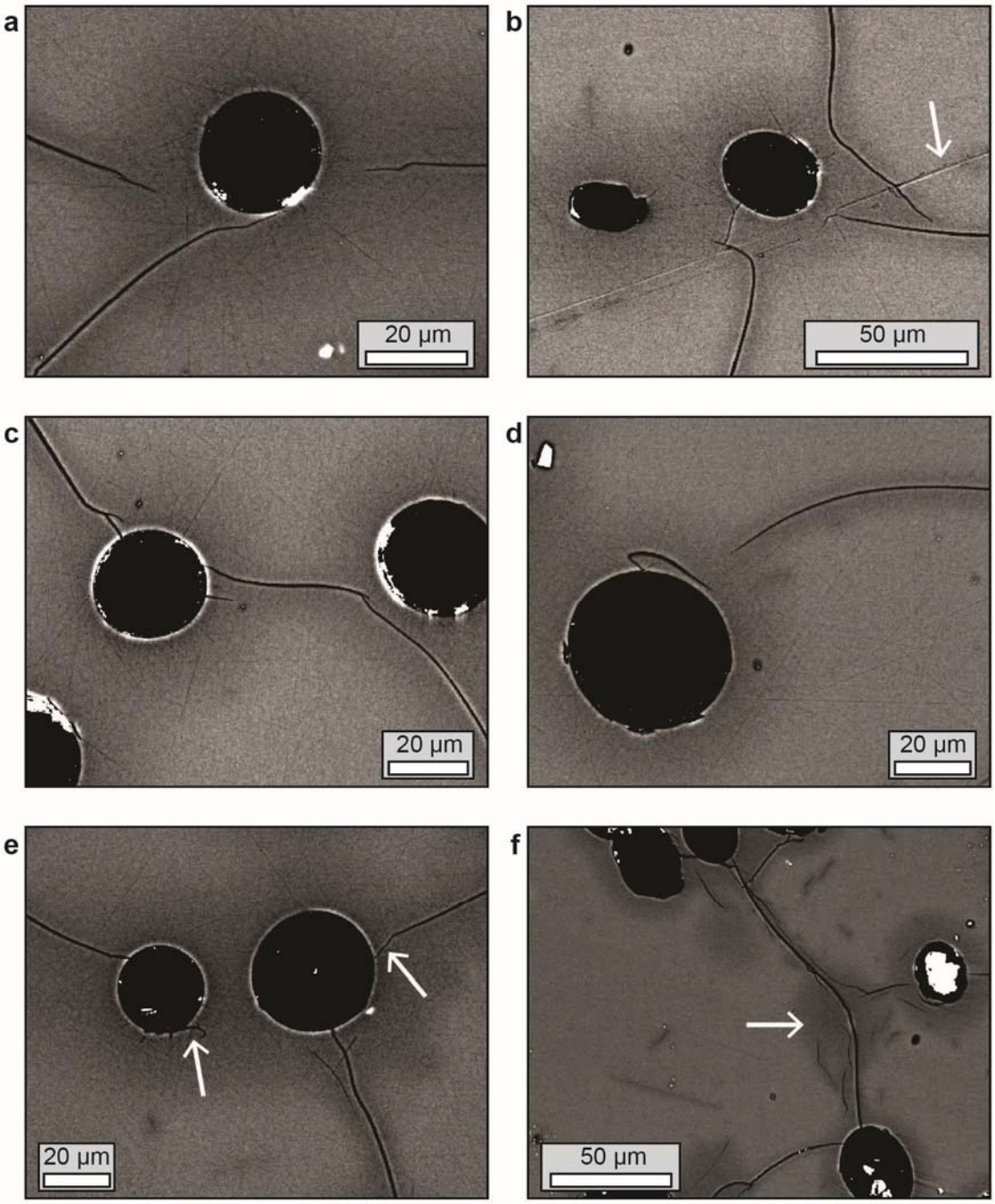

Fig. 5.2 Cracks in the far field and at vesicle walls

Many cracks seen in the far field terminate or change direction as they enter the resorption halo (dark glass) around vesicles or change direction so that they become aligned parallel to the vesicle wall (**a** – **c**). Short radial cracks are seen at vesicle walls and may join up with far field cracks (**c**, **e**), while some change orientation with distance from the wall and change from radial to parallel to the wall (**d**). Far field cracks may curve in areas where there are no vesicles however greyscale variations reveal the presence of an associated 'ghost bubble' (**f**, white arrow). Far field cracks have H_2O_t-rich margins of variable width. White arrow in **b** indicates scratch caused during sample prep. A – e show ABG1; f shows ABG2. See Appendix A4 for further images.

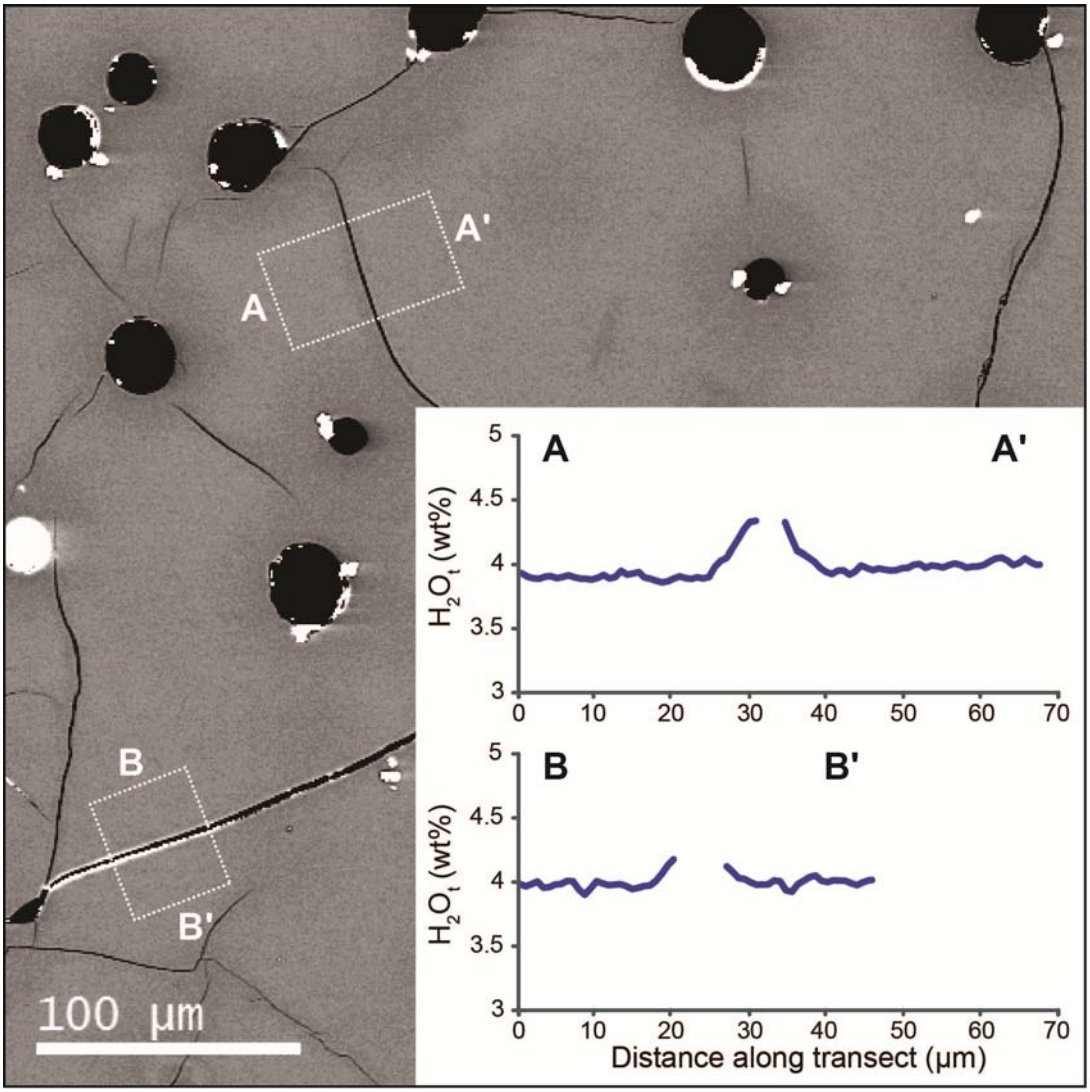

Fig. 5.3 Hydration profiles around far field cracks

Two example profiles taken across far field cracks in ABG1 show increasing H_2O_t at the crack margins. The calculated half-fall distances of these H_2O enrichments are 3 µm for profile A – A' and 1 µm for profile B – B', compared to a calculated half-fall distance of 12 µm for H_2O enrichment in the resorption halos around vesicles in the same sample (see Chapter 4 Section 4.4.3.3.

5.4 Discussion

5.4.1 Temperature of the glass transition

The observed textures are evidence of both ductile behaviour (buckled films) and brittle behaviour (cracks). In order to understand the processes and timing of their formation and their

resulting implications it is necessary to know the temperature of the glass transition, since this determines the temperature, and thus the point in time during quench, at which the transition between the ductile and brittle regimes occurs.

5.4.1.1 Calculating T_g

The temperature of the glass transition, T_g, is dependent on both the H_2O_t content of the melt and the cooling rate at which it is quenched (see Chapter 2 Section 2.4.2). Neither of these parameters is expected to remain constant during the quench of these samples. Chapter 4 has shown that H_2O diffuses back into the melt as bubbles resorb during cooling, which will cause a local increase in H_2O_t in the resorption halo, while the cooling rate is expected to decrease during quench, being initially rapid before slowing as the final (ambient) temperature is approached. The lack of H_2O solubility data for intermediate and low temperatures, and the absence of direct measurements of temperature during quench, severely limits the accuracy with which these variables can be constrained. However the following method provides a way to estimate T_g for these samples, and to consider how T_g may be affected by different quench conditions.

The viscosity of hydrous rhyolite melt is linked to T_g via the empirical relationship:

$$\eta \; at \; T_g = \frac{10^{11.45}}{q} \qquad \text{Equation 5.1}$$

Where η is viscosity in Pa s, q is the quench rate at T_g in K/s, and the H_2O_t content of the melt is in the range 6 ppm to 8 wt% H_2O_t (Youxue Zhang et al. 2003).

In order to find q, the cooling rate at T_g, the change in cooling rate during quench must be modelled. Since the samples are cooled using a water-cooled rapid-quench attachment, the temperature-time history during quench is calculated using the model of Xu & Zhang (2002) for sample quench in water:

$$T = T_{ff} + \left(T_0 - T_{ff}\right) \operatorname{erf}\left(\frac{x}{\sqrt{4\,\kappa\,t}}\right) \qquad \text{Equation 5.2}$$

Where T_{ff} is the temperature of the ambient fluid (here 21 °C), T_0 is the initial temperature of the sample (i.e. T_{exp}), x is the distance from the cooling surface (here the centre of the sample capsule, 1.5 mm), κ is the heat diffusivity of the sample (0.6 mm^2/s, Romine et al. 2012), and t is time.

The quench rate at a given position x is then:

$$q = -\frac{dT}{dt}\Big|_{T=T_{ae}} = \frac{(T_0 - T_{ff})}{\sqrt{4\,\pi\,\kappa\,t_{ae}^3}} \exp\left(-\frac{x^2}{4\,\kappa\,t_{ae}}\right) \qquad \text{Equation 5.3}$$

Where t_{ae} is the time when $T = T_{ae}$ at position x. Here t_{ae} and T_{ae} are the time and temperature of 'apparent equilibrium'. This refers to the equilibrium speciation in the interconversion reaction of H_2O_m and OH and T_{ae} is generally considered equal to T_g (see Chapters 2 and 6 for further discussion).

Using Eq. 5.2 and Eq. 5.3 respectively, the temperature of the sample (T_{sample}) and cooling rate are calculated as a function of time (Fig. 5.4 a, b). At every timestep, Eq. 5.1 is used to calculate what the apparent melt viscosity at T_g would be if the cooling rate at the timestep was the cooling rate at T_g. A nominal temperature (T_n) that would result in this apparent melt viscosity is then calculated using the H_2O_t-dependent viscosity model of Hui & Zhang (2007) (see Chapter 2 Section 2.3.3). At the glass transition, $T_{sample} = T_n = T_g$. This temperature is identified graphically by plotting T_{sample} and T_n for each timestep, with the intersection of the two curves giving the value of T_g, and also the approximate time during quench in which T_g is reached (Fig. 5.4 c, d).

The model of Xu & Zhang (2002) assumes that the sample surface is cooled to the final temperature (T_{ff}) instantaneously and does not account for heat transfer in the quench medium. The calculated quench rates are therefore the maximum possible for the centre of the sample, which would tend to overestimate T_g. When errors from Eq. 5.1 and the viscosity model of Hui & Zhang (2007) are accounted for, the resulting T_g values have an error of ±40° C, and the effect of an overestimated quench rate is likely to fall within this range.

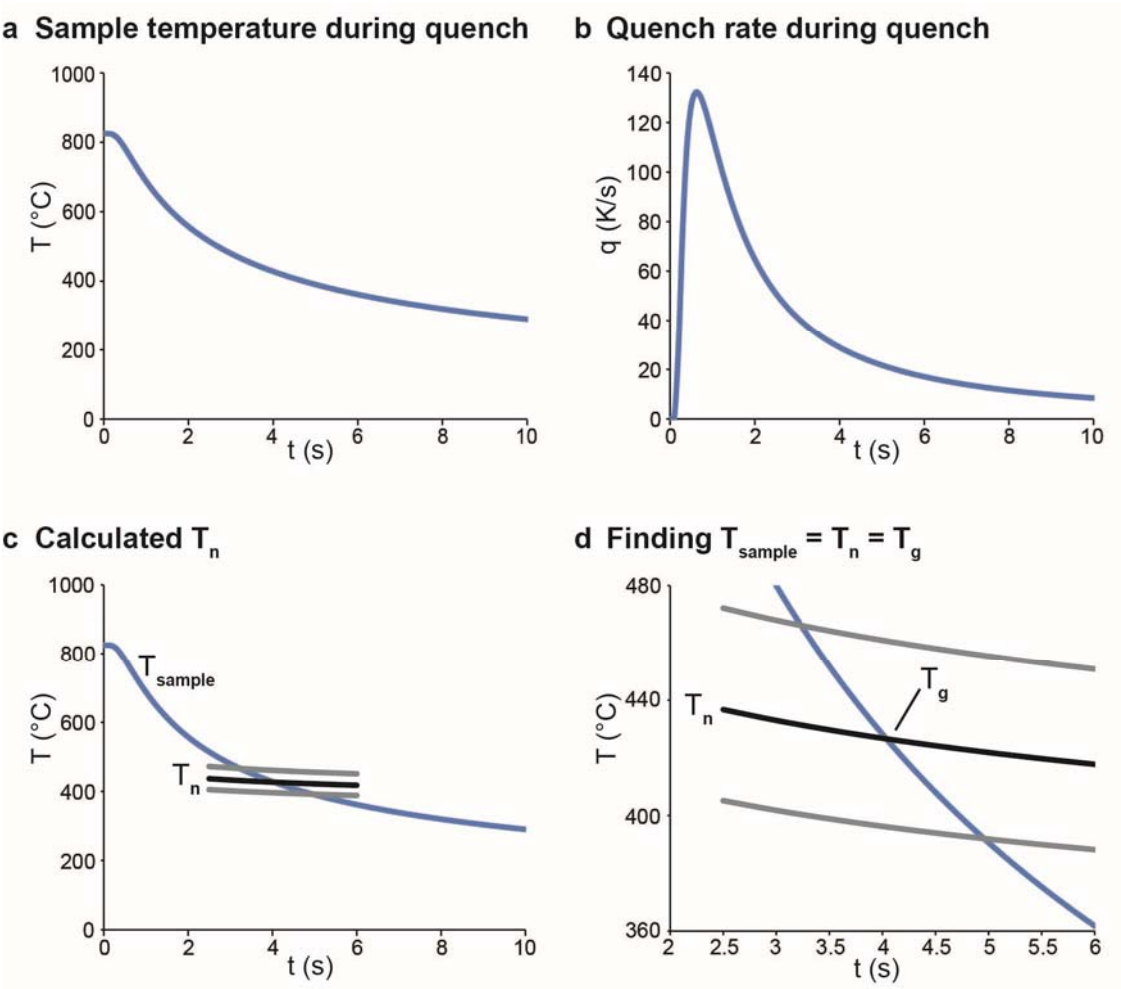

Fig. 5.4 Estimation of timing and temperature of the glass transition

a Temperature-time history of sample (T_{sample}) for first 10 seconds of quench when diffusion profiles are formed (see Chapter 4 Section 4.4.3). **b** Variation in quench rate, *q*, with time. Initial increase results from the time taken for the centre of the sample to begin to cool. **c** For every timestep, the quench rate at that timestep is substituted into Eq. 5.1 to calculate at what temperature the glass transition would occur for this quench rate. The resulting 'nominal temperature' T_n is shown as a black line, with errors propagated from Eq. 1 and the viscosity model of Hui & Zhang (2007) shown in grey. **d** A closer view of the intersection of T_n and T_{sample} shown in **c**. T_g is the temperature at which T_n and T_{sample} intersect, and errors on T_g come from where the errors on T_n intersect T_{sample}.

Applying this methodology to the rapidly quenched, rhyolitic ABG series, a sample containing 4 wt% H_2O_t has a T_g of ~460° C which is reached in ~4 s, whereas a sample containing 5 wt% H_2O_t has a T_g of ~430° C which is reached in ~5 s. While this method has a large error in the absolute value of T_g, the relative variation of T_g with H_2O_t content is more robust, highlighting the effect of H_2O_t content on T_g and the time taken to cross the glass transition during quench.

5.4.2 Bubble film deformation

Above the glass transition, the structural relaxation timescale of the melt is sufficiently rapid that melt can flow. The loss of H_2O vapour from the bubble as H_2O diffuses back into the melt during cooling can therefore be accommodated by a decrease in bubble volume, as melt moves in from all sides so that the internal pressure in the bubble remains in equilibrium with the outside (experimental) pressure. Below T_g, bubble (vesicle) volumes become fixed and further diffusion of H_2O back into the glass no longer results in a volume change. Both glass and vesicles will contract due to cooling in the glass state but this effect is negligible, with the volume of a rhyolite glass containing 4.5 wt% H_2O_t at room temperature (21 °C) being 96% of the volume of the same glass at 500 °C (density computed as for FTIR processing, see Chapter 3 Section 3.3.2.4). The calculation of T_g, above, therefore suggests that bubble resorption is possible in the first 4 to 5 seconds of quench, before T_g is reached. In the case of isolated vesicles, there will be no textural evidence that can confirm that the observed vesicle was once bigger. Textural evidence for significant bubble resorption during quench instead comes from the observation of buckled films between neighbouring vesicles.

Where two bubbles impinge on one another, the melt film between them takes a planar form. Modelling of melt films between growing bubbles in silicic melt suggests that, even at experimental/magmatic temperatures, the viscosity of the melt film is too high to drain freely as the bubbles impinge on one another. Consequently, the mass inside the melt film is conserved by stretching and thinning in order to accommodate bubble growth (e.g. Navon & Lyakhovsky 1998).

In the opposite scenario of resorbing bubbles, if the mass of the melt film is conserved it must thicken and/or buckle as the bubbles shrink. A stretched viscous film will tend to buckle, rather than thicken, if the stretching is reversed. Surface tension will act to reduce the curvature of the buckled film, subject to the relaxation timescale of the interface. Thus if the timescale of quench is faster than the timescale over which the shortening melt film can maintain a planar form, the film will deform and result in a buckled film like those observed.

The timescale for relaxation of the film is given by:

$$\lambda = \frac{\eta_0 \, r}{\Gamma}$$ Equation 5.4

Where η_0 is the melt viscosity in Pa s, r is the radius of curvature of the deformed film in m, and Γ is surface tension in N/m (Llewellin et al. 2002). This timescale is determined by the smallest radius of curvature, which will be the tightest curve in the deformed film (Fig. 5.5).

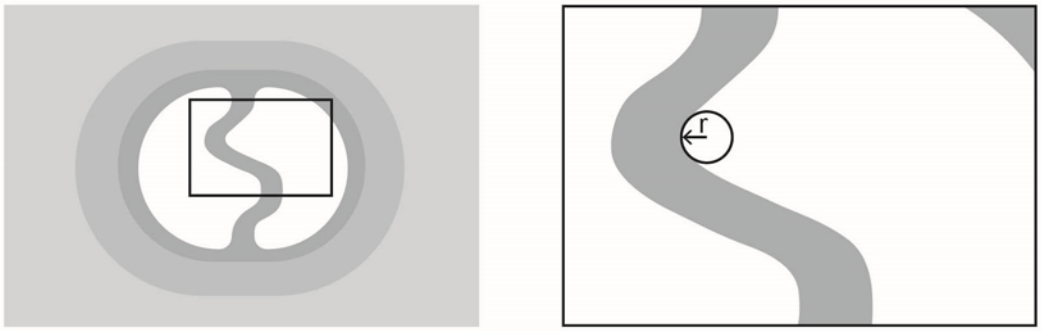

Fig. 5.5 Location of radius of curvature, r
Schematic of two impinging bubbles (white) with surrounding resorption halo, separated by a deformed film. The timescale of melt film relaxation back to a planar film under the influence of surface tension depends on the smallest radius of curvature of the deformed film (r, inset).

According to this relationship, the timescale for melt film relaxation will increase during quench as melt viscosity increases with decreasing temperature (Fig. 5.6 a). For a rhyolite with 4 wt% H_2O_t and a radius of curvature of 5 μm, and assuming a surface tension of 0.1 N/m (Gardner & Ketcham 2011), this timescale varies from 2 seconds at T_{exp} to 15 hours at 500 °C. Increasing the

H_2O_t content to 5 wt% (as is seen to occur near the bubble wall during quench, see Chapter 4) reduces this to 1 s at T_{exp} and 3 hours at 500 °C. It is apparent therefore that the timescale of quench is much faster than the timescale at which the relaxation of melt films between bubbles could maintain planar films during bubble resorption.

An additional consideration is the conditions under which the film would be able to deform in a ductile rather than brittle manner. This is determined by the structural relaxation timescale of the melt (Fig. 5.6 b):

$$\tau_s = \frac{\eta_s}{G^\infty} \qquad \text{Equation 5.5}$$

where τ_s is the structural relaxation timescale, η_s is the shear viscosity and G^∞ is the shear modulus (~10^{10} Pa) (see Chapter 2 Section 2.4.1 for further details). At T_{exp} this timescale is of the order of 10^{-7} s for a rhyolite with 4 wt% H_2O_t, and is still 10^{-2} s by 500 °C, increasing to 10^{-3} s if H_2O increases to 5 wt% as a consequence of resorption. The quench timescale is much longer than the structural relaxation timescale of the cooling melt. Consequently the melt is expected to be in the ductile field throughout the bulk of the quench process.

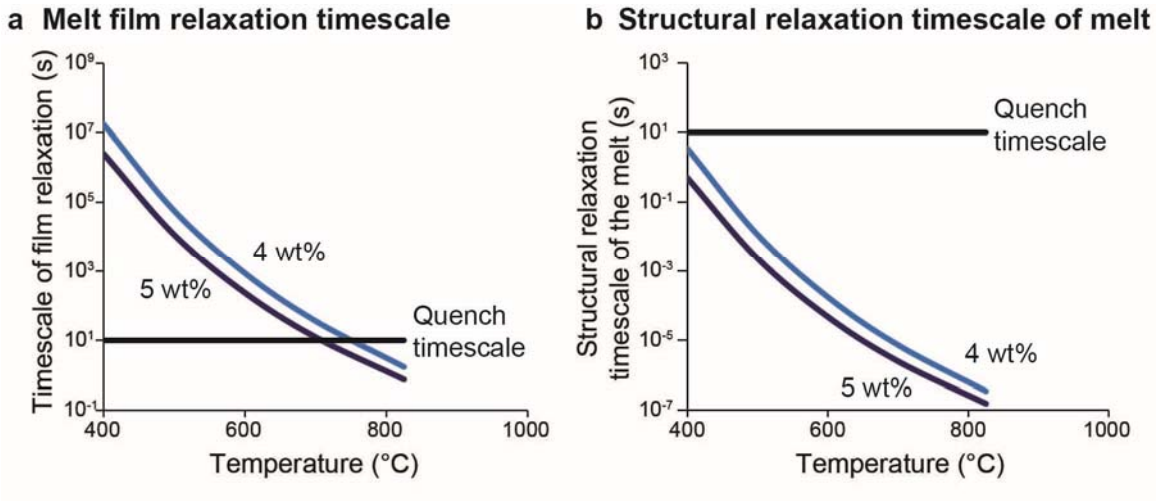

Fig. 5.6 Comparison of melt film relaxation, structural relaxation and quench timescales

a The timescale of melt film relaxation (given by Eq. 5.4) for melt with 4 wt% H_2O_t (light blue) and 5 wt% H_2O_t (dark blue) increases dramatically with decreasing temperature during quench (note logarithmic axis). A maximum quench timescale of 10 seconds is shown, within which time the

melt quenches to glass. The timescale of melt film relaxation is therefore too long to maintain planar melt films during quench resorption. **b** The structural relaxation timescale of the melt (given by Eq. 5.5) for melt with 4 wt% H_2O_t (light blue) and 5 wt% H_2O_t (dark blue) increases with decreasing temperature during quench but does not exceed the quench timescale until the glass transition. Buckled melt films are therefore able to deform in a ductile rather than brittle fashion until the glass transition.

5.4.3 Thermal effects on bubble volumes

In addition to mass loss via H_2O diffusion back into the melt, bubble volumes may also be altered by the increase in fluid density that accompanies cooling. Fig. 5.7 shows the change in fluid density and accompanying change in bubble volume for a bubble cooling from T_{exp} to 450 °C, calculated using the equation of state for H_2O above the critical point (Pitzer & Sterner 1994). In this example, a bubble with a radius of 31 µm at T_{exp} will shrink to a radius of 22 µm by 450 °C as a result of vapour volume changes alone. This volume decrease will therefore combine with the diffusive mass loss of H_2O back into the melt to reduce bubble volumes even further.

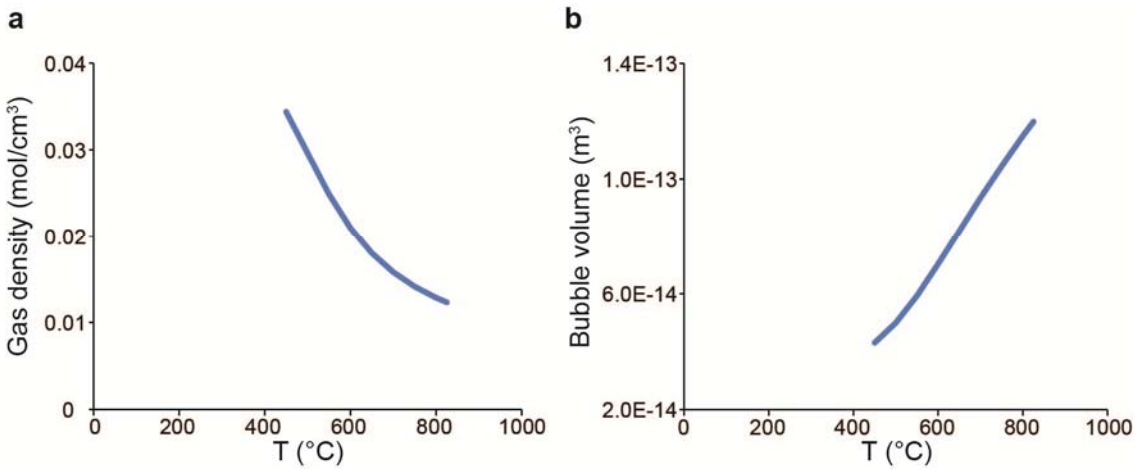

Fig. 5.7 Thermal contraction of bubbles

a H_2O gas density increases with decreasing temperature (Pitzer & Sterner 1994). **b** Decrease in bubble volume due to thermal contraction of H_2O vapour alone. Graph corresponds to a bubble radius of 31 µm at 825 °C, decreasing to 22 µm at 450 °C.

5.4.4 Bubble resorption mechanism

The following model is proposed to explain the observed buckled films. Prior to quench, two neighbouring bubbles impinge upon each other, resulting in a planar melt film between them (Fig. 5.8). As the melt begins to cool, the diffusion of H_2O back into the melt and contraction of the vapour phase leads to a reduction in bubble volume. The original melt film is too long for the new bubble volumes and so has a tendency to buckle. The only elastic force which could restore the film to a planar form comes from the surface tension driven relaxation of the film. However, the increase in the timescale of film relaxation with decreasing temperature (and the continuing reduction of bubble volume) prevents the film from returning to planar before T_g is reached, at which point it is finally quenched to glass in the shape observed. Since T_g is strongly H_2O_t dependent and these films, being bubble walls, will have the highest H_2O_t contents during quench, they will be able to continue to deform even as the rest of the sample solidifies.

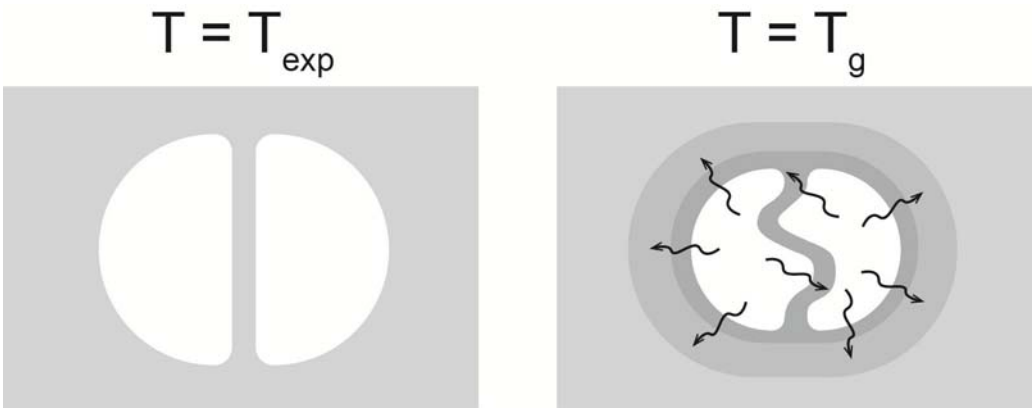

Fig. 5.8 Model of buckled melt films

Prior to quench, neighbouring bubbles impinge on one another and are separated by a planar film of melt. During quench, diffusion of H_2O (black arrows) back into the melt and thermal contraction of H_2O vapour leads to a reduction of bubble volume and formation of a resorption halo of hydrated melt. The timescale for melt film retraction is too slow to maintain a planar film, causing buckling of the original film length. This texture is preserved when the melt cools through the glass transition.

This interpretation of these buckled films is in contrast to that proposed by Castro et al. (2012), whose study of vesicular experimental and natural samples found that experimental samples (including ABG1) showed multiple examples of 'dimpled' bubbles, where the melt film is deformed such that one bubble penetrates another (Fig. 5.9). Multiply-dimpled bubbles were also common and in these cases dimple penetration often occurred in the same direction i.e. one penetrated bubble in turn penetrates another, regardless of bubble size. These dimple features were interpreted to result from melt film stretching and differential pressure gradients resulting from bubble growth, and thus to be preserved evidence of a new mechanism of coalescence. Their absence from the natural samples studied was attributed to the decreasing significance of this coalescence mechanism at lower pressures, as melt viscosity and bubble expansion increase, and to slower quenching rates which prevented dimple preservation as bubbles relaxed back to a spherical shape under surface tension.

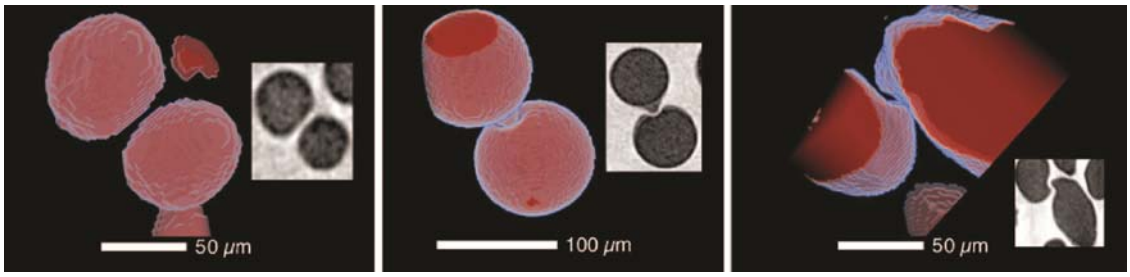

Fig. 5.9 Melt film morphologies seen in experimental samples (Castro et al. 2012)
X-ray computed microtomography (μ-CT) data of typical melt film morphologies in experimentally decompressed vesicular glasses investigated by Castro et al. Films vary from planar and semi-planar films to 'dimples' and buckled films (reproduced from Fig. 3, Castro et al. 2012)

This interpretation was made before the analysis of H_2O_t concentration profiles in the ABG samples (Chapter 4) demonstrated that temperature decrease during quench could lead to bubble resorption. The new interpretation presented in this chapter is consistent with the evidence from H_2O_t profiles. In addition, the new interpretation removes the need to explain how dimples form where large bubbles can penetrate smaller bubbles. Typically, where bubbles of

different sizes impinge on one another, the smaller bubble is expected to penetrate the larger as a result of higher internal pressure in the smaller bubble (e.g. Blower et al. 2001). In the new buckled film model, difference in internal pressure may make the film more likely to warp in a certain direction but is not necessarily a strong control. Similarly, the observed directionality of multiple dimples may reflect the effect of gravity, or the propagation of an initial melt film deformation into neighbouring bubbles in a chain as a result of knock-on pressure effects.

As proposed by Castro et al., the rarity of buckled films in natural samples may reflect quench timescales which are longer than the timescale of relaxation. An additional potential cause suggested by the new model is that H_2O diffusivity during quench may have been lower for the natural samples (e.g. due to lower H_2O_t concentration) and so bubble resorption may not have been of a sufficient magnitude to create buckled films.

5.4.5 Cracks in far field glass

5.4.5.1 Hydration of crack margins

The long curving cracks seen in the far field (Fig. 5.2, 5.3) have margins of H_2O_t-rich glass. SIMS-calibrated BSEM image analyses of these margins in ABG1 show that the half-fall distance of the enrichment is typically ≤ 3 µm, compared to a half-fall distance around vesicles of 12 µm (Chapter 4). The observed hydration lengthscales around cracks depend on the angle at which the cracks intersect the sample surface, and will appear wider than the true hydration width if the angle of intersection differs from 90° (Fig. 5.10). The measured half-fall distances of hydration around cracks should therefore always be considered a maximum value, and differences in hydration lengthscales around cracks may relate to timing of crack formation (e.g. longer hydration widths associated with earlier cracking) but may also simply be the result of different angles of intersection with the sample surface.

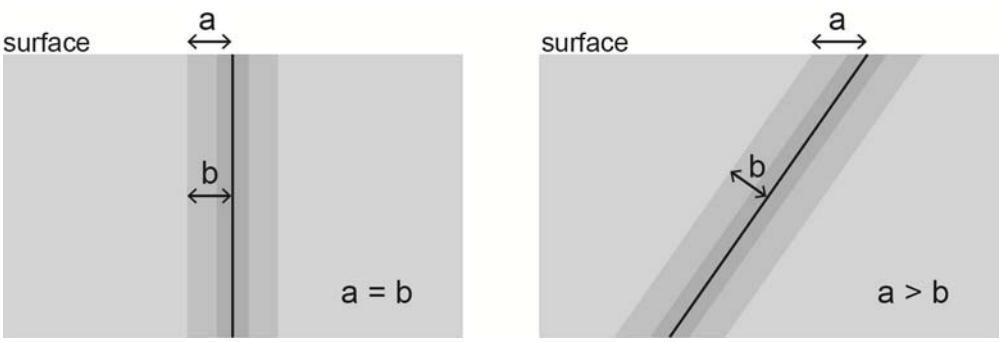

Fig. 5.10 Influence of crack angle on observed hydration lengthscale

The angle at which a crack intersects the surface affects the observed lengthscale of hydration around the crack. If the crack intersects the surface at 90°, the observed lengthscale (a) is equal to the true hydration lengthscale (b). If the crack is inclined then the observed lengthscale is greater than the true lengthscale. Observed hydration lengthscales therefore represent a maximum value.

Hydration along cracks occurs as a result of cracks intersecting a vesicle, or another crack that intersects a vesicle, which provides a pathway for H_2O vapour to move along. Cracks can only form once the sample has cooled to below T_g, and therefore there is less time for H_2O diffusion around cracks than around bubbles (which were present at the beginning of quench). In addition, the temperature dependence of H_2O diffusivity means that by the temperature of the glass transition (~430 – 460 °C) H_2O diffusivity is over an order of magnitude slower than at the beginning of quench (e.g. Chapter 2 Fig. 2.12). Consequently, the observed hydration along cracks in the far field is evidence that they must have formed at intermediate temperatures at or near T_g, when H_2O diffusivity was still sufficiently rapid to form the observed lengthscales in the time available. Most importantly, the short diffusion lengthscales seen around cracks are evidence that the bulk of H_2O_t diffusion that creates the vesicle diffusion profiles described in Chapter 4 occurs at $T > T_g$ and is therefore associated with bubble resorption, as opposed to glass hydration.

5.4.5.2 Shape of far field cracks

The long cracks in the far field are interpreted to form as a result of tensile stress created by thermal contraction of the glass as it cools. Such fractures might be expected to originate at vesicle walls, since cracks often nucleate at point defects such as pore spaces. Instead however the cracks terminate near the edge of the resorption halo, and may exhibit a change in orientation to run parallel to the vesicle walls. Two different mechanisms may account for this. Where cracks terminate at the margin of the resorption halo without being deflected, this may be because the crack encountered an area that was still plastic, and so could not propagate further. Due to the difference in H_2O_t-content, the melt in the far field is expected to cross the glass transition earlier, at a higher temperature, than the melt in the resorption halos (see Section 5.4.1.1.). Such cracks might therefore be expected to have larger half-fall distances as a result of hydration over a longer timescale and starting at a higher temperature, hence diffusivity. However the difference in glass transition temperatures of the far field and resorption halos is only ~30 °C and the difference in the timing of onset is likely to be of the order of ~ 1 second, so any such differences are expected to be slight, and the influence of the angle at which the crack intersects the sample surface on observed hydration lengthscales (Fig. 5.10) precludes this kind of analysis.

In the case of cracks that change orientation on approaching vesicles, it is proposed that the origin of cracking remains the same (tensile cracking of far field glass as a result of thermal stress) but that the cracking, or continuation of cracking, occurs when the resorption halos have crossed the glass transition. Diffusion continues below T_g (as evidenced by the hydration along crack margins) and so there will be hydration of the glass in the resorption halos. Glass hydration is accompanied by an increase in glass volume, and these volume changes are expected to cause compressive stress in the region of the resorption halo. A crack approaching from the far field may therefore begin to reorient itself as the local stress field changes from tension to compression. Similar cracks assumed to form from volume changes associated with glass hydration and crystallisation

are found around spherulites, where exsolution of volatiles from the growing crystal hydrates glass and causes concentric cracks which run parallel to the spherulite boundary (von Aulock et al. 2013).

5.4.6 Cracks at vesicle edges

Some vesicles show signs of cracking at the vesicle wall that is distinct from the far field cracking described above. These cracks extend radially from the vesicle wall and may curve sharply and continue parallel to the vesicle wall, and are contained within the resorption halo (Fig 5.2). No distinct hydration signal is associated with these cracks that can be distinguished from the overall H_2O variation within the resorption halo.

The morphology of these cracks is similar to those found by Romano et al. (1996). In their study of experimental vesicular glasses containing either H_2O, CO_2, or Xe, they found that vesicles in CO_2- or Xe-bearing samples had pristine vesicle walls without cracks, but that H_2O-bearing samples had vesicles that exhibited small 'microcracks' extending radially from the vesicle wall which sometimes continued parallel to the vesicle wall. In this and a related study (Mungall et al. 1996) these cracks were interpreted to result from changes in the internal pressure of the vesicle during quench. In their model, they propose that once the sample passes through the glass transition the volume of the vesicle becomes fixed, and the vapour contained inside must continue to cool isochorically. The internal vapour pressure therefore decreases with continued cooling and reaches a point where it falls out of equilibrium with the H_2O in the surrounding glass. H_2O therefore begins to diffuse into the vesicle from glass within a diffusive boundary layer around the vesicle. As this glass dehydrates its volume decreases, generating tensile stresses tangential to the vesicle wall that, if they exceed the tensile strength of the glass, can trigger radial cracks to propagate from the vesicle wall. These cracks stop when they encounter the isotropic stress field beyond the dehydrated boundary layer, or may be deflected parallel to the vesicle wall if the tangential stress component becomes tensile (Romano et al. 1996; Mungall et al. 1996).

The width of the dehydrated boundary layer, and thus the length of the expected fractures, is expected to change with quench rate. Samples quenched at 200 °C/s are expected to have boundary layer widths on the order of hundreds of nm, while samples quenched at 200 °C/min are expected to have boundary layers of 5 – 10 μm (Romano et al 1996; Mungall et al 1996). The ABG samples considered here were quenched rapidly (on the order of 70 °C/s, Fig. 5.4 b), and therefore if a dehydrated boundary layer exists in these samples the associated concentration gradient would be lost within the analytical 'edge effect' where H_2O_t data cannot be extracted (see Chapter 3). Whether the observed cracks at vesicle margins are created by the mechanism of Romano et al. and Mungall et al. can therefore not be tested here. However, cracks created in this manner would form at some point below the T_g of the melt in the resorption halo, when the vesicle volume became fixed. They are therefore not expected to be associated with any further dehydration or hydration of the adjacent glass since H_2O diffusivity at these temperatures would be too low to hydrate over a significant lengthscale in the time available.

The model of volume change-induced cracks occurring as a result of dehydration raises the question of whether cracks may be induced by the observed hydration in the resorption halos. Long radial cracks have also been observed around spherulites, in addition to the concentric cracks described above, and these are also attributed to the effects of volume change (von Aulock et al. 2013). It should be noted however that spherulite growth is associated with not only volatile exsolution and glass hydration but also growth of the spherulite and replacement of glass by crystal phases with densities different from the glass, which complicates the comparison between the two systems. The deflection of cracks approaching vesicles is evidence that the hydrated glass in the resorption halos is under compression. It is possible that the observed cracks at vesicle walls therefore result from hydration and compression, rather than dehydration and tension. This might explain why they are larger than those predicted by the model of Mungall et al., since the observed hydration lengthscale is larger than would be expected for dehydration of a boundary layer as a result of vapour underpressure.

5.4.7 Model of quench processes

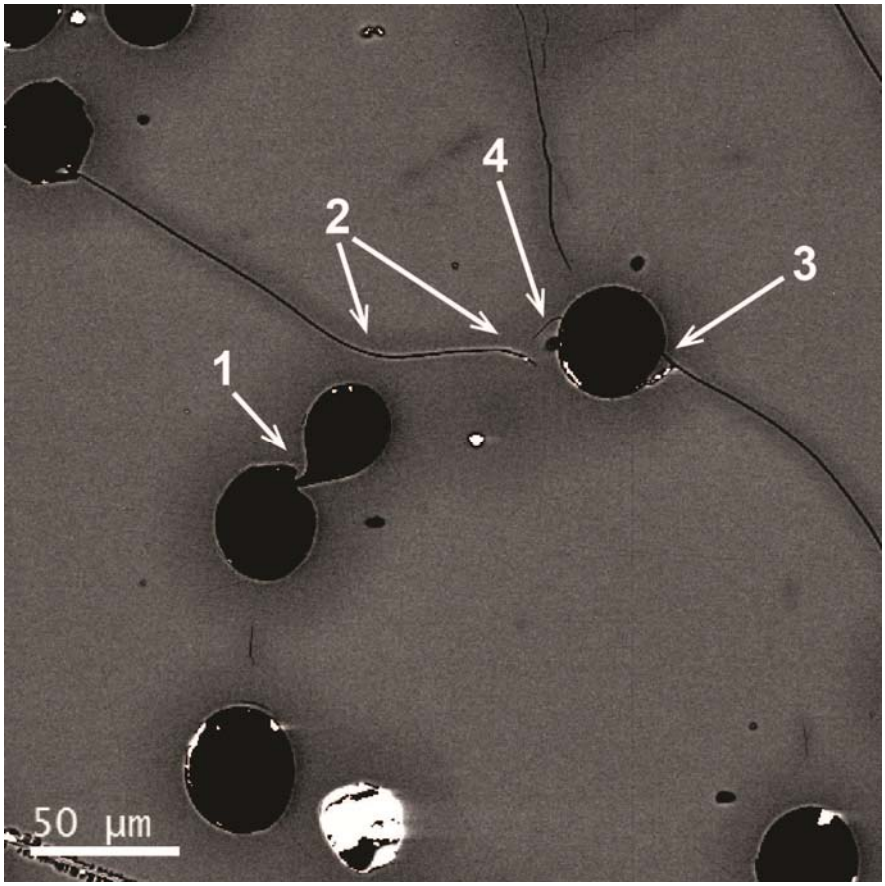

Fig. 5.11 Development of observed quench textures

Observed textures in sample ABG1. Numbers indicate the relative timing of formation during quench. See text for full discussion

The following model is therefore proposed for the textures formed during quench resorption:

1 – At temperatures above the glass transition, increasing H_2O solubility with decreasing temperature leads to bubble resorption and the formation of resorption halos (dark grey in BSEM) and buckled films between neighbouring bubbles.

2 – Around the glass transition temperature, the relatively H_2O_t-poor far field melt crosses the glass transition while the H_2O_t-enriched melt in resorption halos remains plastic. If far field cracks encounter plastic resorption halos they may terminate before the vesicle wall; they may also

reorient themselves as they approach resorption halos as a response to changes in the local stress field caused by glass hydration.

3 – Later cracks may crack the now solidified resorption halo and reach the vesicle wall, or earlier crack terminations may be extended.

4 – Below the glass transition, continued cooling and contraction of H_2O vapour within the now fixed bubble volume causes the vesicle to become underpressured according to the model of Mungall et al. and Romano et al. H_2O in the glass at the vesicle wall begins to diffuse into the vesicle, resulting in tensile stress and the propagation of cracks outwards and then tangential to the vesicle wall.

5.5 Implications

5.5.1 Effect on porosity

The deformed bubble films of the ABG samples are evidence that bubble volumes decreased during quench. The limited lengthscale of hydration observed along crack margins compared to around vesicles suggests that the majority of diffusion responsible for the H_2O_t concentration profiles described in Chapter 4 took place above T_g, when bubbles were able to resorb. It is therefore possible to make a first order estimate of how much H_2O was resorbed during quench, and how sample porosity would be affected as a result, with and without the additional effect of thermal contraction of H_2O vapour.

ABG1 was from an equilibrium experiment and so is expected to have had a uniform H_2O_t concentration in the melt prior to quench, equal to the equilibrium H_2O solubility (H_2O_{eq}) for the experimental pressure and temperature conditions. Consequently, any excess H_2O in the resorption halo surrounding a vesicle represents H_2O that was resorbed into the melt from that bubble during quench. By quantifying this excess H_2O, and calculating the volume it would have

occupied at the experimental pressure and temperature conditions, it is possible to calculate the original volume of the bubble prior to quench, under the assumption that the resorption is exactly compensated by a loss of bubble volume.

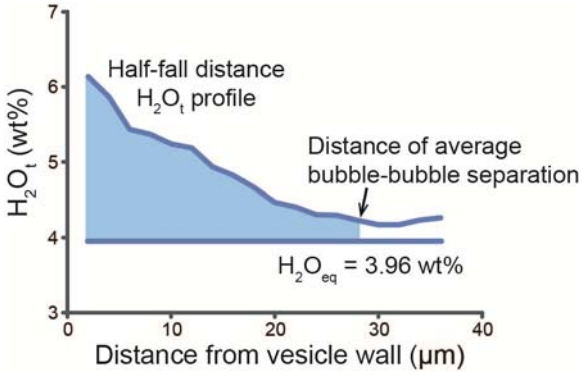

Fig. 5.12 Calculation of resorbed H_2O for sample ABG1

The light blue area underneath the half-fall distance H_2O_t profile and above the expected H_2O_t content (H_2O_{eq}) corresponds to H_2O_t that was resorbed from the vesicle during quench. The integration calculation is extended to the distance of average bubble-bubble separation in the samples.

This calculation utilises the H_2O_t profile of the vesicle from which the half-fall distance was calculated in Chapter 4 (Section 4.4.3.3), i.e. the vesicle sectioned closest to the equator and therefore with the steepest H_2O_t profile. The resorption halo is conceptualised as a series of concentric melt shells with widths of 2 µm, beginning at the vesicle wall and extending to the edge of the shell of melt associated with a typical vesicle. The distance s to the edge of the shell is calculated according to Hao & Riman (2006):

$$s = r\left(\frac{1}{\sqrt[3]{\varphi}} - 1\right) \qquad \text{Equation 5.6}$$

where r is the mean vesicle radius and φ is the gas volume fraction (with r and φ taken from Burgisser & Gardner (2005)).

The mean H_2O_t concentration in each melt shell and the density data of Silver et al. (1990) are used to calculate the melt density of each shell as a function of its H_2O_t concentration. The volume and density of the shell are used to calculate the mass of the melt in each shell. From this the mass of H_2O_t in each shell can be calculated (since SIMS H_2O_t data are in wt%), hence the number of moles of H_2O in each shell. Subtracting the number of moles of H_2O that would be present if the melt shells had a uniform concentration of H_2O_{eq} yields the number of moles of H_2O that resorbed from the bubble during quench.

Since H_2O is above its critical point at the pressure and temperature conditions of the experiment the equation of state of Pitzer & Sterner (1994) is used to calculate the density of H_2O at T_{exp}, from which is calculated the number of moles contained within the observed volume of the vesicle after quench. Combining this with the amount of moles of 'excess' H_2O in the resorption halo thus reveals what volume the original bubble had prior to quench resorption.

Undertaking this calculation for ABG1 suggests that 40% by mass of the H_2O that was in the bubble at the end of the experimental run was resorbed into the melt during the subsequent quench. If it is assumed that this resorption is exactly compensated by a corresponding decrease in bubble volume, then the observed bubble volume is only 60% of the pre-quench volume.

From the change in bubble volume, the original sample porosity can be calculated from the observed porosity. Sample porosity and bubble volume are related according to:

$$\varphi_{obs} = \frac{Vb_{obs}}{Vb_{obs} + V_{melt}} \qquad \text{Equation 5.7}$$

where φ is porosity, Vb is the volume of the bubble, V_{melt} is the volume of the melt, and the subscript 'obs' refers to observed values. The same equation applies to the porosity of the original, pre-quench bubble, denoted by the subscript 'orig'. Rearranging Eq. 5.7 to give the unknown, V_{melt}, in terms of the known values of observed porosity and bubble volume, this is substituted into the equation for the original porosity:

$$\varphi_{orig} = \frac{Vb_{orig}}{Vb_{orig} + \left(\frac{Vb_{obs}}{\varphi_{obs}} - Vb_{obs}\right)}$$ Equation 5.8

Substituting values for sample ABG1, the original porosity is calculated to be 9%. The observed porosity of 5.6% is therefore only ~62% of the original value.

This calculation is likely to slightly overestimate the amount of bubble resorption since it assumes all excess H_2O in the melts shells was derived from the bubble while it was still able to resorb, whereas the evidence of hydrated crack margins suggests at least some diffusion happened below T_g. Similarly it is possible that as T_g is approached, the increasing structural relaxation timescale of the melt may make it difficult for the reduction in bubble volume to keep pace with the loss of H_2O vapour. This calculation however does not account for the additional change in bubble volume that accompanies thermal contraction of the H_2O vapour. In the above calculation, if it is assumed that the volume of the observed vesicle corresponds to the number of moles of H_2O present at a temperature of 500 °C, rather than T_{exp} (825 °C) as previously assumed, then there is a greater mass of H_2O in the observed bubble volume and therefore the calculated original bubble volume is also larger. In this case the observed bubble volume is only 32.3% of the original volume, and the observed porosity (5.6%) is only 36.3% of the original porosity (15.4%). Fig. 5.13 shows the change in observed bubble diameter that would be expected for bubble resorption through H_2O mass loss alone, and by the combined effects of H_2O mass loss and thermal contraction of H_2O vapour.

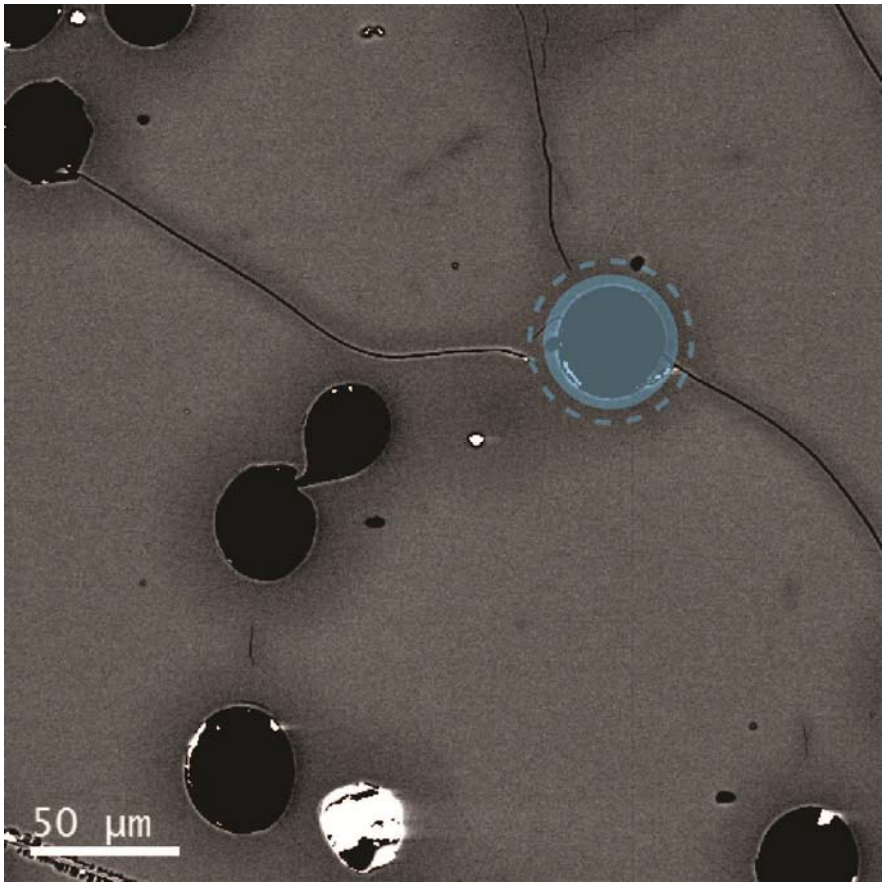

Fig. 5.13 Effect of quench resorption on observed vesicle diameter

The calculated reduction in bubble volume is applied to an observed vesicle in ABG1. The inner circle corresponds to the size of the original bubble prior to quench if only H_2O mass loss through quench resorption is considered; the dashed outer circle corresponds to the size of the original bubble if both H_2O mass loss and thermal contraction of H_2O vapour are accounted for.

5.5.2 Consequences of porosity reduction

5.5.2.1 Experimental samples

The magnitude of bubble resorption that can occur even with a rapid experimental quench apparatus has major implications for experimental studies of vesicular glasses. It has already been shown that studies of bubble textures such as buckled films (e.g. Castro et al. 2012) must also account for the effect of decreasing bubble volumes from bubble resorption and thermal contraction (see Section 5.4.4). The effect of bubble resorption on sample porosities can also have profound implications for other interpretations of experimental samples. The ABG samples

discussed here are from an experimental suite that was used to investigate how sample porosity changes with different decompression rates, in order to study how magma ascent rate affects magma degassing (Burgisser & Gardner 2005). In this and similar studies, sample porosity is used as an indicator of the degree to which bubble populations are in equilibrium with the melt (e.g. Gardner et al. 1999; Mangan & Sisson 2000; Gardner 2007; Larsen 2008). If the effect of quench resorption on sample porosities is not accounted for, measured sample porosities may be considerably lower than the equilibrium value. Consequences of this error on bubble volumes and sample porosities could include misattribution of the decompression rate at which bubble growth is affected by disequilibrium degassing, with quench resorption suggesting that disequilibrium degassing occurs at slower decompression rates than in reality.

The effect of bubble resorption on overall sample porosity is smaller for samples with higher pre-quench porosity (Fig 5.14). For the same mass fraction of H_2O lost from bubbles during quench, the reduction in porosity is proportionally highest at low original porosity (Fig 5.14). The impact of reduced observed porosities in experimental studies will therefore be greatest at high pressures where porosity is low, and will decrease with decreasing pressure and increasing sample porosities. Burgisser & Gardner (2005) found that for the same decompression rate, sample porosities are lower than expected equilibrium values at high pressures but return to equilibrium values at lower pressures. This was concluded to be a result of a transition from a slow to a fast bubble growth regime, but may instead be at least partly explained by the effect of bubble resorption on sample porosities.

Any studies using similar experimental samples (i.e. vesicular melts with high H_2O_t contents) are likely to have been affected by quench resorption, and their results may require reinterpretation. The SIMS-calibrated BSEM methodology used here is an effective way of doing so. Samples can be checked using BSEM to look for H_2O concentration gradients resulting from quench resorption. If these are found, then SIMS can be used to obtain a quantitative measurement of how much H_2O

has been resorbed thereby enabling a recalculation of the original porosity. Additionally, the potential impact on observed bubble volumes and porosities of thermal contraction of H_2O vapour must also be considered, by using the equation of state for H_2O (e.g. Pitzer & Sterner 1994).

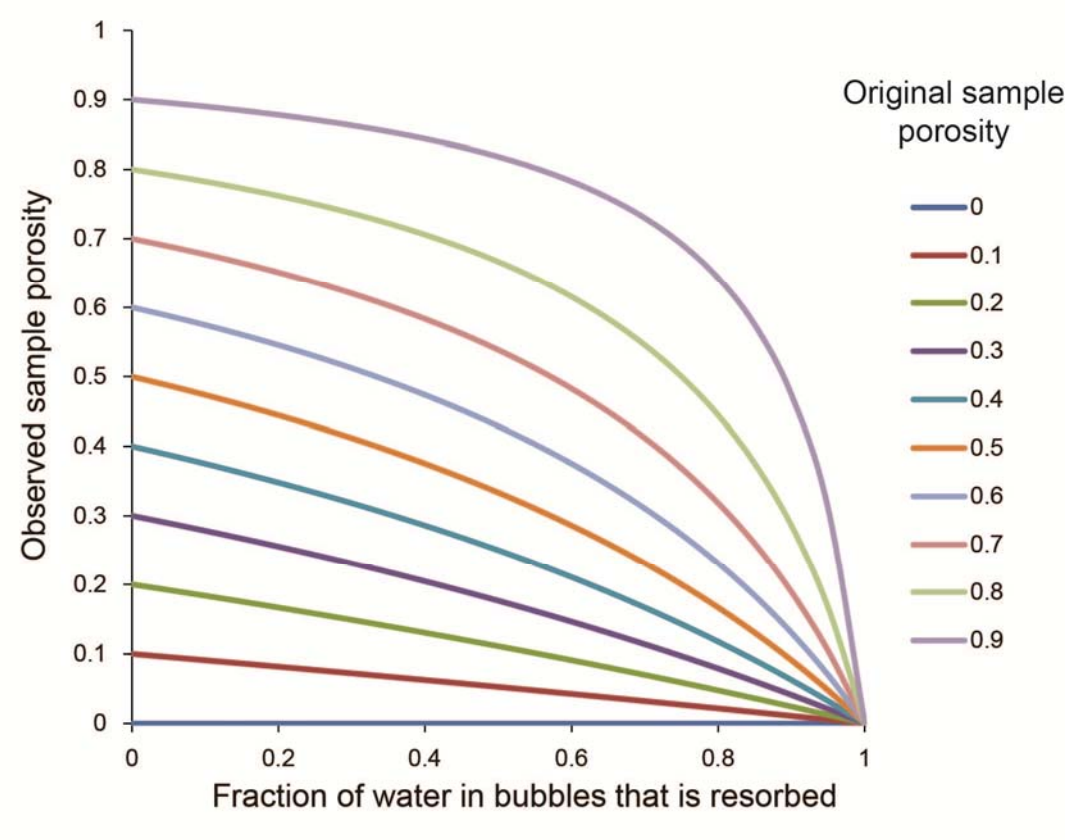

Fig. 5.14 Effect of bubble resorption on samples of differing original porosities

The effect of bubble resorption on observed sample porosity is smaller for samples with higher porosity. For the same mass fraction of H_2O resorbed from bubble populations the proportional effect on the observed porosity is greatest for low original porosities.

5.5.2.2 Natural samples

Studies of naturally-erupted samples use bubble sizes and sample porosities to make inferences about eruption processes (e.g. Moitra et al. 2013; Shea et al. 2010); these samples may be affected by bubble shrinkage in the same way as studies of experimental samples. The degree to which bubble resorption will occur during quench depends on factors controlling H_2O diffusivity

(primarily temperature and H_2O_t concentration) and the temperature-time history of quench (i.e. how long is spent above T_g, when bubbles can resorb). These factors can vary widely for different eruption styles and settings.

The decreasing impact of bubble resorption with increasing sample porosity may mean that subaerially erupted samples, such as pumice, will be less affected than low porosity samples created experimentally at high pressure. Additionally, high porosity samples erupted subaerially will tend to exist in extensively degassed melt with low H_2O_t concentrations. H_2O diffusivity will therefore be lower than for high pressure (hence high H_2O content) experimental samples, and the associated bubble resorption profiles will be shorter. The additional factor of higher T_g (since T_g is dependent on H_2O_t concentration) may also, depending on the overall quench timescale, reduce the time available for bubble resorption above the glass transition. These limitations may explain why buckled films like those described in Section 5.4.2 are not commonly seen in such samples (e.g. Castro et al. 2012), although it might be hard to distinguish such features where vesicles are distorted by crowding from neighbouring vesicle and additional deformation during flow.

Quench resorption is therefore likely to be more significant in natural samples formed under conditions of high H_2O_t concentrations and/or slow quench timescales. High H_2O_t concentrations will be encountered where magma is erupted under the confining pressure of an overlying body of ice or water, or for samples that quench at high pressure such as in conduit margins. Cooling rates of erupted samples can span many orders of magnitude (e.g. Zhang & Xu 2007) with cooling as low as 0.003 K/min recorded in the base of rheomorphic flows (Gottsmann & Dingwell 2001). Where cooling rates are this low, even low H_2O_t melt may spend significant time above T_g and experience bubble resorption. For slow quench timescales, bubble resorption may be sufficient to lead to complete resorption of bubbles and the production of vesicle-free glass. This loss of melt porosity and associated increase in melt H_2O_t concentration and decrease in T_g (e.g. Chapter 4)

may therefore make quench resorption a significant factor in the formation of obsidian and rheomorphic flows.

5.5.3 Implications of quench resorption cracks

The far field cracks described in this chapter provide information on the magnitude of the H_2O diffusion that occurs below T_g as hydration of glass. Although the observed hydration lengthscales are affected by the angle at which the cracks intersect the surface, the comparison of hydration lengthscales around cracks and around vesicles is a method for assessing the magnitude of diffusion above the glass transition. Similarly the deviation of these cracks as they enter the resorption halo may be indicative of bubble resorption and glass hydration, and where they are preserved they may indicate that vesicles were affected by quench resorption.

The smaller cracks that appear at vesicle margins may be produced according to the model of Mungall et al.1996 and Romano et al. 1996, and will therefore be associated with the dehydration of glass at the vesicle wall. Although the cracks are small and no dehydration signal is observed in the samples presented here, it may be more significant in samples that experience slower quench timescales. In this case, dehydration of vesicle walls at temperatures below T_g would result in further modification of the H_2O_t concentration profiles around bubbles, which would add complexity to observed H_2O_t profiles and their implications for understanding bubble growth, resorption, and quench histories.

5.6 Conclusions

The evidence presented in this chapter has demonstrated that the H_2O_t profiles formed during quench, presented in Chapter 4, are associated with reductions in bubble volumes and sample porosities. This conclusion is reached on the basis of observations of buckled films between vesicles and limited lengthscales of hydration along crack margins, which indicate that the bulk of diffusion that formed the observed profiles occurs at temperatures above the glass transition.

This bubble resorption is also likely to be accompanied by thermal contraction of the H_2O vapour phase, resulting in an additional reduction of bubble volumes.

The orientation of far field cracks and their terminations provide evidence that bubble resorption locally depresses the T_g in resorption halos, enabling extended timescales for bubble resorption. Smaller cracks at vesicle walls may form as a result of dehydration of proximal glass at temperatures below the glass transition, as proposed in the model of Mungall et al. (1996) and Romano et al. (1996). This effect may have implications for further modification of H_2O_t concentration profiles near the bubble wall for samples with slower quench than the experimental samples considered here.

The impact of bubble resorption on observed bubble volumes and sample porosities will vary according to the H_2O_t concentration, quench timescale and original porosity of the sample, and is likely to be greatest for samples that are quenched slowly or at high pressure. Possible alteration of bubble volumes and porosities must be considered when interpreting both experimental and natural samples, and future experimental studies could be designed so as to limit these impacts. For both experimental and natural samples, the impact of quench resorption can be explored using BSEM and SIMS-calibrated BSEM analysis.

Chapter 6: Insights from H_2O speciation

6.1 Introduction

The data presented in Chapters 4 and 5 demonstrate that the vesicular experimental samples studied began to resorb H_2O during the quench to glass, as a result of the retrograde temperature-dependence of H_2O solubility in silicate melt. This process occurs rapidly, on the timescale of seconds to minutes, and results in H_2O_t profiles that are characteristic of bubble resorption, regardless of the state of bubble growth prior to the quench process. In this chapter the mechanism of quench resorption is investigated further using H_2O speciation data, leading to the development of a framework in which natural samples may be forensically investigated.

6.2 Samples and Methods

The samples analysed in this chapter are experimentally vesiculated rhyolitic glasses from the MCN series created by Jessica Larsen (Table 6.1, see Chapter 3 Section 3.2.3 for details of composition and production). Five samples were analysed, comprising three solubility experiments (where bubble populations were expected to be in equilibrium with the melt prior to quench) and two decompression experiments (where bubble populations were expected to be growing prior to quench).

Sample		T_{exp} (°C)	P_i (MPa)	P_f (MPa)	dP/dt (MPa)	Duration P_f
Solubility Quench: 30 - 60 s	MCN13 MCN14 MCN28	825 850 825	80 80 100	80 80 100	N/A N/A N/A	72 hr 72 hr 73 hr
Decompression Quench: 3 - 10 s	MCN15 MCN33	825 840	80 120	56 85	4 0.6	1 min 10 min

Table 6.1: Summary of experimental conditions. For further details, see Chapter 3 Section 3.2.3, and Fig. 3.2.

The distribution of dissolved H_2O_t and H_2O_m in these vesicular glasses was analysed using FTIR imaging (for full analytical methodology, see Chapter 3 Section 3.3.2). Quantitative profiles of concentrations of H_2O_t, H_2O_m and OH (by difference) were extracted from these images by processing individual spectra along selected transects. Several such transects around and between vesicles were selected in each sample.

6.3 Results

Each sample is presented in a figure showing the overall sample in reflected and transmitted light and overlaid with the distribution of H_2O_t and H_2O_m as analysed by FTIR imaging. Additional figures show measured H_2O_t, H_2O_m and OH concentrations along representative transects for each sample (Fig.s 6.1 to 6.11).

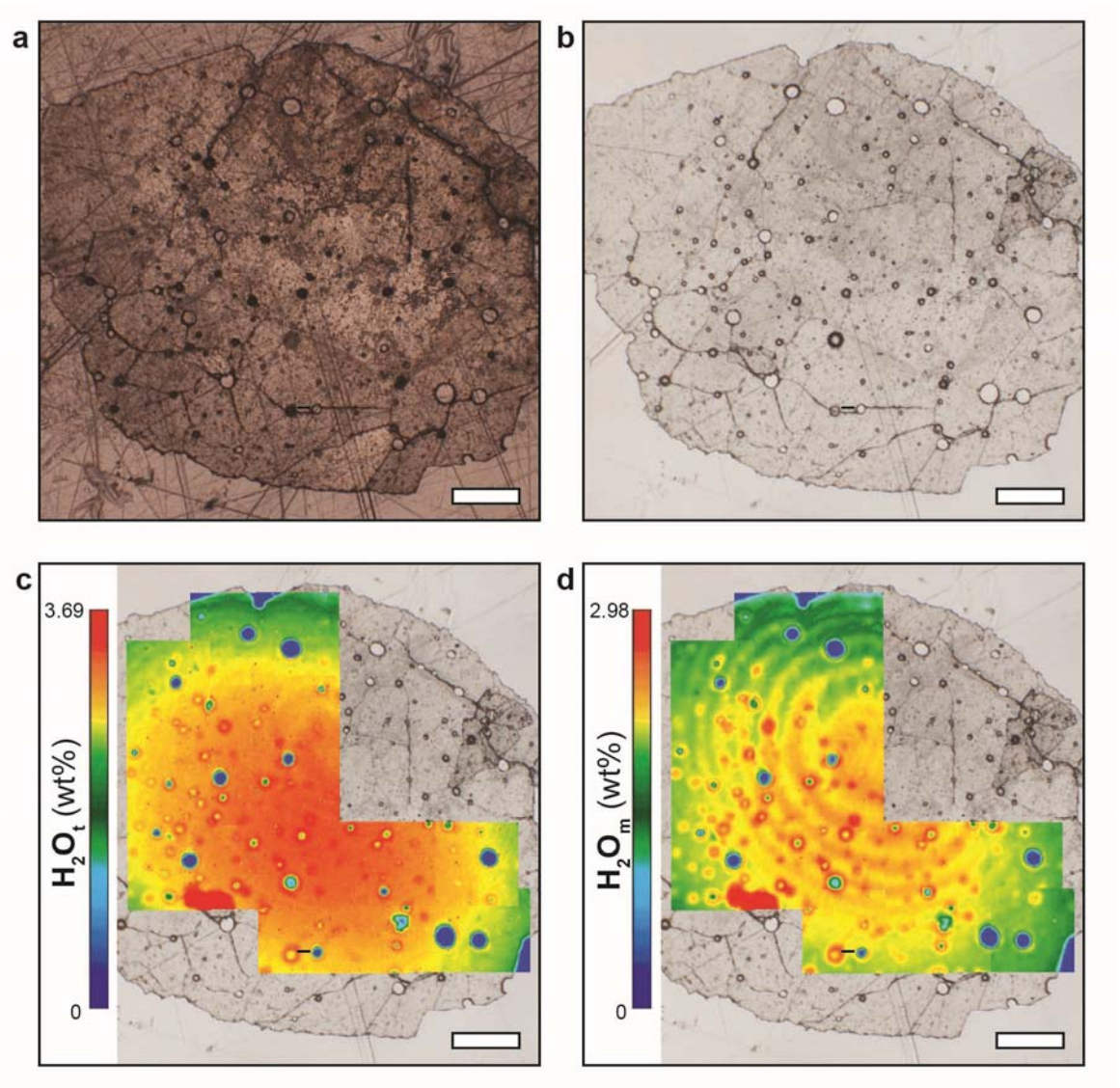

Fig. 6.1 Dissolved H_2O distribution in sample MCN13

Sample as seen in **a** reflected light and **b** transmitted light. FTIR imaging of **c** H_2O_t distribution and **d** H_2O_m distribution. Both H_2O_t and H_2O_m are enriched at vesicle walls. Apparent decrease in H_2O_t and H_2O_m concentration towards edges is caused by sample thinning. Small dark red area in lower left of FTIR images is caused by small fragment of glass adhering to sample surface, resulting in locally increased glass thickness. Figure produced using average thickness of sample (26 µm). Images of H_2O_m distribution are affected by interference fringes resulting in banded appearance. White scalebar is 500 microns. Black line shows location of transect seen in Fig. 6.2.

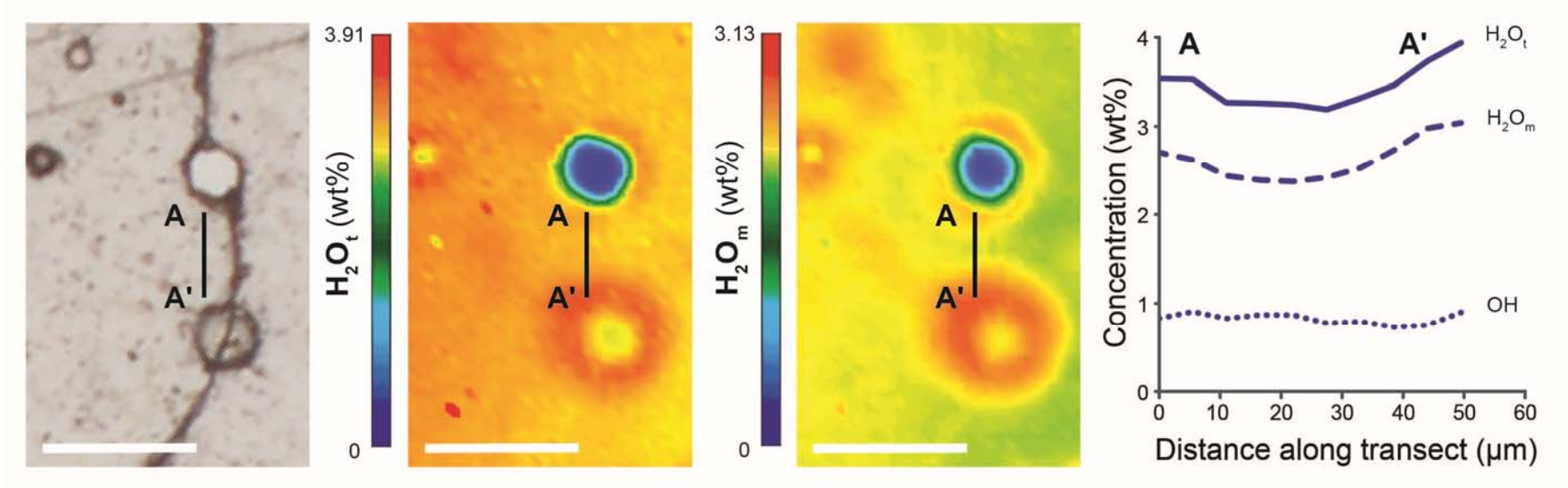

Fig 6.2 H_2O concentration and speciation along transect in sample MCN13

Left to right: Location of transect A – A' seen in transmitted light, H_2O_t FTIR imaging, and H_2O_m FTIR imaging; H_2O_t, H_2O_m and OH concentrations along transect. Transect extends between two vesicles. H_2O_t and H_2O_m concentrations both increase towards vesicle walls, while OH concentration remains constant. Concentrations for image scalebars and graph calculated using average thickness along transect (22 μm). Errors on concentrations are ±15 % relative. White scalebar is 100 μm.

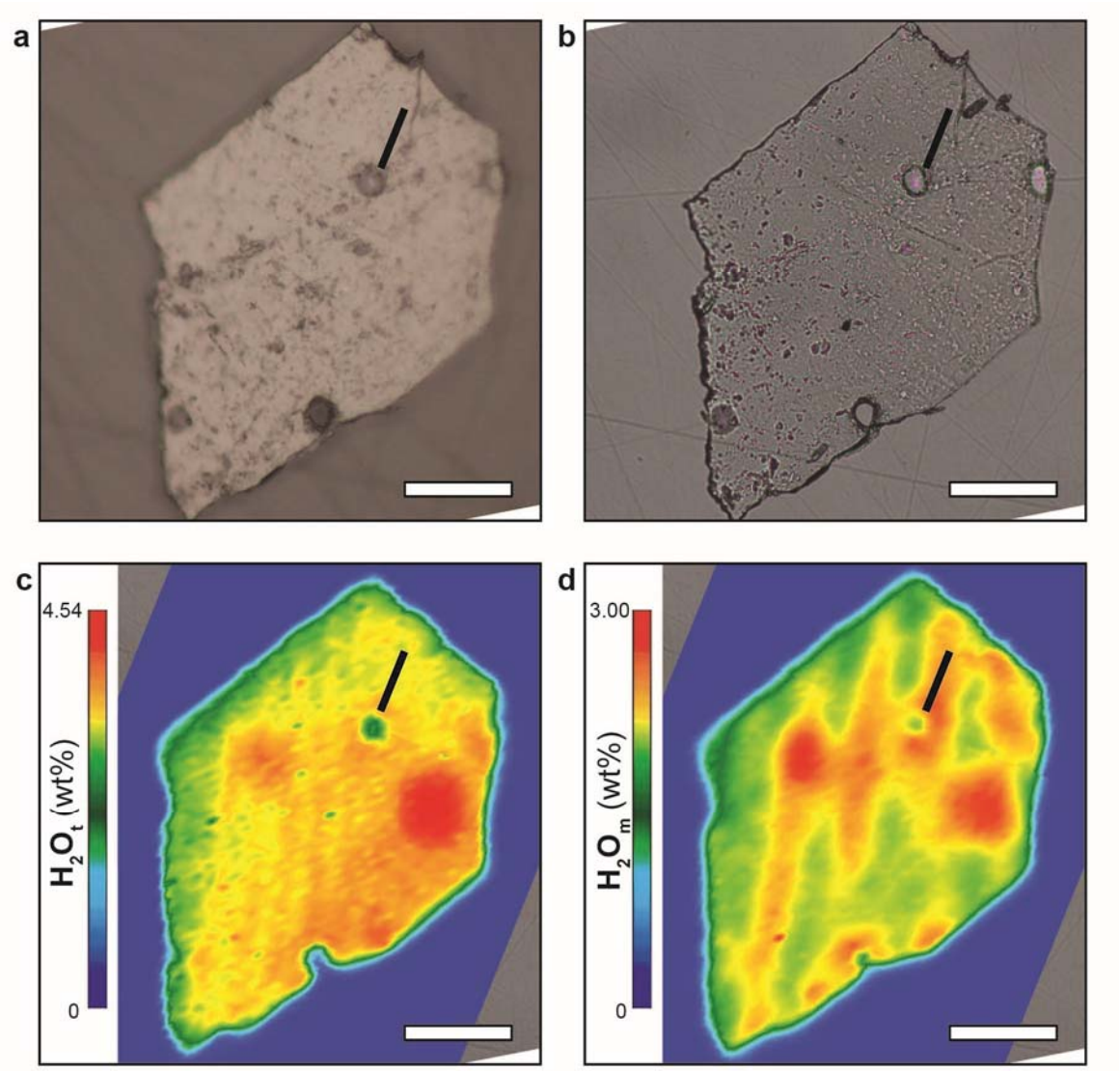

Fig. 6.3 Dissolved H_2O distribution in sample MCN14

Sample as seen in **a** reflected light and **b** transmitted light. FTIR imaging of **c** H_2O_t distribution and **d** H_2O_m distribution. Both H_2O_t and H_2O_m are enriched at vesicle walls. Circular areas of high H_2O_t and H_2O_m concentration correspond to 'ghost' bubbles i.e. the signal from resorption halos corresponding to vesicles either above or below the current sample surface(s). Figure produced using average thickness of sample (10 µm). Images of both H_2O_t and H_2O_m distribution are affected by interference fringes resulting in banded appearance. White scalebar is 100 microns. Black line shows location of transect shown in Fig. 6.4.

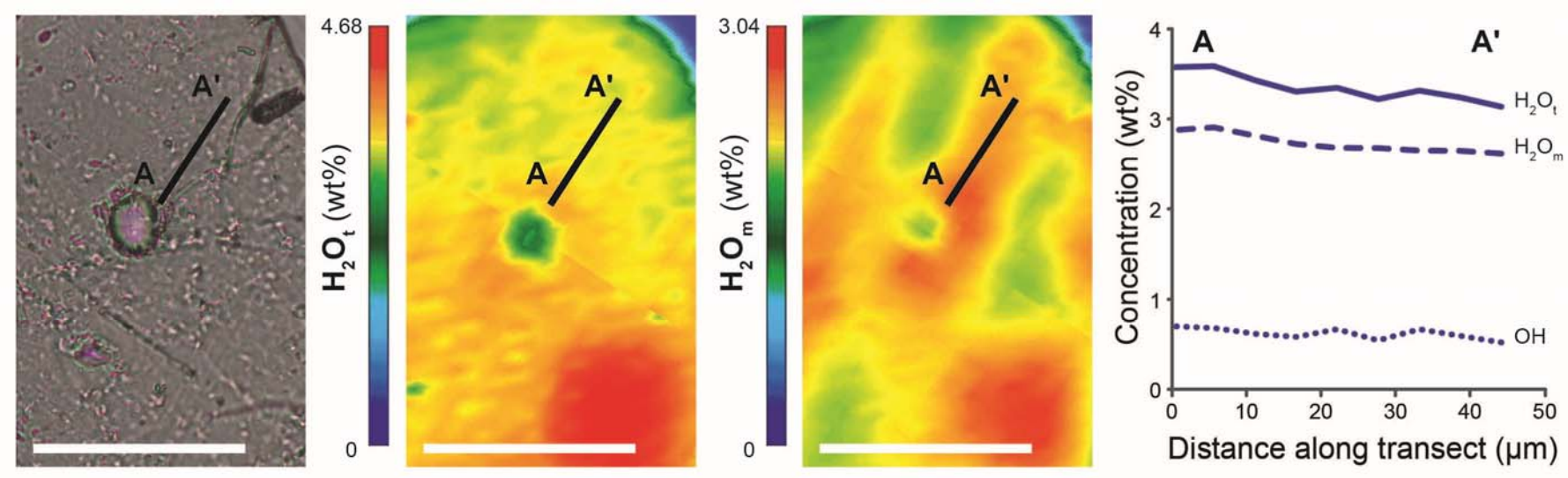

Fig. 6.4 H_2O concentration and speciation along transect in sample MCN14

Left to right: Location of transect A – A' seen in transmitted light, H_2O_t FTIR imaging, and H_2O_m FTIR imaging; H_2O_t, H_2O_m and OH concentrations along transect. Transect extends from vesicle wall out into the far field. H_2O_t and H_2O_m concentrations both increase towards the vesicle wall, while OH concentration remains constant. Concentrations for image scalebars and graph calculated using average thickness along transect (9 µm). Transect is taken parallel to interference fringes visible in H_2O_m image so that concentration profile shapes are representative, although value of H_2O_m (and thus OH) concentration will be affected. White scalebar is 100 µm.

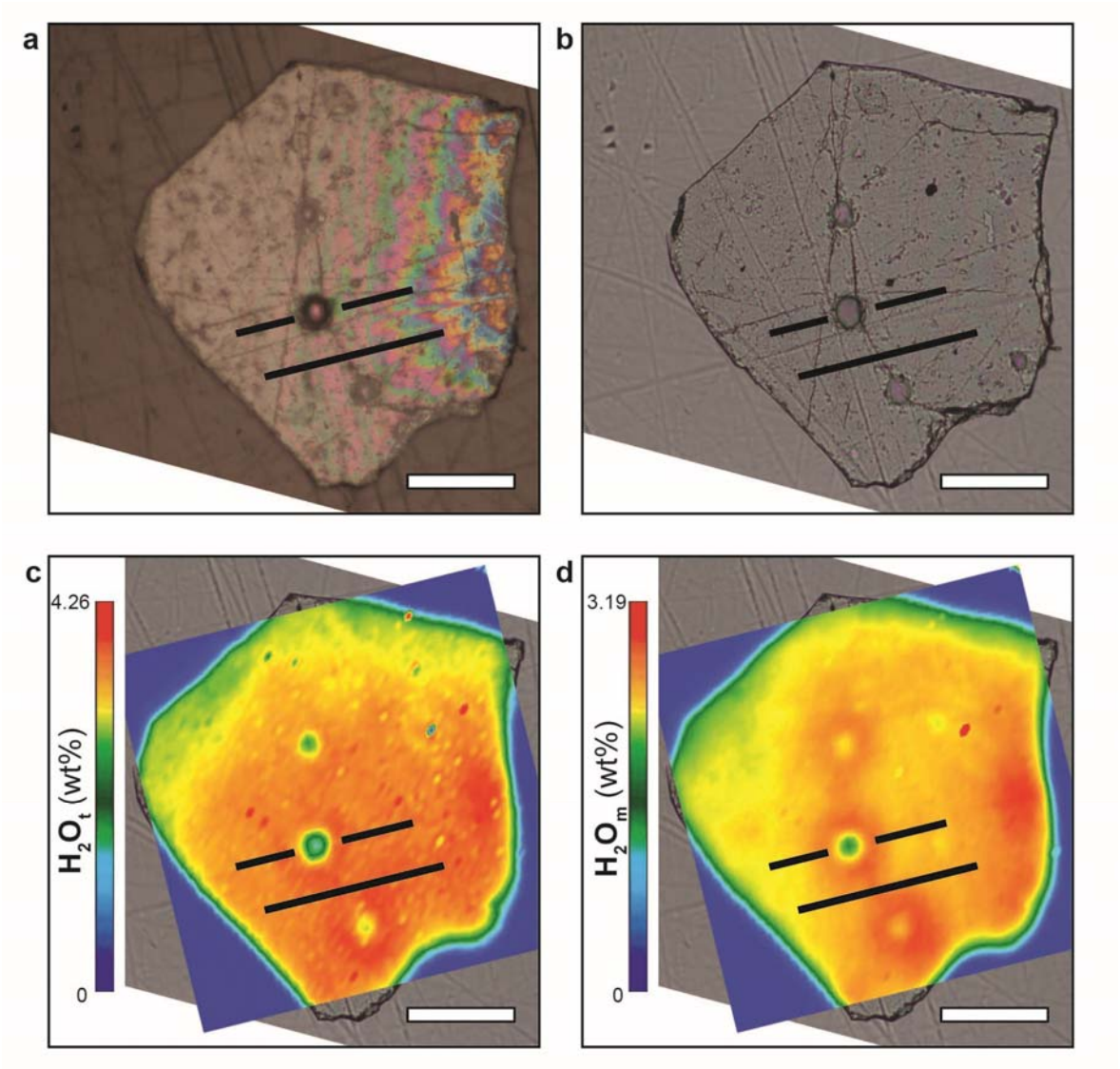

Fig. 6.5 Dissolved H_2O distribution in sample MCN28

Sample as seen in **a** reflected light and **b** transmitted light. FTIR imaging of **c** H_2O_t distribution and **d** H_2O_m distribution. Both H_2O_t and H_2O_m are enriched at vesicle walls. Increased H_2O_m can be seen along the curving crack that links the three vesicles. Figure produced using average thickness of sample (13 μm). White scalebar is 100 microns. Black lines show locations of transects shown in Fig.s 6.6 and 6.7.

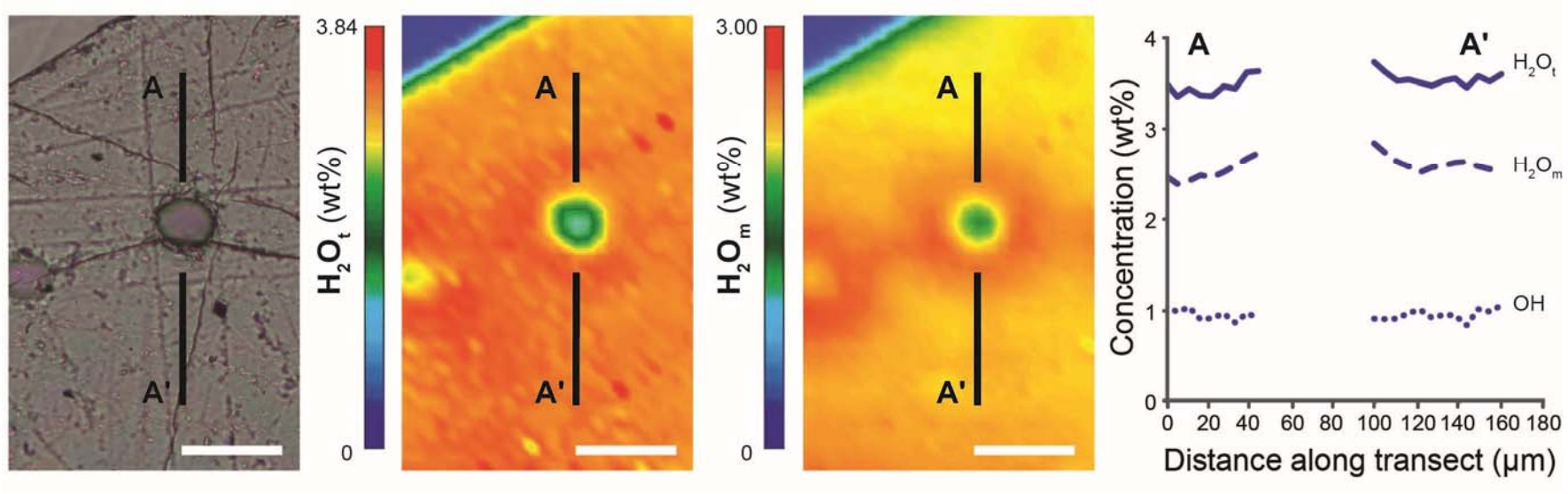

Fig. 6.6 H_2O concentration and speciation along transect in sample MCN28

Left to right: Location of transect A – A' seen in transmitted light, H_2O_t FTIR imaging, and H_2O_m FTIR imaging; H_2O_t, H_2O_m and OH concentrations along transect. Transect extends across vesicle. H_2O_t and H_2O_m concentrations both increase towards the vesicle wall, while OH concentration remains constant. Concentrations for image scalebars and graph calculated using average thickness along transect (13 µm). Errors on concentrations are ±15 % relative. White scalebar is 50 µm.

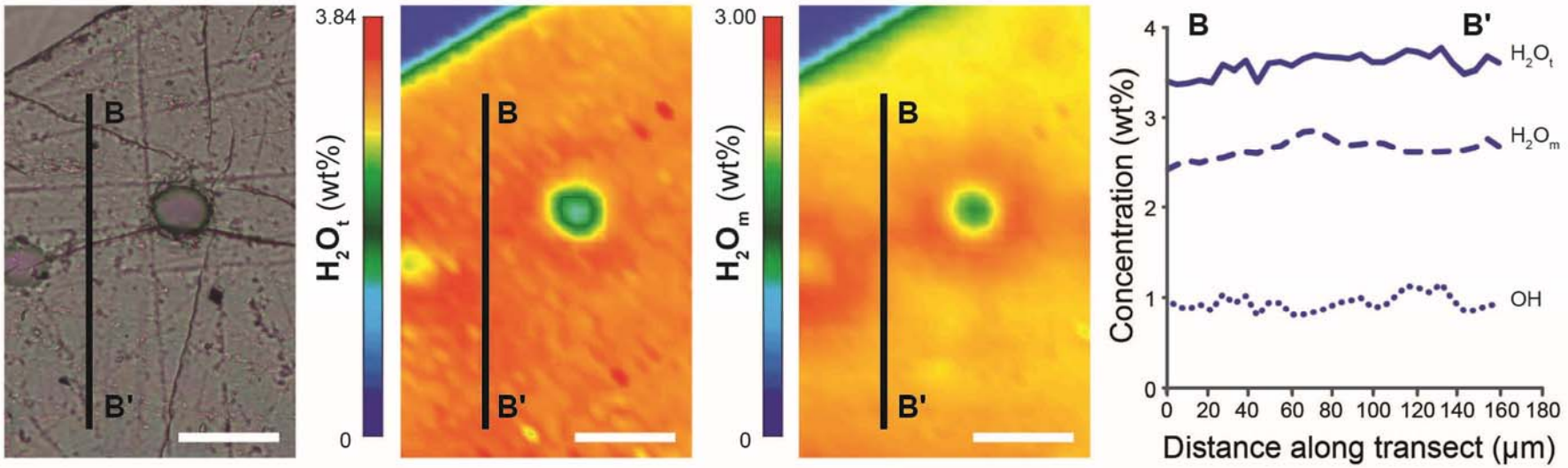

Fig. 6.7 H_2O concentration and speciation along transect in sample MCN28

Left to right: Location of transect B – B' seen in transmitted light, H_2O_t FTIR imaging, and H_2O_m FTIR imaging; H_2O_t, H_2O_m and OH concentrations along transect. Transect extends across crack (located at 70 µm along transect). H_2O_m concentration increases in vicinity of crack but no clear signal is seen H2Ot concentration. Concentrations for image scalebars and graph calculated using average thickness along transect (13 µm). Errors on concentrations are ±15 % relative. White scalebar is 50 µm.

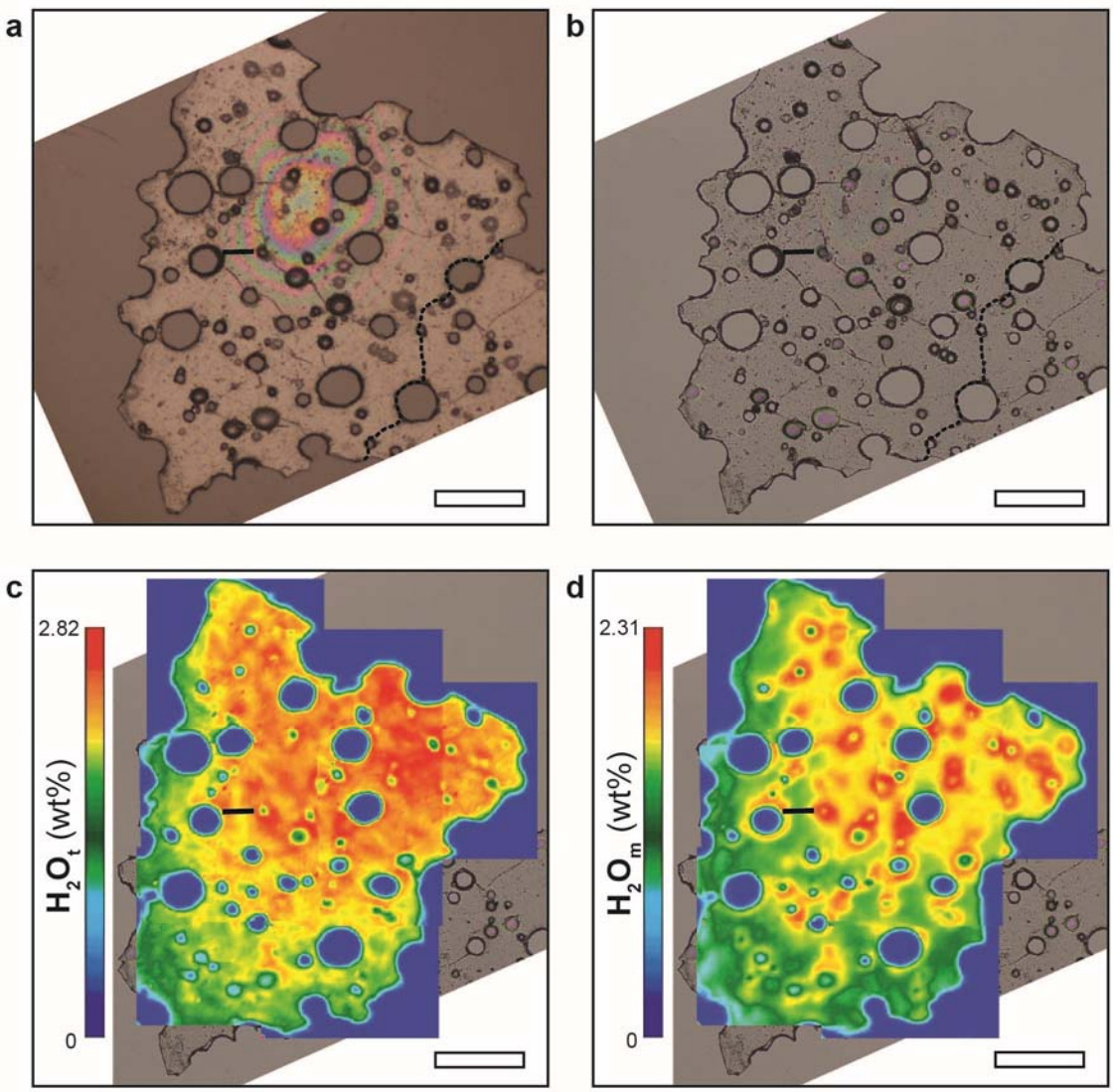

Fig. 6.8 Dissolved H_2O distribution in sample MCN15

Sample as seen in **a** reflected light and **b** transmitted light. FTIR imaging of **c** H_2O_t distribution and **d** H_2O_m distribution. Both H_2O_t and H_2O_m are enriched at vesicle walls. Apparent decrease in H_2O_t and H_2O_m concentrations towards lower left of sample is caused by sample thinning. Figure produced using average thickness of sample (18 µm). Black dashed line in **a**, **b** marks where sample snapped prior to FTIR imaging. White scalebar is 100 microns. Black line shows location of transect shown in Fig. 6.9.

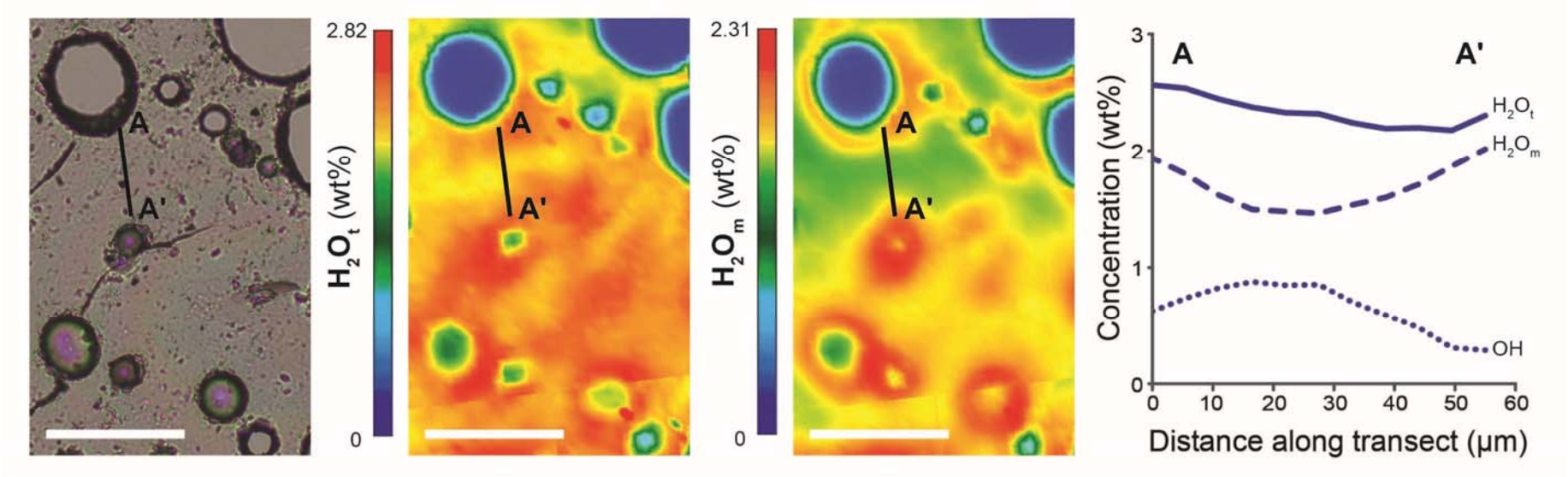

Fig. 6.9 H_2O concentration and speciation along transect in sample MCN15

Left to right: Location of transect A – A' seen in transmitted light, H_2O_t FTIR imaging, and H_2O_m FTIR imaging; H_2O_t, H_2O_m and OH concentrations along transect. Transect extends between two vesicles. H_2O_t and H_2O_m concentrations both increase towards vesicle walls, with H_2O_m increasing more steeply, while OH concentration decreases towards vesicle walls. Concentrations for image scalebars and graph calculated using average thickness along transect (18 µm). Errors on concentrations are ±15 % relative. White scalebar is 100 µm.

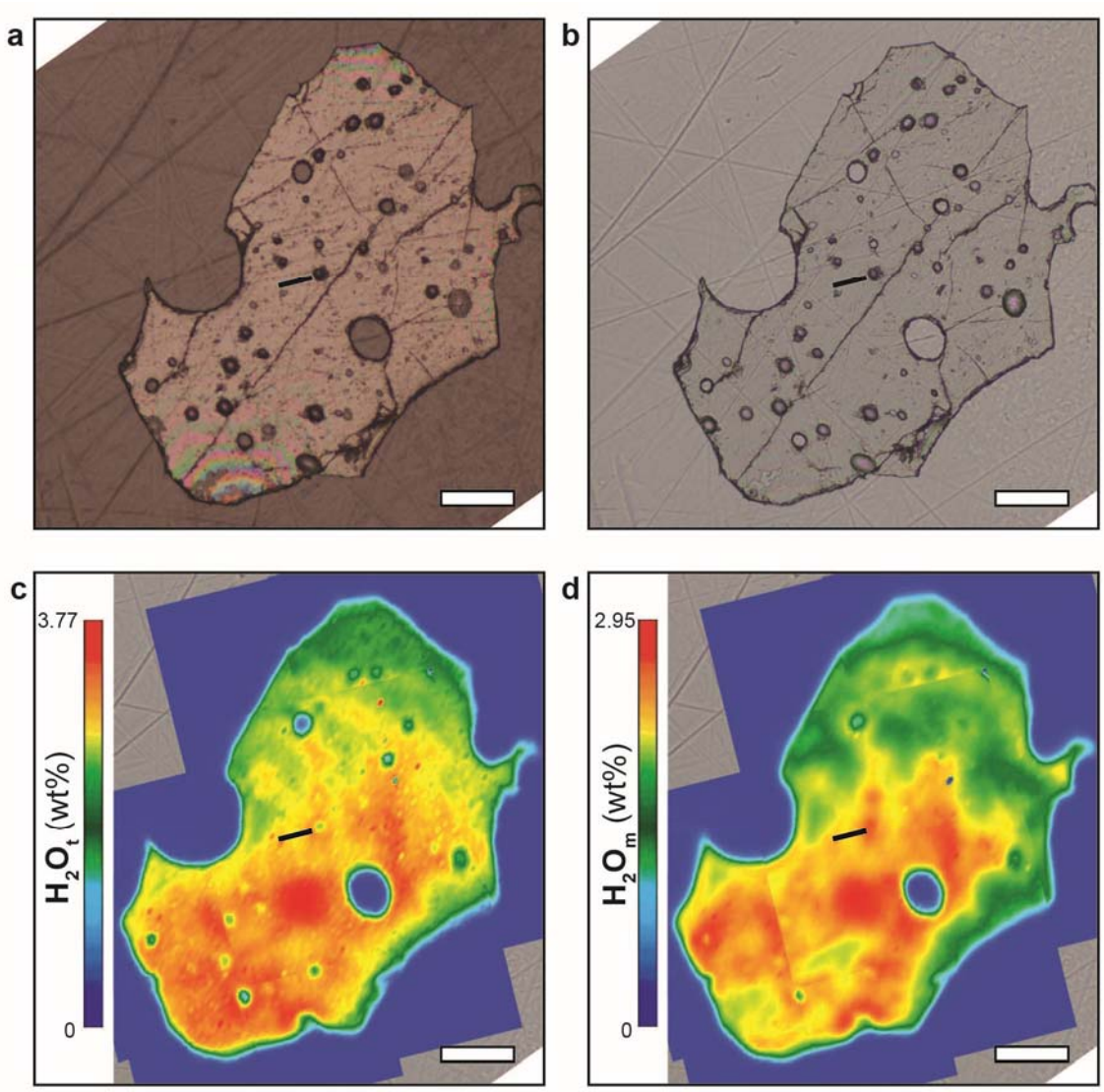

Fig. 6.10 Dissolved H_2O distribution in sample MCN33

Sample as seen in **a** reflected light and **b** transmitted light. FTIR imaging of **c** H_2O_t distribution and **d** H_2O_m distribution. Both H_2O_t and H_2O_m are enriched at vesicle walls. Large red circular area in centre of FTIR images is H_2O_t- and H_2O_m-rich area of glass related to resorption halo of 'ghost' bubble either above or below current sample surface(s). Apparent decrease in H_2O_t and H_2O_m concentrations towards top of sample is caused by sample thinning. Figure produced using average thickness of sample (13 µm). White scalebar is 100 microns. Black line shows location of transect shown in Fig. 6.11.

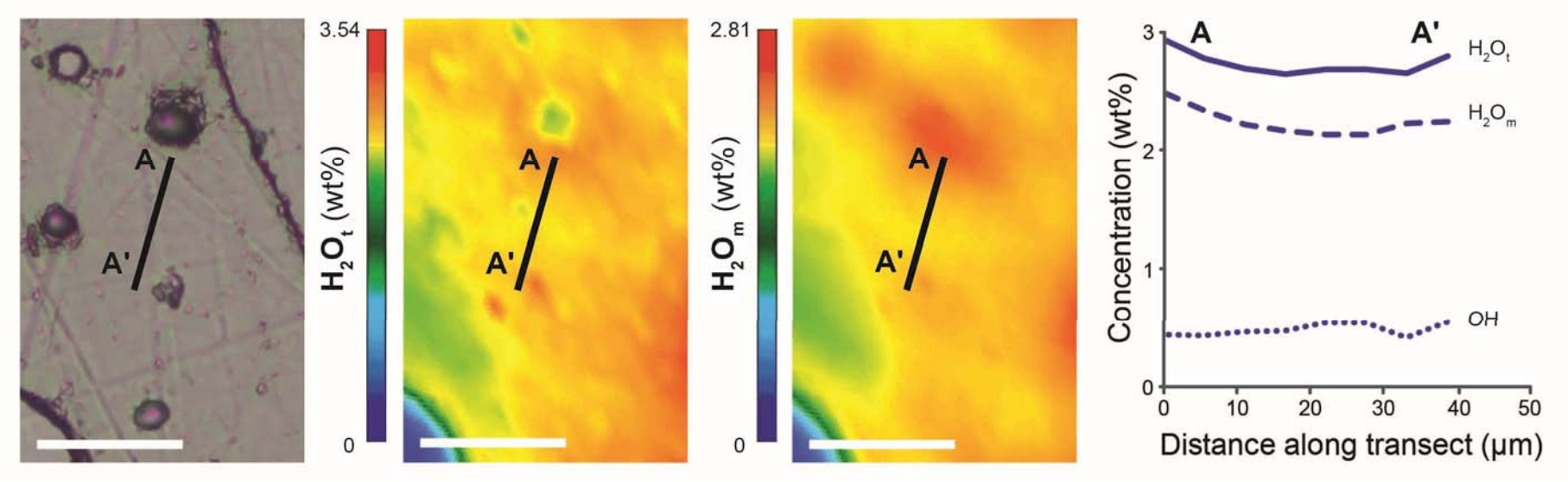

Fig 6.11 H_2O concentration and speciation along transect in sample MCN33

Left to right: Location of transect A – A' seen in transmitted light, H_2O_t FTIR imaging, and H_2O_m FTIR imaging; H_2O_t, H_2O_m and OH concentrations along transect. Transect extends from vesicle out into the far field. H_2O_t and H_2O_m concentrations both increase towards the vesicle wall, while OH concentration decreases very slightly. Concentrations for image scalebars and graph calculated using average thickness along transect (13 µm). Errors on concentrations are ±15 % relative. White scalebar is 50 µm.

6.3.1 Interpreting FTIR images of H_2O contents

FTIR images of H_2O_t and H_2O_m distribution are produced under the assumption of a uniform sample thickness. The thin sample wafers used for these analyses mean that FTIR images of H_2O_t and H_2O_m concentrations are sensitive to variations in sample thickness of a few microns (see Chapter 3 Section 3.3.2.5). Some samples appear to have broadscale variations in H_2O_t and H_2O_m concentrations across the sample wafer, e.g. MCN13 (Fig. 6.1 c, d). Thickness measurements acquired from reflectance spectra show that these apparent concentration variations are due to sample thinning towards the edge of the wafer, rather than a change in the actual H_2O_t and H_2O_m content of the analysed glass. This analytical artefact is noted in the relevant figure captions.

On the smaller scale of individual transects, sample thickness is constant within error along transect and, in particular, shows no systematic variation with distance from the vesicle wall. The presented quantitative concentration profiles are thus not affected by thickness variation along transect. This chapter will therefore focus on the overall pattern of H_2O_t and H_2O_m distribution with distance from vesicle walls as seen in the FTIR images and individual transects.

FTIR images of some samples are affected by interference fringes in the H_2O_m signal (MCN13, Fig. 6.1 d; MCN14, Fig. 6.3 d) and to a lesser extent in the H_2O_t signal (MCN14, Fig. 6.3 c). In these cases, transects were either selected in an unaffected area (MCN13) or parallel to the observed interference fringes so that all spectra were equally affected (MCN14). In the latter example, the interference fringes will affect the absolute concentration values extracted but not the overall shape of the profile.

For a full discussion of these issues, see Chapter 3 Section 3.3.2.5.

6.3.2 H_2O_t distribution

FTIR images of H_2O_t distribution show that glass surrounding vesicles in all samples is enriched in H_2O_t relative to the far field. Quantitative H_2O_t concentration profiles extracted along the

highlighted transects in the sample figures confirm that H_2O_t concentration increases towards vesicles, being lower in the far field.

In some images, circular areas of glass with high H_2O_t content can be seen in the far field where no associated vesicle is seen in the reflected or transmitted light images (e.g. MCN14, Fig. 6.3 c; MCN33, Fig. 6.10 c). As with the similar circular areas of H_2O_t-rich glass seen in BSEM images (e.g. Chapter 4 Fig. 4.1, 4.2) these are interpreted to be enrichments associated with 'ghost bubbles', i.e. a vesicle either above or below the sample surface(s) that has been removed during sample preparation.

6.3.3 H_2O_m distribution

FTIR images of H_2O_m distribution show that in all samples the glass surrounding vesicles is enriched in H_2O_m relative to the far field. Quantitative H_2O_m concentration profiles extracted along selected transects confirm that H_2O_m concentration increases with proximity to vesicles. Circular areas of H_2O_m-rich glass are seen in the same areas as the H_2O_t-rich areas described above (Section 6.3.2), confirming that these enrichments are consistent with those seen at vesicle walls.

The shape of the H_2O_m concentration profile, in terms of gradient and lengthscale of enrichment, is similar to that of the H_2O_t concentration profile for all but one transect. The exception is for sample MCN15 (Fig. 6.9), where the gradient of the profile near vesicle walls is greater for H_2O_m than H_2O_t, and where the lengthscale of enrichment is shorter for H_2O_m than H_2O_t.

6.3.4 OH distribution

OH concentration profiles for individual transects show that OH concentration remains approximately constant with distance from the vesicle wall in all samples except MCN15. Here, OH concentration is observed to decrease towards vesicle walls (Fig. 6.9).

6.4 Discussion

6.4.1 Comparison of H_2O_t distribution with SIMS-calibrated BSEM data

6.4.1.1 Resorption profiles

The observation that, in all samples, H_2O_t is highest at the vesicle wall and decreases with distance into the far field shows that H_2O was diffusing from the bubble/vesicle back into the melt/glass at the time the profiles were formed. These observations agree with the observations of H_2O_t enrichments around vesicles in samples analysed by SIMS-calibrated BSEM imaging (Chapter 4). As these samples were produced in the same manner as those in Chapter 4, it is therefore concluded that the H_2O_t enrichments observed here are also caused by bubble resorption during the quench process.

One sample, MCN13, was analysed by both SIMS-calibrated BSEM imaging and FTIR imaging (Fig. 6.1, 6.2; see Chapter 4 Fig.s 4.2, 4.3 for SIMS and BSEM data). MCN13 is a solubility experiment that was expected to have a bubble population in equilibrium with the melt prior to quench. For the experimental temperature and pressure conditions, the melt was expected to have an equilibrium H_2O_t content (H_2O_{eq}) of 3.48 wt% (Newman & Lowenstern, 2002). This H_2O_t value was observed in the far field by SIMS analysis (Chapter 4 Table 4.3). The lowest far field concentration reached in the FTIR transect shown is 3.19 ±0.48 wt% H_2O_t (Fig 6.2), which is therefore within error of H_2O_{eq}. This is consistent with the interpretation in Chapter 4 that the far field glass retains the equilibrium H_2O content of the experimental conditions prior to quench.

With SIMS-calibrated BSEM analysis, H_2O_t concentration at the vesicle wall in MCN13 was found to be 4.64 wt% (Chapter 4 Fig. 4.3). FTIR data show smaller enrichments at vesicle walls with up to 3.94 ±0.59 wt% H_2O_t observed along the presented transect (Fig. 6.2). The lower enrichments measured by FTIR probably result from the coarser spatial resolution of the FTIR technique, which prevents measurements being made as close to the vesicle wall as for the SIMS-calibrated BSEM

technique and involves volumetric averaging of glass with varying H_2O_t concentrations (see Chapter 3 Section 3.3.2.5). The FTIR observations of H_2O_t enrichment around vesicles are therefore in agreement with the SIMS-calibrated BSEM observations presented in Chapter 4, although it should be noted that the vesicle 'wall' concentrations obtained by FTIR will be lower than if analysed by SIMS and BSEM.

6.4.1.2 Crack hydration

In BSEM images presented in Chapter 5, dark H_2O_t-rich glass is present along cracks formed during quench (Fig. 5.3). This indicates that some diffusion of H_2O still continues when the far field has cooled to below its glass transition temperature. The hydration lengthscales around cracks are smaller than those around vesicles as a result of lower H_2O diffusivity at temperatures below the glass transition temperature. For this reason they are more likely to go unobserved in FTIR data where the spatial resolution is coarser. One possible example of glass hydration around cracks seen in FTIR data is found in sample MCN28 (Fig. 6.5). A long crack connects the three vesicles seen in transmitted light (Fig. 6.5 b) and corresponds to an enrichment in H_2O_m that can be seen in both the FTIR image (Fig. 6.5 d) and transect (Fig. 6.7). The same signal cannot however be reliably discerned in the H_2O_t data (Fig 6.5 c; Fig. 6.7). For all samples, the H_2O_t dataset is systematically noisier than the H_2O_m dataset, and it is likely that any H_2O_t increase approaching the crack is lost in this noise. From the H_2O_m concentration profile the lengthscale of hydration is comparable to that observed in the BSEM dataset (Chapter 5 Section 5.4.5.1), although it is noted that hydration lengthscales around cracks will vary according to the angle at which they intersect the sample surface (Chapter 5 Fig. 5.10).

6.4.2 Interpreting observed speciation data

6.4.2.1 Controls on H_2O speciation

H_2O_m and OH dissolved in the melt interconvert via the following reaction (Chapter 2, Eq. 2.3, reproduced here for convenience):

$$H_2O_{m(melt)} + O^o_{(melt)} \leftrightarrow 2OH_{(melt)},$$

in which H_2O_m reacts with bridging oxygens (O^o) in the melt to produce OH groups that are bound to the silicate polymer framework (Stolper 1982a). The equilibrium constant of this reaction, *K*, determines the proportion of H_2O_m and OH present for a given H_2O_t concentration. The dominant control on *K* is temperature, with higher temperatures corresponding to higher values of *K* (hence lower H_2O_m:OH) and lower temperatures corresponding to lower values of *K* (hence higher H_2O_m:OH). For a given value of *K* (resulting from, say, a given temperature) the proportions of H_2O_m and OH in a melt will also vary with total H_2O_t concentration for stoichiometric reasons, with lower H_2O_m:OH ratios at low total H_2O_t concentration and higher H_2O_m:OH ratios at higher total H_2O_t concentration (for full details see Chapter 2 Section 2.5).

H_2O speciation in the melt is also affected by pressure and anhydrous melt composition. Pressure effects are generally considered to be negligible (e.g. Hui et al. 2008), while the effect of melt composition is small, and is significant only for large compositional variations (e.g. between basalt and rhyolite) (e.g. Silver et al. 1990). Consequently, the effects of pressure and melt composition on H_2O speciation can be discounted for the purposes of this discussion, leaving temperature and H_2O_t concentration as the principal factors to be considered.

6.4.2.2 The quench effect

When considering the observed H_2O speciation data it is necessary to account for the 'quench effect' that results from the decreasing rate of the interconversion reaction with decreasing temperature (see Chapter 2 Section 2.5.2.1). For the samples presented here, T_{exp} is sufficiently high (825 – 840 °C) that the measured speciation data are likely to have been affected by this quench effect. Thus the measured speciation can be used to obtain the 'apparent equilibrium' constant, *Q*, from which, in turn, the 'temperature of the apparent equilibrium', T_{ae}, can be obtained (see Chapter 2 Section 2.5.3 for further details).

As discussed in Chapter 3 Section 3.2.3, the quench rates of these samples were not measured. The solubility samples were quenched by cooling the pressure vessel with compressed air until the vessel stopped visibly glowing, and then placing the vessel in water to cool to ambient temperature. The whole process takes several minutes and it is estimated that the glass transition temperature is reached in 30 – 60 seconds (J. Larsen, *pers. comm.*), which is consistent with cooling rates in compressed air obtained by Xu & Zhang (2002).

The decompression samples (MCN15, MCN33) presented here were quenched rapidly following a similar procedure to the ABG samples discussed in Chapter 4, and are expected to have similar thermal histories. The average quench rate to T_g for these samples is therefore estimated to be ~70 K/s (see Chapter 5 Section 5.4.1). This cooling rate is the same as that investigated by Zhang et al. (2000), who found that a rhyolite containing 2.5 wt% H_2O_t and equilibrated at 727 °C has a T_{ae} of 527 °C when quenched at this rate. It is therefore expected that the speciation in both types of experiments will have been affected to some extent by the quench effect, with the solubility experiments likely to exhibit lower T_{ae} than the decompression experiments.

6.4.2.3 Calculating expected equilibrium speciation

Interpreting the observed H_2O speciation profiles requires some knowledge of how speciation would be expected to vary for different scenarios. Provided that values of K and H_2O_t concentration are known, the equilibrium proportions of H_2O_m and OH can be calculated by rearranging the equilibrium speciation equation (for full methodology, see Appendix A3). H_2O_t values can be derived either from observed H_2O_t profiles or from theoretical considerations such as H_2O_{eq}. To determine K, a relationship between K and temperature must be used. Of the different published relationships (see Chapter 2 Section 2.5.2.1), the one that is most appropriate for the range of conditions relevant here is that of Nowak & Behrens (2001):

$$K = 27.98e^{-4210/T} \qquad \text{Equation 6.1}$$

Where T is the temperature in Kelvin. This equation is valid for hydrous haplogranitic melts (76.14 wt% SiO_2, 13.53 wt% Al_2O_3, 4.65 wt% Na_2O, 5.68 wt% K_2O) with 1.27-5.15 wt% H_2O_t for 100-300 MPa and 773-1073 K (500-800 °C). The authors give errors of ±15% on this relationship, but note that extrapolating far beyond the range of conditions investigated may result in much larger errors.

6.4.3 The speciation case for quench resorption

There are two key observations to be made of the speciation data shown in the transects from Fig.s 6.2 to 6.11. The first is that all samples exhibit high H_2O_m:OH ratios, with H_2O_m concentration typically being between two and three times the value of the OH concentration. The second is that in all solubility samples the OH profile remains constant with distance from the vesicle wall, even as H_2O_m increases in the resorption halo. By contrast, in the decompression sample MCN15 the OH concentration decreases towards vesicle walls, while in the second decompression sample MCN33 the OH signal is more uniform.

The elevated H_2O_t concentrations observed around vesicles result from an increase in the equilibrium H_2O solubility value. Such an increase could be caused by either an increase in pressure or a decrease in temperature. Previous chapters have ruled out a pressure cause and concluded that the observed resorption is caused by the decrease in temperature during quench. In the following section, both the pressure increase and temperature decrease mechanisms are considered by comparing the observed H_2O speciation data with what would be expected for each mechanism.

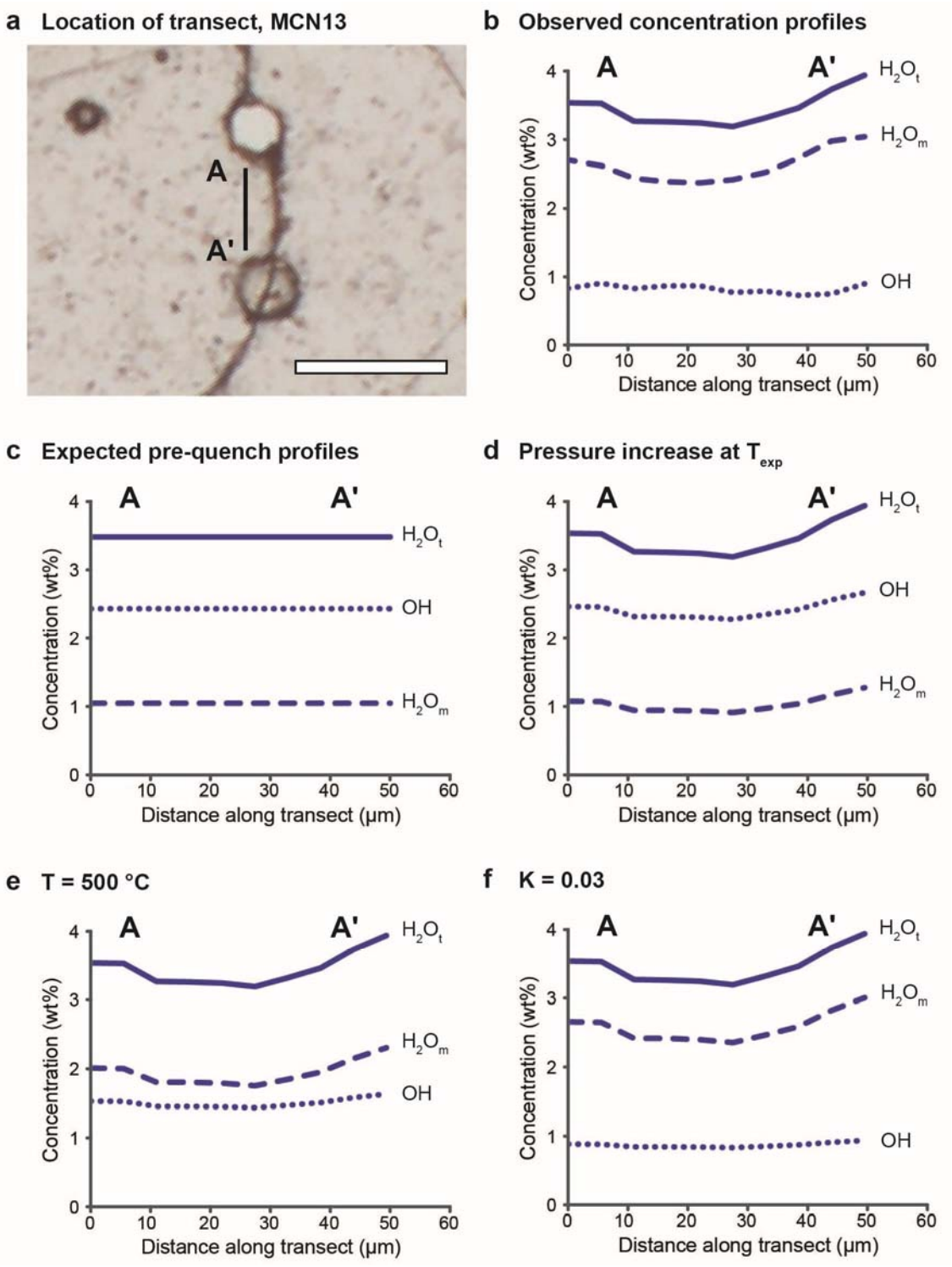

Fig. 6.12 Comparison of observed and expected speciation in MCN13

a, b Location of transect and observed concentration profiles (also shown in Fig 6.2) **c** Expected concentration profiles along transect prior to quench (P_f, T_{exp}, H_2O_{eq}) **d** Expected speciation if observed H_2O_t profile caused by pressure increase at T_{exp} **e** Expected speciation for observed H_2O_t profile at 500°C **f** Expected speciation for observed H_2O_t profile if equilibrium constant K = 0.03. Speciation data calculated using equation for K of Nowak & Behrens (2001), which is valid for 500 - 800°C (K = 0.12 – 0.60).

6.4.3.1 Eliminating a pressure origin

The solubility sample MCN13 was equilibrated at 825 °C and 80 MPa prior to quench. Using the transect presented in Fig 6.2 as an example, the expected speciation for different scenarios is calculated for comparison (Fig. 6.12). The relationship of Nowak & Behrens (2001) gives an equilibrium constant of K = 0.60 for T_{exp}, although it requires a slight extrapolation from the lower pressure limit (100 MPa) and upper temperature limit (800 °C) of their model. Using this value for K and the expected equilibrium H_2O_t concentration (H_2O_{eq}) for the experimental conditions (3.48 wt% H_2O_t, Newman & Lowenstern 2002) the expected concentrations of H_2O_m and OH in the melt prior to quench are calculated (Fig. 6.12 c). Prior to quench the bubbles were in equilibrium with the melt and so both the H_2O_m and OH profiles are constant along the transect. In this case, the OH concentration is considerably higher than the H_2O_m concentration, a reversal of what is seen in the FTIR data (Fig. 6.12 b).

If bubble resorption was caused by an increase in pressure at the beginning of quench (see Chapter 3 Section 3.2), this resorption would occur at T_{exp}. Any change in H_2O_m:OH along the transect would be caused only by the effect of increasing H_2O_t concentration near the bubble walls for a constant value of K, since pressure has a negligible effect on equilibrium speciation. Using the same value of K as for the pre-quench conditions the expected profiles of H_2O_m and OH are recalculated using the observed H_2O_t concentrations along the transect (Fig. 6.12 d). In these calculated profiles both OH and H_2O_m concentrations increase towards the vesicle walls. In addition, the ratio of H_2O_m:OH also increases slightly towards the vesicle walls from 0.40 in the centre of the transect to 0.48 at A', indicating the slight impact that total H_2O_t concentration has on equilibrium speciation, with higher H_2O_t favouring higher H_2O_m:OH. The overall proportions of H_2O_m and OH however remain much the same as for the equilibrium profiles prior to bubble resorption (Fig. 6.12 c), with higher concentrations of OH than H_2O_m.

The observed speciation data (Fig. 6.12 b) show no increase in OH concentration towards the vesicle walls, and exhibit much higher H_2O_m:OH ratios than expected for a pressure increase mechanism. However the high experimental temperature and relatively slow quench rate of MCN13 makes it likely that the observed speciation have been affected by the 'quench effect', which results in higher H_2O_m:OH values than existed at high temperature (see Section 6.4.2.2). The expected speciation data for a pressure increase mechanism were therefore recalculated to include the potential impact of the quench effect (Fig. 6.12 e). This was done by using the value of *K* at 500 °C, which represents the lower temperature limit of the Nowak & Behrens relationship (see Section 6.4.2.3). This calculation shows that if the observed bubble resorption was caused by a pressure increase at high temperature and the speciation data were then subsequently affected by the quench effect, H_2O_m would become the dominant species observed, but both H_2O_m and OH concentrations would still be expected to increase towards the vesicle walls (Fig. 6.12 e).

The observed speciation data have a higher H_2O_m:OH ratio than either of these scenarios, and OH does not increase towards the vesicle walls. The higher observed H_2O_m:OH ratio could still be explained by a pressure increase followed by the quench effect if the glass transition temperature (T_g) was lower than 500 °C, since this would correspond to lower T_{ae} and thus higher H_2O_m:OH. Similarly, the predicted increase in OH concentration towards the vesicle walls for this scenario (Fig. 6.12 e) is small, and could be too small to be resolved by the analytical resolution of the FTIR data. The flat OH concentration profiles observed in the solubility samples therefore do not by themselves preclude a pressure increase mechanism for bubble resorption.

However, the OH concentration in sample MCN15 decreases towards the vesicle wall (Fig. 6.9). MCN15 was a decompression experiment and was expected to have a bubble population that was growing at the time of quench (see Chapter 3 Section 3.2.3). H_2O_t, H_2O_m and OH concentrations would therefore all have been decreasing towards the bubble wall prior to quench. If bubble resorption occurred at high temperature as a result of a pressure increase, the interconversion

reaction would be sufficiently rapid that equilibrium speciation would be maintained and any increase in H_2O_t at the wall would be accompanied by increases in both H_2O_m and OH. Even if the data were subsequently affected by the quench effect, this could not cause the observed decrease in OH. There is thus no scenario in which the bubble resorption observed in sample MCN15 could be caused by a pressure increase. It is therefore concluded, as in previous chapters, that the observed bubble resorption is not caused by a pressure increase.

6.4.3.2 Evidence for a temperature origin

According to the hypothesis that the observed bubble resorption is caused by temperature decrease during quench, the solubility of H_2O in the melt continuously increases during cooling. H_2O in bubbles is present as H_2O_m and will therefore enter the melt as H_2O_m. To maintain equilibrium speciation of H_2O in the melt some of this additional H_2O_m would have to be converted to OH. The rate at which the interconversion reaction can convert H_2O_m to OH (and vice versa) is strongly dependent on temperature and so as the melt cools during quench, it reaches a point where the equilibrium proportions of H_2O_m and OH for a given temperature cannot be attained in the time available. This is the same process that creates the 'quench effect' (Section 6.4.2.2). In the case of bubble resorption however, the breakdown of the interconversion reaction over the timescale of quench means that excess H_2O_m entering the melt from resorbing bubbles is not converted to OH.

This disequilibrium speciation should have two key impacts. Firstly, the OH concentration profile should remain largely unaltered during quench, and should therefore reflect pre-quench conditions. Secondly, H_2O_m:OH ratios should be elevated relative to both the pre-quench conditions and the impact of the quench effect, since H_2O_m is being added to the system and remaining unconverted.

The data from the decompression sample MCN15 are therefore consistent with a temperature origin. Observed H_2O_m:OH ratios are strongly disequilibrium within the resorption halos. The

shape of the OH profile, which decreases towards the vesicle walls, suggests that the rapid quench can indeed preserve the original OH concentration profile, in this case corresponding to bubble growth. Although, as discussed in Section 6.4.3.1, the data from the solubility samples cannot by themselves discount a pressure origin, the high H_2O_m:OH ratios and flat OH concentration profiles are also consistent with a temperature origin for the observed bubble resorption.

The final speciation calculation for the MCN13 transect (Fig. 6.12 f) was used to interpret the observed speciation data (Fig. 6.12 b) in the context of this temperature decrease mechanism. For every point along the transect, the value of *K* that would give the observed H_2O_m concentration for the observed H_2O_t concentration was calculated. The average of these values (*K*=0.03) was then used to calculate the expected concentrations of H_2O_m and OH. As is to be expected, these calculated profiles reproduce the observed profiles well.

This suggests that the observed H_2O_m:OH values for MCN13 correspond to a *K* (or rather, *Q*) value of 0.03. This in turn corresponds to a temperature of apparent equilibrium, T_{ae}, of 345°C. Since T_{ae} has been shown to be equivalent to the temperature of the glass transition, T_g, this implies a T_g of ~345°C (e.g. Dingwell & Webb, 1990). T_g is dependent on both H_2O content and quench rate (see Chapter 2 Section 2.4.3). For a rhyolite with 4 wt% H_2O_t, a T_g of 345 °C would require a cooling rate of less than 0.1 K/s. This is two orders of magnitude lower than might be expected for quenching in compressed air (Xu & Zhang 2002; see Section 6.4.2.2).

There is likely to be considerable error on the value of T_{ae}, since it requires the relationship for *K* of Nowak & Behrens to be extrapolated far beyond its recommended temperature range (see Section 6.4.2.3). This alone may explain the anomalously low T_{ae} (hence cooling rate) derived from the measured speciation. Another possible explanation however is the occurrence of disequilibrium speciation during quench. The use of T_{ae} to derive T_g assumes that the observed H_2O_m:OH ratio represents equilibrium speciation at the time of the glass transition, but quench

resorption has been shown to result in disequilibrium speciation conditions. The breakdown in the interconversion reaction over quench timescales will lead to higher than expected H_2O_m:OH ratios. These elevated H_2O_m:OH ratios would in turn correspond to lower values of T_{ae} and T_g, and could therefore explain the anomalously low cooling rate derived from these values.

Speciation measurements made in truly far field areas, which have not been affected by H_2O_m influx within resorption halos, would be expected to maintain T_{ae} values that reflect the actual temperature of the glass transition. For the MCN13 transect presented, all far field H_2O_m:OH ratios give similarly low T_{ae} values, suggesting that even the 'far field' glass in the centre of the transect may have been affected by disequilibrium speciation accompanying bubble resorption. It is known from SIMS-calibrated BSEM analysis of the same sample that the half-fall distance of bubble resorption in MCN13 is ~10 µm (Chapter 4 Table 4.3). This is the distance from the vesicle wall at which the H_2O_t concentration falls to half the near-wall and far field values, and so the actual distance from the vesicle wall affected by elevated H_2O_m:OH ratios will be larger. Given that the vesicles investigated in MCN13 are only 60 µm apart, it is reasonable to assume that the entire transect could have been affected by their resorption halos.

A caveat to this interpretation of T_{ae} is that the observed H_2O_t concentration along the same transect is within error of the expected H_2O_{eq} at the final experimental conditions (see Section 6.4.1.1). If H_2O_m concentration in the centre of the transect has been increased by bubble resorption then it would be expected that H_2O_t concentration in the far field would also increase, and therefore be greater than H_2O_{eq}. However the errors on the FTIR-derived concentrations are large (at least 15%; see Chapter 3 Section 3.3.2.5) as a result of errors on sample thickness determination. The observed H_2O_t concentrations could therefore also be consistent with hydration of the 'far field' glass.

The error on sample thickness is particularly important for these thin samples. If the sample thickness has been overestimated by even a few microns, this would also explain the apparent

paradox of the OH concentration. If cooling during quench induces disequilibrium speciation that prevents conversion of H_2O_m to OH, then the observed OH profile should closely resemble that which is expected at high temperature, pre-quench (Fig. 6.12 c), or that which is expected after some modification by the quench effect (Fig. 6.12 e). Although there is uncertainty on what these values of OH should be (since T_g is not independently constrained and large errors may result from extrapolation of the *K* relationship) the observed OH concentrations appear to be lower than expected. If the sample thickness has been overestimated slightly however, then the observed OH concentration will indeed match that which is expected, while H_2O_m and H_2O_t concentrations would also be higher and would therefore be consistent with the evidence from H_2O_m:OH ratios that the entire transect has been hydrated by bubble resorption.

The interpretation of the observed speciation data are therefore complicated by unmeasured quench timescales, analytical issues (chiefly relating to determination of sample thickness), and a lack of data on how *K* and the rate of the interconversion reaction vary between high and intermediate temperatures. While this restricts the information that can be obtained from the observed H_2O_m:OH ratios, it is nevertheless clear that the observations of high H_2O_m:OH ratios, uniform OH concentrations in solubility samples, and, crucially, decreasing OH concentrations in the decompression sample MCN15 are all consistent with bubble resorption occurring as a result of temperature decrease during quench. Having eliminated a pressure cause, and considering the evidence of previous chapters, it is concluded that quench resorption is indeed caused by temperature decrease, and is characterised by disequilibrium speciation processes.

6.4.4 Reconstructing pre-quench conditions

The discovery that disequilibrium speciation preserves the original pre-quench OH concentration profile provides a method of investigating pre-quench conditions in samples affected by quench resorption. A good example of this is the comparison of MCN15 and MCN33. Both were decompression experiments that were rapidly quenched (see Section 3.2.3). OH concentration

shows a marked decrease towards the vesicle wall for MCN15 (Fig. 6.9), yet remains reasonably uniform in MCN33 (Fig. 6.11). This difference results from their contrasting experimental conditions.

MCN15 was rapidly decompressed and then held at the final experimental pressure for 1 minute prior to quench (see Table 6.1). This is expected to have resulted in highly disequilibrium degassing of the melt (in the sense that the far field would be strongly H_2O supersaturated) and therefore H_2O_t (and H_2O_m and OH) concentration profiles are expected to have had a steep gradient near the bubble prior to quench. This is consistent with the decrease in OH concentration seen in the quenched sample.

MCN33 however was decompressed an order of magnitude more slowly than MCN15, and held for 10 minutes prior to quench (Table 6.1). It is therefore expected to have a bubble population that had either reached or were approaching their equilibrium size prior to quench. In this scenario, H_2O_t, H_2O_m and OH concentration would be uniform or near-uniform along the profile prior to quench. This is consistent with the OH concentration profile seen in the quenched sample.

The shape of OH concentration profiles of samples affected by quench resorption can therefore be used to reconstruct their pre-quench conditions. Here the shape of the profiles is shown to be consistent with their different decompression, and therefore bubble growth, histories. With better constraints on variations in speciation during quench, this aspect could be further developed to provide a quantitative tool for investigating the bubble growth histories of samples.

6.5 Implications

6.5.1 Determining the cause of resorption in natural samples

Bubble resorption can be caused by both a pressure increase and a temperature decrease. The previous two chapters have already made the case that the bubble resorption seen in MCN13 and similar experimental samples must be caused by temperature decrease – hence temperature decrease during quench – and not by any increase in pressure. The evidence from H_2O speciation of elevated H_2O_m:OH ratios and the preservation of the shape of the OH concentration profile derived from pre-quench experimental conditions are further evidence that these resorption profiles were created as a result of a temperature decrease, and offer an insight into how pressure and temperature causes of bubble resorption may be distinguished in samples where pre-quench conditions are not well constrained.

If bubble resorption is triggered by a pressure increase in the conduit, as has been suggested for natural erupted clasts from Mono Craters by Watkins et al. (2012), then this resorption would be expected to take place at magmatic temperatures when the interconversion reaction rate is sufficiently rapid to maintain equilibrium speciation. As such, the H_2O_m:OH ratios in the resorption halos would be expected to be in equilibrium with the observed H_2O_t concentration along the whole length of the profile. H_2O_m:OH would therefore increase with increasing H_2O_t towards the vesicle wall (see Chapter 2 Section 2.5.2).

Regardless of bubble resorption mechanism, observed speciation of samples originally at high temperature (> 800 °C) is expected to modified to some extent by the quench effect and will result in a lower T_{ae}; this effect would be more pronounced for slower quench. The quench effect would only change the H_2O_m:OH ratio however, and so the shape of the H_2O_m and OH profiles towards the vesicle walls should remain similar. These profile shapes provide a tool for evaluating the cause of observed bubble resorption and may distinguish between pressure and temperature mechanisms.

However, the evidence outlined in this thesis demonstrates that even experimental samples subjected to rapid laboratory quench processes (MCN15 and MCN33, the ABG series presented in earlier chapters) experience cooling-induced bubble resorption during quench. Thus, even in the case that a pressure increase at high temperature caused bubble resorption, it must be expected that such samples would also be affected by additional bubble resorption caused by the increase in H_2O solubility during quench. As seen in this chapter, the characteristic signal of cooling-induced bubble resorption during rapid and moderate quench is that of disequilibrium speciation in the resorption halos, with H_2O_m increasing towards vesicle walls while the OH profile retains its pre-quench shape, being either flat (for bubbles previously in equilibrium with the melt) or decreasing towards the vesicle wall (for bubbles that were previously growing). Crucially to the interpretation of these samples, the OH concentration does not increase towards the vesicle walls.

A caveat to this is that if quench is slower, for example in a thick deposit, then the interconversion reaction rate may be able to keep pace with cooling. In this scenario, excess H_2O_m entering the melt would more readily be converted to OH and equilibrium speciation may be maintained. This may cause OH concentration to increase towards vesicle walls, even though the cause of bubble resorption is temperature decrease and not pressure increase. Here, however, theoretical considerations (for example, modelling of the cooling of the deposit interior) could be used to evaluate the likely contribution of pressure and temperature mechanisms to the observed profiles. Even for samples where pressure is the original cause of bubble resorption, slow quench may lead to the overprinting of the concentration data by temperature-controlled quench resorption. Indeed, it may be that for cooling rates that are sufficiently slow to avoid disequilibrium speciation during bubble resorption, diffusivity is sufficiently high to either fully equilibrate the 'resorbing' bubble with the surrounding melt, or for the bubble to be entirely resorbed.

6.5.2 Interpreting pre-quench bubble growth history

For the samples presented here, the uncertainties in the measured concentrations and H_2O_m:OH ratios combined with limited constraints on how pre-quench profiles will change during quench limit the interpretation of pre-quench bubble growth profiles to the shape, rather than values, of the observed OH concentration profile. Profile shape can distinguish between bubble populations that are in or near equilibrium with the melt, and those that are experiencing active growth. Just as the width of the resorption halo can give insight into processes operating during quench (e.g. the half-fall distance and DH_2O_{ch}, Chapter 4), so might the lengthscale of the remaining OH profile provide insight into the processes operating prior to quench. For example, the gradient and width of the OH depletion may be interpreted in terms of how the bubble was responding to changing conditions, such as decompression during magma ascent. In order to be more quantitative it is necessary to improve the understanding of speciation changes during quench.

6.5.3 Impact of disequilibrium speciation

The finding that bubble resorption during quench takes place under disequilibrium speciation conditions has implications for studies of vesicular magmatic glasses. Proportions of H_2O_m and OH are often used in geospeedometry studies to investigate the cooling rates and glass transition temperatures of erupted clasts through the measurement of T_{ae} (e.g. Zhang et al. 1995; Zhang et al. 1997; Zhang et al. 2000; Zhang & Xu 2007). If a vesicular sample has undergone quench resorption, the proportions of H_2O_m and OH in the resorption halo will be affected by disequilibrium speciation and will result in inaccurate calculations of T_{ae}, and thus T_g. Where bubble resorption halos are sufficiently wide that they interact with neighbouring resorption halos, not only will H_2O_t concentrations in the 'far field' be hydrated (Chapter 4) but the observed H_2O_m:OH ratio will be artificially increased. If the impact of disequilibrium speciation during quench resorption is not accounted for, it is possible that factors such as cooling rate and T_g could be misinterpreted.

Another impact of disequilibrium speciation during quench concerns H_2O diffusivity. Most studies of H_2O diffusivity are conducted under conditions of equilibrium; however it has been shown that disequilibrium speciation conditions affect measured diffusivity (see Chapter 2 Section 2.7.2.2). This occurs because H_2O_m is the diffusing species. Under conditions of disequilibrium speciation, dehydration experiments will have lower than expected DH_2O_t diffusivity, because the supply of diffusing H_2O_m is limited by the slow conversion of OH groups to (try to) maintain equilibrium speciation. Similarly, hydration experiments exhibit faster than expected DH_2O_t, because the addition of H_2O_m is not offset by conversion to OH groups, and there is therefore more H_2O_m available for diffusion (Zhang et al. 1991; Jambon et al. 1992).

The process of quench resorption is analogous to these disequilibrium hydration experiments. As H_2O_m from the bubble re-enters the melt, it does so as H_2O_m. The breakdown of the interconversion reaction over quench timescales means that this excess H_2O_m is not converted to structurally bound OH groups, but is instead free to continue diffusing away from the bubble. The diffusivity that controls the lengthscale of the resorption halo is therefore DH_2O_m, not DH_2O_t. In order to successfully model quench resorption, it is therefore necessary to not only fill in the data gap for DH_2O_m and DH_2O_t at intermediate and ambient temperatures, but also to understand how diffusivity may be affected by disequilibrium speciation.

An interesting sidenote is that a similar effect may happen in reverse for issues such as spherulite growth-induced H_2O diffusion gradients, where crystallisation enriches the melt in OH groups that must be converted to H_2O_m before it can diffuse away. Since spherulites grow in cooling magmas and may continue to grow below the temperature of the glass transition, it is possible that the associated H_2O diffusion occurs at temperatures at which the interconversion reaction cannot maintain equilibrium speciation. Thus for a given measured H_2O_t concentration at a spherulite wall, diffusion may be slower than expected under conditions of equilibrium speciation. This would have implications for calculating timescales of spherulite growth and subsequent

interpretation of the cooling history of the magma body (e.g. Castro et al. 2008; Watkins et al. 2008; Gardner et al. 2012; von Aulock et al. 2013). If disequilibrium speciation did occur during spherulite growth the area around the spherulite would be expected to contain excess OH. Spherulites often occur in H_2O_t-poor obsidian (< 0.2 wt% H_2O_t) however, so it may not be possible to resolve the concentrations of the individual H_2O species (e.g. Gardner et al. 2012).

6.6 Conclusions

The speciation data presented in this chapter support the conclusion of previous chapters that the observed bubble resorption profiles are caused by temperature decrease during quench, and not by a pressure increase. It has been shown that during temperature decrease, excess H_2O entering the melt from resorbing bubbles as H_2O_m is not converted to OH groups because the rate of the speciation interconversion reaction decreases dramatically with decreasing temperature and therefore cannot maintain equilibrium speciation for the changing temperature conditions. This breakdown of the interconversion reaction during quench resorption leads to elevated H_2O_m:OH ratios and the preservation of the shape of the original pre-quench OH profile.

The disequilibrium speciation that occurs during quench resorption has implications for the interpretation of measured speciation data in vesicular glasses, for example the temperature of the glass transition (as determined by T_{ae}) and the cooling history of the sample. Furthermore, disequilibrium speciation may result in faster than expected H_2O diffusivity, akin to that seen during hydration experiments conducted under disequilibrium speciation conditions. Finally, disequilibrium speciation and the preservation of the original pre-quench OH profile during quench resorption present a new framework for distinguishing between pressure and temperature mechanisms of bubble resorption, and for reconstructing the bubble growth history of the sample prior to quench.

Chapter 7: Discussion and Conclusions

7.1 Introduction

In this chapter the conclusions derived from the analysis of experimentally-vesiculated volcanic glasses in previous chapters are synthesised in order to identify the conditions for which quench resorption is expected to be most significant. The findings of a recent study of bubble resorption are discussed in order to highlight the importance of considering a quench resorption mechanism in studies of bubble resorption in natural samples, and a framework for investigating such samples is suggested. Finally, the data required for future studies of quench resorption are discussed.

7.2 Quench resorption in experimental samples

All the experimental samples analysed in this thesis have been affected by bubble resorption during the quench to glass at the end of the experiment. This quench resorption has been shown to be capable of reducing sample porosities by a factor of two, altering H_2O concentration and speciation distributions within a resorption halo that extends for tens of microns, and creating distinctive textures such as deformed melt films. As discussed in Chapter 4, the width of the resorption halo will be controlled by the characteristic diffusivity of H_2O during quench and the timescale of quench itself. The majority of the samples analysed here experienced quench timescales of only a few seconds, which are typical of the fastest quench timescales available for experimental samples, yet significant modification of sample H_2O distributions occurred during this time. This is because the high pressures (and corresponding H_2O concentrations) and

temperatures of these experiments result in high H_2O diffusivity. These conditions are common among experimental studies of magma degassing and so it is likely that the H_2O distribution (both concentration and speciation) in similar samples has been significantly modified from the original distribution prior to quench.

Although changes in H_2O distribution could affect studies of H_2O solubility or speciation, the main impact of quench resorption for experimental studies is the modification of vesicle size and sample porosities since these criteria are widely used to assess the degree to which degassing occurs in equilibrium. Experimental studies are particularly vulnerable to changes in porosity for three reasons. First, the amount of resorption will be controlled by the flux of H_2O back into the melt, and this will be greatest for conditions of high H_2O diffusivity. Second, the high H_2O contents of many experimental samples result in low glass transition temperatures, which increase the time for H_2O diffusion when the sample is still molten and bubbles can respond by shrinking. Finally, the reduction in sample porosity as a result of quench resorption is greatest for samples with low original porosity (Fig. 7.1). Experimental samples are often quenched at high pressures with porosities that are lower than samples quenched at lower or atmospheric pressures, and so the magnitude of porosity reduction for a given amount of H_2O resorption will be greater.

The impact of quench resorption is therefore expected to be wide-ranging for studies of vesicular experimental samples. The analysis of samples from Burgisser & Gardner (2005) suggests that studies of samples created under similar temperature, pressure and quench conditions (e.g. Larsen 2008; Mongrain et al. 2008) may have experienced similar modification by quench resorption. Consideration of the controls of characteristic H_2O diffusivity, quench timescale and original porosity on quench resorption (summarised in Fig.s 7.1 and 7.3) will enable the results of other reported studies to be evaluated for the possible effect of quench resorption. For example, the study of Westrich & Eichelberger (1994), which tested the foam collapse model of obsidian formation, focused on samples with high original porosities (up to 80 vol%) and so observed

porosities might be expected to be little affected by quench resorption. However, the sample quench to 350 °C took 1 to 2 minutes, in contrast to the < 10 seconds estimated for the Burgisser & Gardner (2005) study, and so this longer quench timescale increases the potential for a significant amount of H_2O resorption, hence porosity reduction.

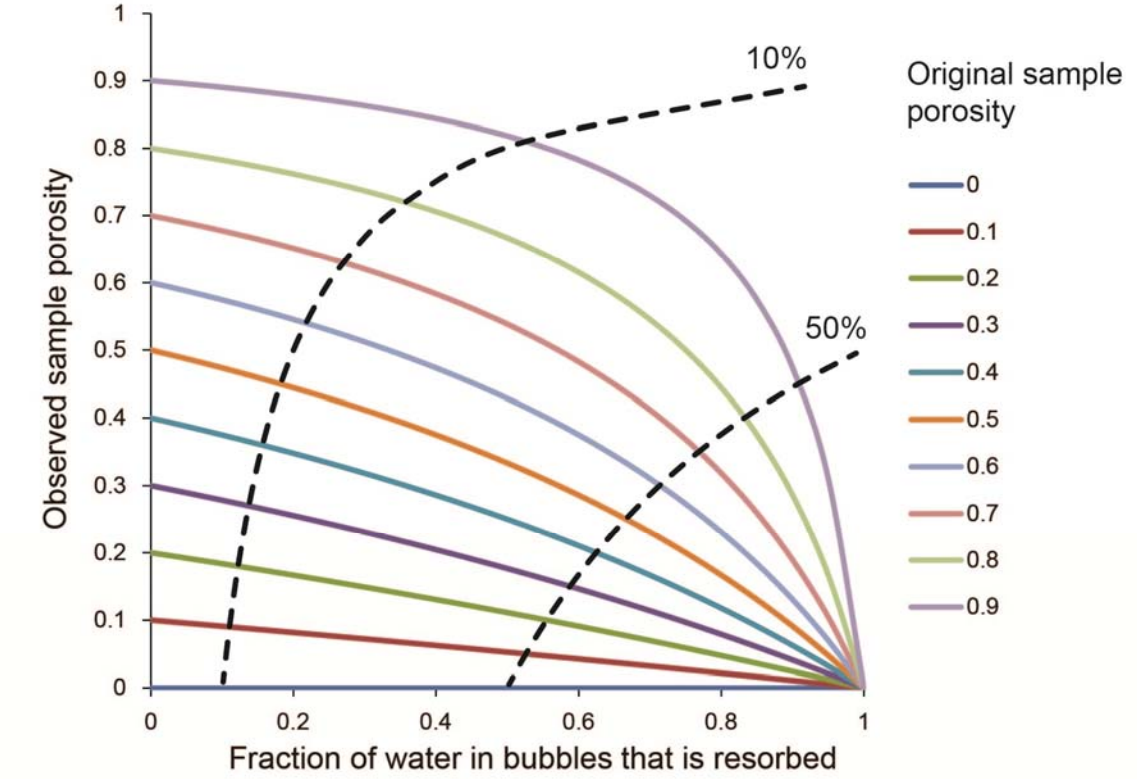

Fig. 7.1 Impact of bubble resorption as a function or original sample porosity

For a given amount of H_2O resorption, the reduction in the observed porosity will vary as a function of the original sample porosity. The black dashed contour lines show the fraction of H_2O that must be resorbed in order to achieve a 10% and 50% decrease between the original and observed sample porosity.

In a similar way, these controls on quench resorption can be considered when designing future experimental studies in order to minimise undesirable modifications to bubble populations where possible. Where samples are affected by quench resorption, BSEM image analysis can provide a rapid, qualitative assessment of resorption by evaluation of the half-fall distance of extracted greyscale profiles, while more quantitative assessments can be made using SIMS-calibrated BSEM

imaging analysis, and may ultimately be used to correct observed sample porosities to their pre-quench values.

7.3 Watkins et al. (2012): a case study

Watkins et al. (2012) analysed H_2O_t and CO_2 profiles around vesicles in obsidian clasts from the ca. 1340 AD eruption of Mono Craters, California (Fig. 7.1). These clasts were sourced from site 'bb' and are thought to be fragments from chilled margins of feeder dykes and conduits that were subsequently entrained in the eruption as the conduit was eroded (Newman et al. 1988). Watkins et al. present profiles around two vesicles (Bubble A and Bubble B) which show higher H_2O_t adjacent to the vesicle wall (Fig. 7.2). CO_2 data are more heterogeneous and does not vary systematically with distance from the vesicle walls. The authors interpret the observed H_2O_t concentration profiles as evidence of bubble resorption and attribute this to a pressure increase in the conduit of ~10 MPa. The heterogeneity of the observed CO_2 profiles is attributed to concentration variations associated with rewelded fractures and collapsed bubbles caused by earlier cycles of pressure increase and decrease, which are preserved in CO_2 profiles but not H_2O_t profiles because of the slower diffusivity of CO_2 relative to H_2O.

In reaching their conclusions, Watkins et al. (2012) eliminate a temperature decrease as a potential cause of the observed resorption on the basis of the population of small vesicles which surround Bubble B (Fig 7.2). These bubbles are inferred to have nucleated in a shell of H_2O_t-enriched melt surrounding the larger bubble (i.e. in its resorption halo). They state that the observed H_2O_t concentrations at the walls of Bubbles A and B would correspond to equilibrium H_2O solubility at temperatures around the glass transition of the melt. The authors conclude that temperature decrease could not cause the observed bubble resorption, since the melt surrounding the resorbing bubble would be too viscous for the secondary bubble population to nucleate. However, according to the conceptual framework developed in this thesis, the presence

of the secondary bubble population is entirely consistent with a temperature decrease as the cause of bubble resorption. When the chilled, marginal clasts were entrained in the erupting magma they would have experienced a transient reheating and depressurisation. The secondary bubble population surrounding Bubble B could therefore have formed because this reheating exceeded T_g, enabling the now-supersaturated melt in the hydrated halo to foam.

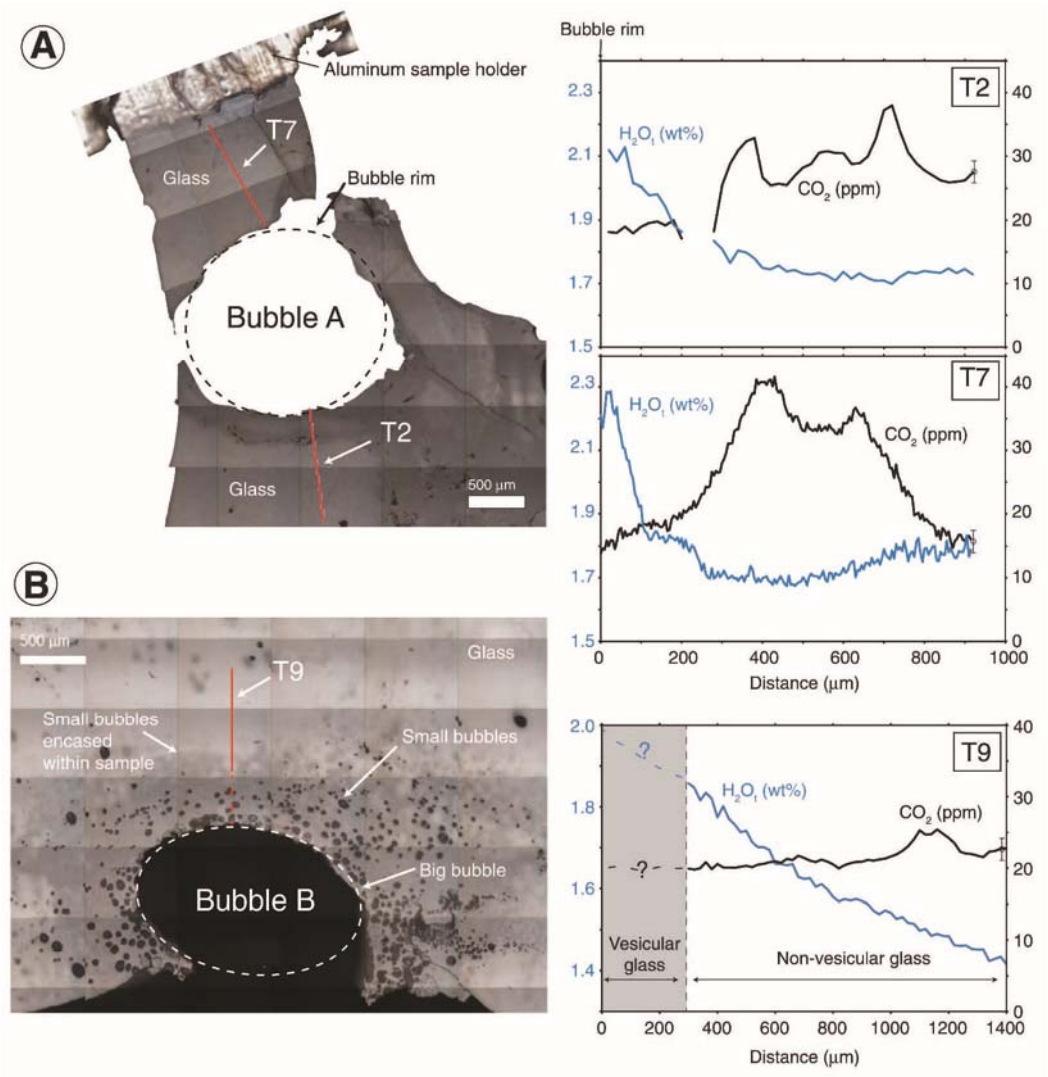

Fig. 7.2 Bubble resorption H_2O_t concentration profiles of Watkins et al. (2012)

H_2O_t (blue) and CO_2 (black) concentration profiles measured around vesicles in pyroclastic obsidian fragments from Mono Craters, California, by Watkins et al. (2012).

H_2O-CO_2 solubility models suggest that cooling to ~600°C would be required to cause the observed increase of H_2O_t at the bubble walls (Newman & Lowenstern 2002; Liu et al. 2005; Watkins et al. 2012). The very interpretation that these clasts represent fragments of a chilled conduit margin is based on speciation data which shows that they cooled to at least 600°C (Newman et al. 1988; Stolper 1989); cooling that could not have taken place at atmospheric pressure after eruption without the H_2O-rich melt exsolving to form a foam (Newman et al. 1988). Geospeedometry work on obsidian fragments from the same site using hydrous speciation suggests that cooling in the conduit occurred at ~0.1 K/s (Zhang et al. 2000), which would be sufficient to create the observed hydration lengthscales with a characteristic H_2O diffusivity (DH_2O_{ch}) of ~10^{-10} - 10^{-11} m^2/s (Fig. 7.3). This is comparable with the DH_2O_{ch} values calculated for the experimental samples analysed in previous chapters (Fig. 7.3), and would be lower if, as in the experimental samples, some of the diffusion that produced the observed profiles of Watkins et al. occurred below the glass transition (increasing *t*, hence decreasing DH_2O_{ch}). The observed vesicle wall H_2O_t concentrations and resorption lengthscales of Watkins et al. can therefore be explained by cooling within the conduit without the need to infer a pressure increase.

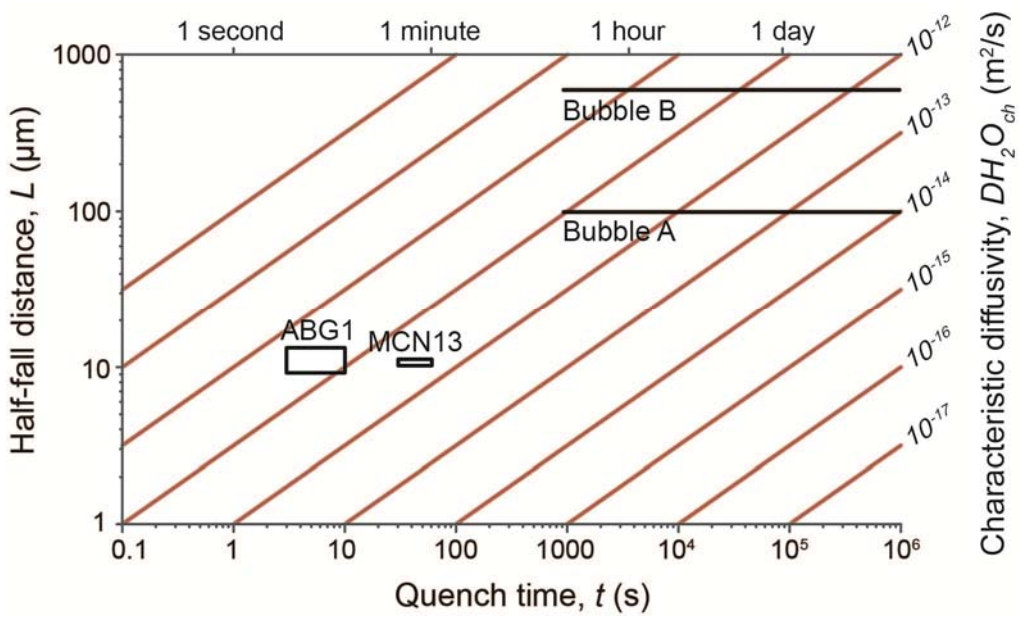

Fig. 7.3 Characteristic diffusivity and quench time of Watkins et al. (2012) H_2O_t profiles

Figure showing the relationship of half-fall distance, quench time and characteristic diffusivity during quench (c.f. Chapter 4 Fig. 4.8). Half-fall distances of the concentration profiles for Bubbles A and B of Watkins et al. (2012) are compared to those of the experimental samples ABG1 and MCN13 (Chapter 4). Lower *t* value for Watkins profiles are based on cooling from 850 °C – 600 °C at 0.1 K/s.

Further geospeedometry work on clasts from Mono Craters has concluded that some clasts experienced transient reheating on the order of seconds to minutes during eruption before a final rapid quench (Zhang et al. 1995b, 1997, 2000), which supports the alternative interpretation that the secondary bubble population around Bubble B is consistent with a temperature, rather than pressure, mechanism. In addition to explaining the observed secondary bubble population around Bubble B, this thermal history of slow cooling in the conduit, transient reheating in the eruption column and fast final quench may explain some of the data contained in the Supplementary Information of Watkins et al. (2012) (Fig 7.4). In a supplementary figure they present additional data from a single clast where one vesicle has a H_2O_t concentration profile consistent with bubble growth (T10) while another vesicle has a uniform H_2O_t concentration profile consistent with an equilibrium state (T11). The two bubbles are separated by a distance of 5.5 mm. Since the thermal

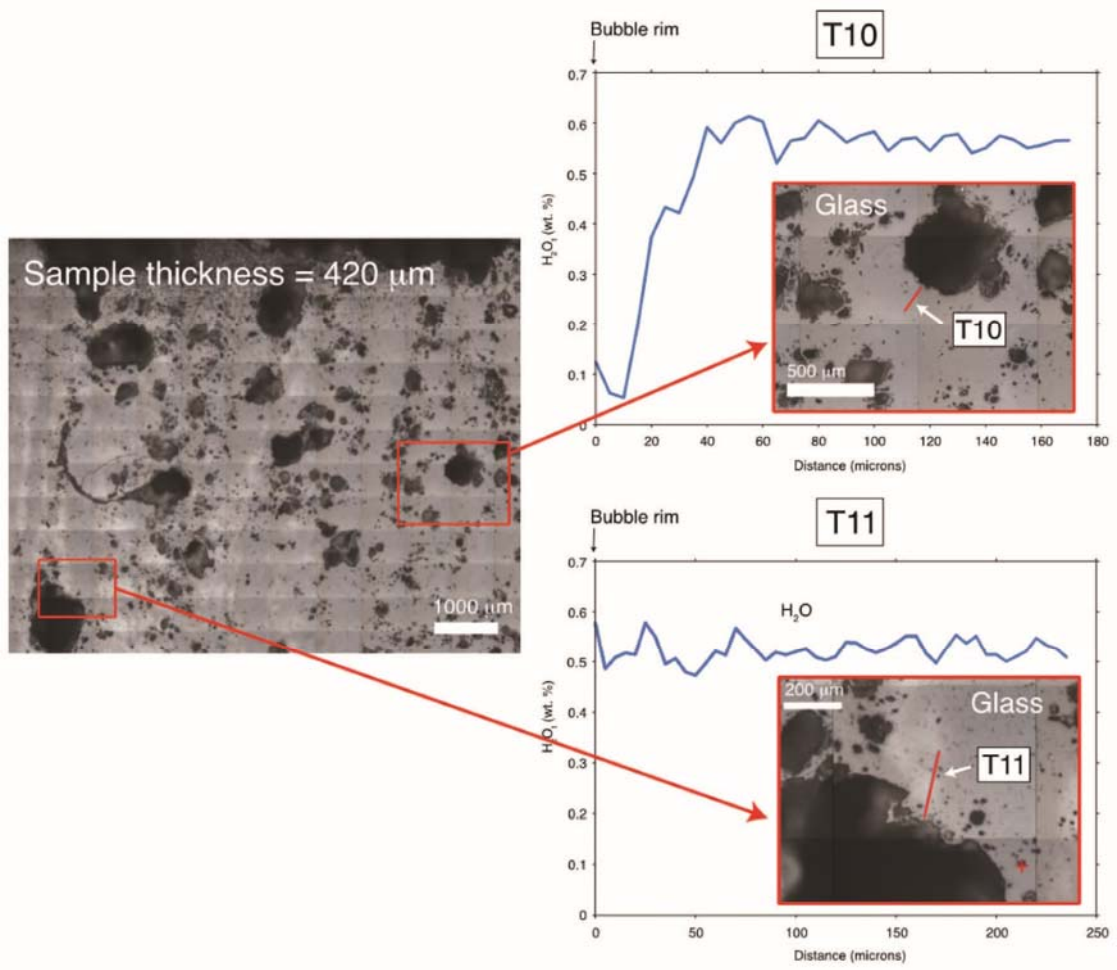

Fig. 7.4 Additional H_2O_t transects of Watkins et al (2012) Supplementary Information

Additional H_2O_t concentration profiles presented in the Supplementrary Information of Watkins et al. (2012), showing a single clast containing a vesicle with a concentration profile consistent with bubble growth (T10) and another that is consistent with being in equilibrium with the melt (T11).

diffusivity of a rhyolite glass or melt of similar H_2O_t content is 0.5 – 0.55 mm^2/s (Romine et al. 2012) it would take ~60 seconds for the temperature increase to propagate across the clast from one bubble to the other. If the equilibrium vesicle was in the interior of the clast and the growing vesicle closer to the surface, the surface bubble could experience sufficient reheating to start growing while the interior bubble remained unaffected by reheating during the brief timescale of entrainment and eruption. This is consistent with data on heat conduction within clasts (e.g. Xu & Zhang 2002, Zhang et al. 2000). It is also interesting to note that Bubble A (Fig. 7.2) has a decrease in H_2O_t over the closest ~20 µm to the bubble wall, which may suggest a brief period of bubble

growth following the original bubble resorption. Such a profile could form in ~13 s at DH_2O_t = 7.88 x 10^{-12} m^2/s (assuming reheating to 850 °C; Ni & Zhang, 2008).

It is therefore clear that, while a pressure increase mechanism for bubble resorption at Mono Craters is plausible, a temperature decrease mechanism is also plausible. In particular, the evidence of secondary bubble populations within the resorption halos of larger vesicles alone cannot be used to discount a thermal mechanism for bubble resorption, since they can be caused by cooling and subsequent reheating. Instead, they are merely indicators that H_2O solubility first increased and then decreased. Further evidence is then required to determine the mechanism by which this variation in H_2O solubility occurred. In the scenario of a fragment chilled at a conduit margin and then incorporated into an erupting magma, it is to be expected that pressure and temperature histories may combine in complex ways to determine the pattern of H_2O concentration profiles around vesicles. It is probable that the use of H_2O speciation data would provide some additional insight into the bubble growth and resorption histories of such clasts.

7.4 FTIR speciation data as a forensic tool for investigating natural samples

As demonstrated in Chapter 6, H_2O speciation data for concentration profiles around vesicles can be used to identify bubble resorption caused by temperature decrease during quench. As a result of the decreasing rate of the speciation interconversion reaction with decreasing temperature, excess H_2O entering the melt as H_2O_m during bubble resorption cannot be converted to OH groups over the timescale of quench. Such temperature controlled bubble resorption is therefore characterised by disequilibrium speciation in the resorption halo, with higher H_2O_m:OH ratios than would otherwise be expected. Where quench is sufficiently rapid, the original OH profile relating to the pre-quench experimental conditions is preserved.

This characteristic disequilibrium, high H_2O_m:OH signal may be used to distinguish quench resorption from pressure-driven resorption in otherwise unconstrained natural samples. Fig. 7.5 shows the variation in H_2O speciation and H_2O_m:OH ratio with H_2O_t concentration, for 825 °C and 500 °C (derived using the *K* relationship of Nowak & Behrens 2001). These data represent equilibrium speciation at these temperatures. If bubble resorption is caused by pressure increase in the conduit, where temperature is high and the interconversion reaction rate is rapid, then the variation in H_2O_m:OH along the bubble concentration profile should follow the equilibrium speciation for the measured H_2O_t concentration. If, during sample quench, the speciation data are modified by the 'quench effect' (but not by any further temperature-controlled resorption), then H_2O speciation will still be in equilibrium but with a lower temperature. If, however, bubble resorption is caused by temperature decrease, the H_2O_m:OH ratio will increase in the resorption halo by a larger amount than can be explained by the equilibrium variation in H_2O_m:OH with H_2O_t concentration.

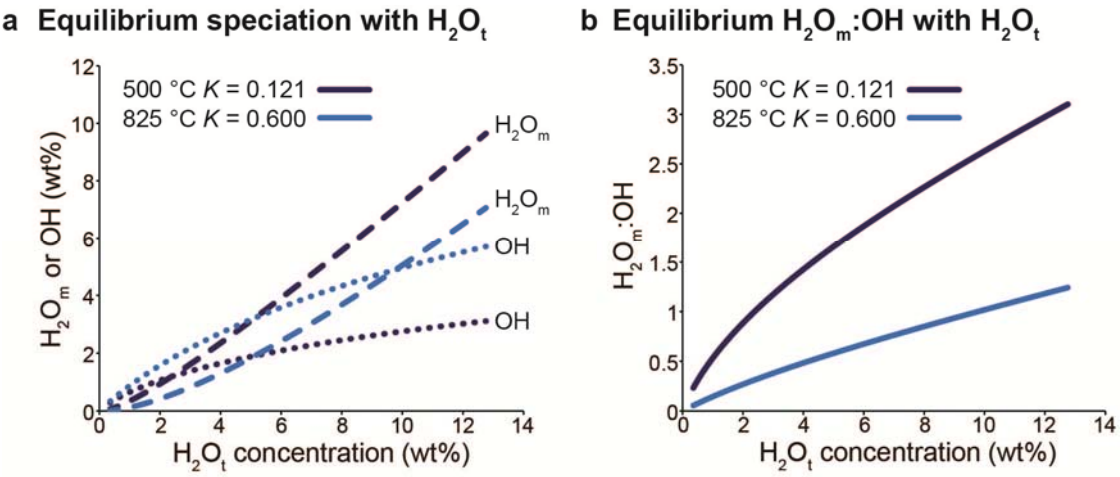

Fig. 7.5 Variation of H_2O speciation with H_2O_t concentration and temperature

a The variation in concentration of H_2O_m and OH with H_2O_t concentration in rhyolite melt for equilibrium speciation at 500 °C (dark blue) and 825 °C (light blue). **b** Variation in the ratio H_2O_m:OH with H_2O_t concentration for equilibrium speciation at 500 °C (dark blue) and 825 °C (light blue). Figures constructed using the *K* relationship of Nowak & Behrens (2001)

Utilising this concept, Fig. 7.6 outlines schematic H_2O_t, H_2O_m and OH profiles that might be expected from pressure-controlled and temperature-controlled bubble resorption, for both fast and slow quench timescales. All fast quench profiles have the same far field H_2O_t, H_2O_m and OH concentrations (hence H_2O_m:OH) as the pre-quench profile, since it is assumed that quench is sufficiently rapid to prevent modification via the quench effect. Since the original pre-quench profile corresponds to high temperatures, the concentration of OH is therefore greater than the concentration of H_2O_m (Nowak & Behrens 2001). Profiles corresponding to slow quench however are assumed to have been affected by the quench effect. Far field concentrations therefore correspond to a lower temperature than the original pre-quench profile, and so the concentration of H_2O_m is shown as greater than the concentration of OH.

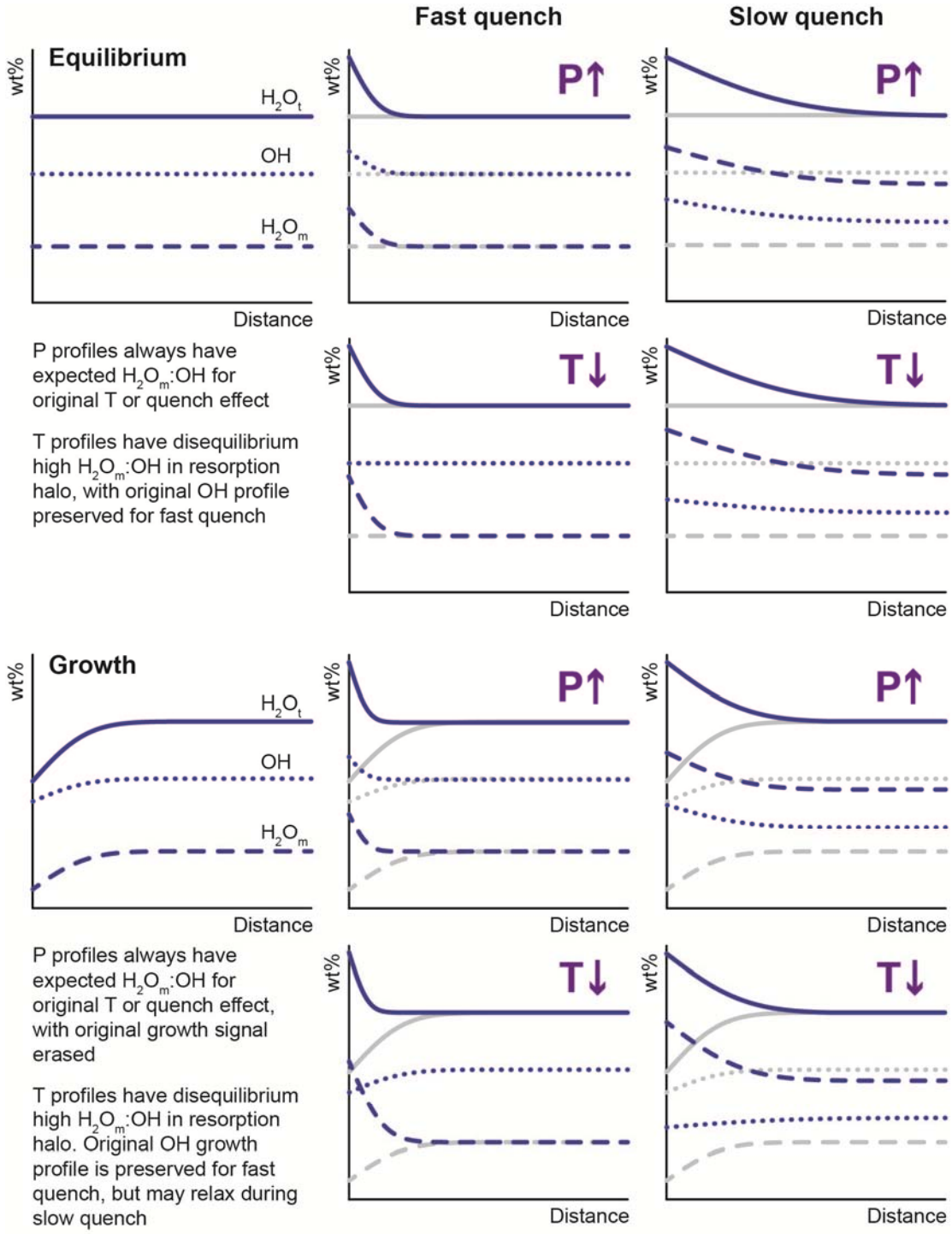

Fig. 7.6 Possible H_2O concentration and speciation profiles for different resorption conditions

Schematic figures showing how initial pre-quench profiles derived from equilibrium (top) and bubble growth (bottom) conditions may alter as a result of bubble resorption due to pressure (P)

increase at high temperature followed by fast or slow quench; and as a result of temperature (T) decrease during fast or slow quench. See text for full discussion.

For a bubble previously in equilibrium with the melt (upper half of Fig. 7.6), if a pressure increase at high temperature causes it to begin resorbing, the H_2O_m:OH ratio increases within the resorption halo as a consequence of increasing H_2O_t concentration. If quench is fast, the equilibrium speciation corresponding to high temperature is preserved; if quench is slow, H_2O_m:OH along the profile will be in equilibrium with a lower temperature. If the bubble was originally growing (lower half of Fig. 7.6) prior to resorption caused by a pressure increase, the observed concentration profiles and H_2O_m:OH will be the same as for the equilibrium bubble. The only difference will be a shorter half-fall distance, since the original concentration depletion at the bubble wall would need to be filled in in order for the concentration profile to propagate further. Bubble resorption caused by pressure increase at magmatic temperature will therefore remove all record of the previous bubble growth history.

If bubble resorption is caused by temperature decrease during quench, however, this previous growth history may be preserved. If an equilibrium bubble begins to resorb during fast quench, the original flat OH concentration profile will be preserved, while only H_2O_m will increase in the resorption halo. The flat OH concentration and highly disequilibrium increase in H_2O_m:OH within the resorption halo will therefore identify both a temperature cause for bubble resorption and the previous state of bubble growth. If the same equilibrium bubble is quenched more slowly however, it may be difficult to distinguish it from the profiles created by pressure-driven bubble resorption. If the interconversion reaction has time to act during the initial stages of quench, some of the influx of H_2O_m from the resorbing bubble will be converted to OH. The original OH profile will therefore be modified and will increase towards the vesicle wall, as for pressure-driven bubble resorption. Although the eventual breakdown of the interconversion reaction will lead to disequilibrium H_2O_m:OH ratios, the degree of disequilibrium will be smaller than for fast quench

and may be lost within analytical uncertainty. Moreover, the increase in the OH profile could also be interpreted as evidence of pressure-driven bubble resorption prior to quench.

In the case of an original bubble growth concentration profile prior to quench, temperature-controlled resorption during fast quench will result in preservation of the original OH profile and greatly elevated H_2O_m:OH ratios in the resorption halo. The temperature cause of bubble resorption and the previous bubble growth history could therefore be distinguished. In the case of slower quench however, the original OH concentration profile may begin to relax as some of the H_2O_m from bubble resorption is converted to OH. Such a profile could in fact be misinterpreted as evidence of a rapidly quenched equilibrium bubble, unless the far field speciation shows that the glass transition temperature was low and therefore that quench was slow.

It is clear therefore that reconstruction of the mechanism of observed bubble growth and the reconstruction of previous bubble growth history will be most successful for samples that are quenched quickly with respect to the timescale of the interconversion reaction. Further complications will arise if there is another volatile species present, such as CO_2, and if bubble growth and resorption is affected by vapour fluxing (e.g. Gonnermann & Manga 2005; Yoshimura & Nakamura 2008).

In the dynamic pressure and temperature conditions of a volcanic system, it is likely that bubbles could experience a range of potentially complex pressure and temperature histories that will modify their volatile concentration profiles. In all the scenarios described in Fig 7.6, it is assumed that profiles derived from pressure-induced resorption at high temperature are not subsequently affected by additional bubble resorption as a result of cooling during quench. The evidence presented in this thesis however demonstrates that it is possible to have significant resorption even during rapid quench. Therefore it is unlikely that bubble resorption profiles derived from pressure increase will ever be unmodified by subsequent quench resorption. All volcanic glasses will experience a temperature decrease during their final quench and so could potentially be

affected by quench resorption. The effects of cooling must therefore be evaluated before further inferences can be made about bubble growth histories, and FTIR analyses of H_2O speciation data provide a tool to do so.

7.5 Analysis of quench resorption in natural samples

By considering the controls on quench resorption investigated in this thesis, the significance of bubble resorption can be estimated for different volcanic contexts. It has been shown that the amount of H_2O that is lost from a vesicle depends on the time spent above the glass transition during quench and on factors controlling H_2O diffusivity, principally H_2O_t concentration. The impact that this H_2O mass loss will have on bubble volumes and sample porosities will in turn vary with the original sample porosity prior to quench, with the greatest reduction in sample porosities expected for low original sample porosities.

Unlike experimental samples, which are quenched isobarically, quench in natural samples typically follows decompression, or occurs simultaneously. Depressurisation of magma causes bubble growth both by diffusion of H_2O into the bubble (since H_2O solubility decreases with decreasing pressure) and also by decompressive expansion, which becomes increasingly important as the magma approaches the surface. In many natural samples therefore, continuous degassing during ascent may, by lowering H_2O concentration in the melt, reduce H_2O diffusivity to the extent that significant resorption cannot occur during the timescale of quench, for example in an eruption column. Meanwhile, if magma ascent rates are sufficiently rapid that bubbles remain overpressured relative to the ambient pressure, bubbles may continue to expand due to ongoing decompressive expansion even as cooling may begin to increase H_2O solubility at the bubble wall.

In natural samples, two main categories will therefore be expected to be significantly affected by quench resorption. Conditions of high H_2O_t concentrations and low initial sample porosity are most likely to prevail in samples quenched at pressure, either by eruption under the confining

pressure of an ice or water body, or by cooling within the conduit. On the other hand, long quench timescales may make quench resorption important even for melts with low initial H_2O_t concentrations, and so quench resorption may also be significant in situations such as the formation of obsidian and rheomorphic flows.

For such samples, quench resorption represents both a challenge to and a tool for interpretation. Disequilibrium speciation resulting from quench resorption will obscure the original H_2O_t and H_2O_m concentration profiles and may alter speciation data that could otherwise be used to calculate cooling rates and the temperature of the glass transition. However, in rapidly quenched samples, the same disequilibrium speciation offers a way to identify samples affected by quench resorption and preserves evidence from the pre-quench bubble growth history, while in slowly quenched samples, it is likely that it is the effect of quench resorption on the cooling process itself which is of interest.

Fortuitously, the same conditions that make quench resorption significant are also the conditions that make samples suitable for speciation analysis using FTIR. High H_2O_t contents are necessary either to extract independent H_2O_m and OH speciation using the 5200 and 4500 cm^{-1} peaks, or to keep sample wafers thin relative to vesicle size (hence to reduce errors from volumetric averaging) and extract speciation data using the 3500 H_2O_t and 1630 cm^{-1} H_2O_m peaks, as in this study. Similarly, low sample porosities enable long concentration profiles to be derived without interaction of the resorption halos surrounding neighbouring vesicles. For samples with low H_2O_t concentrations where speciation data cannot be extracted, or with resorption profiles that are too short to be analysed by FTIR given the constraints of spatial resolution, H_2O_t resorption profiles can be investigated quantitatively using SIMS-calibrated BSEM imaging, or qualitatively using BSEM imaging alone. These data alone would not however determine the cause of bubble resorption, and so the likely pressure, temperature and chemical histories of such samples would each have to be considered in turn.

Correct attribution of the bubble resorption mechanism is critical to the interpretations that are then made about eruption dynamics. Bubble resorption profiles have the potential to inform ideas about volcanic processes such as repeated cracking and annealing of fractures at conduit margins as a result of pressure cycling (Watkins et al. 2012), timescales of magma convection (Carey et al. 2013) and the impact of vapour fluxing (Yoshimura & Nakamura 2008). This thesis has demonstrated that quench resorption and modification of melt H_2O concentrations can be added to these, and, since all samples experience cooling, must be accounted for before other resorption mechanisms can be invoked. To achieve better interpretations of observed bubble resorption in the future, it will be necessary to improve the understanding of how quench resorption varies with different conditions. Ideally, this will involve better constraints on H_2O solubility and diffusivity at low and intermediate temperatures, and on how the rate and position of the speciation interconversion reaction vary not only with temperature but also with H_2O_t concentration, pressure and melt composition. Such data could then be utilised in modelling of quench resorption processes. In the absence of these extended datasets, better understanding of quench resorption may be achieved by analysis of samples produced under conditions of controlled quench, so that the significance of parameters such as cooling rate, H_2O_t concentration and initial bubble growth state can be investigated.

7.6 Conclusions

In this study, the distribution of H_2O around vesicles in experimentally vesiculated volcanic glasses was investigated using SIMS-calibrated BSEM imaging and FTIR spectroscopy. Extracted H_2O concentration profiles show that H_2O was diffusing from the bubble/vesicle back into the melt/glass at the time of profile formation. Analysis of the observed concentration profiles within the context of the controlled pressure and temperature conditions of sample production lead to the conclusion that they are formed as a result of the increase of H_2O solubility with decreasing temperature during the quench process. Consideration of lengthscale and timing of the observed

profiles suggests that the majority of the observed H_2O diffusion during quench occurs at temperatures above the glass transition when loss of H_2O may be accompanied by reduction of bubble volumes; this process is therefore referred to as quench resorption.

The H_2O concentration profiles formed by quench resorption are controlled by the temperature-time history during quench, the H_2O concentration profile and the initial shape of the concentration profile prior to quench. The magnitude of bubble resorption will vary as a result of how these factors control the amount of H_2O lost back to the melt before the glass transition is reached, and will also vary with the initial porosity of the sample, being greater for lower initial sample porosities. Bubble volume reduction during quench resorption will also be influenced by thermal contraction of the H_2O vapour phase within the bubble. Where the magnitude of bubble resorption is large and the quench timescale is short, buckled melt films between neighbouring vesicles provide textural evidence of bubble volume reduction. The re-orientation of cracks as they encounter H_2O-enriched resorption halos around vesicles provides evidence that the temperature of the glass transition is locally depressed within the resorption halo, and that continued hydration of glass below the glass transition temperature may alter the local stress field as a result of volume changes.

H_2O speciation data obtained using FTIR reveal that quench resorption is characterised by disequilibrium speciation as a result of the breakdown of the speciation interconversion reaction over fast quench timescales. This characteristic signal of disequilibrium speciation within the resorption halo can be used to identify samples affected by quench resorption, and for rapid quench may preserve the OH concentration profile derived from pre-quench bubble growth conditions. H_2O speciation data are therefore likely to be critical in distinguishing between different causes of bubble resorption in order to make inferences about volcanic processes.

Quench resorption will be greatest for samples with long dwell times above the glass transition temperature, high H_2O concentrations and low initial porosities. Experimental studies are

therefore likely to be significantly affected by quench resorption, which may affect conclusions drawn from data on bubble volumes, sample porosities and H_2O concentration and speciation within glass affected by resorption halos. In natural settings, the effect of quench resorption will be greatest for samples quenched at high pressure, such as eruptions underneath ice or water bodies, or quenched within the volcanic conduit, and for samples that are quenched slowly, for example in thick volcanic deposits. Quench resorption will alter observed bubble volumes, sample porosities and H_2O distribution in the melt in these samples, and may act as an important mechanism for rehydrating melt and decreasing vesicularity. Since all natural and experimental samples experience a decrease in temperature during the final quench to glass, the effects of quench resorption must be evaluated before any further interpretation of affected parameters can be made, and may in itself provide insight into volcanic processes occurring both before and during final quench.

Appendices

"The earth hath bubbles, as the water has,

And these are of them. Whither are they vanished?"

Shakespeare's Macbeth, Act I Scene 3

Appendix 1: Calculating sectioning effects

Assuming Fickian diffusion in one dimension, the radial concentration profile for a resorbing bubble can be calculated according to:

$$[H_2O_t] = [H_2O_{t,far}] + ([H_2O_{t,wall}] - [H_2O_{t,far}])\ erfc\left(\frac{x}{2\sqrt{Dt}}\right)$$ Equation A1.1

where x is the distance along the profile from the bubble wall.

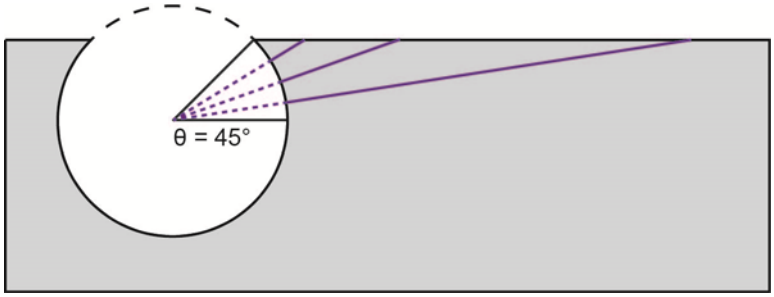

Fig. A1.1 Relating observed and radial distance to the vesicle wall

For vesicles sectioned at a different latitude to the equator, the concentration observed at a point along the measured profile will be controlled not by the distance to the vesicle wall as seen in plan view, but by the radial distance (*d*) to the bubble wall as seen in cross-section (solid purple lines).

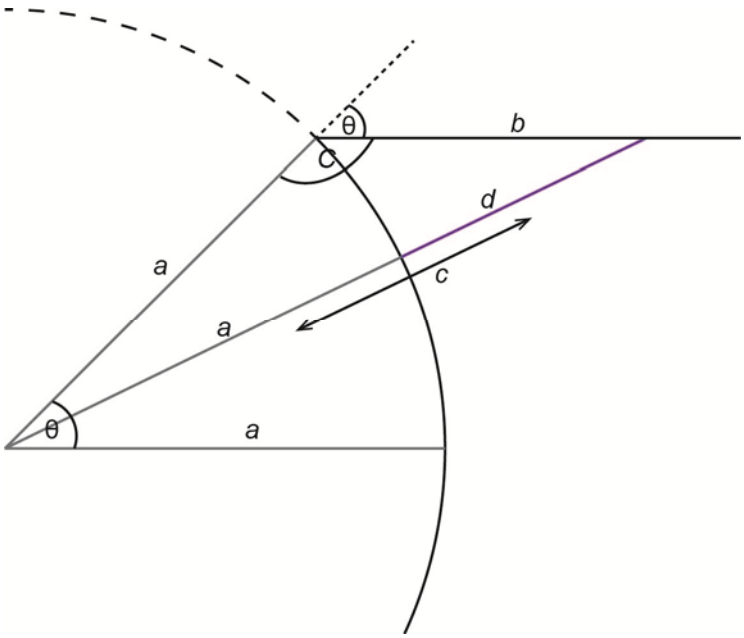

Fig. A1.2 Parameters used in calculation of sectioned profiles

The figure shows a close up of the vesicle wall and the sectioned surface (*b*) along which the H_2O concentration profile is measured. The distance that controls the observed H_2O concentrations is not *b* but instead the distance *d*. Use of the cosine rule enables the calculation of *d*.

In order to calculate how the measured profile would vary with angle of sectioning, for every distance along the measured profile (*b*) the true distance from the bubble wall along a radial profile must be determined (Fig A1.1, Fig A1.2). This distance, *d*, is calculated using the cosine rule, where *a* is the bubble radius, *b* is the distance from the bubble wall along the measured profile, *c* is the distance from the bubble centre along a radial profile, and θ is the latitude of the section. Since the angle $C = 180 - \theta$, and $d = c - a$, the cosine rule can be solved to give *d* as a function of measured distance along the profile (*b*) and latitude (θ):

$$c^2 = a^2 + b^2 - 2ab\,cosC$$

$$c^2 = a^2 + b^2 - 2ab\cos(180 - \theta)$$

$$c = (a + b - 2ab\cos(180 - \theta))^{\frac{1}{2}}$$

$$d = (a + b - 2ab\cos(180 - \theta))^{\frac{1}{2}} - a$$

By substituting *d* for x in the diffusion equation (Eq. A1.1), the concentration profile of a bubble can be calculated for different latitudes of sectioning. Thus for a vesicle of radius 100 μm and bubble wall and far field H_2O_t concentrations of 5 and 3 wt%, respectively, the measured profile for 10 seconds of diffusion at a diffusivity of 1 x 10^{-11} m^2/s will vary with the latitude of sectioning (Chapter 3 Fig. 3.11). The error in the concentration profile is small for latitudes within 30° of the equator, and decreases with vesicle size.

Appendix 2: SIMS-calibrated BSEM imaging datasets

This appendix contains figures showing the full H_2O dataset obtained using SIMS-calibrated BSEM imaging for the samples analysed in Chapter 4. These datasets were used to derive the mean H_2O concentration profiles for each sample shown in Chapter 4 Fig. 4.3. Although the extracted H_2O data extend to large distances from the vesicle wall, the mean H_2O concentration profile (shown also in these figures) was calculated for only a portion of this distance. This reflects the decreasing number of datapoints with distance from the vesicle wall, which would affect the calculated mean profile since data would be increasingly biased towards particular images (hence particular SIMS calibrations) where longer profiles were possible. In addition, although observed spacing between bubbles (Voronoi cells) was considered when extracting profiles in order to avoid moving beyond a vesicle's region of influence, the average bubble-bubble spacing in these samples is typically less than the profile lengthscale shown. Considering the spacing of vesicles in 3D, it is therefore not plausible to extend the calculated mean concentration profiles further since distant H_2O concentrations are likely to be determined by the resorption halos around other vesicles.

In all figures, the solid line shows the calculated mean H_2O_t profile and semi-opaque lines indicate twice the standard error of the mean.

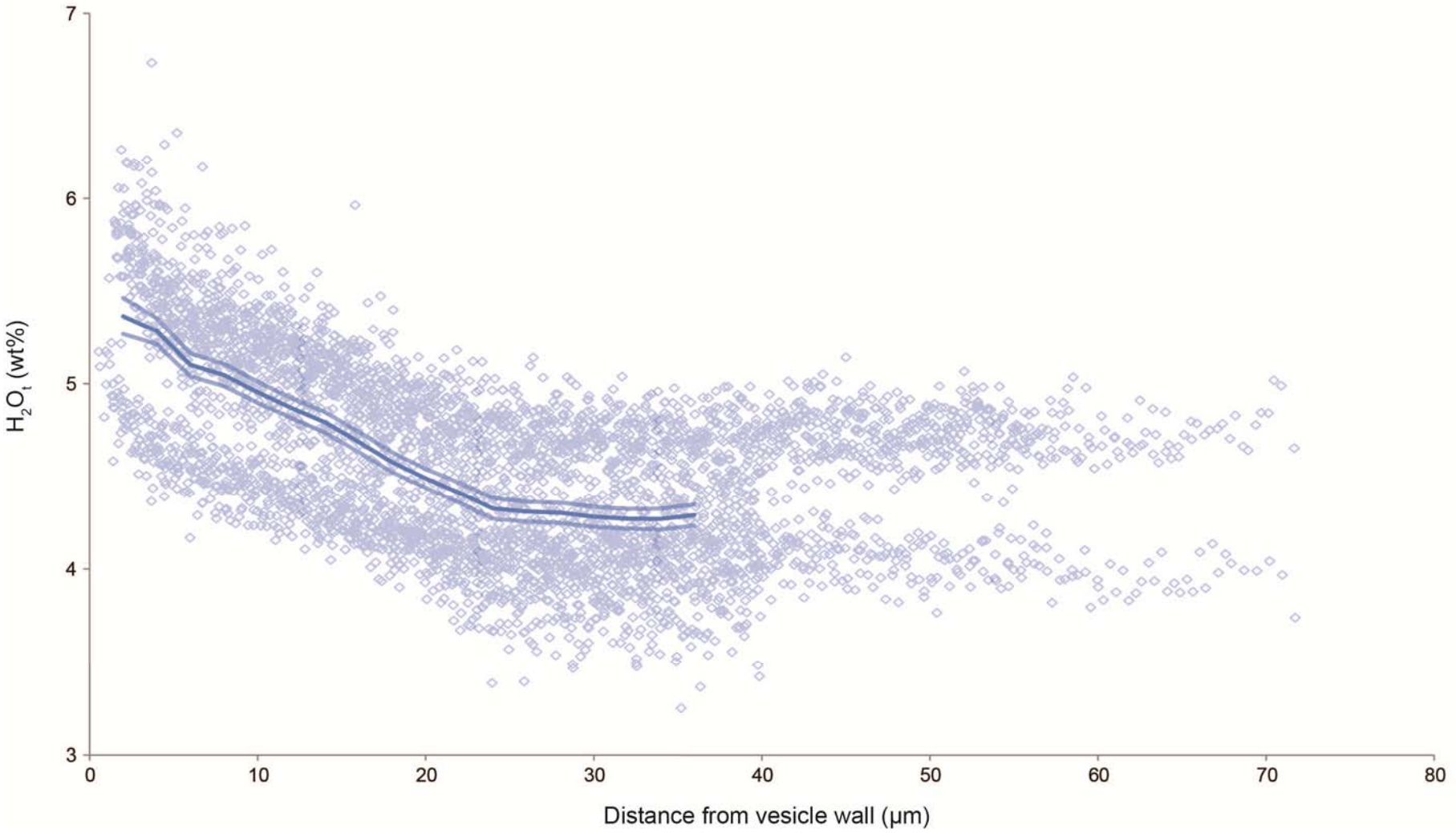

Fig. A2.1 Full extracted H_2O_t dataset and calculated mean H_2O_t concentration profile for sample ABG1

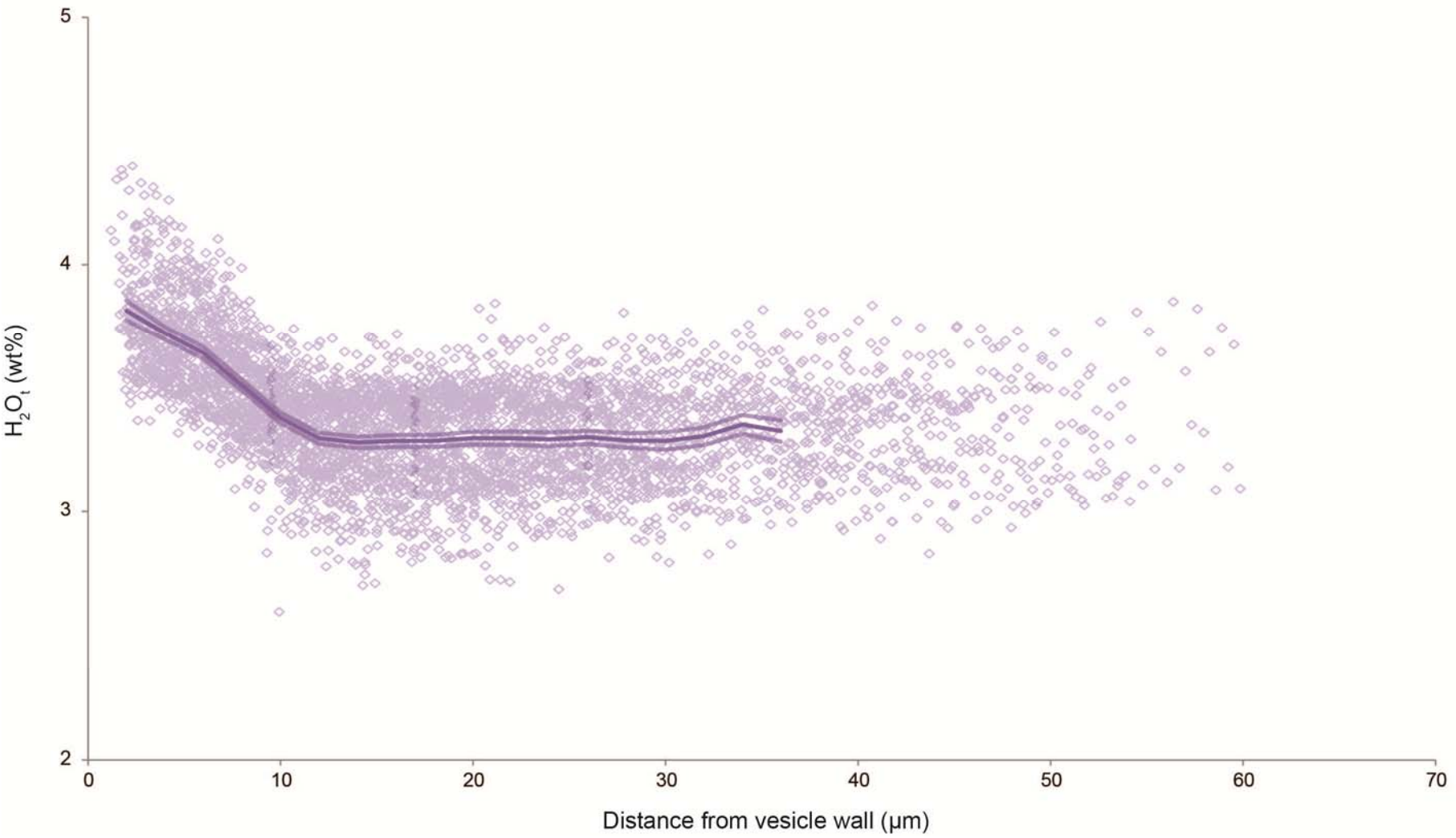

Fig. A2.2 Full extracted H_2O_t dataset and calculated mean H_2O_t concentration profile for sample ABG2

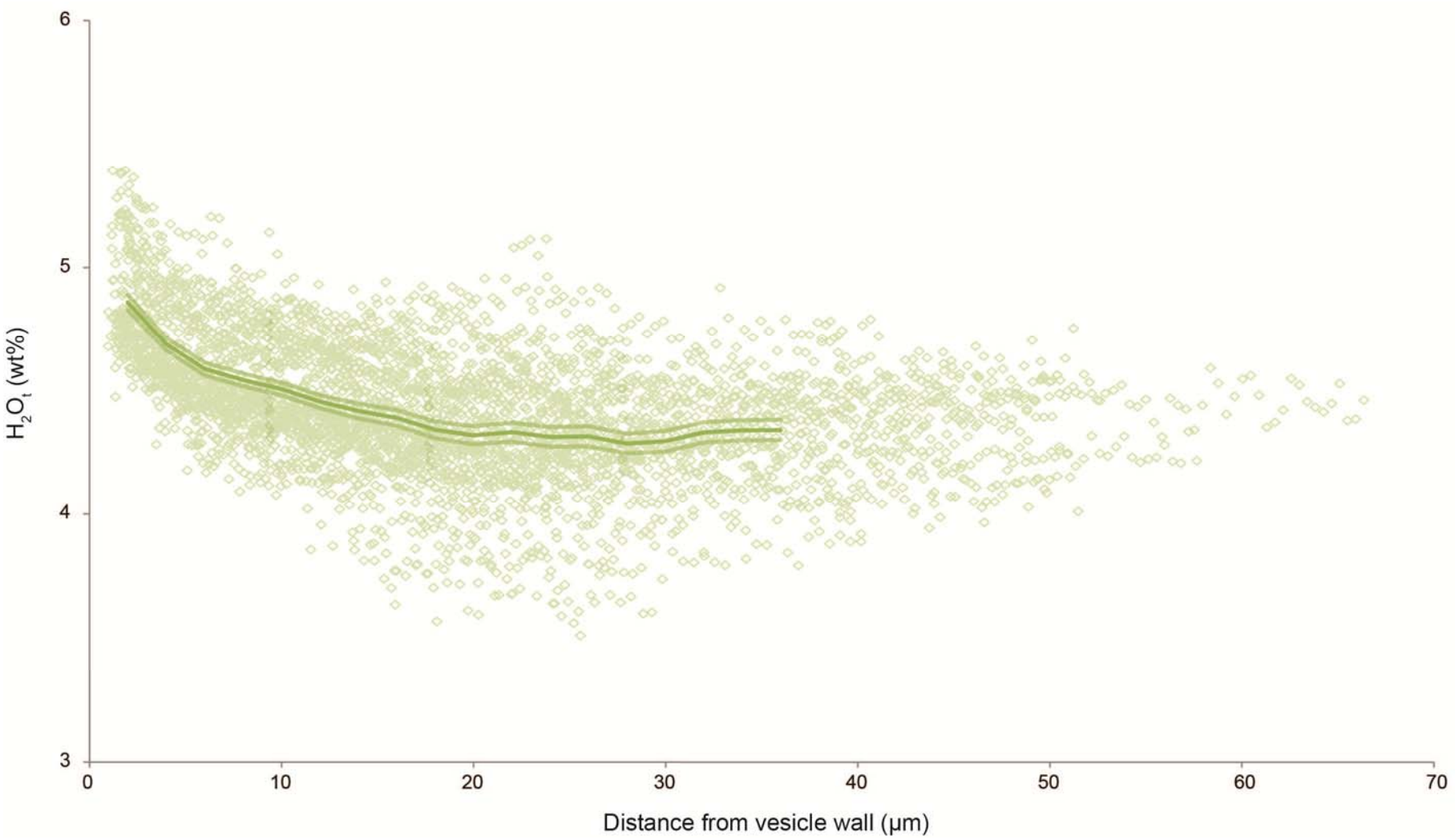

Fig. A2.3 Full extracted H_2O_t dataset and calculated mean H_2O_t concentration profile for sample ABG6

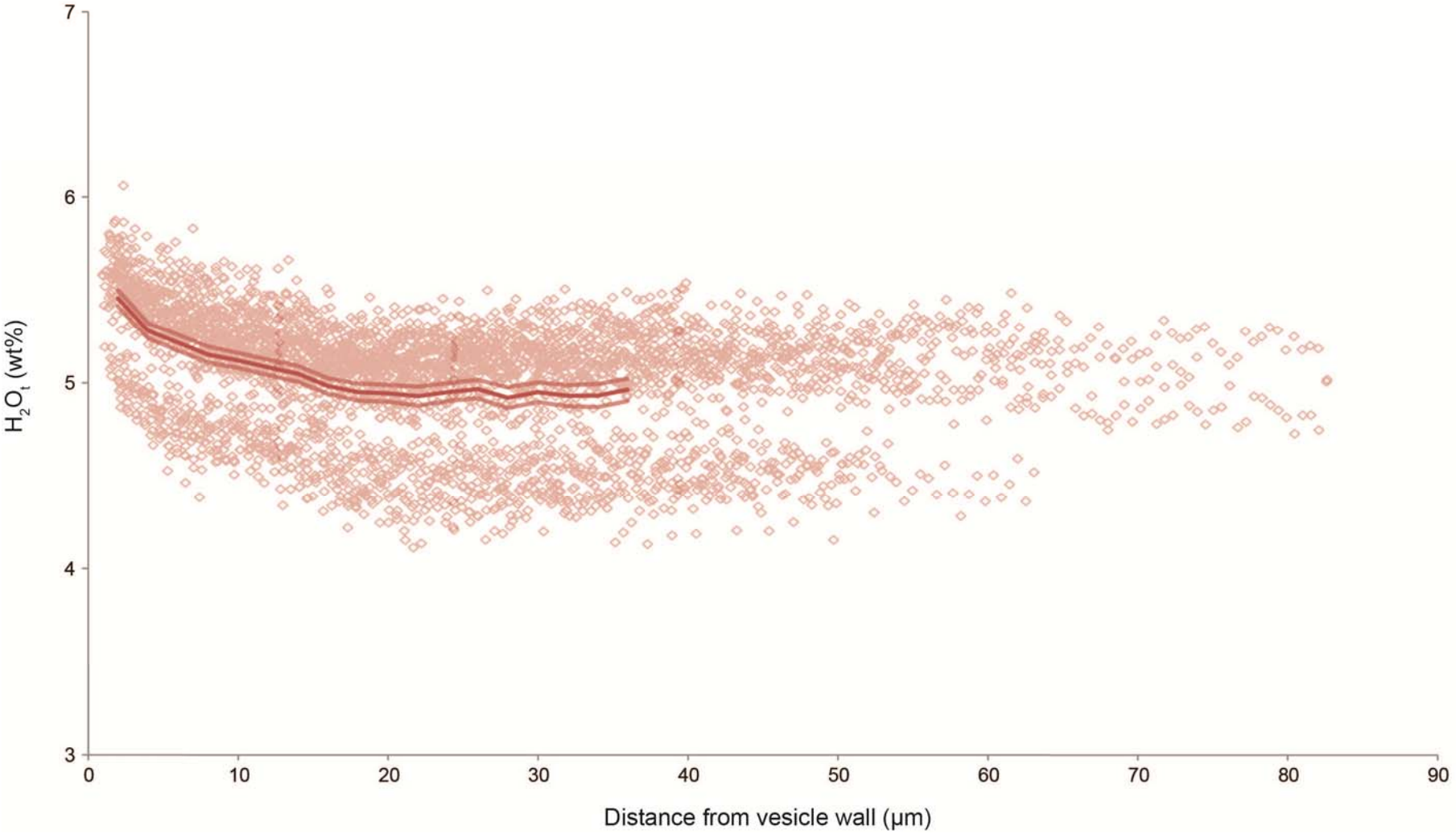

Fig. A2.4 Full extracted H_2O_t dataset and calculated mean H_2O_t concentration profile for sample ABG14

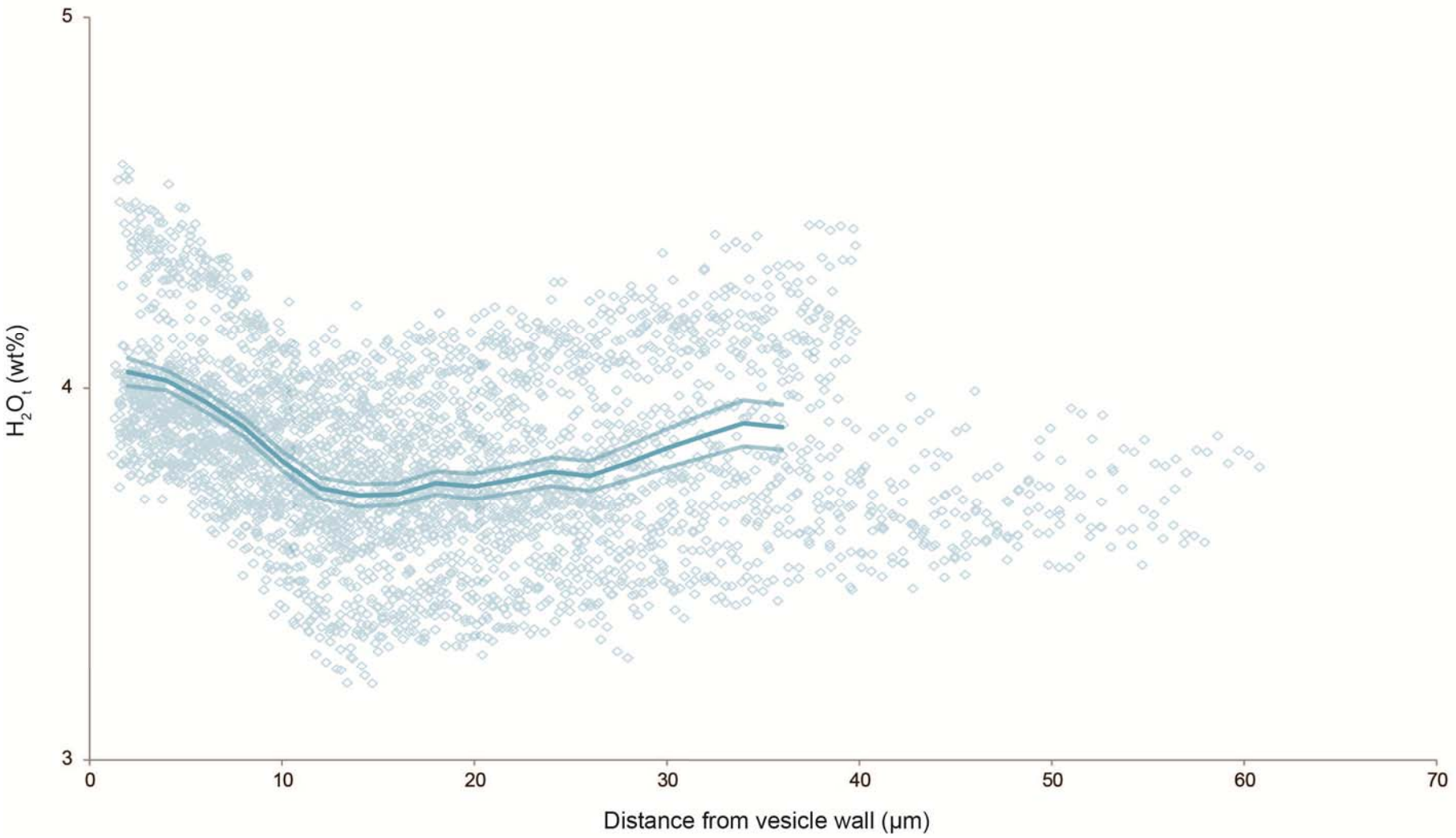

Fig. A2.5 Full extracted H_2O_t dataset and calculated mean H_2O_t concentration profile for sample ABG15

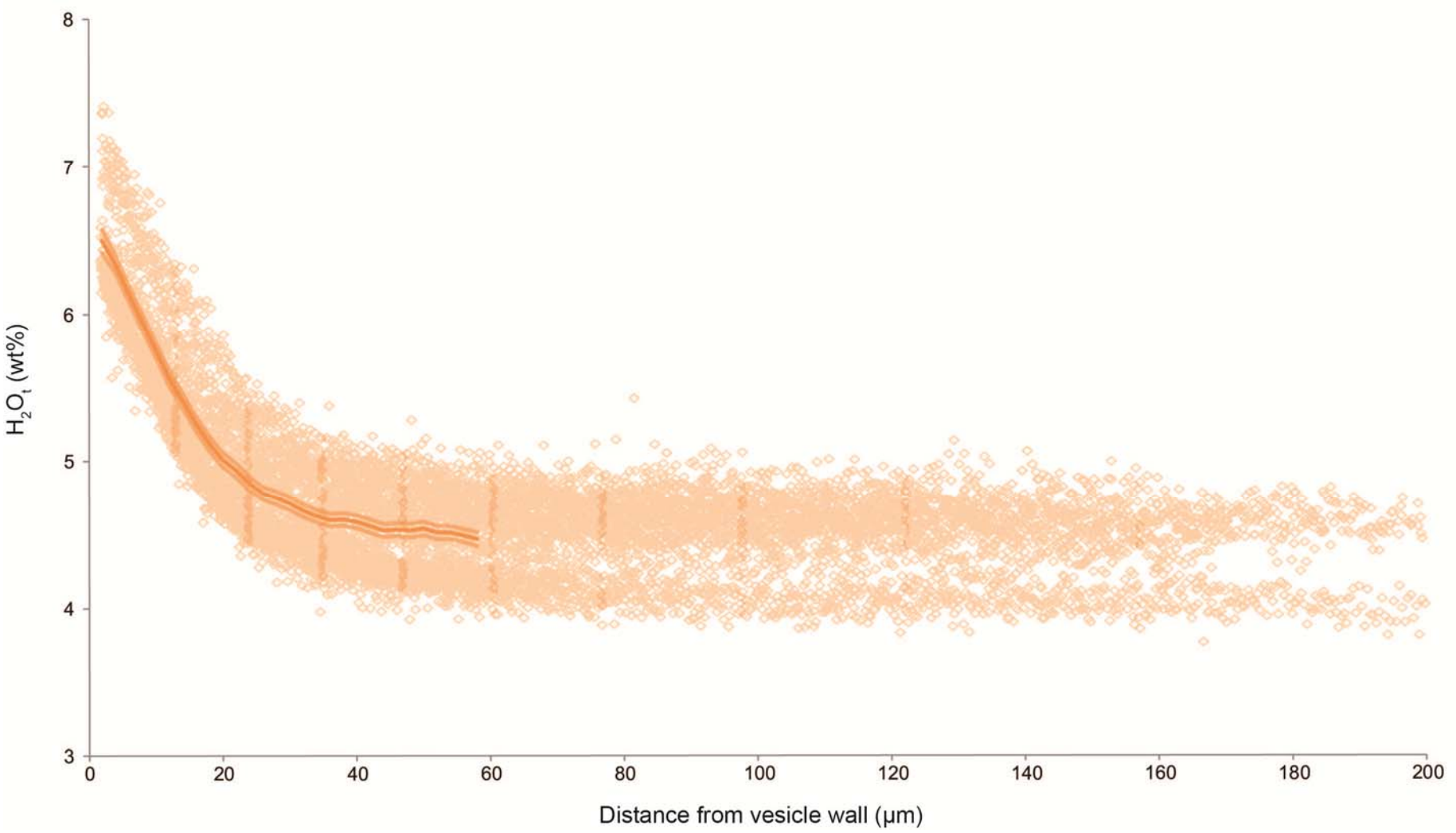

Fig. A2.6 Full extracted H_2O_t dataset and calculated mean H_2O_t concentration profile for sample IS14

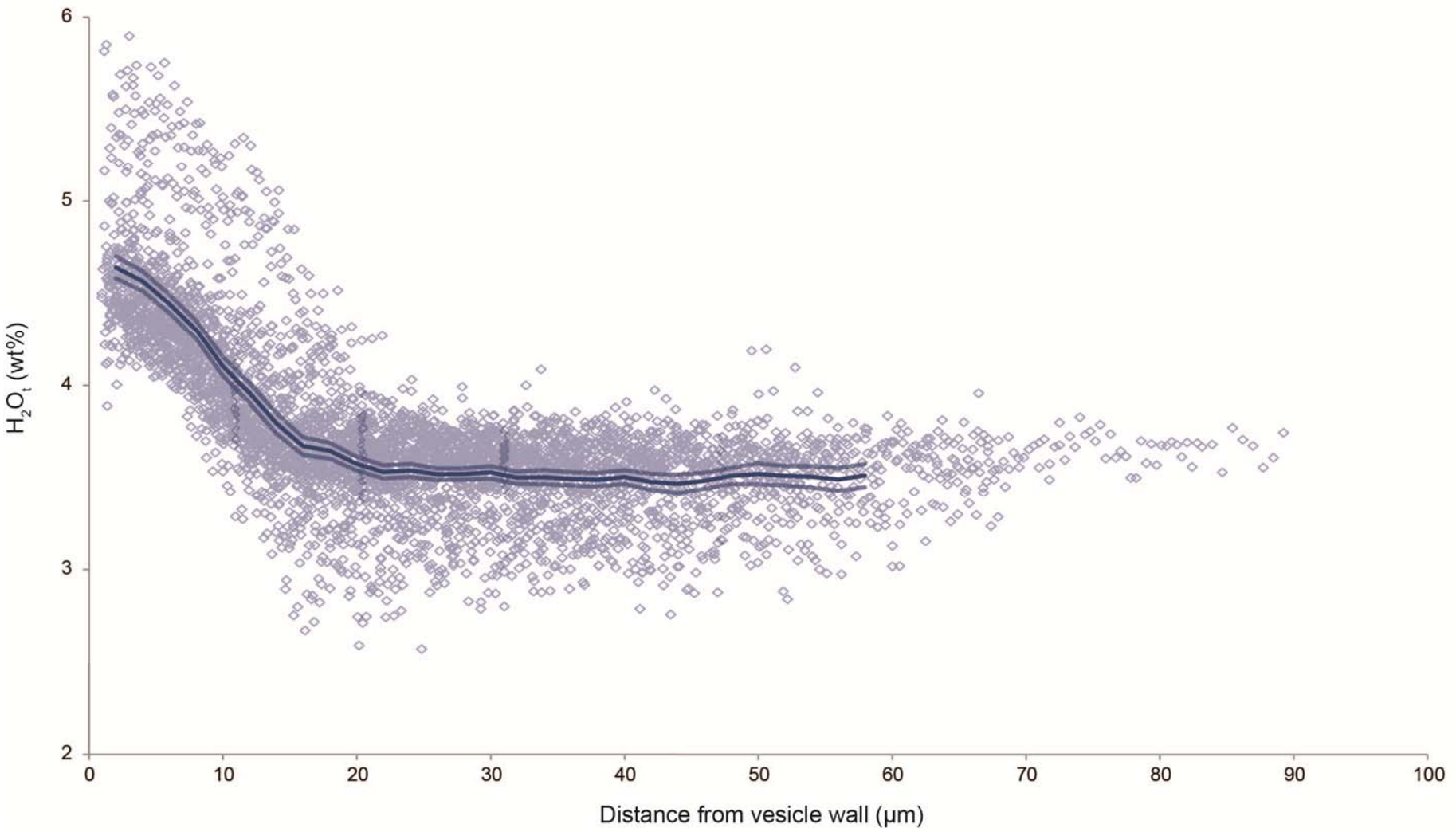

Fig. A2.7 Full extracted H_2O_t dataset and calculated mean H_2O_t concentration profile for sample MCN13

Appendix 3: Calculating equilibrium speciation

The equilibrium constant *K* for the H_2O speciation interconversion reaction can be defined in terms of the mole fractions of the components, according to:

$$K = \frac{[\mathrm{OH}]_\mathrm{e}^2}{[\mathrm{H_2O_m}]_\mathrm{e}\,[\mathrm{O}]_\mathrm{e}}$$

where square brackets represent mean activities approximated by mole fractions, and the subscript 'e' refers to a stable or metastable equilibrium (e.g. Zhang & Ni 2010).

The individual mole fractions are defined as (Zhang & Ni 2010):

$$[H_2O_t] = \frac{\frac{C_w}{18.015}}{\frac{C_w}{18.015} + \frac{(100 - C_w)}{W}}$$

$$[H_2O_m] = \frac{C_1}{C_w}\,[H_2O_t]$$

$$[OH] = 2([H_2O_t] - [H_2O_m])$$

$$[O] = 1 - [H_2O_m] - [OH]$$

where C_w is the wt% of H_2O_t, C_1 is the wt% of H_2O_m, and W is the molar mass of the dry melt on a single oxygen basis.

For a measured value of H_2O_t and a given value of *K*, the only unknown in this system of equations is C_1, the wt% of H_2O_m. By rearranging the equations in terms of C_1, it is possible to calculate C_1, hence the equilibrium concentrations in wt% of H_2O_m and OH, for any input value of H_2O_t and *K*.

References

Anovitz, L M et al., 2004. Isothermal time-series determination of the rate of diffusion of water in Pachuca obsidian. *Archaeometry*, 46(2), pp.301-326.

Anovitz, Lawrence M et al., 1999. The Failure of Obsidian Hydration Dating: Sources, Implications, and New Directions. *Journal of Archaeological Science*, 26, pp.735-752.

Anovitz, Lawrence M. et al., 2006. Obsidian hydration: A new paleothermometer. *Geology*, 34(7), p.517. Available at: http://geology.gsapubs.org/cgi/doi/10.1130/G22326.1 [Accessed March 13, 2012].

von Aulock, F.W. et al., 2013. Timescales of texture development in a cooling lava dome. *Geochimica et Cosmochimica Acta*, 114, pp.72-80. Available at: http://linkinghub.elsevier.com/retrieve/pii/S0016703713001543 [Accessed June 11, 2013].

Baker, D.R. & Alletti, M., 2012. Fluid saturation and volatile partitioning between melts and hydrous fluids in crustal magmatic systems: The contribution of experimental measurements and solubility models. *Earth-Science Reviews*, 114(3-4), pp.298-324. Available at: http://linkinghub.elsevier.com/retrieve/pii/S0012825212000773 [Accessed September 3, 2012].

Bartholomew, R.F. et al., 1980. Infrared spectra of a water-containing glass. *American Ceramic Society Journal*, 63, pp.481-485.

Le Bas, M.J. & Streckeisen, A.L., 1991. The IUGS systematics of igneous rocks. *Journal of the Geological Society, London*, 148, pp.825-833.

Behrens, H. & Zhang, Youxue, 2001. Ar diffusion in hydrous silicic melts : implications for volatile diffusion mechanisms and fractionation. *Earth and Planetary Science Letters*, 192, pp.363-376.

Behrens, Harald, Zhang, Youxue & Xu, Z., 2004. H2O diffusion in dacitic and andesitic melts. *Geochimica et Cosmochimica Acta*, 68(24), pp.5139-5150. Available at: http://linkinghub.elsevier.com/retrieve/pii/S0016703704005393 [Accessed September 21, 2013].

Blank, J.G., Stolper, E.M. & Carroll, M.R., 1993. Solubilities of carbon dioxide and water in rhyolitic melt at 850°C and 750 bars. *Earth and Planetary Science Letters*, 119(1-2), pp.27-36. Available at: http://linkinghub.elsevier.com/retrieve/pii/0012821X9390004S.

Blower, J.D., Mader, H M & Wilson, S D R, 2001. Coupling of viscous and di ¡ usive controls on bubble growth during explosive volcanic eruptions. , 193, pp.47-56.

Blundy, J. & Cashman, K., 2005. Rapid decompression-driven crystallization recorded by melt inclusions from Mount St. Helens volcano. *Geology*, 33(10), p.793. Available at: http://geology.gsapubs.org/cgi/doi/10.1130/G21668.1 [Accessed September 29, 2013].

Botcharnikov, R., Behrens, H & Holtz, F, 2006. Solubility and speciation of C–O–H fluids in andesitic melt at T=1100–1300°C and P=200 and 500MPa. *Chemical Geology*, 229(1-3), pp.125-143. Available at: http://linkinghub.elsevier.com/retrieve/pii/S0009254106000568 [Accessed September 21, 2013].

Bottinga, Y. & Weill, D.F., 1972. The viscosity of magmatic siilicate liquids: a model for calculation. *American Journal of Science*, 272, pp.438-475.

Burgisser, A. & Gardner, J.E., 2005. Experimental constraints on degassing and permeability in volcanic conduit flow. , pp.42-56.

Burnham, C.W., 1979. The importance of volatile constituents. In H. S. Yoder, ed. *The Evolution of Igneous Rocks, Fiftieth Anniversay Perspectives*. Princeton, NJ: Princeton University Press, pp. 439-482.

Burnham, C.W., 1981. The nature of multicomponent aluminosilicate melts. In D. T. Rickard & F. E. Wickman, eds. *Chemistry and Geochemistry at High Temperatures and Pressures*. New York: Pergamon Press, pp. 197-229.

Burnham, C.Wayne, 1975. Water and magmas; a mixing model. *Geochimica et Cosmochimica Acta*, 39(8), pp.1077-1084. Available at: http://linkinghub.elsevier.com/retrieve/pii/0016703775900502.

Cabrera, A. et al., 2011. Melt fracturing and healing : A mechanism for degassing and origin of silicic obsidian. *Geolog*, 39, pp.67-70.

Carey, R.J. et al., 2013. Convection in a volcanic conduit recorded by bubbles. *Geology*, 41(4), pp.395-398. Available at: http://geology.gsapubs.org/cgi/doi/10.1130/G33685.1 [Accessed March 20, 2013].

Di Carlo, I. et al., 2006. Experimental Crystallization of a High-K Arc Basalt: the Golden Pumice, Stromboli Volcano (Italy). *Journal of Petrology*, 47(7), pp.1317-1343. Available at: http://www.petrology.oxfordjournals.org/cgi/doi/10.1093/petrology/egl011 [Accessed May 15, 2013].

Carroll, M. & Blank, J., 1997. The solubility of H2O in phonolitic melts. *American Mineralogist*, 82, pp.549-556.

Castro, J. M. et al., 2008. Timescales of spherulite crystallization in obsidian inferred from water concentration profiles. *American Mineralogist*, 93(11-12), pp.1816-1822. Available at: http://ammin.geoscienceworld.org/cgi/doi/10.2138/am.2008.2904 [Accessed May 8, 2012].

Castro, Jonathan M. et al., 2012. Mechanisms of bubble coalescence in silicic magmas. *Bulletin of Volcanology*, 74(10), pp.2339-2352. Available at: http://www.springerlink.com/index/10.1007/s00445-012-0666-1 [Accessed December 10, 2012].

Crank, J., 1975. *The Mathematics of Diffusion*, Oxford: Clarendon Press.

Delaney, J.R. & Karsten, J.L., 1981. Ion microprobe studies of water in silicate melts. Concentration-dependent water diffusion in obsidian. *Earth and Planetary Science Letters*, 52(1), pp.191-202. Available at: http://linkinghub.elsevier.com/retrieve/pii/0012821X8190220X.

Della Ventura, G. et al., 2010. Application of micro-FTIR imaging in the Earth sciences. *Analytical and bioanalytical chemistry*, 397(6), pp.2039-49. Available at: http://www.ncbi.nlm.nih.gov/pubmed/20506014 [Accessed April 24, 2012].

Dingwell, D. B., 2006. Transport Properties of Magmas: Diffusion and Rheology. *Elements*, 2(5), pp.281-286. Available at: http://elements.geoscienceworld.org/cgi/doi/10.2113/gselements.2.5.281.

Dingwell, Donald B. & Webb, S.L., 1990. Relaxation in silicate melts. *European Journal of Mineralogy*, 2(4), pp.427-229.

Dingwell, Donald B. & Webb, S.L., 1989. Structural relaxation in silicate melts and non-Newtonian melt rheology in geologic processes. *Physics and Chemistry of Minerals*, 16(5), pp.508-516.

Dixon, J.E., Stolper, Edward M & Holloway, John R, 1995. An Experimental Study of Water and Carbon Dioxide Solubilities in Mid-Ocean Ridge Basaltic Liquids . Part I : Calibration and Solubility Models. , 3.

Fanara, S., Behrens, Harald & Zhang, Youxue, 2013. Water diffusion in potassium-rich phonolitic and trachytic melts. *Chemical Geology*, 346, pp.149-161. Available at: http://linkinghub.elsevier.com/retrieve/pii/S0009254112004573 [Accessed May 31, 2013].

Friedman, I. & Long, W., 2013. Rate of Obsidian Hydration. , 191(4225), pp.347-352.

Friedman, I. & Long, W., 1976. Rate of Obsidian Hydration. *Science*, 191(4225), pp.347-352.

Gardner, J.E., 2007. Bubble coalescence in rhyolitic melts during decompression from high pressure. *Journal of Volcanology and Geothermal Research*, 166(3-4), pp.161-176. Available at: http://linkinghub.elsevier.com/retrieve/pii/S0377027307002302 [Accessed March 20, 2012].

Gardner, J.E. et al., 2012. Compositional gradients surrounding spherulites in obsidian and their relationship to spherulite growth and lava cooling. *Bulletin of Volcanology*, 74(8), pp.1865-1879. Available at: http://www.springerlink.com/index/10.1007/s00445-012-0642-9 [Accessed November 5, 2012].

Gardner, J.E., Hilton, M. & Carroll, Michael R., 1999. Experimental constraints on degassing of magma: isothermal bubble growth during continuous decompression from high pressure. *Earth and Planetary Science Letters*, 168(1-2), pp.201-218. Available at: http://linkinghub.elsevier.com/retrieve/pii/S0012821X99000515.

Gardner, J.E. & Ketcham, R. a., 2011. Bubble nucleation in rhyolite and dacite melts: temperature dependence of surface tension. *Contributions to Mineralogy and Petrology*, 162(5), pp.929-943. Available at: http://link.springer.com/10.1007/s00410-011-0632-5 [Accessed September 7, 2013].

Giachetti, T. & Gonnermann, H.M., 2013. Water in volcanic pyroclast: Rehydration or incomplete degassing? *Earth and Planetary Science Letters*, 369-370, pp.317-332. Available at: http://linkinghub.elsevier.com/retrieve/pii/S0012821X13001623 [Accessed May 25, 2013].

Giordano, D et al., 2004. The combined effects of water and fluorine on the viscosity of silicic magmas. *Geochimica et Cosmochimica Acta*, 68(24), pp.5159-5168.

Giordano, D., Nichols, A.R.L. & Dingwell, D.B., 2005. Glass transition temperatures of natural hydrous melts: a relationship with shear viscosity and implications for the welding process. *Journal of Volcanology and Geothermal Research*, 142(1-2), pp.105-118. Available at: http://linkinghub.elsevier.com/retrieve/pii/S0377027304004056 [Accessed February 27, 2013].

Giordano, Daniele, Russell, J.K. & Dingwell, Donald B., 2008. Viscosity of magmatic liquids: A model. *Earth and Planetary Science Letters*, 271(1-4), pp.123-134. Available at: http://linkinghub.elsevier.com/retrieve/pii/S0012821X08002240 [Accessed February 12, 2013].

Gonnermann, H. & Manga, M., 2005. Nonequilibrium magma degassing: Results from modeling of the ca. 1340 A.D. eruption of Mono Craters, California. *Earth and Planetary Science Letters*, 238(1-2), pp.1-16. Available at: http://linkinghub.elsevier.com/retrieve/pii/S0012821X05005029 [Accessed April 7, 2012].

Goranson, R.W., 1938. Silicate-water systems: phase equilibria in the NaAlSi3O8-H2O and KAlSi3O8-H2O systems at high temperatures and pressures. *American Journal of Science*, 35A, pp.71-91.

Goranson, R.W., 1931. The solubility of water in granite magmas. *American Journal of Science*, 22, pp.481-502.

Gottsmann, J. & Dingwell, D B, 2001. Cooling dynamics of spatter-fed phonolite obsidian flows on Tenerife , Canary Islands. *Journal of Volcanology and Geothermal Research*, 105, pp.323-342.

Hao, T. & Riman, R.E., 2006. Calculation of interparticle spacing in colloidal systems. *Journal of Colloid and Interface Science*, 297(1), pp.374-7. Available at: http://www.ncbi.nlm.nih.gov/pubmed/16515794 [Accessed May 22, 2013].

Hauri, E. et al., 2002. SIMS analysis of volatiles in silicate glasses 1 . Calibration , matrix effects and comparisons with FTIR. *Chemical Geology*, 183, pp.99-114.

Helo, C. et al., 2013. High and highly variable cooling rates during pyroclastic eruptions on Axial Seamount, Juan de Fuca Ridge. *Journal of Volcanology and Geothermal Research*, 253, pp.54-64. Available at: http://linkinghub.elsevier.com/retrieve/pii/S0377027312003538 [Accessed April 7, 2013].

Hess, K.-U. & Dingwell, Donald B., 1996. Viscosities of hydrous leucogranitic melts : A non-Arrhenian model. *American Mineralogist*, 81, pp.1297-1300.

Holloway, John R, Dixon, J.E. & Pawley, A.R., 1992. An internally heated, rapid-quench, high-pressure vessel. *American Mineralogist*, 77(1991), pp.643-646.

Hui, H. et al., 2008. Pressure dependence of the speciation of dissolved water in rhyolitic melts. *Geochimica et Cosmochimica Acta*, 72(13), pp.3229-3240. Available at: http://linkinghub.elsevier.com/retrieve/pii/S0016703708001750 [Accessed December 5, 2012].

Hui, H. & Zhang, Youxue, 2007. Toward a general viscosity equation for natural anhydrous and hydrous silicate melts. *Geochimica et Cosmochimica Acta*, 71(2), pp.403-416. Available at: http://linkinghub.elsevier.com/retrieve/pii/S0016703706020722 [Accessed February 27, 2013].

Humphreys, M.C.S. et al., 2008. Magma ascent rates in explosive eruptions: Constraints from H2O diffusion in melt inclusions. *Earth and Planetary Science Letters*, 270(1-2), pp.25-40. Available at: http://linkinghub.elsevier.com/retrieve/pii/S0012821X08001581 [Accessed April 7, 2012].

Iacono, G., Schmidt, B.C. & Dolfi, D., 2007. Equilibrium and disequilibrium degassing of a phonolitic melt (Vesuvius AD 79 " white pumice ") simulated by decompression experiments. , 161, pp.151-164.

Iacono Marziano, G., Schmidt, B.C. & Dolfi, D., 2007. Equilibrium and disequilibrium degassing of a phonolitic melt (Vesuvius AD 79 "white pumice") simulated by decompression experiments. *Journal of Volcanology and Geothermal Research*, 161(3), pp.151-164. Available at: http://linkinghub.elsevier.com/retrieve/pii/S0377027306004069 [Accessed May 15, 2012].

Jacobs, G.K. & Kerrick, D.M., 1980. A simple rapid-quench design for cold-seal pressure vessels. *American Journal of Science*, 65, pp.1053-1056.

Jambon, a, Zhang, Y & Stolper, E M, 1992. Experimental dehydration of natural obsidian and estimation of DH2O at low water contents. *Geochimica et cosmochimica acta*, 56, pp.2931-5. Available at: http://www.ncbi.nlm.nih.gov/pubmed/11537205.

Karsten, J.L., Holloway, J.R. & Delaney, J.R., 1982. Ion microprobe studies of water in silicate melts: Temperature-dependent water diffusion in obsidian. *Earth and Planetary Science Letters*, 59(2), pp.420-428. Available at: http://linkinghub.elsevier.com/retrieve/pii/0012821X82901431.

Lange, R.A. & Carmichael, I.S.E., 1987. Densities of Na20-K20-Ca0-Mg0-Fe0-Fe203-A1203-Ti02-Si02 liquids : New measurements and derived partial molar properties. *Geochimica et Cosmochimica Acta*, 51, pp.2931-2946.

Larsen, J.F., 2008. Heterogeneous bubble nucleation and disequilibrium H2O exsolution in Vesuvius K-phonolite melts. *Journal of Volcanology and Geothermal Research*, 175(3), pp.278-288. Available at: http://linkinghub.elsevier.com/retrieve/pii/S0377027308001157 [Accessed May 15, 2012].

Larsen, J.F., Denis, M.-H. & Gardner, J.E., 2004. Experimental study of bubble coalescence in rhyolitic and phonolitic melts. *Geochimica et Cosmochimica Acta*, 68(2), pp.333-344. Available at: http://linkinghub.elsevier.com/retrieve/pii/S0016703703004125 [Accessed March 19, 2012].

Lensky, N.G, Navon, O & Lyakhovsky, V, 2004. Bubble growth during decompression of magma: experimental and theoretical investigation. *Journal of Volcanology and Geothermal Research*, 129(1-3), pp.7-22. Available at: http://linkinghub.elsevier.com/retrieve/pii/S0377027303002294 [Accessed March 25, 2012].

Lensky, Nadav G., Lyakhovsky, Vladimir & Navon, Oded, 2001. Radial variations of melt viscosity around growing bubbles and gas overpressure in vesiculating magmas. *Earth and Planetary Science Letters*, 186(1), pp.1-6. Available at: http://linkinghub.elsevier.com/retrieve/pii/S0012821X01002278.

Lesne, P. et al., 2011. Experimental Simulation of Closed-System Degassing in the System Basalt-H2O-CO2-S-Cl. *Journal of Petrology*, 52(9), pp.1737-1762. Available at: http://www.petrology.oxfordjournals.org/cgi/doi/10.1093/petrology/egr027 [Accessed February 28, 2013].

Liu, Y., Zhang, Youxue & Behrens, Harald, 2005. Solubility of H2O in rhyolitic melts at low pressures and a new empirical model for mixed H2O–CO2 solubility in rhyolitic melts. *Journal of Volcanology and Geothermal Research*, 143(1-3), pp.219-235. Available at: http://linkinghub.elsevier.com/retrieve/pii/S0377027305000442 [Accessed April 16, 2012].

Llewellin, E.W., Mader, H. M. & Wilson, S. D. R., 2002. The rheology of a bubbly liquid. *Proceedings of the Royal Society A: Mathematical, Physical and Engineering Sciences*, 458(2020), pp.987-1016. Available at: http://rspa.royalsocietypublishing.org/cgi/doi/10.1098/rspa.2001.0924 [Accessed September 7, 2013].

Long, W. & Friedman, I., 1968. The refractive index of experimentally hydrated rhyolite glass. *American Mineralogist*, 53, pp.1754-1756.

Lowenstern, J., 2001. Carbon dioxide in magmas and implications for hydrothermal systems. *Mineralium Deposita*, 36(6), pp.490-502. Available at: http://link.springer.com/10.1007/s001260100185 [Accessed May 30, 2013].

Mangan, M. & Sisson, T., 2000. Delayed , disequilibrium degassing in rhyolite magma : decompression experiments and implications for explosive volcanism. *Earth and Planetary Science Letters*, 183, pp.441-455.

Di Matteo, V. et al., 2004. Water solubility in trachytic melts. *Chemical Geology*, 213(1-3), pp.187-196. Available at: http://linkinghub.elsevier.com/retrieve/pii/S0009254104003419 [Accessed September 21, 2013].

Moitra, P. et al., 2013. Relating vesicle shapes in pyroclasts to eruption styles. *Bulletin of Volcanology*, 75(2), p.691. Available at: http://link.springer.com/10.1007/s00445-013-0691-8 [Accessed February 19, 2013].

Moore, G., Vennemann, T. & Carmichael, I.S.E., 1998. An empirical model for the solubility of H 2 O in magmas to 3 kilobars. *American Mineralogist*, 83(1964), pp.36-42.

Mourtada-Bonnefoi, C.C. & Laporte, D., 2004. Kinetics of bubble nucleation in a rhyolitic melt: an experimental study of the effect of ascent rate. *Earth and Planetary Science Letters*, 218(3-4), pp.521-537. Available at: http://linkinghub.elsevier.com/retrieve/pii/S0012821X03006848 [Accessed March 19, 2012].

Mungall, J.E. et al., 1996. Numerical modelling of stress generation and microfracturing of vesicle walls in glassy rocks. *Journal of Volcanology and Geothermal Research*, 73(1-2), pp.33-46. Available at: http://linkinghub.elsevier.com/retrieve/pii/0377027396000170.

Nakamoto, K., 1978. *Infrared and Raman spectra of inorganic and coordination compounds* 3rd ed., New York: Wiley.

Navon, Oded & Lyakhovsky, Vladimir, 1998. Vesiculation processes in silicic magmas. *Geological Society of London Special Publications*, 145, pp.27-50.

Newbury, D.E., 1975. Image formation in the scanning electron microscope. In J. I. Goldstein & H. Yakowitz, eds. *Practical Scanning Electron Microscopy*. New York: Plenum Press, pp. 95-148. Available at: http://link.springer.com/chapter/10.1007/978-1-4613-4422-3_4 [Accessed June 17, 2013].

Newman, S., Epstein, S. & Stolper, Edward M, 1988. Water, carbon dioxide, and hydrogen isotopes in glasses from the ca. 1340 A.D. eruption of the Mono Craters, California: Constraints on degassing phenomena and initial volatile content. *Journal of Volcanology and Geothermal Research*, 35(1-2), pp.75-96. Available at: http://linkinghub.elsevier.com/retrieve/pii/0377027388900078.

Newman, S. & Lowenstern, J.B., 2002. VolatileCalc: a silicate melt–H2O–CO2 solution model written in Visual Basic for excel. *Computers & Geosciences*, 28(5), pp.597-604. Available at: http://linkinghub.elsevier.com/retrieve/pii/S0098300401000814.

Newman, S., Stolper, Edward M & Epstein, S., 1986. Measurement of water in rhyolitic glasses : Calibration of an infrared spectroscopic technique. *American Mineralogist*, 71, pp.1527-1541.

Ni, Huaiwei, Liu, Y., et al., 2009. Water speciation and diffusion in haploandesitic melts at 743–873 K and 100MPa. *Geochimica et Cosmochimica Acta*, 73(12), pp.3630-3641. Available at: http://linkinghub.elsevier.com/retrieve/pii/S0016703709001823 [Accessed May 10, 2013].

Ni, Huaiwei, Behrens, Harald & Zhang, Youxue, 2009. Water diffusion in dacitic melt. *Geochimica et Cosmochimica Acta*, 73(12), pp.3642-3655. Available at: http://linkinghub.elsevier.com/retrieve/pii/S0016703709001872 [Accessed September 21, 2013].

Ni, Huaiwei, Xu, Z. & Zhang, Youxue, 2013. Hydroxyl and molecular H2O diffusivity in a haploandesitic melt. *Geochimica et Cosmochimica Acta*, 103, pp.36-48. Available at: http://linkinghub.elsevier.com/retrieve/pii/S0016703712006400 [Accessed May 10, 2013].

Ni, Huaiwei & Zhang, Youxue, 2008. H2O diffusion models in rhyolitic melt with new high pressure data. *Chemical Geology*, 250(1-4), pp.68-78. Available at: http://linkinghub.elsevier.com/retrieve/pii/S0009254108000806 [Accessed December 16, 2012].

Nichols, A.R.L. & Wysoczanski, R.J., 2007. Using micro-FTIR spectroscopy to measure volatile contents in small and unexposed inclusions hosted in olivine crystals. *Chemical Geology*, 242(3-4), pp.371-384. Available at: http://linkinghub.elsevier.com/retrieve/pii/S0009254107001763 [Accessed May 22, 2013].

Nowak, M. & Behrens, Harald, 2001. Water in rhyolitic magmas: getting a grip on a slippery problem. *Earth and Planetary Science Letters*, 184(2), pp.515-522. Available at: http://linkinghub.elsevier.com/retrieve/pii/S0012821X00003435.

Nowak, M. & Behrens, Harald, 1997. An experimental investigation on diffusion of water in haplogranitic melts. , (March 1996), pp.365-376.

Ochs III., F.A. & Lange, Rebecca A., 1997. The partial molar volume, thermal expansivity, and compressibility of H2O in NaAlSi3O8 liquid: new measurements and an internally consistent

model. *Contributions to Mineralogy and Petrology*, 129(2-3), pp.155-165. Available at: http://link.springer.com/10.1007/s004100050329.

Okumura, S. & Nakashima, S., 2006. Water diffusion in basaltic to dacitic glasses. *Chemical Geology*, 227(1-2), pp.70-82. Available at: http://linkinghub.elsevier.com/retrieve/pii/S0009254105003931 [Accessed May 15, 2012].

Papale, P., Moretti, R. & Barbato, D., 2006. The compositional dependence of the saturation surface of H2O+CO2 fluids in silicate melts. *Chemical Geology*, 229(1-3), pp.78-95. Available at: http://linkinghub.elsevier.com/retrieve/pii/S0009254106000532 [Accessed April 16, 2012].

Pitzer, K.S. & Sterner, S.M., 2000. Equations of state valid continuously from zero to extreme pressures for H20 and CO2. *Journal of Chemical Physics*, 01(4), pp.3111-3116.

Pitzer, K.S. & Sterner, S.M., 1994. Equations of state valid continuously from zero to extreme pressures for H20 and CO2. *Journal of Chemical Physics*, 101(4), pp.3111-3116.

Potts, P.J., 1987. *A Handbook of Silicate Rock Analysis*, Blackie.

Prousevitch, A.A., Sahagian, D.L. & Anderson, A T, 1993. Dynamics of Diffusive Bubble Growth in Magmas ' Isothermal. *Journal of Geophysical Research*, 98, pp.22283-22307.

Riciputi, L.R. et al., 2002. Obsidian Diffusion Dating by Secondary Ion Mass Spectrometry: A Test using Results from Mound 65, Chalco, Mexico. *Journal of Archaeological Science*, 29(10), pp.1055-1075. Available at: http://linkinghub.elsevier.com/retrieve/pii/S0305440301906922 [Accessed March 25, 2012].

Romano, C. et al., 1996. Tensile strengths of hydrous vesicular glasses: An experimental study. *American Mineralogist*, 81, pp.1148-1154.

Romine, W.L. et al., 2012. Thermal diffusivity of rhyolitic glasses and melts: effects of temperature, crystals and dissolved water. *Bulletin of Volcanology*, 74(10), pp.2273-2287. Available at: http://www.springerlink.com/index/10.1007/s00445-012-0661-6 [Accessed December 10, 2012].

Schmidt, B.C. & Behrens, Harald, 2008. Water solubility in phonolite melts: Influence of melt composition and temperature. *Chemical Geology*, 256(3-4), pp.259-268. Available at: http://linkinghub.elsevier.com/retrieve/pii/S0009254108002672 [Accessed May 15, 2012].

Scholze, H., 1960. Zur Frage der Unterscheidung zwischen H2O Molekeln und OH-Gruppen in Glasern und Mineralen. *Naturwissenschaften*, (47), pp.226-7.

Shaw, H.R., 1974. Diffusion of H2O in granitic liquids, I: experimental data; II: mass transfer in magma chambers. In A. W. Hofmann et al., eds. *Geochemical Transport and Kinetics*. Washington: Carnegie Institute of Washington, pp. 139-170.

Shaw, H.R., 1964. Theoretical Solubility of H2O in Silicate Melts Quasi-Crystalline Models. *The Journal of Geology*, 72(5), pp.601-617.

Shaw, H.R., 1972. Viscosities of magmatic silicate liquids: an empirical method of prediction. *American Journal of Science*, 272, pp.870-893.

Shea, T. et al., 2010. Linking experimental and natural vesicle textures in Vesuvius 79AD white pumice. *Journal of Volcanology and Geothermal Research*, 192(1-2), pp.69-84. Available at: http://linkinghub.elsevier.com/retrieve/pii/S0377027310000570 [Accessed May 15, 2012].

Silver, L.A., Ihinger, Phillip D. & Stolper, Edward M, 1990. The influence of bulk composition on the speciation of water in silicate glasses. *Contributions to Mineralogy and Petrology*, 104(2), pp.142-162. Available at: http://www.springerlink.com/index/10.1007/BF00306439.

Silver, L.A. & Stolper, Edward M, 1985. A Thermodynamic Model for Hydrous Silicate Melts. *Journal of Geology*, 93(2), pp.161-177.

Sparks, R.S.J., 1978. The dynamics of bubble formation and growth in magmas: a review and analysis. *Journal of Volcanology and Geothermal Research*, 3, pp.1-37.

Stolper, E. M., 1982. Water in Silicate Glasses: An Infrared Spectroscopic Study. *Contributions to Mineralogy and Petrology*, 81, pp.1-17.

Stolper, Edward M, 1989. Temperature dependence of the speciation of water in rhyolitic melts and glasses. *American Mineralogist*, 74, pp.1247-1257.

Stolper, Edward M, 1982. The speciation of water in silicate melts. *Geochimica et Cosmochimica Acta*, 46, pp.2609-2620.

Tamic, N., Behrens, Harald & Holtz, François, 2001. The solubility of H2O and CO2 in rhyolitic melts in equilibrium with a mixed CO2–H2O fluid phase. *Chemical Geology*, 174(1-3), pp.333-347. Available at: http://linkinghub.elsevier.com/retrieve/pii/S0009254100003247.

Tuffen, H., Dingwell, Donald B. & Pinkerton, H., 2003. Repeated fracture and healing of silicic magma generate flow banding and earthquakes? *Geology*, 31(12), p.1089. Available at: http://geology.gsapubs.org/cgi/doi/10.1130/G19777.1 [Accessed September 6, 2013].

Wallace, P.J., Dufek, J. & Anderson, Alfred T, 2003. Cooling rates of Plinian-fall and pyroclastic-flow deposits in the Bishop Tuff : inferences from water speciation in quartz-hosted glass inclusions. *Bulletin of Volcanology*, 65, pp.105-123.

Wasserburg, G.J., 1957. The Effects of H2O in Silicate Systems. *The Journal of Geology*, 65(1), pp.15-23.

Watkins, J. et al., 2008. Diffusion-controlled spherulite growth in obsidian inferred from H2O concentration profiles. *Contributions to Mineralogy and Petrology*, 157(2), pp.163-172. Available at: http://www.springerlink.com/index/10.1007/s00410-008-0327-8 [Accessed February 14, 2013].

Watkins, J.M., Manga, M. & DePaolo, D.J., 2012. Bubble geobarometry: A record of pressure changes, degassing, and regassing at Mono Craters, California. *Geology*, 40(8), pp.699-702. Available at: http://geology.gsapubs.org/cgi/doi/10.1130/G33027.1 [Accessed January 24, 2013].

Whittington, A. et al., 2001. The viscosity of hydrous phonolites and trachytes. *Chemical Geology*, 174(1-3), pp.209-223. Available at: http://linkinghub.elsevier.com/retrieve/pii/S000925410000317X.

Witham, F. et al., 2012. SolEx: A model for mixed COHSCl-volatile solubilities and exsolved gas compositions in basalt. *Computers & Geosciences*, 45, pp.87-97. Available at: http://linkinghub.elsevier.com/retrieve/pii/S0098300411003554 [Accessed September 19, 2013].

Xu, Z. & Zhang, Youxue, 2002. Quench rates in air, water, and liquid nitrogen, and inference of temperature in volcanic eruption columns. *Earth and Planetary Science Letters*, 200, pp.315-330.

Yamashita, S., 1999. Experimental Study of the Effect of Temperature on Water Solubility in Natural Rhyolite Melt to 100 MPa. *Journal of Petrology*, 40(10), pp.1497-1507. Available at: http://www.petrology.oxfordjournals.org/cgi/doi/10.1093/petroj/40.10.1497.

Yoshimura, S. & Nakamura, M., 2010. Chemically driven growth and resorption of bubbles in a multivolatile magmatic system. *Chemical Geology*, 276(1-2), pp.18-28. Available at: http://linkinghub.elsevier.com/retrieve/pii/S0009254110001749 [Accessed May 15, 2012].

Yoshimura, S. & Nakamura, M., 2008. Diffusive dehydration and bubble resorption during open-system degassing of rhyolitic melts. *Journal of Volcanology and Geothermal Research*, 178(1), pp.72-80. Available at: http://linkinghub.elsevier.com/retrieve/pii/S0377027308000565 [Accessed May 15, 2012].

Zhang, Y., 2010. Diffusion in Minerals and Melts: Theoretical Background. In *Reviews in Mineralogy and Geochemistry*. pp. 5-59. Available at: http://rimg.geoscienceworld.org/cgi/doi/10.2138/rmg.2010.72.2 [Accessed September 17, 2013].

Zhang, Y. & Ni, H., 2010. Diffusion of H, C, and O Components in Silicate Melts Youxue Zhang & D. J. Cherniak, eds. *Reviews in Mineralogy and Geochemistry*, 72(1), pp.171-225. Available at: http://rimg.geoscienceworld.org/cgi/doi/10.2138/rmg.2010.72.5 [Accessed July 28, 2012].

Zhang, Youxue, 1999. H20 IN RHYOLITIC GLASSES AND MELTS ’ MEASUREMENT ,. , pp.493-516.

Zhang, Youxue, Belcher, R., et al., 1997. New calibration of infrared measurement of dissolved water in rhyolitic glasses. *Geochimica et Cosmochimica Acta*, 61(15), pp.3089-3100.

Zhang, Youxue et al., 2007. SILICATE MELT PROPERTIES AND VOLCANIC ERUPTIONS. *Reviews of Geophysics*, (2006), pp.1-27.

Zhang, Youxue & Behrens, Harald, 2000. H2O diffusion in rhyolitic melts and glasses. *Chemical Geology*, 169(1-2), pp.243-262. Available at: http://linkinghub.elsevier.com/retrieve/pii/S0009254199002314.

Zhang, Youxue, Jenkins, J. & Xu, Z., 1997. Kinetics of the reaction H2O+O=2OH in rhyolitics glasses upon cooling: Geospeedometry and comparison with glass transition. *Geochimica et Cosmochimica Acta*, 61(11), pp.2167-2173.

Zhang, Youxue & Stolper, E M, 1991. Water diffusion in a basaltic melt. *Nature*.

Zhang, Youxue, Stolper, E M & Ihinger, P D, 1995. Kinetics of the reaction H2O + O = 2OH in rhyolitic and albitic glasses: Preliminary results. *American Mineralogist*, 80, pp.593-612.

Zhang, Youxue, Stolper, E M & Wasserburg, G.J., 1991. Diffusion of a multi-species component and its role in oxygen and water transport in silicates K = [OH] 2 /{[H20][Odry] }. , 103, pp.228-240.

Zhang, Youxue & Xu, Z., 2007. A long-duration experiment on hydrous species geospeedometer and hydrous melt viscosity. *Geochimica et Cosmochimica Acta*, 71(21), pp.5226-5232. Available at: http://linkinghub.elsevier.com/retrieve/pii/S0016703707005200 [Accessed December 8, 2012].

Zhang, Youxue, Xu, Z. & Behrens, Harald, 2000. Hydrous species geospeedometer in rhyolite : Improved calibration and application. *Geochimica et Cosmochimica Acta*, 64(19), pp.3347-3355.

Zhang, Youxue, Xu, Z. & Liu, Y., 2003. Viscosity of hydrous rhyolitic melts inferred from kinetic experiments, and a new viscosity model. *American Mineralogist*, 88(1996), pp.1741-1752.